NASA Technical Memorandum 107318

RL10A–3–3A Rocket Engine Modeling Project

Michael Binder
NYMA, Inc.
Brook Park, Ohio

Thomas Tomsik and Joseph P. Veres
Lewis Research Center
Cleveland, Ohio

January 1997

National Aeronautics and
Space Administration

TABLE OF CONTENTS

15. Figures

Figures—Continued

1. INTRODUCTION

The RL10A rocket engine is an important component of the American space infrastructure. Two RL10 engines form the main propulsion system for the Centaur upper stage vehicle, which boosts commercial, scientific, and military payloads from a high altitude into Earth orbit and beyond (planetary missions). The Centaur upper stage is used on both Atlas and Titan launch vehicles. The initial RL10A-1 was developed in the 1960's by Pratt & Whitney, under contract to NASA. The RL10A-3-3A, RL10A-4, and RL10A4-1 engines used today incorporate component improvements but have the same basic configuration as that of the original RL10A-1 engine. RL10's have been highly reliable servants of America's space program for over 30 years.

The RL10's high reliability record has been marred in recent years by two in-flight failures. In the first instance, the cause was initially believed to be Foreign Object Damage of the fuel pump. In the second instance, the cause of failure was determined to be contamination of the fuel pump by atmospheric nitrogen which leaked through a check valve during launch ascent. The nitrogen froze on the impeller and prevented pump rotation during start. In hindsight, it is likely that the first failure was also due to frozen atmospheric nitrogen. During the course of the accident investigations, the desire for an independent RL10 simulation capability was expressed within NASA and by the Air Force. At that time, the only system models for the engine were the property of Pratt & Whitney and of the Aerospace Corporation. These models are not suitable for public dissemination or government use. The Space Propulsion Technology Division (SPTD) at the NASA Lewis Research Center took up the challenge of creating an independent and accurate model of the RL10A-3-3A engine.

The SPTD began developing a computer model of the RL10A-3-3A in 1990 (Reference 1). The first system model was based entirely on data and information provided by Pratt &Whitney. Component data from Pratt & Whitney was integrated to form a system model using the ROcket Engine Transient Simulator (ROCETS) code. In 1993, a project team was formed, consisting of experts in the areas of turbomachinery, combustion, and heat transfer. The goals of this project have been to enhance our understanding of the RL10 engine and its components, and to improve the baseline engine system model where possible. A combination of simple engineering correlations, detailed component analyses and engineering judgement have been used to accomplish these tasks. If desired, it should be a relatively simple task to create models of the RL10A-4 and RL10A4-1 as well, using the work done here for the RL10A-3-3A as a foundation.

A second goal of this project was to benchmark our tools and methods for modeling new rocket engine components and systems, for which test data may not yet be available. An existing engine with a long test and flight history (the RL10A-3-3A) was used as the validation test-case.

In this report, we introduce the reader to the RL10 engine, define the SPTD project organization and goals, briefly discuss results of the various component modeling efforts, and describe the new RL10 system model created. The appendices contain detailed descriptions of the various component analyses performed in support of the project.

2. OVERVIEW OF THE RL10A-3-3A ROCKET ENGINE

2.1 Engine system configuration and operation

The RL10 engine is based on an expander cycle, in which the fuel is used to cool the main combustion chamber and the thermal energy added to the fuel drives the turbopumps. A schematic diagram of the engine is shown in Figure 2.1.1. The fuel turbine drives both the fuel and oxidizer pumps (the latter being driven via a gear train). The RL10 engine starts by using the pressure difference between the fuel tank and the nozzle exit (upper atmospheric pressure), and using the ambient heat stored in the metal of the cooling jacket walls. The engine 'bootstraps' to full-thrust within two seconds after ignition. The RL10A-3-3A system normally operates at a chamber pressure of 475 psia, a mixture ratio (O/F) of 5.0, and a thrust of 16,500 lbf (73400 N).

Before start, the fuel pump is cooled with hydrogen from the tanks to prevent cavitation at engine start. The fuel cooldown valves (see Figure 2.1.1) are open and the main fuel shut-off valve (FSOV) is closed. The fuel flow is vented overboard through the cooldown valves and does not flow through the rest of the system; the latent heat in the metal of combustion chamber cooling jacket is therefore available to help drive the start transient. The LOX pump is pre-chilled by a flow of oxygen, which passes through the Oxidizer Control Valve (OCV) and is vented through the combustion chamber and nozzle.

A typical plot of valve movement during engine start is shown in Figure 2.1.2. To initiate start, the FSOV is opened and the fuel-pump discharge cool-down valve (FCV2) is closed. The interstage cool-down valve (FCV1) remains partially open in order to avoid stalling of the fuel pump during engine acceleration. The pressure drop between the fuel inlet and the combustion chamber drives fuel through the cooling jacket, picking up heat from the warm metal. This pressure difference also drives the warmed fluid through the turbine, starting rotation of the pumps, which drive more propellant into the system. At start, the OCV also closes partially, restricting the flow of oxygen into the combustion chamber. This is done to limit chamber pressure and ensure a forward pressure difference across the fuel turbine after ignition of the thrust chamber.

Ignition of the main combustion chamber usually occurs approximately 0.3 seconds after the main-engine start signal is given (for first-burns). The ignition source is an electric spark. Ignition provides more thermal energy to drive the turbine. As the turbopumps accelerate, engine pneumatic pressure is used to close the interstage cooldown valve completely and open the OCV at pre-set fuel and LOX pump discharge pressures. The OCV typically opens very quickly and the resultant flood of oxygen into the combustion chamber causes a sharp increase in system pressures. During this period of fast pressure rise, the thrust control valve (TCV) is opened, regulated by a pneumatic lead-lag circuit to control thrust overshoot. The engine then settles to its normal steady-state operating point.

The primary difference between first and second burn start transient is the initial cooling jacket metal temperature; it is about 540 R for a first start, and about 350 R for the second. Other parameters which may vary from engine to engine, or from run to run include the turbopump friction torque, the propellant tank conditions, and the time of ignition.

Figure 2.1.3 shows valve movement for a typical shutdown sequence. The FSOV and Fuel Inlet Valve (FINV) close as the fuel-pump cooldown valves open, allowing fuel to drain out of the system through the overboard vents. The combustion process is soon starved of fuel and the

flame goes out. The OCV and Oxidizer Inlet Valve (OINV) begin to close next, cutting off the flow of oxygen through the engine. The turbopump decelerates due to friction losses and drag torque created by the pumps as they evacuate the remaining propellants from the system. During this process, pump cavitation and reverse-flow are likely.

The symbols and model component names used herein are found in appendixes I and J.

2.2 Fuel Turbopump

A cross sectional view of the fuel turbopump is shown in Figure 2.2.1. The fuel pump consists of two stages, separated by an interstage duct, which is vented via the interstage cooldown valve (FCV1) during start. Both fuel pump stages have centrifugal impellers, vaneless diffusers and conical exit volutes; the first stage also has an inducer.

The RL10 turbine is a two-stage axial-flow, partial admission, impulse turbine (Reference 1). Downstream of the turbine blade rows, exit guide vanes reduce swirling of the discharged fluid. The turbine is driven by hydrogen and powers both the fuel and oxidizer pumps.

There are a number of shaft seals which permit leakage from the pump discharge in order to cool the bearings. The fuel pump and turbine are on a common shaft; power is transferred to the LOX pump through a series of gears. The seals, bearings, and gear train all contribute to rotordynamic drag on the turbopump.

Table 2.2.1
Summary of Fuel Turbopump Characteristics

	1st stage	2nd stage
Pump Impeller Diameter	7.07 in	7.07 in
Pump Exit Blade Height	0.230 in	0.220 in
Pump Head[1]	16969 ft	17989 ft
Pump Mass Flow[1]	6.051 lbm/sec	6.008 lbm/sec
Pump Temperature Rise[1]	9.23 R	10.2 R
Pump Efficiency[1]	0.5810	0.5619
Shaft Speed[1]	31537 rpm	

	Combined stage
Turbine Meanline Diameter	5.90 in
Turbine Pressure Ratio (T-T)[1]	1.39
Turbine Mass Flow[1]	5.89 lbm/sec
Turbine Temperature Drop[1]	24.5 R
Shaft Speed[1]	31537 rpm

TP Mass Moment of Inertia (incl. Ox Pump)[2]	0.0776 lbf•in•sec^2
TP Drag Torque (incl. Ox Pump)[2]	20.0 lbf•in

[1] values taken at typical engine operating point as predicted by the model.
[2] values are taken with reference to the fuel pump shaft.

2.3 Oxygen (LOX) Pump

A cross section view of the LOX pump is shown in Figure 2.3.1. The LOX pump consists of an inducer and a single centrifugal impeller, followed by a vaneless diffuser and conical exit volute. The LOX pump is driven by the fuel turbine though a gear train as described above. The turbopump speed sensor is located on the LOX pump shaft.

Table 2.3.1
Summary of LOX Pump Characteristics

Pump Impeller Diameter	4.20 in
Pump Exit Blade Height	0.251 in
Pump Head[1]	1212 ft.
Pump Mass Flow[1]	31.40 lbm/sec
Fluid Temperature Rise[1]	3.85 R
Pump Efficiency[1]	0.6422
Shaft Speed[1]	12615 rpm

[1] values taken at typical engine operating point as predicted by the model.

2.4 Regenerative cooling jacket

The regenerative cooling jacket serves several functions in the RL10 engine. The basic configuration is a pass-and-a-half stainless-steel tubular design, as depicted in Figure 2.4.1 (from Reference 2). Fuel enters the jacket via a manifold located just below the nozzle throat. A set of 180 'short' stainless-steel tubes carry coolant to the end of the nozzle. At the nozzle exit plane, a turn-around manifold directs flow back through a set of 180 'long' tubes. The long tubes are interspersed with the short tubes in the nozzle section and comprise the chamber cooling jacket above the inlet manifold. Coolant flow exits through a manifold at the top of the chamber. The cooling tubes are brazed together and act as the inner wall of the combustion chamber and nozzle. The structure of the chamber is reinforced with metal bands and a 'girdle' around the throat section. The cooling jacket therefore acts as a structural component of the chamber, provides cooling of the chamber walls, and transfers thermal energy required to drive the turbomachinery.

Table 2.4.1
Summary of Cooling Jacket Characteristics

Total Coolant Volume	966.1 cu.in
Typical Hot Wall Thickness	0.013 in
Hot-gas-side Effective Surface Area	7200 in^2
Pressure Drop[1]	242.1 psid
Mass Flow[1]	5.973 lbm/sec
Temperature Rise[1]	344.4 R
Total Heat Transfer Rate[1]	7994 Btu/sec

[1] values taken at typical engine operating point as predicted by the model.

2.5 Combustion Chamber and Nozzle

The combustion chamber and nozzle walls are composed of the cooling tubes as described above. A silver throat (as shown in Figure 2.4.1) is cast in place for the RL10A-3-3A and increases the nozzle expansion ratio for higher specific impulse.

The injector has 216 coaxial elements; the LOX is injected through the center of each element and hydrogen through the annulus (Figure 2.5.1). One-hundred-Sixty-two (162) of the LOX injector elements have ribbon flow-swirlers that provide enhanced combustion stability .

An augmented spark ignitor is located in the center of the injector face. Gaseous oxygen is supplied to the ignitor from a point in the engine just upstream of the injector inlet manifold. Fuel for the ignitor flows from the fuel injector plenum through holes in the ignitor wall. The fuel and oxygen flows are mixed and ignited with an electric spark.

Table 2.5.1
Summary of Combustion-Chamber / Nozzle Characteristics

Chamber Diameter	5.13 in
Throat Diameter	2.47 in
Nozzle Area Ratio	61.0
Combustion Pressure (injector face static)[1]	482.0 psia
Combustion Temperature[1]	5888 R
Mixture Ratio (O/F)[1]	5.26
Mass Flow[1]	37.36 lbm/sec
Gross Thrust[1]	16452 lbf
c-star Efficiency[1]	0.9892
c-star[1]	7824 in/sec
Specific Impulse[1]	440.3 sec

[1] values taken at typical engine operating point as predicted by the model.

2.6 Valves, Ducts and Manifolds

The RL10A-3-3A includes seven engine valves as shown in Figure 2.1.1 and described in Table 2.6.1. The propellant flows to the engine can be shut off using the Fuel Inlet Valve (FINV) and the Oxidizer Inlet Valve (OINV). The fuel flow into the combustion chamber from the rest of the engine can be stopped by the Fuel Shut-off Valve (FSOV) located just upstream of the injector plenum. Fuel used to pre-chill the fuel pumps before engine start is vented overboard through two valves (FCV1 and FCV2). The Thrust Control Valve (TCV) is used to control thrust overshoot at start and maintain constant chamber pressure during steady-state operation. The valve is actuated by the differential pressure between the turbine inlet and combustion chamber. The Oxidizer Control Valve (OCV) has a two orifices; one regulates the main oxidizer flow and the other controls the bleed flow required during engine start. The main-flow orifice in the OCV is actuated by the differential pressure across the LOX pump. Figure 2.1.2 shows the time schedules of

various valves during start, Figure 2.1.3 shows similar schedules for shutdown.

Ducts and manifolds in the RL10 are generally made out of stainless-steel and are not insulated. The venturi upstream of the turbine is designed to help stabilize the thrust control. The venturi is choked during start but not at the engines intended operating point. Heat transfer in ducts and manifolds is not considered significant during normal engine operation.

Table 2.6.1
Summary of Major Duct and Valve Characteristics

Resistence Name	Flow Area (in^2)	delta-P (psid) (typical)	Flow (lbm/sec) (typical)
Fuel Inlet Valve[1]	6.34	0.472	6.05
F Pump Interstg Cooldwn Valve[1]	0.60	13.5	0.71
F Pump Disch Cooldwn Valve[1]	0.30	12.5	0.32
Fuel Pump Disch Duct	1.77	39.5	5.97
Fuel Venturi (inlet : throat area)	3.55 : 1.05	17.5	5.97
Thrust Control Valve[2]	0.0158 [3]	234	0.0839
Turbine Disch Housing (inlet : exit)	20.2 : 4.53	18.0	5.89
Turbine Disch Duct	4.53	10.3	5.97
Fuel Shut-off Valve[1]	3.24	38.2	5.97
Fuel Injectors (total)	2.30	62.3	5.97
Oxidizer Inlet Valve[1]	6.34	0.798	31.4
Oxidizer Control Valve[2]	0.615 [3]	84.8	31.4
Oxidizer Injectors (total)	2.08	66.8	31.4

[1] values at full open position
[2] values at nominal full-thrust condition (predicted by model).
[3] this flow area includes the discharge coefficient for the orifice, which is unknown.

3. PROJECT ORGANIZATION AND GOALS

Technical management of the RL10 Modeling Project was organized according to technical discipline. In this case, the discipline areas were 1) turbomachinery, 2) combustion and heat transfer, 3) ducts and valves, and 4) system simulation. The entire team consisted of seven members, including NASA personnel, support service contractors and academic grant participants. A detailed list of the members and their respective disciplines is given in the acknowlegements section at the end of the report. The technical goals for the project are outlined below.

3.1 Turbomachinery Modeling Goals

1) Consolidate data from different sources to create a consistent set of pump and

turbine performance characteristics for normal operating conditions.

2) Extend the pump and turbine performance maps to include engine start and shutdown transient conditions.

3) Benchmark our analytic capabilities for pumps and turbines over a wider range of operating conditions (using available RL10 test data).

3.2 Combustion and Heat Transfer Modeling Goals

1) Develop a computer model of heat transfer in the thrust chamber cooling jacket.

2) Develop a one-dimensional model of combustion in the thrust chamber and of hot gas flow through the nozzle.

3) Develop improved hydrogen-oxygen combustion property tables to replace the tables delivered with the ROCETS program.

4) Extend existing data tables of combustion and nozzle performance (c*-efficiency and specific impulse) to better cover start and shut-down transient conditions.

5) Develop a model of two-phase flow through the nozzle throat.

6) Develop a model of the fuel-to-oxidizer heat transfer in the injector plenum.

7) Benchmark our analytic capabilities for thrust chamber injectors, nozzles, and cooling jackets (using available RL10 test data).

3.3 Ducts, Manifolds, and Valves Modeling Goals

1) Determine flow areas, lengths, and volumes for engine components based on blueprints. Verify estimates using information provided by Pratt & Whitney.

2) Determine flow resistances for engine components based on simple one-dimensional correlations. Verify using information provided by Pratt & Whitney.

3) Develop models of two-phase flow for the fuel cool-down valves, oxidizer control valve, and oxidizer injector.

3.4 System Modeling Goals

2) Evaluate the results of all component analyses described above. Identify those results which warrant inclusion in the system model.

3) Use available engine test data to refine typical valve actuation schedules specified by Pratt & Whitney.

4) Run simulations with the new system model and compare output with available test data (start transient operation, steady-state performance, shut-down transient behavior).

5) Use the new system model to characterize the effects of variations in operating conditions on system performance (time to accelerate, steady-state levels, etc.).

6) Benchmark our overall analytic capabilities for rocket propulsion systems.

4. COMPONENT MODELING RESULTS

4.1 Turbomachinery Modeling Results

4.1.1 Verification of Pump Performance Test Data

Several sources of RL10 pump performance data exist. The systems group at Pratt & Whitney provided NASA LeRC with a set of pump performance maps and polynomial functions. We also received a separate set of pump test data from the Pratt & Whitney turbomachinery group. The first task was therefore to consolidate these different sources of data, if possible.

The performance maps provided by the P&W systems group show head coefficient and efficiency as functions of flow coefficient for each of the three pump stages. Maps of speed correction factors to pump efficiency were also provided. The performance characteristics of the fuel and LOX pump inducers had been lumped with those of the impellers in these maps. These maps are shown in Figures 4.1.1 through 4.1.8.

Comparison of these map data with those provided by the turbomachinery group indicate that the two data sets are approximately the same. It appears, however, that the maps provided by the systems group are actually extrapolations from test data for flow coefficients greater than 0.62. This conclusion was supported by subsequent discussions with P&W engineers. A number of other small discrepancies (on the order of 1% to 2%) were also noted, and may be due to non-ideal speed effects, changes in fluid density between pump stages, or differences in rotating clearance.

Despite these minor differences, it was concluded that the performance maps provided by the P&W systems group are based on test data for flows near the design conditions. Map data at very high values of flow coefficient were, however, concluded to be extrapolations only, and can be replaced when extending the maps to cover start conditions.

4.1.2 Extension of Pump Maps for Start and Shutdown Conditions

At start, the pumps are not rotating although there is an appreciable cool-down flow. The flow coefficients during start are much higher than the values found in the test data, and it is necessary to extend the maps to cover this region of operation. During shutdown, a very wide range of flow-coefficients are encountered; both cavitation and surge are likely to occur.

The first consideration that must be addressed when extending the pump maps is their form. In order to represent pump performance for conditions ranging from zero speed with non-zero flow to the zero flow with non-zero speed, a rather unconventional map form is required. Common practice is to plot pump performance as efficiency and head-coefficient (which is the head divided by speed-squared) as a function of flow coefficient (which is volumetric flow divided by speed). Using this mapping approach, however, the head-coefficient and flow-coefficient would both be undefined (infinite) at zero speed. A less conventional approach is to map head and torque, divided by the sum of the squares of the volumetric flow and speed, plotted versus the arctangent of speed over flow.

$$h = \Delta Head / (N^2 + Q^2) \text{ vs. } atan(N/Q)$$

$$\beta = \tau / (N^2 + Q^2) \text{ vs. } atan(N/Q)$$

This method eliminates most concerns of zero quantities producing singularities . To simplify the comparison with generic map curves, it is possible to normalize these relations using the head, torque, speed, and volumetric flow at the point of maximum pump efficiency (Reference 3).

4.1.2.1 Extension of Pump Maps to START Conditions : In order to extend the RL10 pump maps to cover the start conditions, two approaches were considered. The first approach considered was to use detailed one-dimensional pump performance analysis programs. These codes use the pump geometry and inlet fluid conditions to predict the head-rise and efficiency as functions of flow and shaft speed (References 4 and 5). In order to test the accuracy of the detailed pump models, the predicted performance was compared first with test data at conditions around the engine design point. The predicted head maps were reasonably close to test data but the predicted efficiencies were significantly lower than test data would indicate. Normally, empirical data would be used to adjust certain parameters in the model to match the pump design performance. This was not done for the RL10 because one of our research objectives was to test our capability to model new designs for which test data does not yet exit. Because this design-point adjustment to test data was not done for the RL10, there was some doubt on how accurate predictions of the low-speed performance would be. Low-speed pump simulations were done to provide qualitative information about performance at start. A more detailed discussion of these analyses are given in Appendix B.

The second approach considered was to use a combination of available test data, qualitative information from the detailed analyses, and generic pump performance curves found in References 3, 6, and 7. The generic maps were derived primarily for water pumps; their application to cryogenic pumps appears valid based on the results from the detailed analyses. The generic pump maps and analysis results were used to define only the shapes of the map extensions; these curve shapes were fit to match the RL10 pump test-stand data at near-design conditions.

The generic performance curves for head-rise and torque (from Reference 3) are shown in Figures 4.1.9. There were two basic shapes that the generic data could take for head-rise, one curve levels off at low-speeds and the other shape turns down (depending on pump specific-speed). The detailed pump analyses indicated that the head curves would turn down at low speeds for the first stage fuel pump; this might be due to the backward sweep of the impeller or the axial flow through the inducer section. These analyses also indicated that the second stage fuel pump and LOX pump head-rise maps should level-out at low speeds; these pump stages have radial blades, although the LOX pump also has an axial-flow inducer. Simple sub-system models of the pumps were used to find zero-speed map values that would be consistent with engine test data. Finally, complete performance curves were fit to match the test data at higher speeds, pass through the zero-speed intercepts and have the desired shape for each pump stage. The final results are shown in Figures 4.1.10 through 4.1.15. The extended torque performance curves shown in the figures are further modified by the appropriate speed correction curves given in Figures 4.1.5 and 4.1.8.

4.1.2.2 Extension of Pump Maps to SHUT-DOWN Conditions : During the engine shutdown, a different combination of off-design conditions appears to exist, including pump cavitation and reverse flow. Proper simulation of these effects is complicated by their interaction with each other. From available test data and simulation output, it appears that as the fuel inlet valve closes and the cool-down valves open, the pump first cavitates due to a combination of changes in pump loading and cut-off of the inlet flow. The cavitation causes the pump performance to degrade rapidly until the pump cannot prevent the reverse flow of fluid as it comes backward through the cooling jacket. When the reversed flow reaches the closed fuel inlet valve, however, extreme transients of pressure and flow are created. Similar effects are encountered in the LOX pump during shutdown as well.

The pump head and torque performance characteristics during this period of operation are, of course, not extensively documented in test data. The generic pump characteristics found in References 3 and 6 have been used again to extend the performance maps for cavitation and reverse flow. The maxima and minima of the curves in this operating region were varied until a reasonable match with engine shutdown test data was achieved. Due to limitations of schedule and manpower, no attempt was made to predict the post-cavitation and stall behavior of the pumps using the detailed component analysis tools available. It is likely, in any case, that these tools would require significant modification to examine such pump conditions; modifications of this kind were beyond the scope of this project.

The pump map extensions for engine shutdown are included in Figures 4.1.10 through 4.1.15. Although the engine start and shutdown models use the same pump performance maps, the cavitation and reverse flow effects also require additional logic. This logic is not required (or even desirable) in the start model. The interested reader is referred to subroutines PUMPSD, FPASDMP, FPBSDMP and OPSDMP in the model (see Appendix A) for documentation of these changes.

4.1.2.3 Effects of Density Changes on Pump Performance Models : The issue of propellant phase-change (liquid to gas) has not been adequately addressed in the generic maps or detailed analyses described above. It has been noted that using cryogens, numerical instabilities were encountered in the start simulation due to the effects of fluid changing density in the pumps. Engine test data, although limited, appears to indicate that these density instabilities do not actually occur in the pumps during start. In order to obtain stable and reliable calculations, it was necessary to limit density changes within each stage of the pumps until pumped operation begins . For the start simulation, if the discharge density is lower than the inlet density, the discharge pressure is calculated from head-rise using only the inlet density.

$$P_{discharge} = P_{inlet} + \Delta Head * \rho_{inlet}$$

Once pumped operation begins, the standard expression for discharge pressure is used in the start model:

$$P_{discharge} = (P_{inlet}/\rho_{inlet} + \Delta Head) * \rho_{discharge}$$

During engine shutdown, the propellant densities at the pump inlets may, in reality, approach zero. Numerical instabilities will arise using either the upstream or downstream

density alone. For the shutdown model, we will instead use the average fluid density:

$$P_{discharge} = P_{inlet} + \Delta Head * \rho_{average}$$

This expression is used throughout the shutdown model, regardless of conditions at the inlet or discahrge. Because the expressions for discharge pressure differ between start and shutdown models, the predicted steady-state operating points will also be slightly different for the two models.

4.1.3 Verification of Fuel Turbine Performance Test Data

The turbine performance maps provided by Pratt & Whitney depict the combined performance of the two stages. The turbine's flow resistance is modeled as isentropic flow through an orifice and the map describes the effective area (area times discharge coefficient) as a function of velocity ratio (u/c_0) for several different pressure ratios. In the course of this project, two different flow-resistance models were found. The first model was based on linear functions and were intended for use only near the design operating conditions. The second model was represented by non-linear map curves and were apparently better suited for start transient engine simulations. The two models unfortunately disagree at the design point, which has lead to errors in engine steady-state performance predictions. Attempts to consolidate the two data sets have not been satisfactory. Nor have we been able to locate additional data or human experts who could resolve the differences in data. We decided to use the transient (non-linear) data map (as shown in Figure 4.1.16) and accept the steady-state error for now. Additional research may succeed in resolving this conflict in the future.

The combined two-stage turbine efficiency map provided by P&W is shown in Figure 4.1.17. No additional data was available to cross-check this map.

4.1.4 Extension of Turbine Maps

The turbine maps provided by Pratt & Whitney (as discussed above) already extend to the low speed region (to zero speed) and did not require extension (see Figures 4.1.16 and 4.1.17). Although these maps may also have been extrapolated from higher speed data, the low-speed information was judged to be reasonable for the turbine.

In order to calculate the starting torque of the turbine (no rotation as flow starts), it was necessary to address a zero-divided-by-zero problem (zero efficiency divided by zero speed). This was resolved using l-Hopital's Rule, which states that when approaching a 0/0 point, the value of the ratio is the same as the slope of the ratio at that point. It was found that using this solution, the predicted starting torque approximately equals the value estimated from engine test data.

A detailed component analysis of the turbine was also performed for this project (Reference 8). Preliminary analyses predicted overall (two-stage) turbine efficiency values that were 2% to 10% lower than those specified by Pratt & Whitney. The modeling results for turbine flow resistance were not able to resolve the conflict between the two different data sets as discussed in the previous section. As with the pump analysis discussed previously, it is common practice to adjust the turbine model to better match test data, when available. Such adjustments were considered inconsistent with the research goal of benchmarking our capability to model new designs, and therefore no adjustments were made. The detailed turbine analysis was not pursued further but is described in Appendix C.

In the course of our modeling work with the RL10 turbine, it was discovered that even slight

differences in the turbine efficiency map may cause significant differences in the start timing of the engine. The extreme sensitivity of the engine start timing to small variations in turbine efficiency may have profound significance for our ability to accurately model the start of new engines for which detailed component test data is not yet available. This issue is discussed in greater detail in Appendix C.

4.2 Combustion and Heat Transfer Modeling Results

4.2.1 Enhanced combustion gas properties

The ROCETS code (Reference 9) was originally developed with a built-in set of hydrogen/oxygen combustion tables. These tables provided gas thermal and transport properties at a specified pressure, temperature and mixture ratio. Many of the calculations in these tables involved applying corrections to more basic tables and assumed ideal, isentropic gas behavior. A comparison of the property table output with the NASA CET93 one-dimensional-equilibrium (ODE) code (Reference 10) indicated some significant discrepancies. The original tables have therefore been replaced with data tables generated specifically for the RL10A-3-3A model using the CET93 code. CET93 was used to determine the equilibrium-composition hot-gas properties at several axial locations along the length of the thrust chamber and nozzle.

Generating a complete set of tables for all conditions and expansion ratios proved to be more difficult than expected. At the extreme limits of pressure and mixture ratio present during the RL10 start transient, the propellants may actually freeze as they expand through the nozzle, creating a snow flurry at the engine discharge. Given the injector-face pressure, propellant mixture enthalpy and mixture ratio, the pressure, temperature and enthalpy of the combustion products were tabulated at several values of expansion ratio throughout the thrust chamber and nozzle. The other thermal and transport properties required by the system model were tabulated as functions of pressure, temperature and mixture ratio (and are not considered explicit functions of expansion ratio). Table 4.2.1 gives the range of conditions and the expansion ratios included in the new RL10 hot-gas property tables.

4.2.2 Cooling Jacket Heat Transfer Model

In this project, several approaches were explored for modeling the heat-transfer in the RL10A-3-3A cooling jacket. These approaches included empirical models, first-principle physical models, and several combinations of theory and test data. In this section, we describe only the analytic approach selected for the final engine system model. The other methods which we considered are discussed in greater detail in Appendix D.

Predicting heat transfer appears to be something of an art. The original jacket cooling model for the RL10 steady-state model was based on test data alone and was inadequate for predicting transient heat transfer behavior. Subsequent cooling jacket models used in the RL10 system model have been more sophisticated and scientific but also tend to be less accurate in reproducing test data. Several expert sources have indicated that the state of the art in predicting heat transfer behavior is +/- 20% accuracy (Reference 11). Greater accuracy was desired for the RL10A-3-3A system model.

The detailed one-dimensional analysis was performed using the RTE (Reference 12) program developed by NASA. RTE calculates hot-gas-side heat transfer based on the enthalpy gradient, which predicts the variation of heat transfer coefficient with mixture ratio more accurately than models based on temperature gradient. The RTE program also calculates the effects of tube curvature on heat transfer to the coolant. The basic form of the equations used to predict heat transfer are shown below.

Bartz correlation for hot-gas-side heat transfer coefficient:

$$h_{gr} = 0.026 \frac{k_{gr}}{D_{hyd}} \left(\frac{c_{p_{gr}}}{k_{gr} \mu_{gr}} \right)^{0.4} \left(\frac{\dot{m}_g D_{hyd}}{A_{chmb}} \right)^{0.8} \left(\frac{T_g}{T_{gr}} \right)^{0.8}$$

Enthalpy-driven heat transfer coefficient:

$$h_g = \frac{h_{gr}}{c_{p_{gr}}}$$

Enthalpy-driven heat transfer rate

$$\dot{q}_{hw} = h_g A_{sm_{hw}} (H_{aw} - H_{hw})$$

In the above equations, the *g* subscript denotes free-stream gas properties, *hw* denotes the hot-wall metal conditions, and *r* denotes reference enthalpy conditions which are averaged between the free-stream and wall-metal conditions. The *aw* subscript denotes adiabatic wall conditions (refer to Appendix D for definition). $A_{sm\text{-}hw}$ is the hot-wall metal surface area, A_{chmb} is the cross-sectional flow area of the combustion chamber and D_{hyd} is the equivalent hydraulic diameter at each point.

The Colburn correlation for coolant-side heat transfer coefficient is

$$h_c = 0.023 \frac{k_{Cf}}{D_C} \left(\frac{c_{p_{Cf}}}{k_{Cf} \mu_{Cf}} \right)^{0.4} \left(\frac{\dot{m}_C D_C}{A_C} \right)^{0.8} \phi_{curv}$$

The heat transfer rate is then

$$\dot{q}_{cw} = h_c A_{sm_{cw}} (T_{cw} - T_c)$$

In the coolant-side equations, the *cw* subscript denotes the cold-side wall metal conditions, *c* denotes the bulk coolant conditions and *Cf* denotes the film coolant film conditions which are an average of the coolant-bulk and cold-wall metal conditions. The ϕ_{curv} term corrects for tube-curvature effects in the coolant flow.

The first modeling issue to be resolved was the axial discretization required to obtain an accurate prediction of heat transfer. Several models with between five and sixty axial elements were considered. It was decided that twenty nodes, distributed axially along the cooling flow circuit, were adequate. Subsequent investigations revealed that using twenty hot-gas and metal-temperature nodes connected to five coolant-property nodes (see Figures 4.2.1 and 4.2.2) would give similar results for heat flux, metal temperature, and coolant properties while significantly improving computational speed. This was the configuration selected for the new RL10 system model. The only parameter which shows a noticeable difference between the five and twenty node models is the static pressure; the overall pressure drop for the five node model is actually somewhat less than for the twenty node model.

As can be seen in Figure 4.2.3, the heat transfer rates predicted using an enthalpy-driven potential provide a much more accurate variation of heat transfer with mixture ratio than the results using a temperature-driven potential. Even so, it was necessary to include a single, constant empirical correction to better match test data. This empirical factor was found to vary somewhat between

different tests and engines; an average value of 1.08 was selected for the new engine model. One possible reason for the required correction is uncertainty about the effective surface area of the cooling tubes exposed to the hot-gas. The effect of brazing material and the degree of conduction through the braze makes a precise calculation difficult. The empirical correction of 1.08 is also within the +/- 20 % deviation considered acceptable by many heat transfer experts.

The RTE code was also used to determine the flow resistance of each section of cooling jacket. Comparison with test data indicates the need for an empirical correction to the predicted jacket flow resistance. Here too, the correction factor varies somewhat across different runs and engines; an average correction of 0.94 was used. Figures 4.2.4 through 4.2.7 show heat flux, metal temperature, coolant temperature and pressure along the cooling jacket as predicted by the new heat transfer model.

For the RL10 system simulation, a simple boiling heat-transfer model was added to the RTE analysis results. The transition between boiling heat-transfer and forced convection was assumed to be instantaneous, without any nucleate boiling.

$$(h_c)_{boiling} = (h_c)_{Colburn}\left(\frac{1}{0.611 + 1.93\chi_{tt}}\right)$$

where χ_{tt} is the Lockhardt and Martinelli parameter (see Appendix D for more information).

Analyses indicate that the temperature difference between the jacket metal and fuel at start is so great that the fuel will flash immediately and should be treated using a forced convection model; there does not appear to be any appreciable film-boiling in the jacket. In the simulations performed thus far, we have not observed any of the oscillations found in test data and attributed to heat transfer instabilities. These instabilities may be due to extremely localized boiling or two-dimensional effects not modeled by RTE.

A more detailed description of the RTE analysis and film-boiling model can be found in Appendix D.

4.2.3 Thrust Chamber Performance Calculations

It was desirable for modeling efficiency to have simple one-dimensional models of the combustion chamber and nozzle. Where two and three-dimensional effects were considered significant, they have been incorporated as tables of correction factors to modify the one-dimensional calculations. Pratt & Whitney had provided tables of RL10 c*-efficiency (η_{c*}), ideal specific-impulse (Isp), and corrections for two-dimensional losses. In order to benchmark our analytic capabilities and extend the range of data provided, we performed several detailed component analyses of the injector, combustion chamber and nozzle using codes available at NASA Lewis.

4.2.3.1 One-dimensional combustion model layout : The model of combustion used in the RL10 system simulation includes just two nodes (not including heat transfer): one at the injector face and the other at the inlet to the converging section of the nozzle. The static conditions at the injector face are used to define the combustion properties. From the static pressure at the injector face, the total pressure at the nozzle inlet is calculated, including a total-to-static conversion and the momentum loss due to burning (Reference 13). The total pressure at the nozzle inlet is then used to calculate the nozzle flowrate.

$$(p_s)_n = (p_s)_{inj}\left(\frac{1 + M_{inj}}{1 + \gamma M_n^2}\right)$$

$$(P_T)_n = (p_s)_n\left(1 + \frac{(\gamma-1)M_n^2}{2}\right)^{\left(\frac{\gamma}{\gamma-1}\right)}$$

Since the combustion temperature predicted by CET93 does not include the effects of various combustion and injector inefficiencies, the predicted temperature must be corrected using η_{c^*}.

$$T_c = \eta_{c^*} \cdot (T_c)_{ideal}$$

4.2.3.2 Detailed modeling of the chamber injector : The ROCCID code (Reference 14) was used to predict η_{c^*}, which reflects primarily injector performance. ROCCID is a two-dimensional analysis program representing physical principles and general observations made in experimental studies. Because the ROCCID code does not include modeling of ribbon swirlers as used in the RL10 design, we attempted to model an equivalent tangential-injection swirler. A number of other design parameters in the model also had to be guessed, and so there is a significant degree of uncertainty in the ROCCID model of the RL10 injector to begin with. Modeling uncertainties and convergence problems experienced with the ROCCID model limited the amount of useful information we could derive from these analyses. The η_{c^*} curves provided by Pratt & Whitney (Figure 4.2.8) have therefore been used in the new system model instead. The ROCCID modeling results are discussed further in Appendix E of this report.

4.2.3.3 Nozzle performance models : The flowrate of hot-gas through the nozzle was calculated with a simple one-dimensional model, as shown below.

$$\dot{m} = \frac{g\,(P_T)_n\,A_{throat}}{c^*_{actual}}$$

This correlation gives a result very similar to that using an ideal-gas, isentropic expansion model. Several different methods were used to estimate the nozzle discharge coefficient (Cd), with similar results. By comparing the effective flow area of the nozzle specified by Pratt & Whitney (18.85 in^2) with the actual physical area of the throat (19.19 in^2), it was determined that the Cd should be approximately 0.982. Using a simple one-dimensional nozzle model, and trimming Cd to match test data for chamber pressure, a Cd of 0.975 was derived. A two-dimensional Navier-Stokes analysis suggested the Cd should be 0.976, which is a good match with the values inferred above. A Two-Dimensional Kinetics (TDK)(Reference 16) analysis also indicated that the nozzle Cd will vary with chamber pressure and mixture ratio. The variable Cd curves predicted by TDK were not well-behaved, however, and we were unable to adequately explain the variations observed. It was decided, based on the above calculations, to use a constant Cd of 0.975 in the RL10 engine system model.

The specific impulse (Isp) of the nozzle was also predicted using TDK. The TDK

predictions for Isp agree with Pratt & Whitney data near the engine design point, and extend over a wider range of pressure and mixture ratio (Figure 4.2.9). By comparing the TDK Isp predictions with those calculated using one-dimensional equilibrium assumptions, a table of thrust-coefficient efficiency (η_{Cf}) was created. This table may be used to correct the one-dimensional Isp predictions for the influence of two-dimensional effects (Figure 4.2.10). In this way, we were able to leverage a relatively small number of TDK runs with a much more comprehensive table of Isp predictions already generated using the CET93 (ODE) program. The predicted ideal Isp data and two-dimensional η_{Cf} corrections have been included in the new RL10 engine system model.

A more detailed description of the analyses discussed here can be found in Appendix E. The results of these analyses, compared with the empirical data provided by P&W, indicate that we can accurately calculate nozzle performance for a new design. Our ability to predict the c*-efficiency for a new design is less certain. ROCCID was created to model injector designs commonly used today, not the type developed for the RL10 thirty years ago. The RL10 may therefor be the wrong choice to benchmark ROCCID's accuracy in modeling new components (those without test data).

4.2.3.4 Two-phase flow through nozzle : Nozzle flow-resistance is predicted using different correlations for the lit and unlit cases. When the chamber is unlit, flow is calculated using an incompressible flow correlation, with the pressure drop limited by the critical pressure ratio for an ideal gas. This type of correlation has been found to be accurate in predicting the critical two-phase flow of a low-quality fluid and is also used for the fuel cool-down valves and LOX injector elements during start. When the chamber is lit, the flow is calculated using the correlation described in the previous section. We have not been completely successful in developing a single correlation capable of accurately predicting the entire range of nozzle flow from the prestart two-phase flow of LOX, to the unlit mixture of warm hydrogen and LOX, to the flow of combustion gases. Different correlations appear to be required for the different operating regimes and the correlations are not necessarily continuous between the regimes.

4.2.4 Injector Heat-Transfer Calculations

A model of heat transfer between the propellants in the injector plena has been developed for the RL10 system model. The potential importance of heat transfer from the warm fuel to the cold LOX in the injector was first suggested in Reference 15. Injector heat transfer has two components: the transfer of heat across the interpropellant bulkhead, and the transfer of heat from hydrogen flowing around the LOX injector elements (see Figure 4.2.11). Both components are modeled using simple, generic, semi-empirical correlations.

For heat transfer coefficient between the fuel and LOX injector elements

$$htc_{fl} = \frac{0.24\, k_{fuel}}{O.D._{tube}} \left(\frac{O.D._{tube} \rho_{fuel} v_{fuel}}{\mu_{fuel}} \right)^{0.6}$$

For heat transfer coefficient between the LOX and the LOX injector elements

$$htc_{ol} = 0.023 \frac{k_{lox}}{(I.D._{tube})^{0.2}} (v_{lox} \rho_{lox})^{0.8} \left(\frac{(c_p)_{lox}}{\mu_{lox}} \right)^{0.4}$$

Heat transfer coefficient for both fuel and LOX with the interpropellant bulkhead wall

$$htc_{blkhd} = \left(\frac{0.055\,k}{L_{plate}}\right) * \left(\frac{L_{plate}\,v\,\rho}{\mu}\right)^{0.75}$$

It is assumed that the thermal inertia of the injector metal is negligible. Figure 4.2.12 shows the heat transfer rate as a function of time for a nominal start transient simulation. No empirical data is available to validate these predictions for the RL10. This model is described in greater detail in Appendix F of this report.

4.3 Duct, Valve, and Manifold Modeling Results

The model information provided to LeRC by Pratt & Whitney included physical dimensions, effective flow areas and appropriate flow correlations for each conduit and valve in the system. This design information also included volume estimates for ducts and manifolds in the system. Table 4.3.1 summarizes this information for the RL10A-3-3A model. Each volume estimate provided typically represents several connected components. An attempt was made to verify the component physical dimensions using engine blueprints, and to verify the resistance of the ducts analytically.

4.3.1 Verification of Duct, Manifold Sizes

A complete set of RL10A-3-3A blueprints on microfilm cards were obtained from Pratt & Whitney. These blueprints were used to estimate the length, area, and volume of all ducts, manifolds, pump and turbine housings in the engine. These estimated values are included in Table 4.3.1, compared with the model data provided by P&W. More detailed descriptions of the ducts and manifolds are given in Appendix G.

In general, the component volumes and areas compare well with the values suggested for the model by Pratt & Whitney. In a few cases, however, significant discrepancies exist. Because of the way that the volumes were lumped in the system model data, it is difficult to be sure we are making a one-to-one comparison between the component sizes. Accurate estimates of some volumes could not be made due to the geometric complexity of the components.

A comprehensive investigation of the effect of the estimated volumes, areas, and duct lengths on the model's behavior was not performed. Except for the cooling jacket model, all of the component size values specified by Pratt & Whitney have been used directly in the new model.

4.3.2 Prediction of Fluid Frictional Resistances

P&W had specified the flow resistance values to be used in the RL10 model. The resistances typically reflected several sections of ductwork, lumped together for simplicity. This may also have been the way P&W flow tested the components. In this study, an attempt was made to predict the flow resistance of ducts and manifolds using simple one-dimensional semi-empirical methods. It was decided to benchmark this predictive capability with a single RL10 component. The duct from the turbine housing discharge flange to the inlet of the Main Fuel Shut-off Valve was selected because it was easiest to identify with a single discrete resistance value as specified by P&W.

In order to estimate the resistance of the selected duct, a simple frictional correlation was assumed,

equivalent to the Darcy equation as described in Reference 17). The friction factor of the duct was assumed to be constant of 0.0095, which is consistent with completely turbulent flow in a pipe with a relative surface roughness of 1.9×10^{-5} (absolute roughness of 4.6×10^{-5} inches and diameter of 2.402 inches). Bends in the pipe were replaced by their equivalent lengths, computed using the Crane's software (Reference 18). These analyses are discussed further in Appendix G. The resistance of the duct derived from this analysis differs approximately 15 % from the value suggested by Pratt & Whitney. This is an acceptable correlation, considering the uncertainty in roughness factor.

Although the simple one-dimensional models appear to give reasonably accurate estimates of flow resistance, the results are not suitably accurate for detailed high-fidelity engine models. Two and three-dimensional analytic tools may increase the accuracy of modeling bends in the pipe, but uncertainty in the wall surface roughness will limit the accuracy for new component designs. For new applications, it may be advisable to include the effects of uncertainty in flow resistance as part of the system simulation activities. For the RL10 application, we could use the duct described above to determine a surface roughness and apply this value to other components in the system. We have instead elected to continue using the flow resistances specified by P&W in the RL10 system model and have not pursued further analysis on the ductwork.

4.3.3 Modeling of Valve Actuator Mechanisms

Most of the valves in the system involve complex orifice shapes and flow paths. Likewise, the actuators and servo-mechanisms which control the valves are complex, involving a number of springs, dampers and masses whose characteristics are not generally known. Dynamic modeling of these actuators, including fluid forces from the propellant flows is considered beyond the scope of this project. We will therefore continue to use relatively simple functions of time and pressure specified by Pratt & Whitney and shown in Figures 2.1.2 and 2.1.3. These schedules may be modified to reflect variations in valve timing as inferred from test data.

4.3.4 Modeling of Critical Two-Phase Flow Through a Valve or Orifice

There are a number of situations that have been found where the flow through a particular valve or orifice may range from liquid to vapor, and from choked (critical) to unchoked flow during the start and shut-down transients. This is true, for example, in the RL10 fuel cool-down valves, oxidizer control valve, and oxidizer injector elements. It was necessary to make a more detailed investigation of these particular components. Past research efforts have met with only limited success in forming a comprehensive description of the different flow regimes and the transitions between them (References 19 through 24.). Much of the available experimental research literature is applicable to steam only. Theoretical treatments (of varying accuracy) typically involve numerical methods which are not practical for inclusion in a transient system model; these methods are discussed in Appendix H. The number of independent variables involved in the theoretical calculations also make it impractical to map the flow for inclusion in the system model. It was necessary, therefore, to use simple correlations which approximate the results of the more detailed analyses and which agree with RL10 engine test data. Special cases of the flow correlations are required for different applications in the RL10 system.

In the new system model, flow through the fuel cool-down valves and the LOX injector are determined using an incompressible flow calculation (upstream density used) regardless of the state of the fluid (even if it begins to vaporize). The value of upstream pressure is used, however, to select the effective pressure drop used to calculate flow, as is described below.

$$\dot{m} = C_d * A * \sqrt{2g * \rho_{inlet} * \delta_p}$$

$\delta_p = (P_{inlet} - P_{exit})$ for $P_{exit} > P_{sat}$

$\delta_p = (P_{inlet} - P_{exit})$ for $P_{crit} < P_{sat}$ and $P_{exit} > P_{crit}$

$\delta_p = (P_{inlet} - P_{sat})$ for $P_{crit} > P_{sat}$ and $P_{exit} < P_{sat}$

$\delta_p = (P_{inlet} - P_{crit})$ for $P_{crit} < P_{sat}$ and $P_{exit} < P_{crit}$

P_{sat} = function of S_{inlet} looked up from tables

$$P_{crit} = \left(\frac{2}{\gamma+1}\right)^{\frac{\gamma}{\gamma-1}}$$

In this way, the flow calculation predicts a continuous transition form liquid to gas flow and from choked to unchoked conditions. This approach appears to provide a good match with RL10 test data, and can also be explained in physical terms as follows. When the inlet pressure is high but the discharge pressure is low, the fluid will tend to flash at the orifice throat or just downstream of it. This condition is described by limiting δ_p using P_{sat}. For inlet pressures closer to saturation, the fluid may actually flash upstream of the throat. In this situation, the static pressure at the throat will (for an ideal gas) be limited to the P_{crit} as defined above, and therefor this value should be used to limit δ_p. A typical plot of predicted mass flux versus inlet pressure for sub-cooled liquid hydrogen venting to a vacuum is shown in Figure 4.3.1.

The model for the OCV is similar to that for the cool-down valves and LOX injector, assuming the inlet pressure is significantly above saturation pressure. When the inlet conditions approach saturation, however, the expressions above predict flow somewhat higher than that indicated by engine test data. P_{sat} is used to limit the downstream pressure until the upstream state approaches a gas. Thereafter, flow is treated as isentropic flow of an ideal gas through an orifice.

$$\dot{m}_{liquid} = C_d * A * \sqrt{2g * \rho_{inlet} * \delta_p}$$

$\delta_p = (P_{inlet} - P_{exit})$ for P_{inlet} and $P_{exit} > P_{sat}$

$\delta_p = (P_{inlet} - P_{sat})$ for P_{inlet} and $P_{exit} < P_{sat}$

$$\dot{m}_{gas} = \sqrt{\frac{g_c \gamma}{R}} \left(\frac{2}{\gamma+1}\right)^{\frac{\gamma+1}{2(\gamma-1)}} \frac{A * P_0}{\sqrt{T_0}}$$

$\dot{m} = \dot{m}_{liquid}$ for $P_{inlet} > 1.2 * P_{sat}$

$\dot{m}$ = maximum of $\dot{m}_{liquid}$ and $\dot{m}_{gas}$ for $P_{inlet} < 1.2 * P_{sat}$

It is not understood why flow through the OCV should behave differently than the other two-phase flow components in the engine. The expressions described here provide continuous functions of flow across the phase boundary and agree well with test data.

4.3.5 Model of flow through Venturi

The venturi downstream of the cooling jacket is intended primarily to help provide stable thrust control using a turbine bypass valve rather than an in-line valve. It is possible that the venturi may also serve in general to inhibit system-wide pressure oscillations due to interactions between the combustion chamber, cooling jacket and turbomachinery. The RL10 venturi is apparently choked during engine start but not at the normal operating conditions.

Most models of flow through a venturi are based on the total-to-static pressure ratio between the inlet and the throat (References 25 and 26). In the case of the RL10, it is desirable to characterize the flow based on the pressure ratio between the venturi inlet and discharge (exit from the diffusing section). By making some assumptions regarding the correlation between inlet-to-throat pressure ratio and inlet-to-exit pressure ratio, the performance map shown in Figure 4.3.2 was derived. This model was found to agree well with the data provided to us by Pratt & Whitney. Although this analysis was not exhaustive, it provided confidence regarding the suitability of the map provided for simulation of start conditions. The performance map represents the venturi flow parameter, FP, which is used to predict mass flow as described below.

$$\dot{m} = \frac{FP * P_{inlet}}{\sqrt{T_{inlet}}}$$

For the shutdown transient simulations, inertial damping logic has been added to the venturi model in order to inhibit oscillations around zero flow once the system is nearly evacuated. Such oscillations can be induced by numerical instabilities; the inertial damping provides a physically meaningful way to damp such oscillations without affecting the normal operation of the venturi model.

4.4 The New RL10A-3-3A System Model

The new RL10A-3-3A engine system model was created by integrating component models using the ROCETS system simulation software (Reference 9). After considering the results of the component analyses, several of these models were selected for inclusion in the new system model. In other cases, the component data and information provided by Pratt & Whitney has been integrated directly with the system model.

4.4.1 Evaluation of Component Models / Integration with New System Model:

Not all of our component analysis results have been used in the new RL10 model. Some of the component results were judged to be incorrect and so were not included. Other results simply verified the P&W component data, which was used directly in the system model. Only those component models which extended the operation range of the model, added flexibility or corrected known deficiencies in the existing models were added. The list of independent component models selected for the new RL10 model are:

1) Pump maps extended to start and shutdown transient conditions using generic data and detailed analyses.

2) New combustion gas property tables from CET93.

3) New heat transfer modules using enthalpy-driven potentials, twenty axial nodes for the metal and hot-gas side calculations, connected to five coolant nodes.

4) A model of heat transfer between the warm fuel and cold oxidizer in the injector plenum.

5) New model of combustion chamber, including the effects of momentum burning losses.

6) Tables of nozzle specific-impulse and thrust-coefficient-efficiency, generated using CET93 and TDK computer codes.

7) Revised models of two-phase flow through the fuel cool-down valves, oxidizer control valve, and LOX injector elements. Extends the range of pressures for which the models will work.

We decided not to use the results of the turbomachinery analyses directly. Nor did we use the results of the injector performance analyses generated by ROCCID; an empirical table of c*-efficiency has been used instead. In general, we have retained the values of duct and manifold size and flow resistance as provided by P&W. We did not attempt to create detailed models of the valves or actuators, but opted to use the characteristics specified by P&W.

4.4.2 Differences between Start and Shutdown System Models :
One of the original goals of the project was to develop a single model that would predict the start transient behavior, steady-state performance and shut-down transient behavior of the RL10 engine. This goal has not been achieved as yet. There are currently two system models, one for start simulations and the other for shut-down. The start transient model is also suggested for making steady-state performance predictions, although the shutdown model quiescent values are very similar. The two models share similar component performance characteristics but differ in the distribution of dynamic volumes and flow inertia around the pumps and turbine (see shaded modules in Figure 4.4.1). The additional volumes as inertias were required in the shutdown model to obtain stable solutions, but lead to transient discrepancies with test data in the start transient simulations. It appears that during the start transient, the pump flows behave as incompressible even though the pressures there appear to be below saturation. If volume dynamics are included in the pumps, the start simulation exhibits compressible characteristics which can significantly delay the onset of normal pumped operation. Similar effects appear in the dynamics downstream of the turbine during engine start simulations. Changing the way in which the turbine discharge volume components are distributed appears to slow the decompression of the turbine discharge as the FSOV opens during start. This reduces the starting torque and slows the start acceleration. Due to limitations of schedule and data, it was decided to maintain two separate models rather than attempting to resolve the dynamic modeling differences.

5. MODELING UNCERTAINTIES

Before discussing the results of the system simulations, it is important to note sources of modeling uncertainty which will affect our ability to model any given test or flight engine firing. There are several sources of modeling uncertainty which effect the RL10 model's ability to simulate any given firing. These uncertainties can be divided into four categories: 1) uncertainty in hardware characteristics, 2) uncertainties in valve dynamic behavior, 3) uncertainties in engine initial

conditions and boundary conditions, and 4) uncertainty in main chamber ignition delay.

5.1 Hardware Uncertainties

In addition to modeling uncertainties due to insufficient data (such as fluid resistances and pump stall characteristics), there are some elements of the hardware which may vary from engine to engine. Information regarding these hardware variations is not readily available for a given test or flight engine, making it difficult to account for such differences in modeling the behavior of that particular engine.

One component which may vary from engine to engine is the fuel pump discharge orifice class used. This orifice is chosen according to knowledge of components in the engine and, on occasion, trim runs of the engine. The choice of orifice class is designed to minimize variations in nominal engine performance (thrust, Isp). It is not clear, though, how these variations might affect the start or shutdown transient behaviors.

Certain apparent variations in heat transfer coefficients and cooling jacket fluid-resistance have also been noted. It has been suggested that the effects of variations in the tube brazing may be the source of variations in heat transfer from engine-to-engine. These variations are not critical to successful engine operation but may perceptibly alter the engine time-to-accelerate.

The fuel pump cooldown valves are another area of uncertainty. It has been suggested that these valves have a discharge coefficient (Cd) which may be different for ground-test and flight because of differences in the size of the duct which vents the cooldown flow overboard (Reference 27). In the RL10 model, the discharge coefficient is set at 0.6 for ground-test and 0.8 for flight. These values were chosen based on discussions with engineers at Pratt & Whitney but no real calibration data is available to verify these values. Figure 5.1.1 shows the variation in simulation for an engine first start with different Cd values between 0.6 and 0.9. In the case of the shutdown transient, the model actually assumes that the discharge coefficient may change with time as the discharge duct fills and cools. This assumption was inferred from engine test data, and has not been verified either. The cooldown valve resistances are a major factor in both the start and shutdown simulations, and the uncertainty in these values may therefore be a significant source of any discrepancy noted between simulated and measured data.

The running torque of the RL10 turbopump (fuel and LOX combined) is another accepted source of engine-to-engine variation. These values are not generally measured for each engine but past studies (Reference 28) have shown that the torques vary from 8 to 36 lbf-in. The same nominal value of 20 lbf-in torque relative to the fuel pump shaft has been used for all the simulations run for comparisons with flight and test data. It is uncertain what the actual values of running torque were for the test and flights considered but it is unlikely that the values were precisely 20 lbf-in. Variations in the simulated start of an engine with different running torques is shown in Figure 5.1.2.

5.2 Valve Uncertainties

The transient behavior of the engine in both start and shutdown is largely determined by the opening and closing of valves. If there are variations in the time and rate at which these valve changes occur, the acceleration of the engine will vary also. The assumed opening and closing schedules for the start and shutdown simulations are shown in Figures 2.6.1 and 2.6.2.

It has been acknowledged that variations in valve timing actually do occur (Reference 26). This

may be due to timing differences in command signals relative to ignition, dynamic response variations of the pneumatic actuation system, and small differences in the dynamic behavior of the servo-mechanisms which control the fuel pump Interstage Cooldown Valve (FCV1), Oxidizer Control Valve (OCV) and Thrust Control Valve (TCV). In some cases, the opening and closing times of valves can be inferred from test data. In most cases, however, this is not possible because of insufficient data and limitations in the dynamic response of the sensors.

Of all valves in the engine system, the OCV poses the greatest uncertainty. This valve is servo-actuated by the pressure rise across the LOX pump and the point at which it opens is the single most significant factor in determining when the chamber pressure rises to its full power level. The model describes the opening of the OCV by a simple function of pump delta-P, with limits on the slew rate to prevent instantaneous changes and toggling. A dynamic model of the actuator is not available and the dynamic response of this mechanism may, in fact, be different from one engine to the next. Figure 5.2.1 shows the variation in engine start timing with different assumed OCV opening pressures between 50 and 150 psid. Figure 5.2.2 shows the inferred OCV schedule based on back-calculation from test data; it should be noted in this case, however, that the data-reduction model did not account for sensor lags, and assumed that the bypass valve opened at the correct time.

5.3 Uncertainty of Initial Conditions

The temperature of the combustion chamber, nozzle and cooling jacket at the beginning of the engine start sequence is an important factor in the engine time-to-accelerate. Unlike the engine inlet pressures and temperatures, there is no reliable measurement of jacket temperature for any given test or flight. Temperatures that are measured on the engine generally show false readings before start due to interaction with the ambient environment, metal conduction with other components, and the absence of propellant flow at that time. The initial temperature of the cooling jacket, ducts, manifolds, and other components is simply guessed, often based on limited information from past testing.

In the RL10 model discussed here, the temperature of the cooling jacket is assumed to be a uniform 540 degrees R because that is the typical ambient temperature in Florida (which is applicable for both ground-tests at Pratt & Whitney and launch from Cape Canaveral). This initial temperature is also suggested to include the effects of a warm nitrogen purge in the vehicle interstage adaptor (650 R gas). The temperature of the cooling jacket metal for second burns is assumed to be uniform 350 degrees R, based on assumptions about the average metal temperatures after the previous firing. The cooling jacket inlet manifold is assumed to be at 200 R because the inlet manifold is exposed to some contact with the fuel pump cooldown flow before start. All other components in the system are assumed to be in thermal equilibrium with the propellant flows at all times (no heat transfer, fully conditioned engine before start). Clearly, these assumptions are rather arbitrary and are likely to be in error to some degree for any given firing. Such assumptions are necessary due to insufficient information regarding the actual ambient conditions and pre-start conditioning. The RL10 system model does not include a complete thermal model of the engine structure that would be required to simulate the pre-start conditioning process.

Figure 5.3.1 shows the variation in engine start due to different assumed chamber temperatures between 250 and 500 R.

5.4 Uncertainty in Ignition Time

For the simulations considered here, the ignition time is set to agree with the measured data.

Predicting the ignition time as well would require an ignition model, which is currently not available. An empirical model would probably be the best solution if such predictive capabilities are desired in the future. For the time being, we must be content to predict the start given a known range of ignition times between 0.10 and 0.40 seconds after the MES signal. The variation of start time with ignition delay is shown in Figure 5.4.1.

5.5 Interaction between uncertain parameters

Because the RL10 (or any expander cycle rocket engine) is a system of highly interdependent components, the variation in engine behavior due to the uncertainties described above cannot be gauged without considering how the variations in components might interact. In order to adequately map the range of engine acceleration times with inlet conditions, initial conditions, running torque, valve characteristics, etc., a large matrix of simulated runs must be performed and the results appropriately analyzed. A study of this type was previously performed by Pratt & Whitney and the Aerospace Corporation (Reference 28), but was not undertaken as part of this project.

6. COMPARISON OF SYSTEM MODEL PREDICTIONS WITH TEST DATA

The start and shutdown models have been run to simulate specific ground-test and flight engine firings. In this section, the simulation results are compared with the measured engine data.

6.1 Verification of Steady State Performance Predictions :

Ten test cases are considered for the steady-state performance predictions. Five tests are based on different quiescent operating points for a single ground-test run of a single engine (Engine P2087, Run 2.01, October 4,1991). The other five tests are based on the final state of five start transient data sets (five different ground-test runs) of a single engine (P2093). Flight data has not been included in this comparison because insufficient data exists to determine the mixture-ratio and trim position of the OCV for those firings. In simulating the first five tests, the OCV position was varied to achieve the desired mixture ratio at each operating point; the actual test was configured to allow changes in the OCV position as well. In the other five tests, it is believed that the OCV would have been set to a single position. Although the OCV trim on the simulations indicated different OCV positions in each of these five tests, an average position was chosen and used for all five runs. A comprehensive performance prediction for a typical case is shown in Table 6.1.1. In general, only a very few parameters are measured on actual engine firings (14 parameters on ground tests, 8 in flight). The engine inlet pressures and temperatures, and the combustion chamber pressure were typically treated as inputs to the model; the other parameters were calculated by the model. A statistical comparison, showing the distribution of error between the measured and predicted parameter values in the ten ground-test cases, is shown in Figure 6.1.1.

The model predictions match the measured values to within 10% for all parameters on all tests (a total of 90 values). Most predictions are within 4% of the test results. The most pronounced and consistent sources of error are in the turbine inlet temperature and the pump discharge pressures. The difference between the predicted and measured turbine inlet temperatures may be attributed to heat transfer uncertainties in the combustion chamber cooling jacket (discussed in section 4.2.2 of this report). The errors in the pump discharge pressures appear to be associated with turbopump speeds that are consistently lower than measured. This discrepancy in speed is most likely due to small errors in the turbine maps and cooling jacket model; these errors cannot be easily corrected for without adversely affecting the predicted start behavior. It was found, in fact, that the turbine performance maps recommended for predicting steady-state performance are not the same as those recommended for simulating engine start. It was decided that the turbine maps suggested for start

transient modeling would be used throughout, and the steady-state error accepted.

6.2 Verification for Start Transient Simulations :
Four engine firings have been plotted in order to compare model predictions with measured data. Figures 6.2.1 through 6.2.8 show the predicted and measured start transient of a single ground-test first-burn. Figure 6.2.9 shows chamber pressure for a ground-test second burn of the same engine. Figures 6.2.10 through 6.2.12 show an Atlas/Centaur (AC-72) flight first-burn and Figure 6.2.13 shows the second-burn for a different flight (AC-74). In each of these runs, the ignition time has been set in the model based on examination of the test or flight data. The difference between ground-test and flight engine simulations is the value chosen for the fuel cooldown valves discharge coefficient (which reflects differences in the vehicle and test-stand ductwork). The difference between first and second burn simulations is the assumed initial temperature of the combustion chamber metal. These variations were discussed in greater detail in section 5.3 above.

As these figures indicate, the start model generally matches the measured time-to-accelerate to within approximately 230 milliseconds, using only guesses for initial temperatures, bearing friction, valve schedules and other factors which may very from run to run and from engine to engine. Table 6.2.1 gives the predicted vs. measured time-to-accelerate (defined here as the time from MES at which the chamber pressure reaches 200 psia) for six ground-test and three flight-engine firings. One of the flight simulations is off by 280 msec (rather than 230 msec), but this appears to be aberration relative to other flight-engine starts; it is likely that the engines for this flight are different in some ways other than their inlet conditions (see section 5 above for a discussion of uncertainty). The model correctly predicts start variations due to different engine inlet conditions, initial thermal conditions, and differences between ground and flight hardware.

The reader may note that there are some transient differences between the predicted and measured overshoot in chamber pressure during start, before the engine reaches its quiescent state. The smaller oscillations evident in the test data are due to oscillations of the TCV servo-mechanism. The simulation does not include a model of the actuator dynamics, but the valve is scheduled to open as a linear function of combustion chamber pressure; it initially overshoots chamber pressure but does not oscillate. In several cases, the simulation exhibits some rather sharp transients before reaching steady-state; these appear to be due to volume dynamics in the LOX pump inlet duct. As the OCV suddenly opens and the LOX system pressurizes, the simulation may predict oscillations caused by fluid compression, inertia, and phase changes. These transients, which are not evident in the test data, may occur in the simulations because the OCV servo dynamics are not included in the model. These transient differences between predictions and test are not considered serious; they may be eliminated if models of the TCV and OCV actuators are developed in the future.

To demonstrate one potential application of the system start model, Figure 6.2.14 shows the predicted metal temperature of the combustion chamber just upstream of the throat (its hottest point) during start. This parameter is not measured, even in ground tests. The temperature in this case peaks at around 1875 R, which is a well below the melting point of the silver throat insert. Information of this kind can be used to help determine component wear and to assess the impact of operational or hardware changes to the engine.

The new RL10 system model may also be used to explore new control options for the engine. Enhancements to the engine's control system are currently being developed, including an electronic controller and electro-mechanical actuators for the valves. These changes will enable much greater control flexibility. As a small demonstration of the benefits that the new control system may afford, the RL10 engine model was used to simulate modifications to the OCV timing during start. The trigger pressure and valve slew-rate were both altered in order to increase the differential

pressure across the ignitor GOX supply line. The goal was to reduce the danger of supply line freeze-up, which may occur if combustion products (water) back-flow into the supply line during start.. The results of the simulation, shown in Figure 6.2.15, indicate that this approach has the desired effect, although the OCV control could be further optimized to maintain the desired delta-P throughout the start operation.

6.3 Verification of Shutdown Transient Simulations :

Two firings have been used for comparison between model predictions and measured data. RL10 engine shutdowns do not appear to have any distinct feature analogous to the time-to-accelerate for start transients. Although there are subtle variations in the rate of deceleration, the nature of these differences is not as well understood as in the case of engine start.

Figures 6.3.1 through 6.3.8 shows the predicted vs. measured shutdown for a ground-test engine. Figures 6.3.9 though 6.3.14 shows similar comparisons for a flight engine. As described in the previous section, the difference between ground-test and flight engine models is the assumed discharge coefficient of the fuel pump cooldown valves. Figures 6.3.15 and 6.3.16 show predicted and measured pump speed for the various predicted shutdown transients for several ground-test firings, giving some indication of the variation due to inlet conditions and initial operating point.

The RL10 shutdown model has captured many interesting effects that occur during shutdown. In Figure 6.3.3, for example, the model and measured data both show a characteristic dip, rise and then falloff in the fuel venturi upstream pressure. This feature is caused by the dynamic interaction of the fuel pump cooldown valve opening and main fuel shutoff valve closing. In Figure 6.3.5, the jump in pump inlet pressure and the shape of the fuel pump discharge pressure curve (not shown) are both due, in part, to reverse flow through the fuel pump.

From inspection of the plots, it appears that there are still some unresolved differences between the predicted and measured engine deceleration rates. In comparing the start and shutdown predictions relative to test data, the reader should note that the time scales of the shutdown traces are much smaller than those of the start transient plots.

The new RL10A-3-3A shutdown model developed here can be used to simulate the effects of various operating scenarios on the engine and vehicle. For example, it may be possible to 'soften' the shutdown transient and minimize the potential for engine damage. The model may also be used to explore shutdown options which will minimize thrust and impulse imbalance for vehicles which use multiple engines.

7. DISCUSSION OF MODELING RESULTS

The technical results of the RL10 modeling project are presented in the previous sections of this report. In this section, the significance of these results is discussed.

7.1 Discussion of Turbomachinery Investigation

The available literature on the low-speed operation of pumps appears to be fairly consistent. Techniques for matching the low-speed generic maps found in the literature to the high-speed test data are qualitative at best, however.

Available computer programs for predicting turbine and pump performance based on component

geometry and operating conditions were also considered in the RL10 modeling project. Most codes of this type are not intended to predict the dissipative operation of pumps at very low speeds nor the reverse flow during pump surge. It is common practice to first anchor component models using test-stand data around design point, before using these models to predict off-design behavior. This a priori requirement for test data will make it difficult to accurately predict the performance of new component designs, for which such data is often not available. Even when test data cannot be used to tune the models, however, the results may be sufficiently accurate to provide designers with useful information. It appears that there is still a significant amount of work required to develop accurate first-principle models of cryogenic turbopumps, especially for transient simulations. The tools used here to model the RL10 turbomachinery are still in the development and technical review phase, and subsequent versions of these tools may be more accurate without requiring adjustment with test data. This subject is discussed in greater detail in Appendices B and C.

It has also been noted that relatively small differences in curve-fits to the turbine efficiency maps at low speeds can create significant differences in the engine time-to-accelerate. Small variations in turbine efficiency are amplified by system interactions; the turbine drives the pumps, which in-turn drive fuel through the cooling jacket to provide power for the turbine. Given the scarce amount of data in the low-speed region, the selection of the proper curve fit through the available data is therefor critical. This effect also has profound implications for our efforts to predict the turbine performance from first-principles. The sensitivity of the system start timing to the turbine performance makes almost any predictive error unacceptable.

7.2 Discussion of Combustion and Heat Transfer Investigation

The three modeling issues which arose regarding the cooling jacket heat transfer are 1) the number of axial heat transfer nodes to be used, 2) the variation of hot-gas properties along the chamber and nozzle, and 3) the variation of heat transfer properties with changes in mixture ratio.

It seems clear from Figure 4.2.6 that the use of differential enthalpy to predict hot-gas-side heat transfer ('enthalpy-driven potential') is significantly more accurate than the corresponding temperature-driven heat transfer model. This method accounts for variations in mixture ratio without requiring an explicit empirical correction for that effect. A single (constant) empirical correction of 1.08 was still required to match test data.

It is uncertain what benefits were gained from including more heat transfer nodes and non-ideal expansion effects. Certainly, more nodes will give a more accurate axial distribution of metal temperatures and heat fluxes along the chamber and nozzle. On the other hand, the overall coolant heat pick-up and pressure drop prediction may not be any more accurate using more nodes; the overall pressure and temperature change are the only quantities that really affect system performance. A comprehensive comparison of the system-level effects of node distribution on predicted engine performance was not within the scope of this project, however, and the hybrid model with twenty metal nodes and five coolant nodes was used in the new system simulations.

An attempt was also made to predict the RL10 combustion efficiency using the ROCCID code. The results of this analysis were somewhat uncertain and require further study. It appears that engineering judgement and estimates for some design parameters is still required to model new designs. Perhaps some methodology or integration with other analyses tools can be made that will refine the modeling process and eliminate modeling uncertainties. TDK and Navier-Stokes analyses were performed to predict the nozzle specific-impulse and discharge coefficient. The Navier-Stokes analysis confirms that the nozzle Cd at engine design conditions is approximately

0.98, as was also inferred from test data. The TDK analysis appears to accurately predict specific impulse, but the results for discharge coefficient and heat flux were somewhat suspect.

7.3 Discussion of Duct, Manifold and Valve Investigation

Estimates of duct and manifold volumes, areas, and lengths based on RL10 blueprints show some differences from the values suggested by Pratt & Whitney. Some of the discrepancies may be due to complex geometries which cannot be estimated properly from the blueprints. In other cases, the values given by Pratt & Whitney may be less accurate than our estimates. For the new model, in general, the volumes, areas and lengths provided by P&W are used.

We have successfully verified the resistance of the duct from the turbine discharge to the main fuel shut-off valve to within +/- 20%. Given the uncertainties in duct surface roughness and the complex series of bends and elbows in the duct, there appears to be no advantage in predicting the resistance of all ducts in the system. The only reliable method to accurately characterize flow resistance is still to run flow tests. More sophisticated flow modeling tools may also be used to improve accuracy of the predicted flow-resistances, but the surface roughness must still be known precisely.

For the new system model, two-phase critical flow is modeled using simple one-dimensional, homogenous correlations. Different correlations are used for the fuel cool-down valves, the oxidizer control valve and the LOX injector elements depending on the propellant vapor pressure and range of operating conditions encountered in each case. Two-phase flow may actually involve a number of complex physical effects. Not all of these effects, it appears, lend themselves to elegant theoretical models or accurate predictions.

7.4 Discussion of System Model Simulation Results

Overall, the new version of the RL10 system model appears to predict the start acceleration, steady-state performance, and shutdown behavior of the engine accurately (compared to test data). The simulated variations in the time-to-accelerate due to changes in engine inlet conditions, ignition time , and the initial thermal conditions track the variations observed in test data. In general, the model predicts the time to accelerate to within approximately 230 milliseconds of the test and flight data results under the conditions considered. Steady-state performance predictions match measured values to within 10% in all cases (and matched most values within 4%). The RL10 shutdown model successfully predicts the transient characteristics of the engine shut-down process, including effects due to reverse flow in the pumps.

8. CONCLUDING REMARKS

The goals of the RL10A-3-3A Modeling Project have been accomplished. Analyses were performed for all major engine components, and many of the results from these studies have been directly incorporated into the new system model. Other analysis results have simply supported the information already found in the baseline model, giving us greater confidence in those aspects of the model. Still other parts of the study have tested the limits of our analytic tools and expertise and found them somewhat wanting. The project has therefore helped to benchmark the detailed component analysis software and techniques currently being used and developed in the Space Propulsion Technology Division at NASA Lewis Research Center. The information derived from this research may be used in refining these analysis tools in the future.

In addition to providing an improved system model of the RL10, the analyses performed under this

project have given us a better understanding of the engine system in general. The effects of various design and operational uncertainties on engine performance have been elucidated through simulation, and many of the transient features visible in test data have been explained using the new system model as well.

The RL10A-3-3A engine system models developed here are available to NASA and other users for studying the behavior of the engine under a wide range of operating conditions. The models can be used to assess various mission scenarios, to investigate test and flight anomalies, and to evaluate potential design changes. These models could also be modified to simulate RL10A-4 and RL10A-4-1 engine configurations.

Finally, this project gives an excellent perspective on the current limitations of engine system modeling from first principles. In any new engine system being considered, there will likely be several unknowns and uncertainties that will require test data to resolve. A priori modeling of a given design can only give a possible range of quantitative predictions, based on uncertainties in component performance. System modeling of a preliminary design can serve to flag issues which stem from such uncertainties, but we cannot expect such models to precisely predict transient behavior before comprehensive component test data are available. Once the uncertainties in component behavior have been resolved, highly accurate and precise system models can be created.

9. RECOMMENDATIONS for FUTURE RESEARCH

On the basis of this study, several recommendations can be made regarding future work which would improve our understanding and models of the RL10A-3-3A rocket engine. No specific work elements are currently planned to accomplish these additional goals.

1. Once code developments are completed, the PUMPA and TURBA codes should be used to repeat the analysis of the RL10A-3-3A turbomachinery. If the new predictions are found to match closely with test data, the models can be used to examine the very low speed performance of the turbopumps. If the new predictions still show some disagreement with the test data near the component design points, appropriate empirical corrections may also be applied before analyzing the low-speed performance characteristics.

2. The work to combine the Rostefinski models of the pump impellers with two-phase critical flow models of the exit diffusers should be pursued further.

3. Research should be expanded, in general, in the areas of transient and far off-design pump operation, including cavitation, stall, reverse flow, etc. Accurate models of these effects do not appear to exist.

4. A more detailed one or two-dimensional model of film boiling in the cooling jacket should be developed. This model should be capable of accurately predicting the amplitude and frequency of pressure oscillations caused by film boiling during engine start.

5. Some investigation regarding the source of engine-to-engine variation in cooling jacket heat transfer coefficient and fluid resistance should be made.

6. The ROCCID code should be modified to better model the RL10 injector elements. ROCCID should also be modified to allow far off-design conditions (such as during engine start and shutdown.

7. The Navier-Stokes code used to determine the design-point nozzle discharge coefficient should be used to map Cd at off-design conditions as well.

8. TDK/MABL should be considered to improve the accuracy of the heat transfer correlations using in the RL10 model.

9. A thorough study should be made on the two-phase flow of cryogens, including transition from choked to unchoked behavior. Only limited data and theoretical treatments appear to exist on this subject.

10. A detailed transient analysis of duct and manifold priming should be performed, especially for the LOX injector plenum during engine start. The abrupt transitions to completely incompressible flow, as predicted using a simple lumped parameter model, are probably not realistic.

11. A comprehensive chill-down model for the RL10 engine should be developed to accurately predict the initial conditions for the start transient. Particular attention should be made to modeling the turbopump and the entire LOX feed system.

12. A model of the RL10 ignitor should be developed that will accurately predict the time of main-chamber ignition with respect to the MES signal.

13. A study should be performed using the current RL10 engine system model to predict the variation in time-to-accelerate due to uncertainty in initial conditions, engine inlet conditions, turbopump drag torque, etc. (similar to the results of Reference 28 but with additional parameters).

10. DEFINITION OF TERMS

Flow Coefficient:

$$\phi = (\pi^2 D^2 b * 0.004329)^{-1} * Q / N$$

where D = impeller exit diameter in inches
b = impeller exit blade height in inches

Flow Parameter

$$\text{Flow Parameter} = \frac{\dot{m} * \sqrt{T_{inlet}}}{P_{inlet}}$$

Head Coefficient:

$$\psi = (\pi^2 D^2 * 5.99 \times 10^{-8})^{-1} * \text{Head}/N^2$$

$$\text{Head} = \left[\frac{P_{out}}{\rho_{out}} - \frac{P_{in}}{\rho_{in}}\right]$$

Reduced Speed

$$\text{Reduced Speed} = \frac{N}{\sqrt{T_{inlet}}}$$

Reynolds Number:

$$Re = \frac{D v \rho}{\mu}$$

where v is flow velocity

Velocity (Speed) Ratio:

$$u = \sqrt{2} * \frac{N * D * \pi}{60}$$

$$c_0 = \sqrt{2g * J * \Delta H_{nozzle}}$$

$$\text{Ratio} = u / c_0$$

where D is the turbine diameter in inches
g is gravitational acceleration (386.1 in/sec^2)
J is mechanical-thermal units conversion (9337.92)

** the (square root of 2 factor is peculiar to the RL10 turbine maps and is probably due to the method by which the Pratt & Whitney analysts combined the two turbine stages in the performance map. This factor would not normally be present for a single turbine stage*

11. ACKNOWLEDGMENTS

This project was performed under contract (NYMA contract) and grant (U.Memphis grant); funding was provided by the Launch Vehicle Project Office and Space Propulsion Technology Division at the NASA Lewis Research Center.

The author would like to acknowledge the participation of the project team mambers for their contributions to this endeavor:

Mr. Tom Tomsik (NASA LeRC-5320) : for performing both empirical and detailed theoretical analyses of the RL10 cooling jacket.

Mr. Joseph P. Veres (NASA LeRC-5320) **:** for obtaining turbomachinery test-stand data used in model verification, and for his detailed pump and turbine component analyses using the PUMPA and TURBA codes.

Dr. Kenneth Kaczynski (NASA LeRC-5320) : for performing detailed analyses of the RL10 combustion chamber and nozzle using the ROCCID code, TDK, and his own Navier Stokes-analysis code.

Mr. Douglas Rapp (NYMA Inc. - LeRC SETAR) : for generating the extensive tables of combustion gas properties required to model the RL10 combustion chamber, nozzle, and cooling jacket.

Mr. Dean Scheer (NYMA Inc. - LeRC SETAR) : for performing analyses of the RL10 pumps using the LSISO program, and using his own code based on methods suggested in Reference 5.

Mr. Al Pavli (NYMA Inc. - LeRC SETAR) : for developing a model of heat transfer in the RL10 injector plenna, as well as providing invaluable information on other aspects of RL10 combustion and heat transfer.

Mr. Bill Tabata (NASA LeRC-5320) : for providing general information and guidance throughout the project. He acted as liason between LeRC and Pratt & Whitney for obtaining data, information, and bluebrints. He also helped to review this report.

Dr. John Hochstein (University of Memphis) : for his assistance in developing two-phase flow models for the Fuel Cool-down Valves.

Other researchers at NASA LeRC and its contractors, too numerous to list here, also provided assistance on elements of the component and engine-system modeling. Their contributions are gratefully acknowleged also.

We would also like to recognize the participation of Pratt & Whitney (West Palm Beach, Florida) and Martin Marrietta (Denver, Colorado). They provided data, information and blueprints on the RL10 which were critical to the success of this project.

Table 4.2.1
Description of Combustion Property Tables for RL10 Model

Pressures (psia)	Mixture Enthalpies (BTU/lb)	Mixture Ratios (O/F)	Expansion Ratios (wrt throat)
5.	-1300.	0.10	1.11 subsonic
10.	-1150.	1.00	1.29 supersonic
20.	-1000.	2.00	1.62 subsonic
50.	-750.	3.00	2.35 supersonic
100.	-500.	4.00	2.72 subsonic
200.	-250.	5.00	3.65 subsonic
400.	0.00	5.50	4.00 subsonic
450.	500.	6.00	4.14 subsonic
500.	1000.	6.50	4.27 subsonic
1000.		7.00	4.29 supersonic
		8.00	6.93 supersonic
		10.00	9.95 supersonic
		15.00	20.7 supersonic
		20.00	33.2 supersonic
		30.00	45.0 supersonic
			56.1 supersonic

* Note that the Mixture Enthalpies are determined by first subtracting a 'reference enthalpy' from each propellant (the reference enthalpy is at Standard Temperature and Pressure).

Table 4.3.1
Comparison of Model Dynamic Volume Sizes

Volume Name	**Size Estimated from Prints** (cubic inches)	**Size Specified in Baseline Model** (cubic inches)
Fuel Pump Inlet	30. (notes 1, 2)	(note 1)
LOX Pump Inlet (and Supply line)	250. (notes 2, 3)	(note 1)
Fuel Pump Interstage Duct	44.8 (note 2)	(note 1)
Fuel Pump Discharge Duct	47.0 (note 2)	(note 1)
Cooling Jacket Inlet Manifold	91.0	110.95
Cooling Jacket Tubes	971.8	915.9
Venturi Duct	167.2	286.6
Turbine Discharge to MFSOV	309.8	428.11
Fuel Injector Plennum	(note 4)	123.98
LOX Injector Plennum	(note 4)	86.87
Combustion Chamber	803.3	931.0

Notes:

1. No information was given from Pratt & Whitney for these volumes; they are used only in the shutdown model.

2. Other minor volumes exist in this area that are too complex to estimate. The actual values used in the model are rounded up to the nearest 10. cubic inches.

3. The lumped volume of the LOX inlet duct is separated into two smaller volumes for dynamic modeling. One piece is assumed to be assigned to the tank, which is not modeled. The volume included in the model at the LOX pump inlet is 150. cubic inches.

4. The geometries of the injector plenna are too complex for accurate estimation.

Table 6.1.1
Steady-state Cycle Performance Prediction for the RL10A-3-3A

NASA Lewis Research Center RL10A-3-3A Engine Model Output

OVERALL ENGINE PERFORMANCE

Chamber Pressure (at injector face)	475.5	psia
Engine Thrust	16412	lbf
Engine Inlet O/F	4.993	
Combustion O/F	5.055	
Specific Impulse	445.6	sec
Fuel Consumption	6.161	lb/sec
Oxidizer Consumption	30.76	lb/sec

COMBUSTION CHAMBER / NOZZLE

Nozzle Stagnation Pressure	473.5	psia
Combustion Temperature	5816	R
c* Efficiency	0.9892	
c* (ideal)	93885	in/sec
Engine Exit Pressure (ambient)	0.01	psia
Fuel-LOX heat transfer at injector	40.36	BTU/sec

FUEL-SIDE ENGINE CONDITIONS

Location	static pressure (psia)	total pressure (psia)	total temp (deg R)	mass flow (lb/sec)	density (lb/cu.ft)	total enthalpy (BTU/lb)
Fuel Tank	27.68	27.68	38.60	.....	4.337	-105.1
Fuel Pump Inlet	26.08	27.19	38.6	6.161	4.337	-105.1
Fuel Pump Interstage	532.2	534.8	47.65	6.118	4.285	-68.21
Fuel Pump Discharge	1058.9	1067.3	57.63	6.082	4.220	-27.84
Cooling Jacket Inlet	1018.3	1026.6	57.94	6.082	4.185	-27.84
Cooling Jacket Exit	816.8	830.9	384.2	6.082	0.3855	1240.5
Turbine Inlet	796.7	813.8	384.2	6.056	0.3767	1240.5
Turbine Hiusing Exit	562.2	576.2	361.1	6.082	0.2868	1149.2
Fuel Injector Plennum	537.9	537.9	359.4	6.082	0.2742	1142.4
Chamber	475.5					

OXIDIZER-SIDE ENGINE CONDITIONS

Location	static pressure (psia)	total pressure (psia)	total temp (deg R)	mass flow (lb/sec)	density (lb/cu.in)	total enthalpy (BTU/lb)
Oxygen Tank	42.35	42.35	174.7	.....	69.07	66.42
Ox Pump Inlet	36.33	39.96	174.7	30.76	69.07	66.42
Ox Pump Discharge	601.5	621.1	178.6	30.75	69.02	68.84
Oxid. Injector Plennum	529.4	539.3	182.1	30.75	68.31	70.15
Chamber	475.5					

TURBOMACHINERY PERFORMANCE

	delta-Head (feet)	Volume Flow (gpm)	Speed (rpm)	Torque (lbf-in)	Efficiency
Fuel Pump					
1st stage	16858	637.8	31494	645.5	0.5854
2nd stage	17901	641.0	31494	700.7	0.5686
LOX Pump	1212	199.9	12598	529.1	0.6408

Turbine Pressure Ratio (T-S)	1.402	
Turbine Exit Pressure (static)	580.6	psia
Turbine Exit Temperature	360.9	R
Turbine delta-H	92.02	BTU/lb
Turbine Efficiency	0.7353	
Turbine Torque	1577.8	lbf-in
Veocity Ratio (U/Co)	0.4581	

COOLING JACKET PERFORMANCE

Cooling Jacket delta-P (total)	195.7	psid
Cooling Jacket delta-T	326.3	R
Total Heat Pick-up	7714.2	BTU/sec
Maximum Metal Temp	1500.8	R

VALVE PERFORMANCE

Thrust Control Open Area	.004836	sq.in.
Turbine Bypass Flow	.02634	lb/sec
Oxidizer Control Open Area	.5783	sq.in.
OCV primary flow	28.10	lb/sec
OCV bypass flow	2.659	lb/sec

Table 6.2.1
Comparison of Measured and Predicted
RL10 Engine Time-to-Accelerate

Type of Run	Simulation Time (sec from MES)	Measure Time (sec from MES)	difference (msec)
Ground Test	2.09	2.26	170 (early)
Ground Test	1.80	1.90	100 (early)
Ground Test	1.51	1.43	80 (late)
Ground Test	1.72	1.70	20 (late)
Ground Test (Relight)	1.91	1.84	70 (late)
Ground Test (Relight)	2.00	2.08	80 (early)
Flight	1.98	1.90	80 (late)
Flight	1.95	1.67	280 (late) *
Flight (Relight)	2.33	2.56	230 (early)

* Note : Although this run had inlet conditions similar to other flights, these engines started about 300 msec earlier relative to MES1. This may indicate a difference in the engine other than inlet conditions (see section of this report on uncertainty).

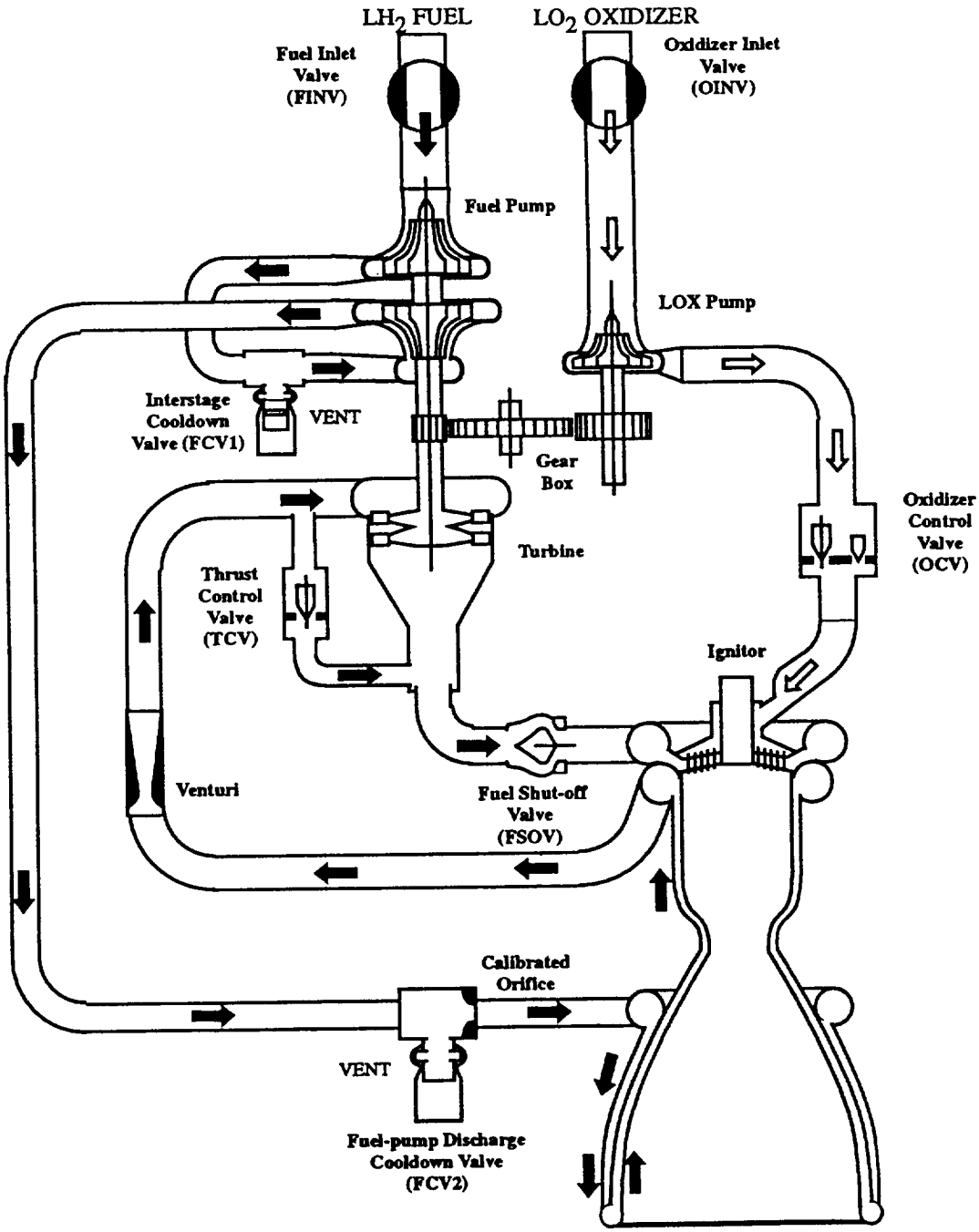

Figure 2.1.1—RL10A-3-3A Engine System Schematic

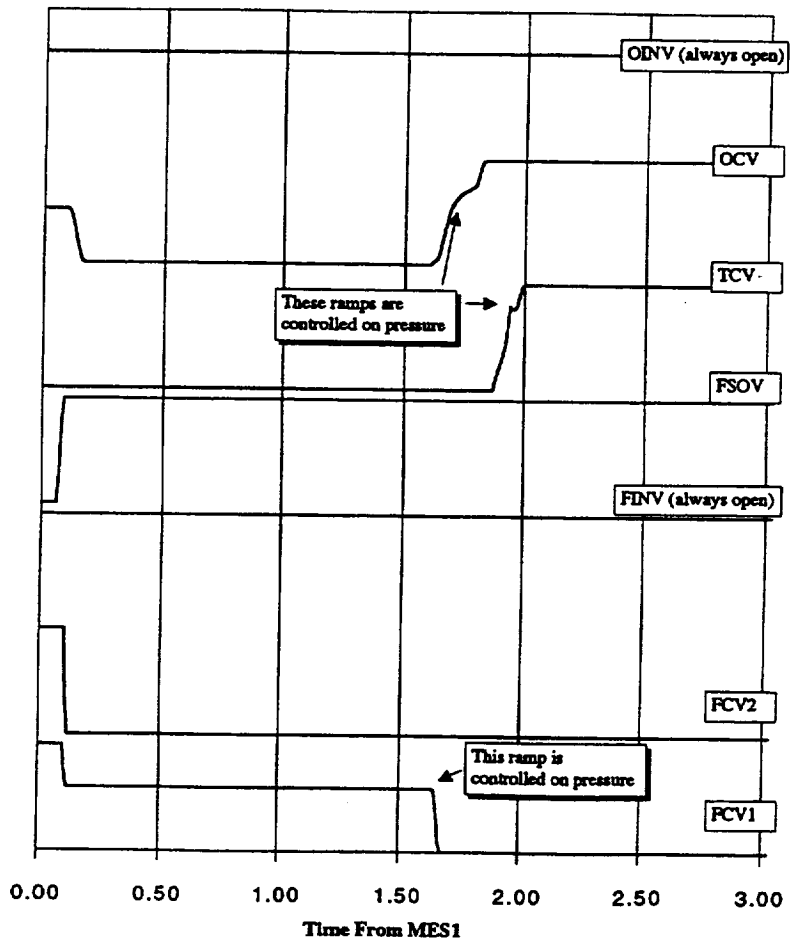

Figure 2.1.2—RL10 Assumed Valve Schedules for Start Simulation

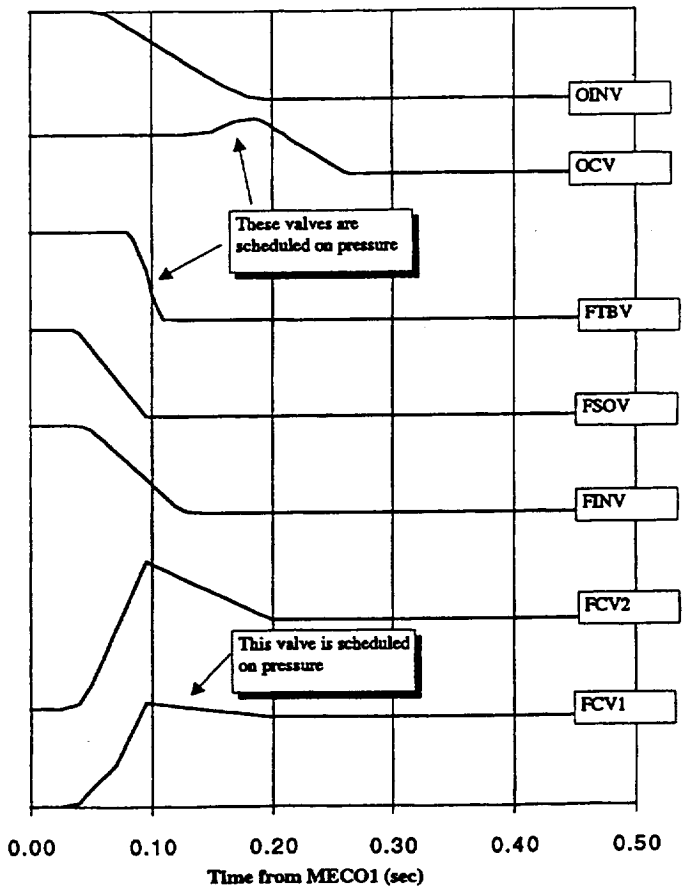

Figure 2.1.3—RL10 Assumed Valve Schedules for Shutdown Simulation

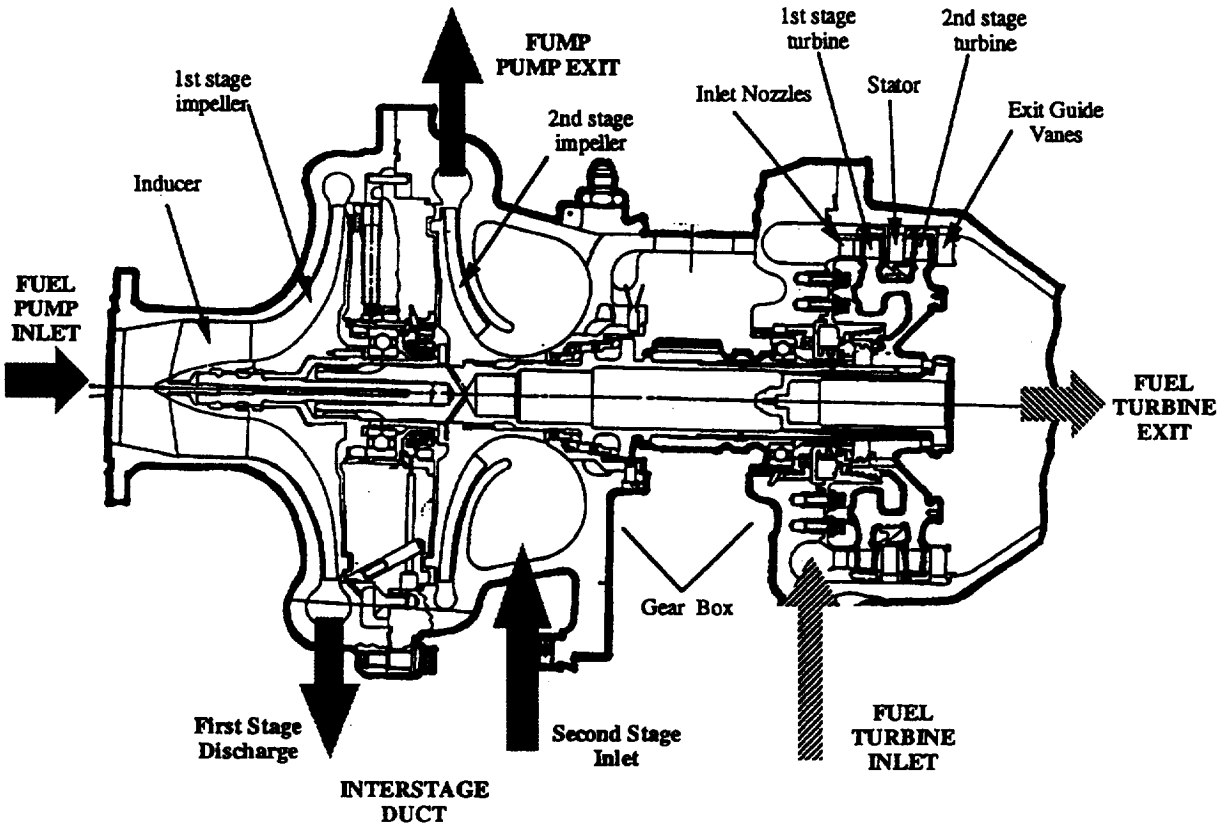

Figure 2.2.1—Cross-Section of Fuel Pump and Turbine

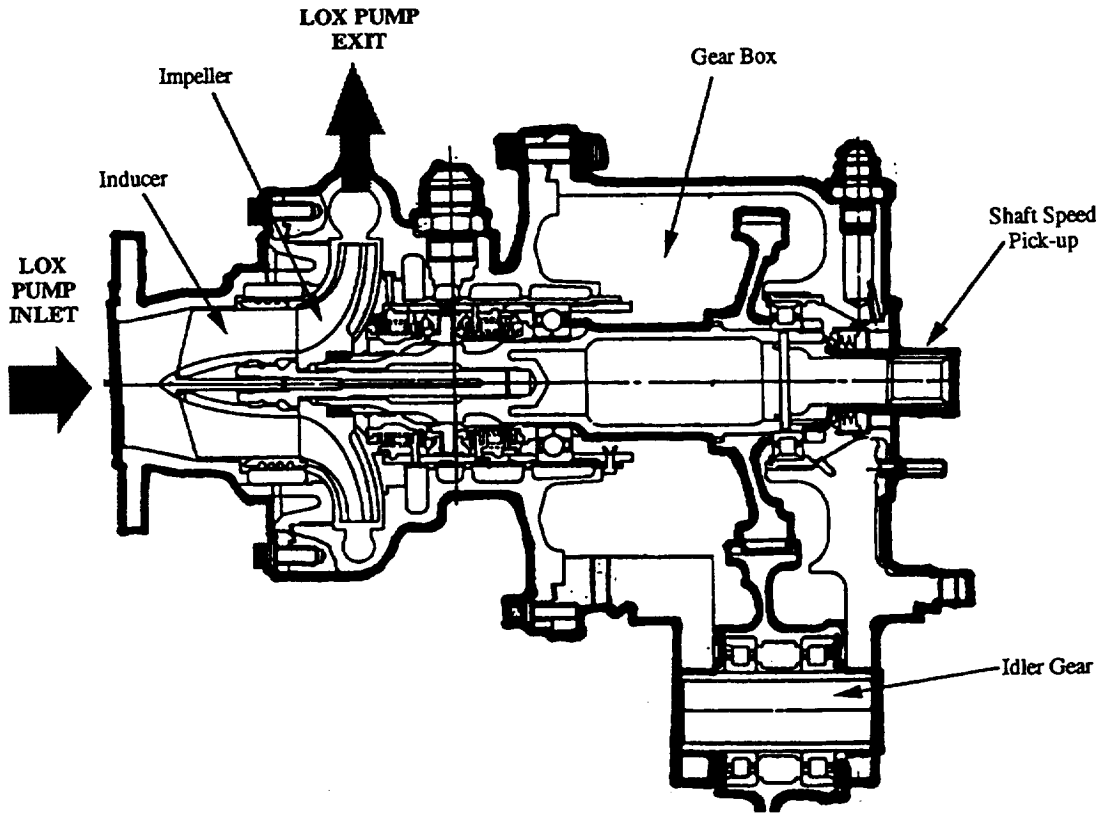

Figure 2.3.1—Cross Section of LOX Pump and GearBox

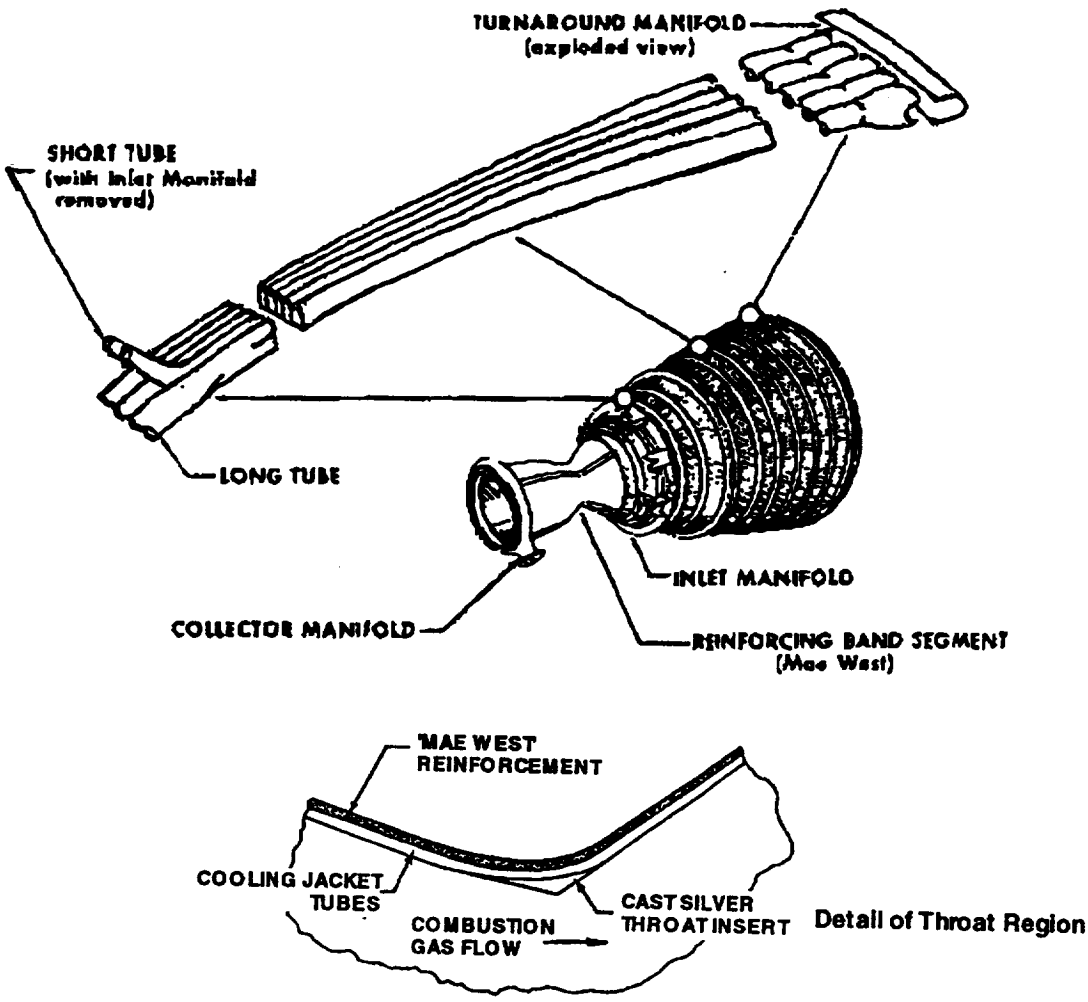

Figure 2.4.1—Structure of Regenerative Cooling Jacket, Chamber and Nozzle

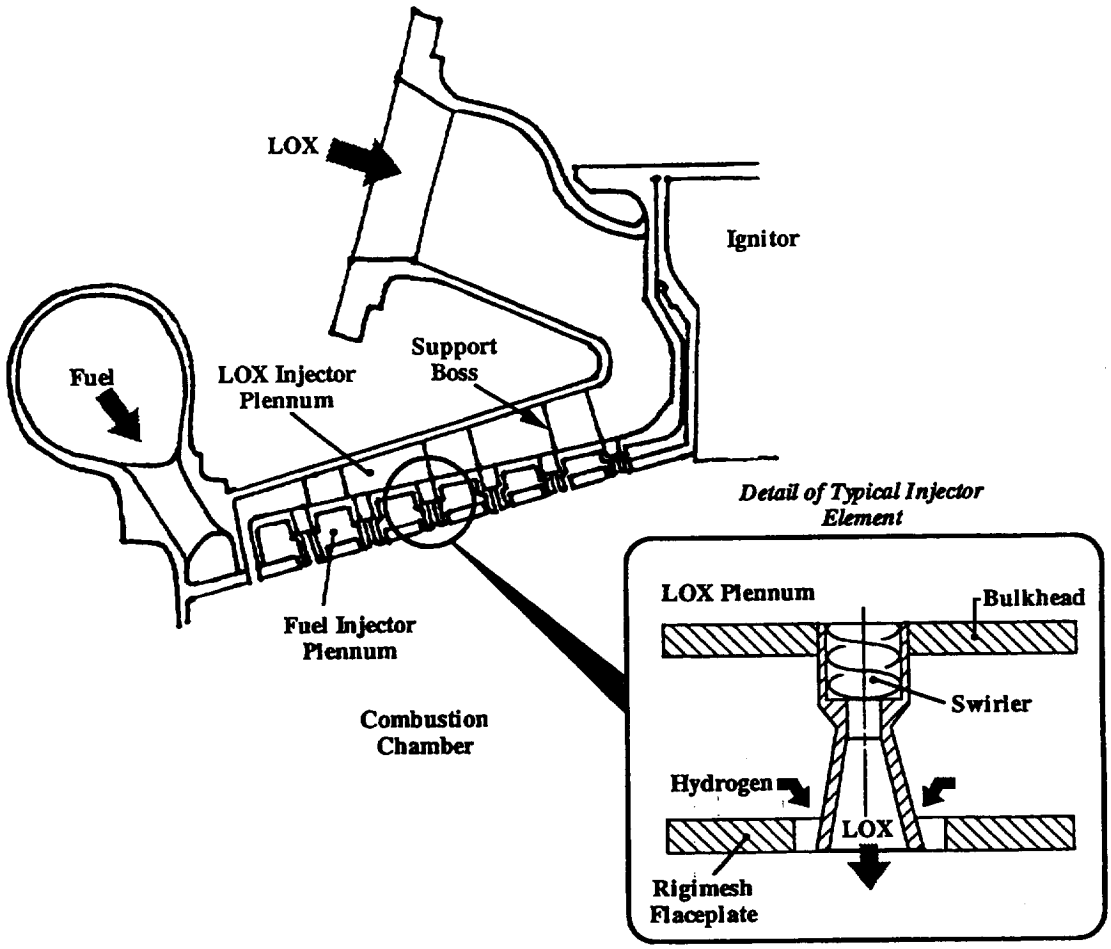

Figure 2.5.1—Injector Design Configuration

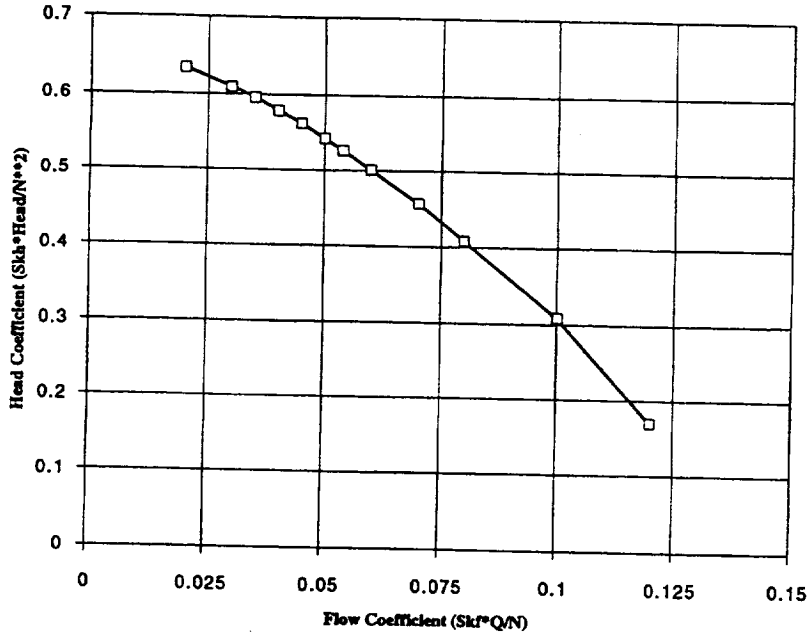

Figure 4.1.1—Original Head Map for Fuel Pump 1st Stage (provided by P&W)

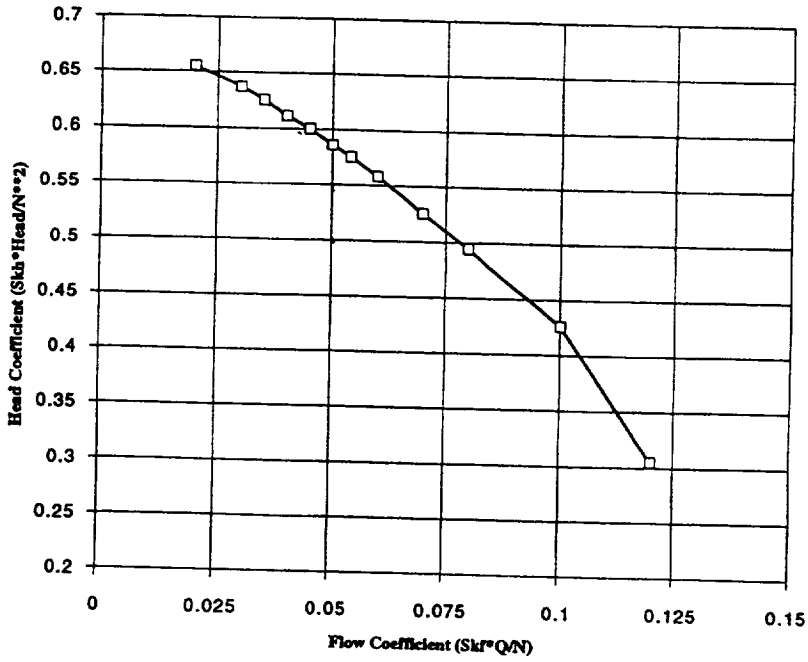

Figure 4.1.2—Original Head Map for Fuel Pump 2nd Stage (provided by P&W)

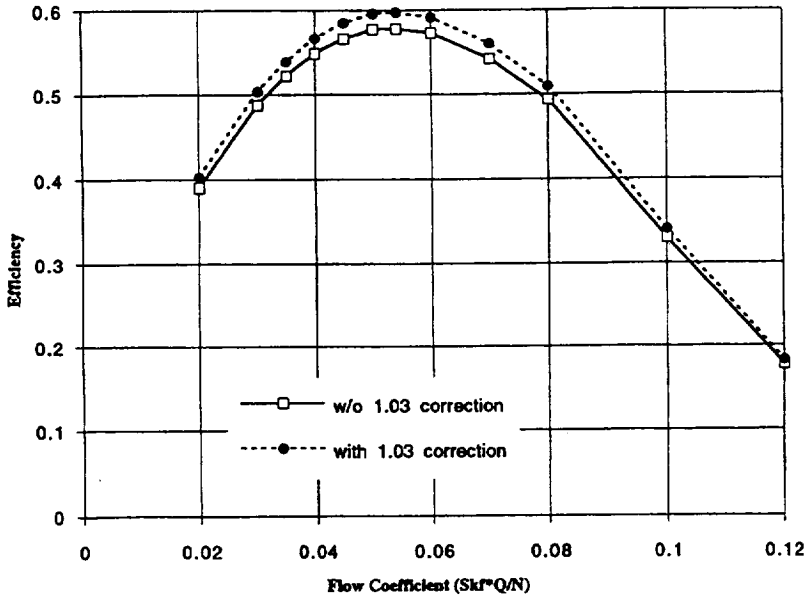

Figure 4.1.3—Original Efficiency Map for Fuel Pump 1st stage (provided by P&W)

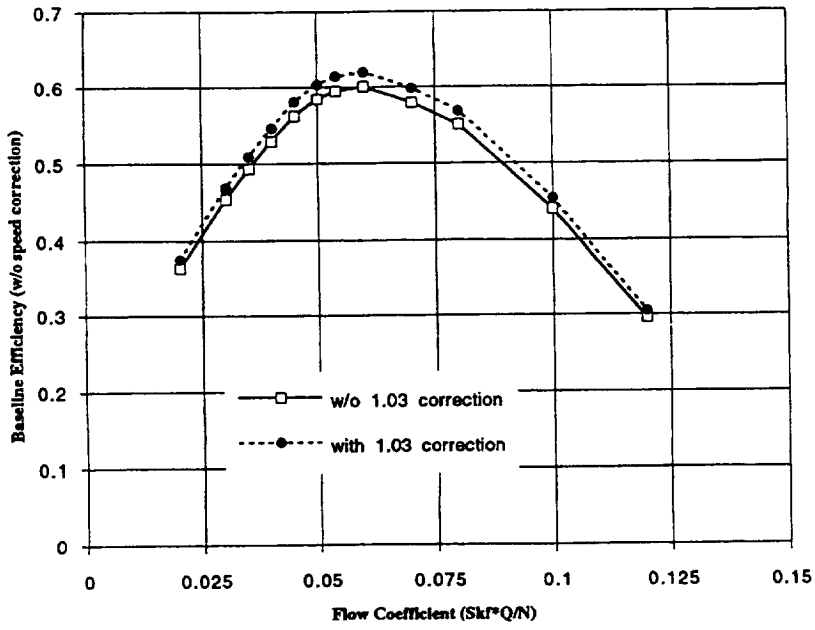

Figure 4.1.4—Original Efficiency Map for Fuel Pump 2nd stage (provided by P&W)

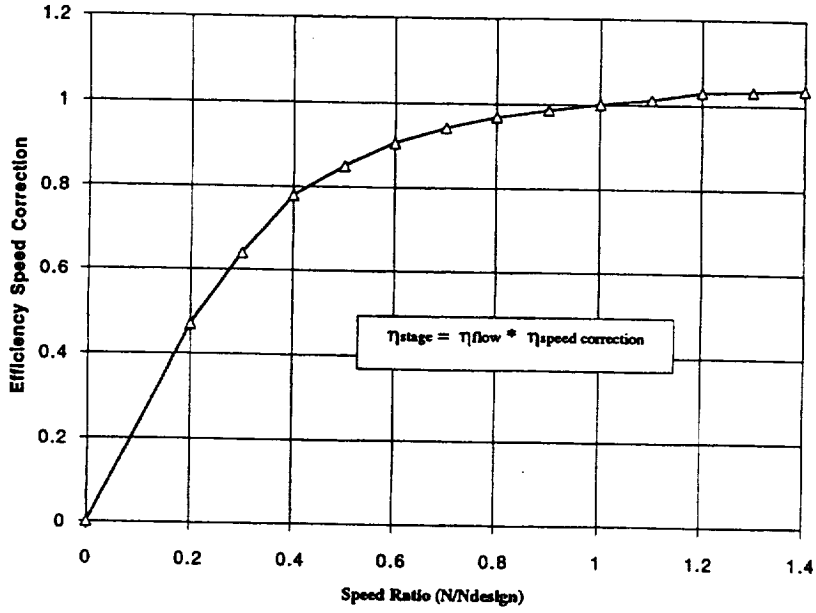

Figure 4.1.5—Efficiency Speed Correction Map for Fuel Pump - both stages (provided by P&W)

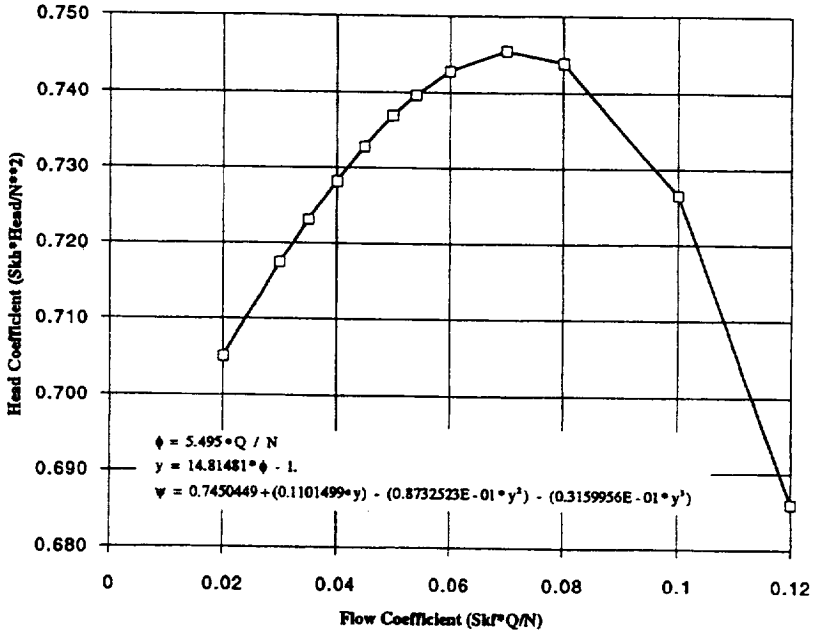

Figure 4.1.6—Original Head Map for LOX Pump (provided by P&W)

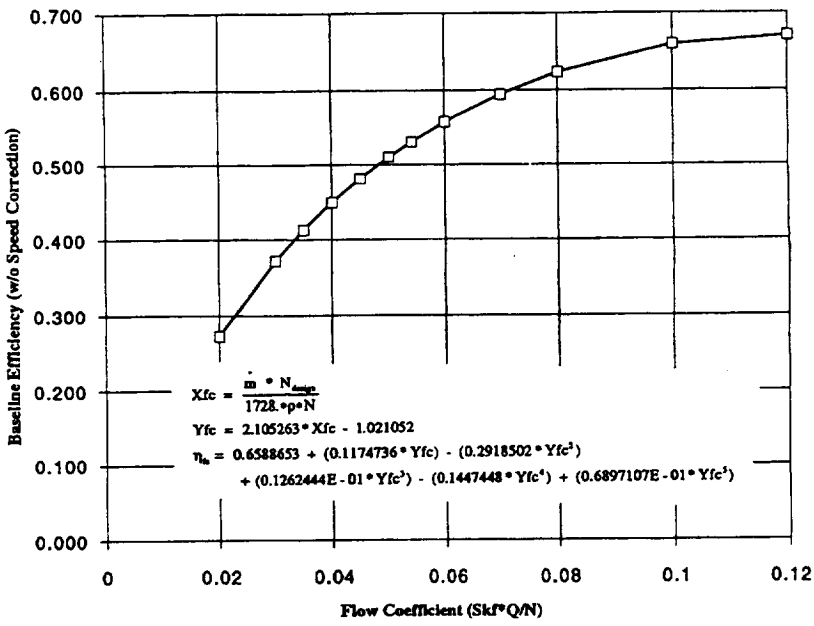

Figure 4.1.7—Original Efficiency Map for LOX Pump (provided by P&W)

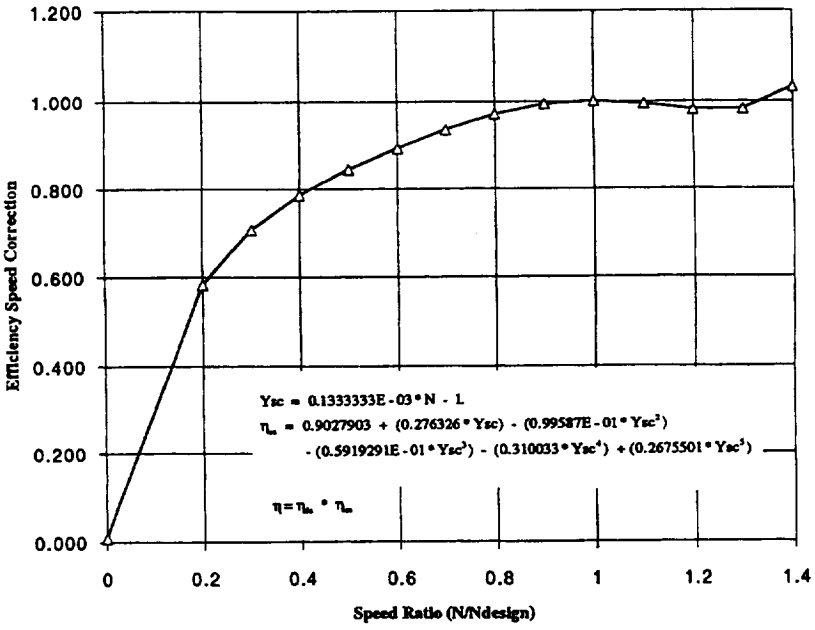

Figure 4.1.8—Efficiency Speed Correction Map for LOX Pump (provided by P&W)

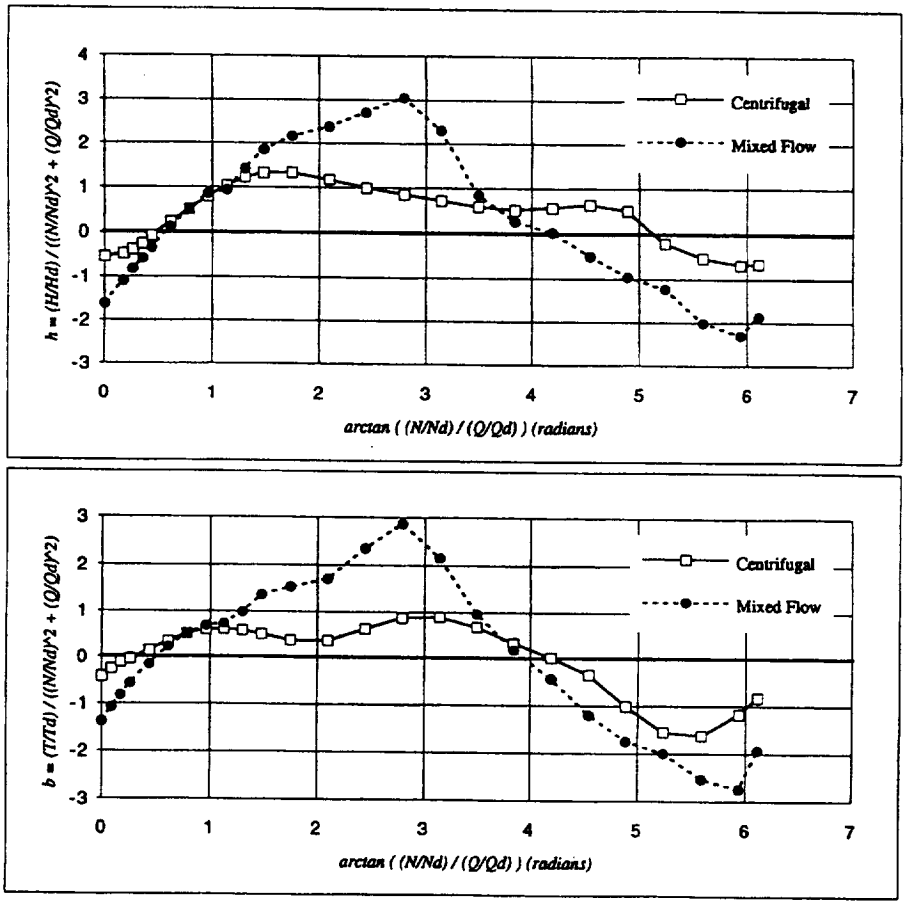

Figure 4.1.9—Generic Wide-Range Performance Maps for Centrifugal and Mixed-Flow Pumps

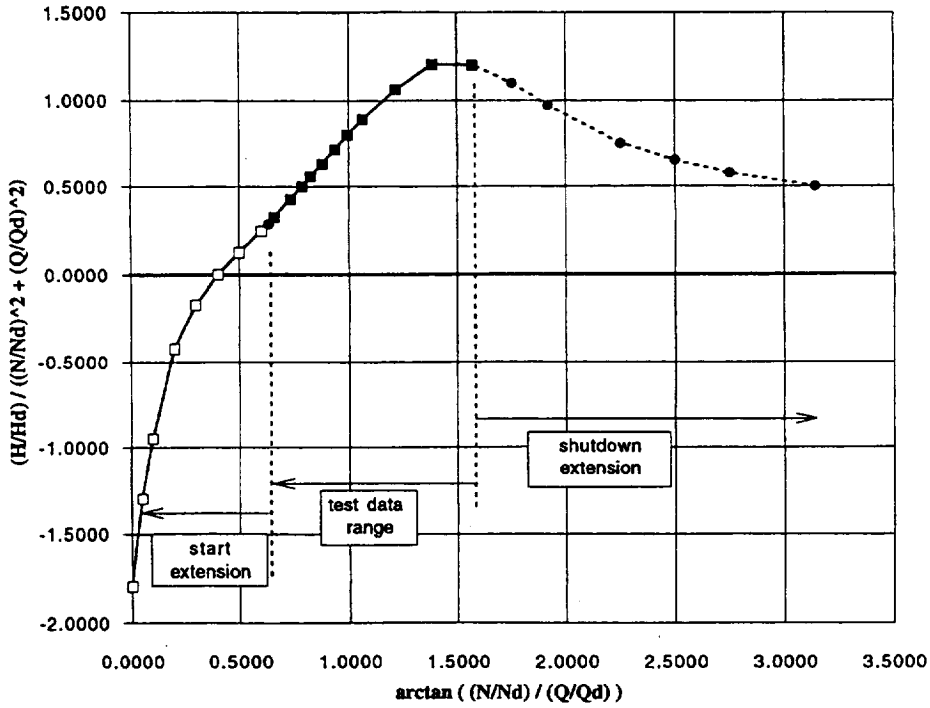

Figure 4.1.10—Extended Head Map for Fuel Pump 1st Stage

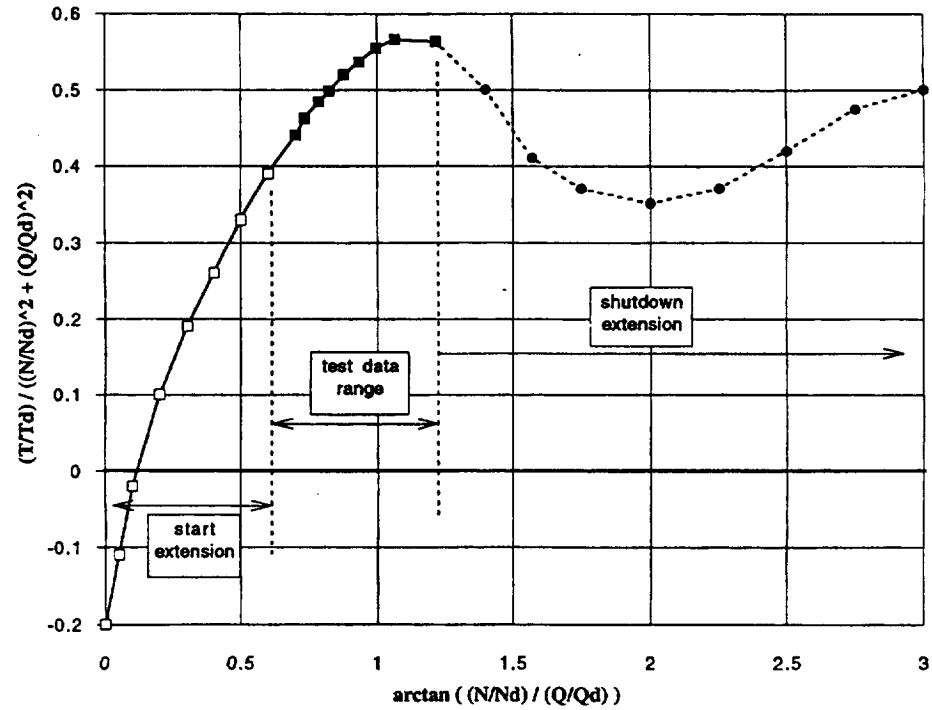

Figure 4.1.11—Extended Torque Map (w/o Speed Correction) for Fuel Pump 1st Stage

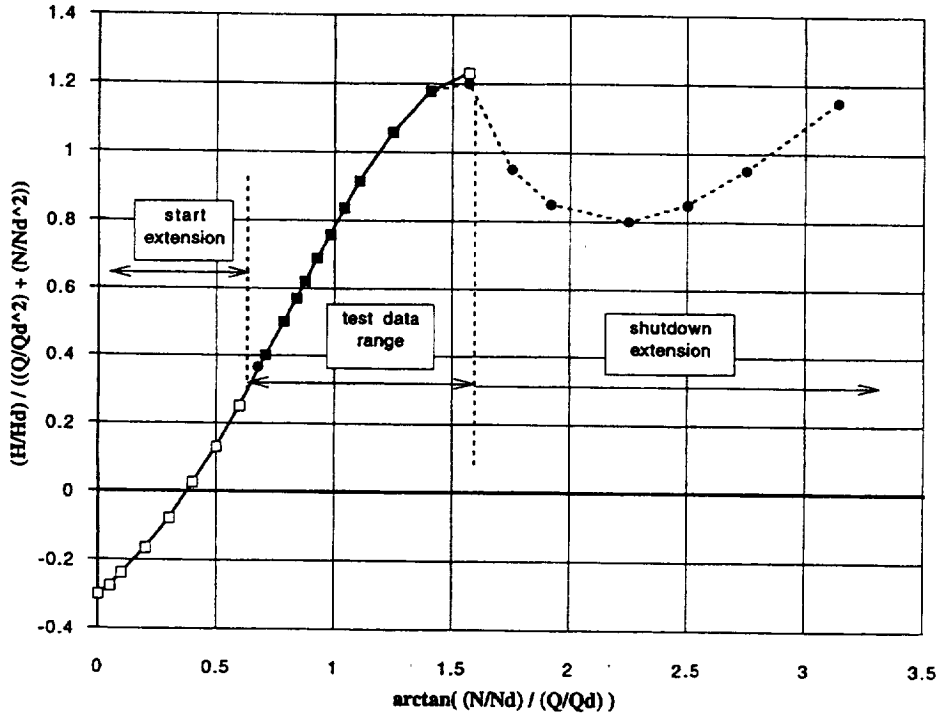

Figure 4.1.12—Extended Head Map for Fuel Pump 2nd Stage

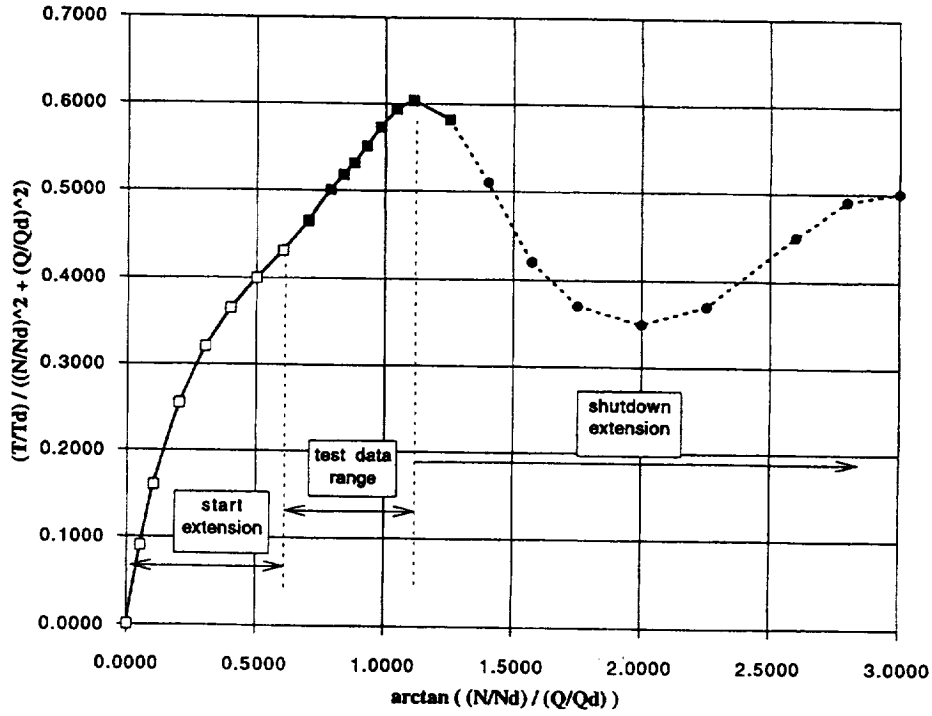

Figure 4.1.13—Extended Torque Map (w/o Speed Correction) for Fuel Pump 2nd Stage

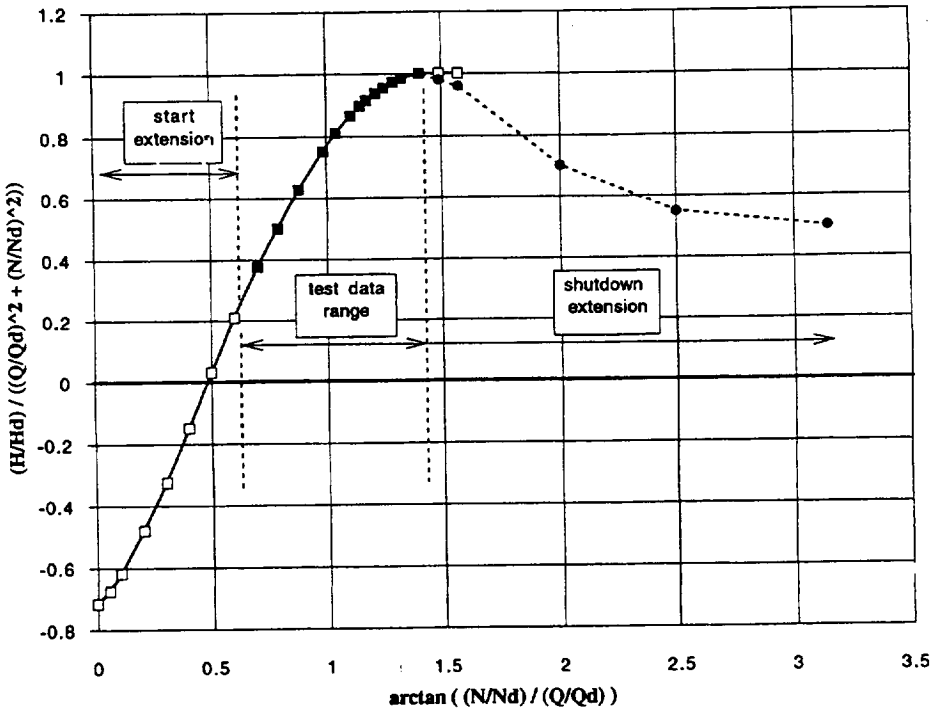

Figure 4.1.14—Extended Head Map for LOX Pump

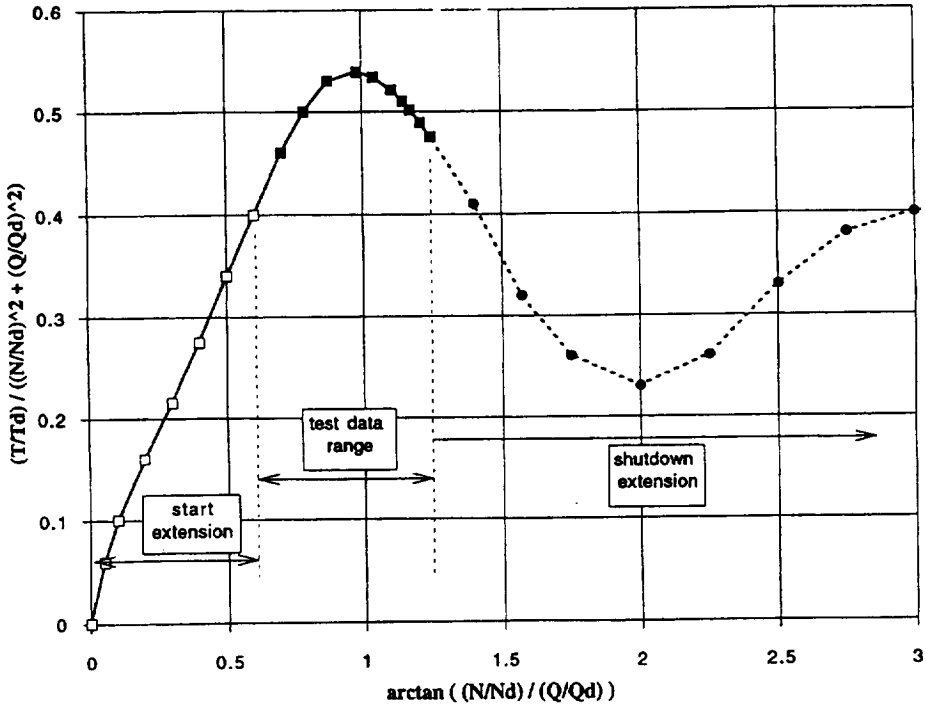

Figure 4.1.15—Extended Torque Map (w/o Speed Correction) for LOX Pump

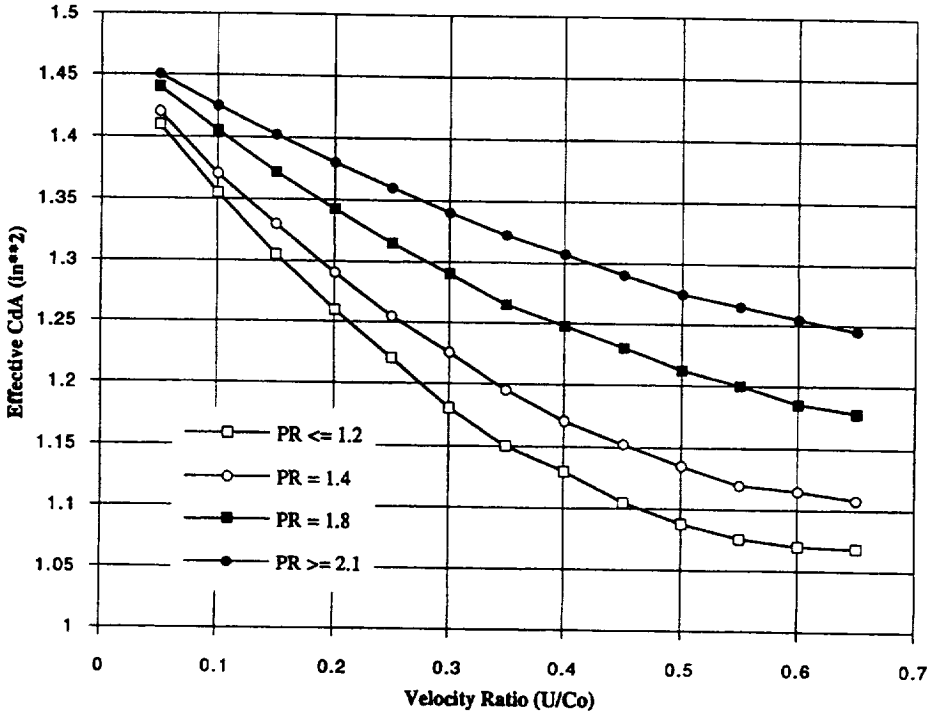

Figure 4.1.16—Fuel Turbine Effective Flow Area Map (provided by P&W and Martin-Marietta)

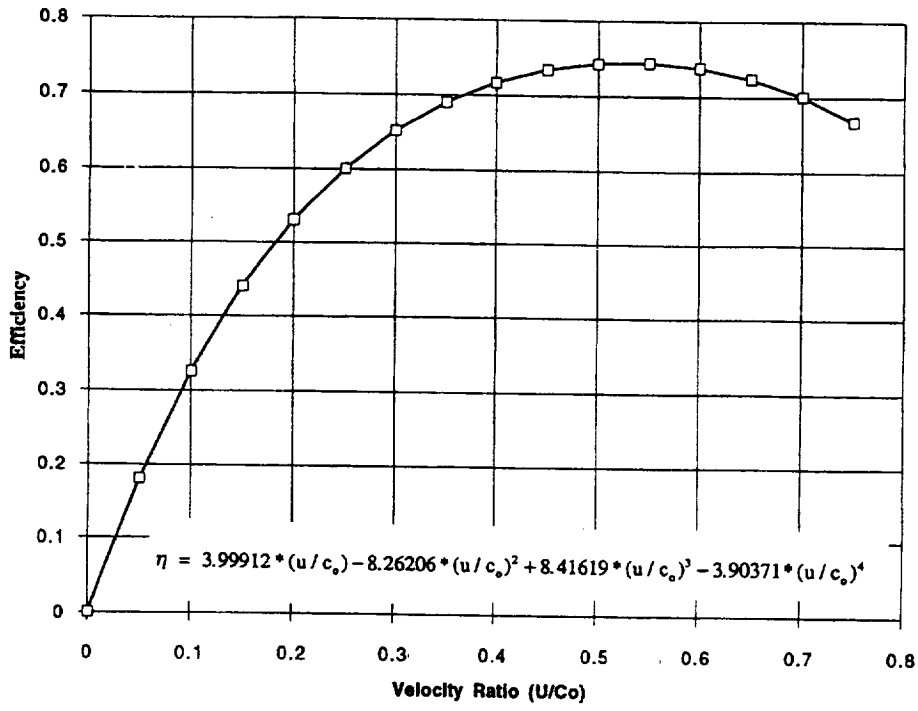

Figure 4.1.17—Fuel Turbine Efficiency Map (provided by P&W and Martin-Marietta)

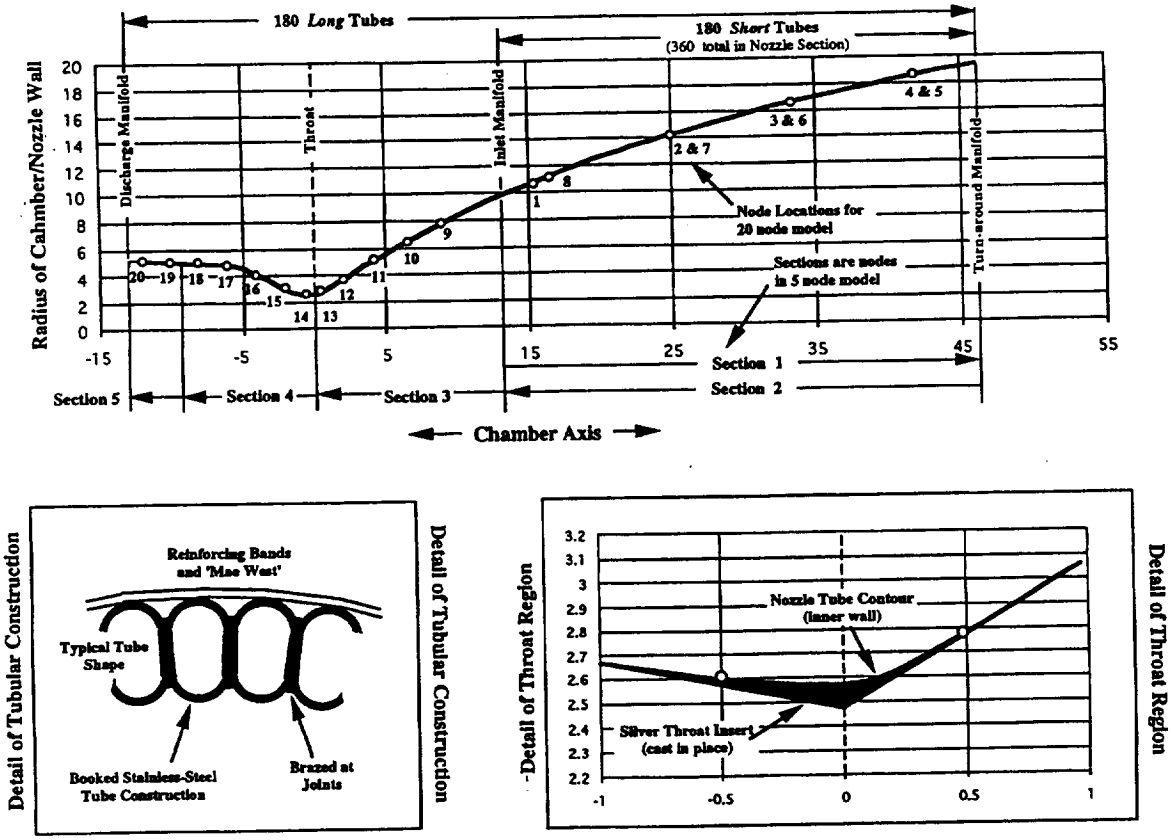

Figure 4.2.1—Configuration of Cooling Jacket and Model

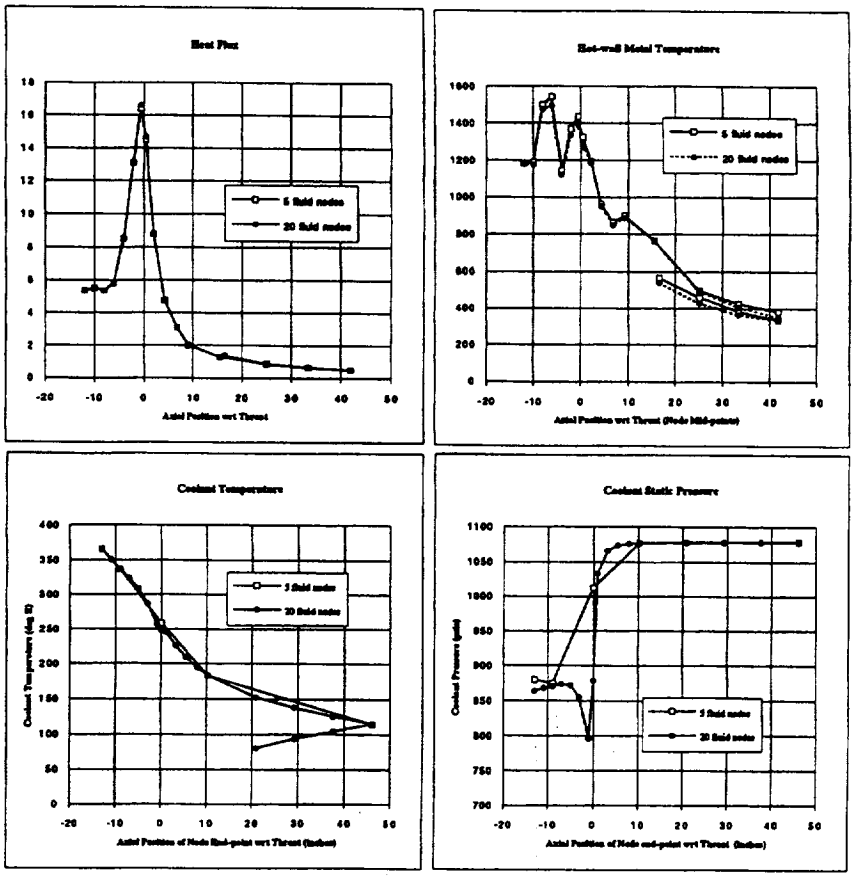

Figure 4.2.2—Comparison of Full 20-Node Model with 20-Metal-Node/5-Fluid-Node Model

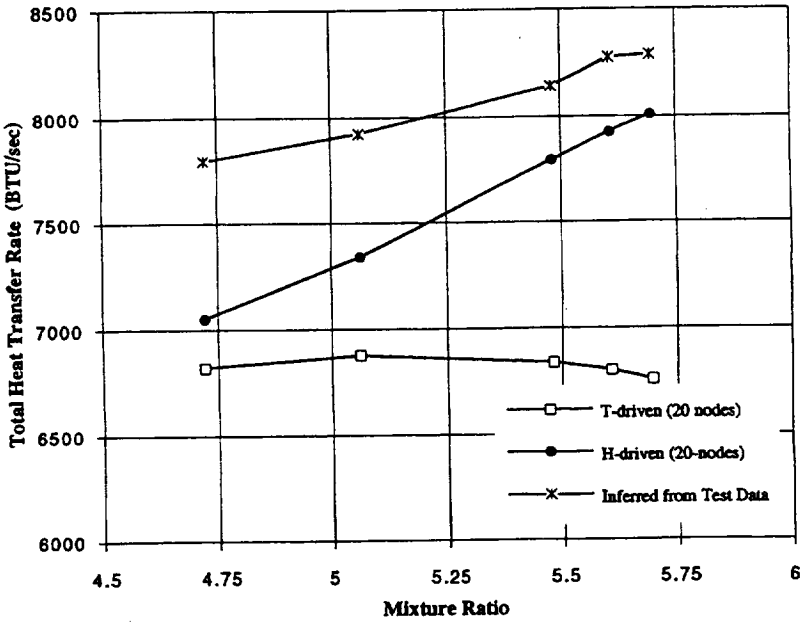

Figure 4.2.3—Comparison of Enthalpy-Driven and Temperature-Driven Potential Predictions

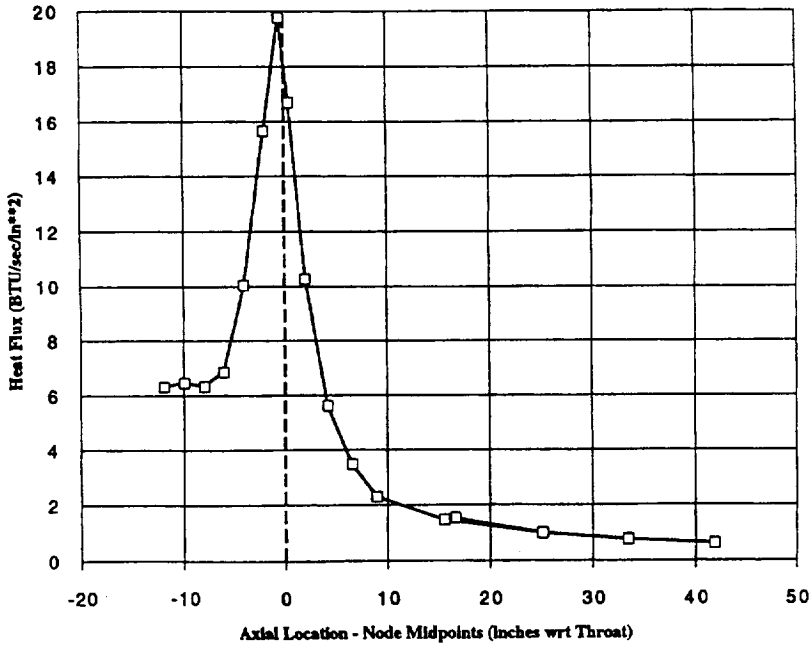

Figure 4.2.4—Predicted Heat Flux Distribution

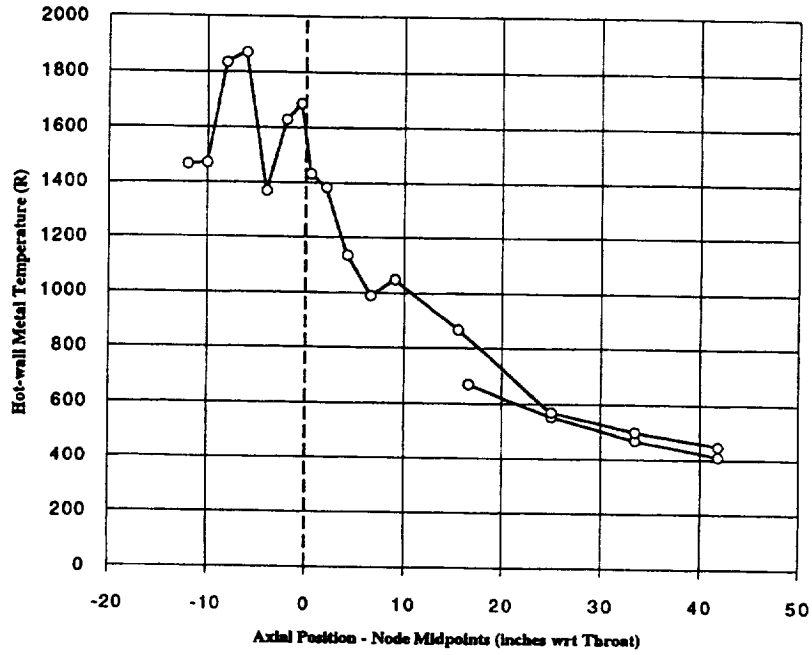

Figure 4.2.5—Predicted Hot-Wall Metal Temperature Distribution

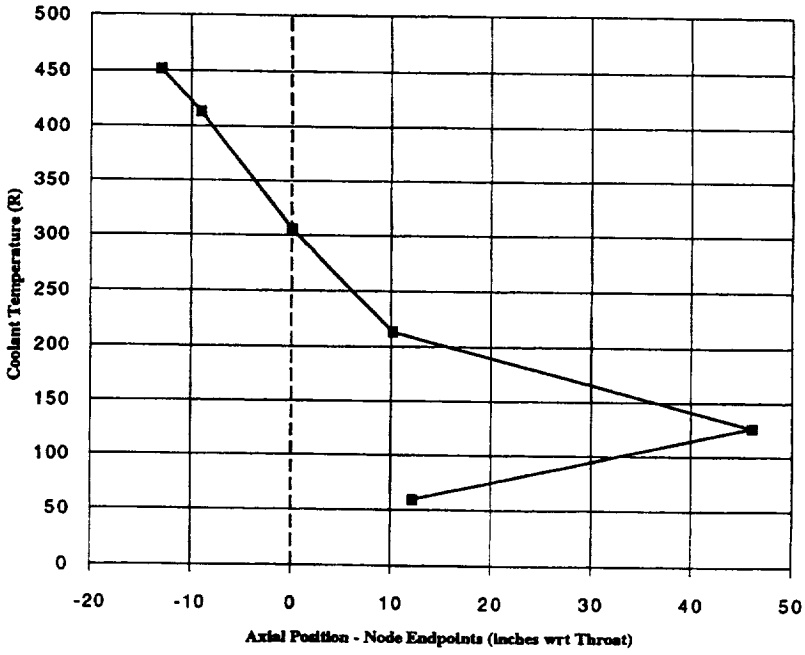

Figure 4.2.6—Predicted Coolant Temperature Distribution

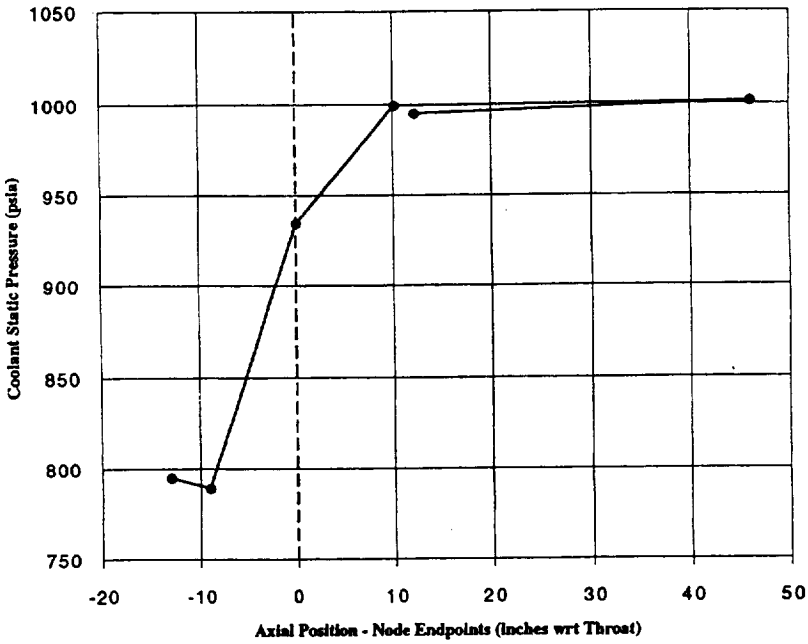

Figure 4.2.7—Predicted Coolant Pressure Distribution

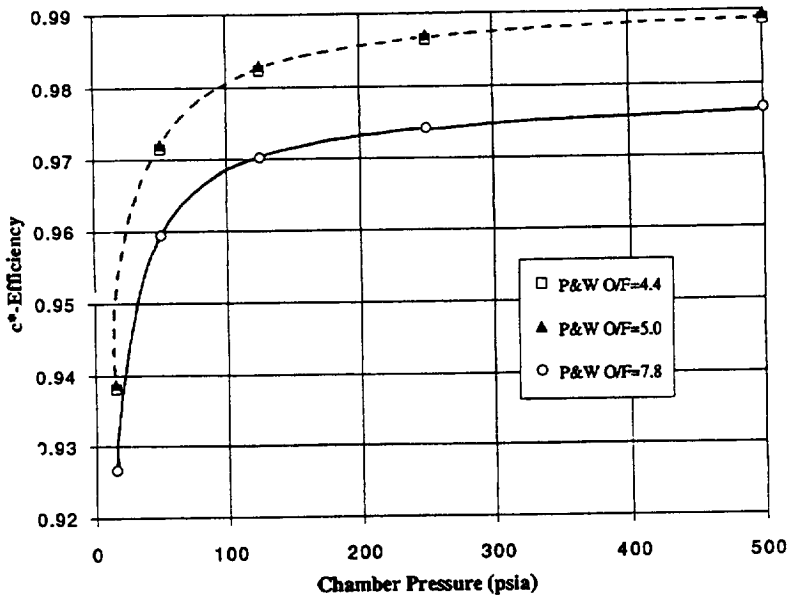

Figure 4.2.8—c*-Efficiency Maps (from P&W)

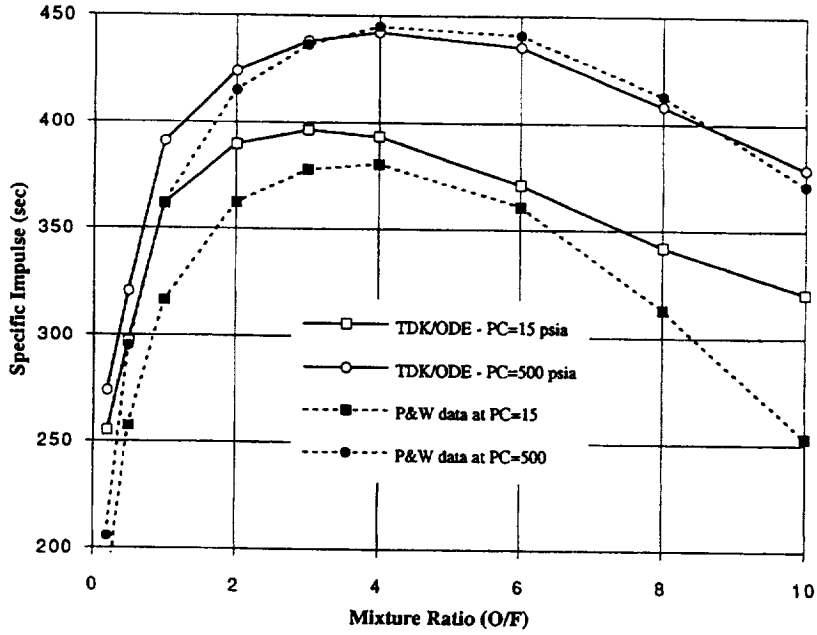

Figure 4.2.9—TDK/ODE Predictions of RL10A-3-3A Actual Isp, compared to data provided by P&W

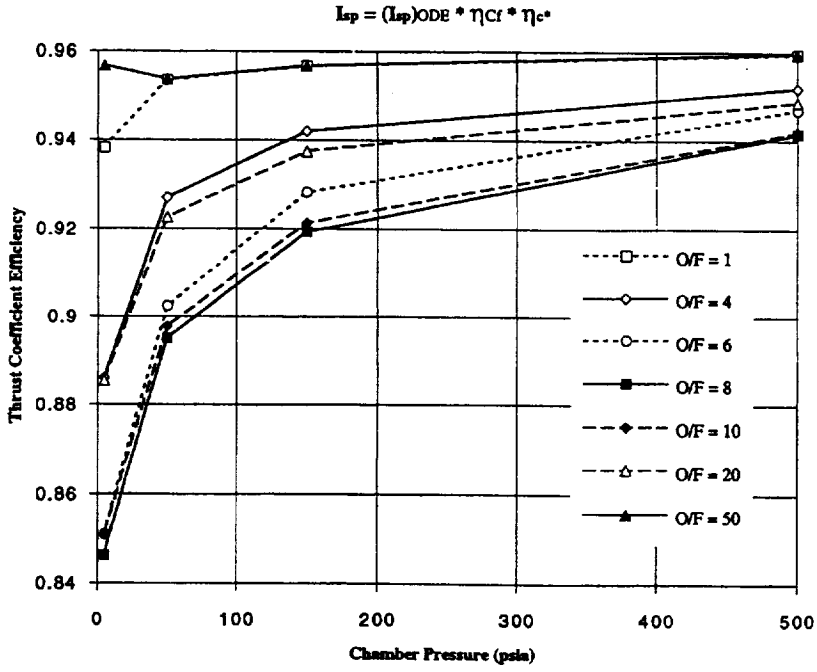

Figure 4.2.10—TDK Predictions of RL10A-3-3A Thrust-Coefficient Efficiency

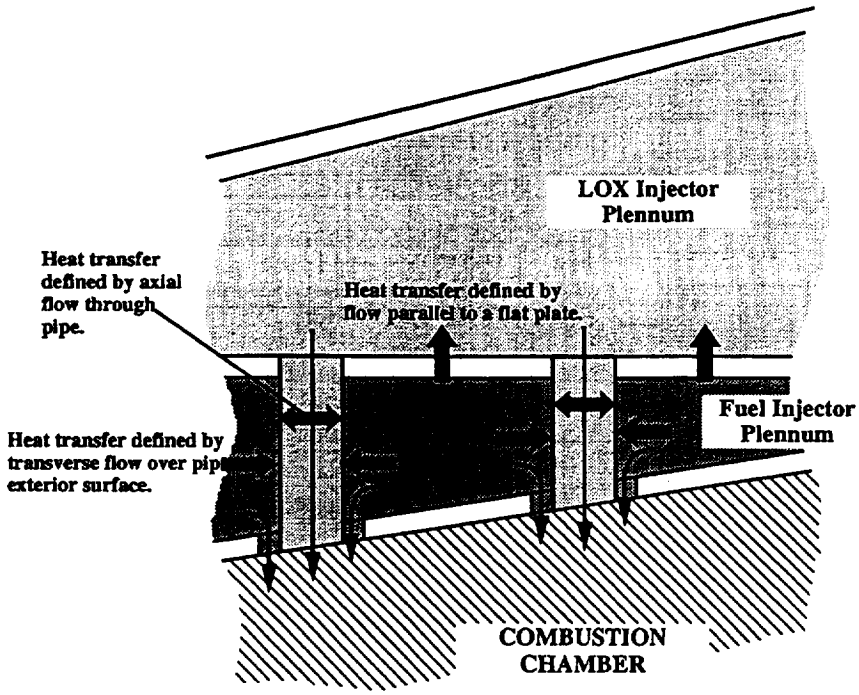

Figure 4.2.11—Injector Heat Transfer Model Configuration

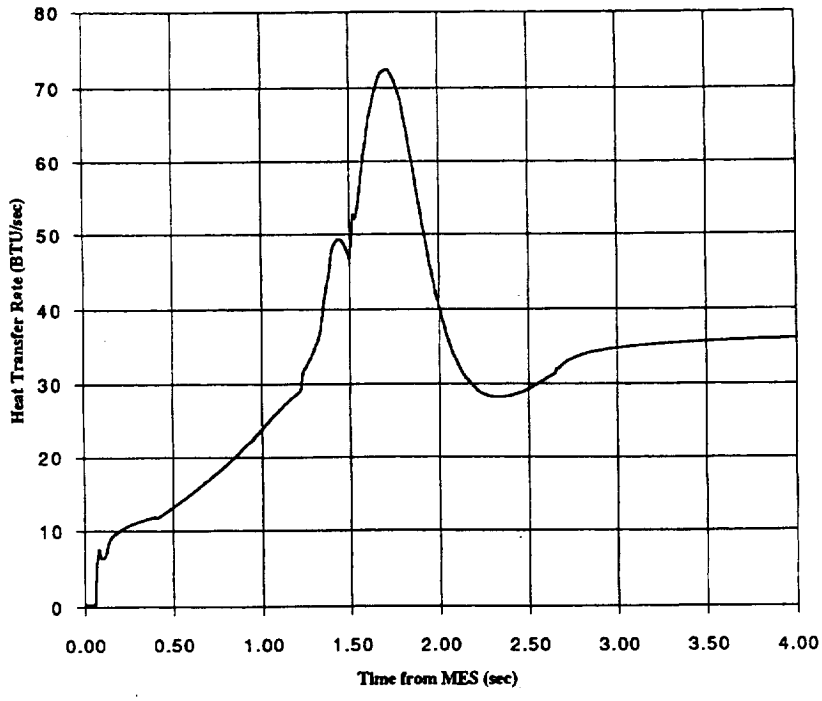

Figure 4.2.12—Injector Heat Transfer Rate during start sequence

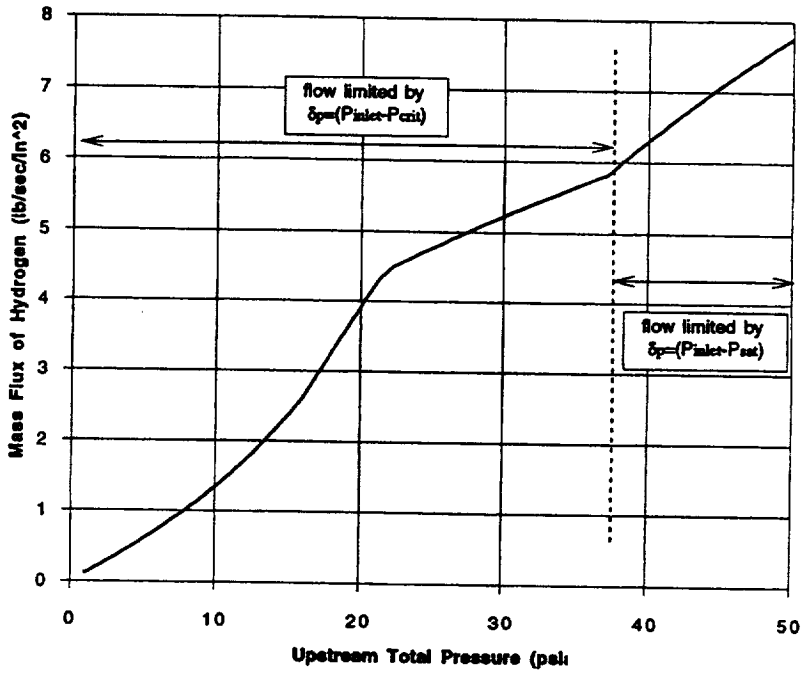

Figure 4.3.1—Predicted Mass Flux for Choked Two-phase Flow

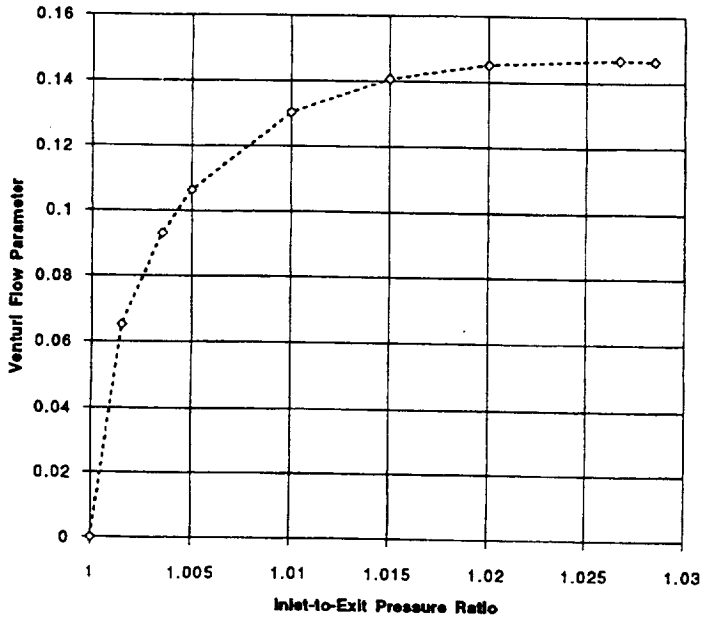

Figure 4.3.2—RL10 Venturi Flow Parameter Map

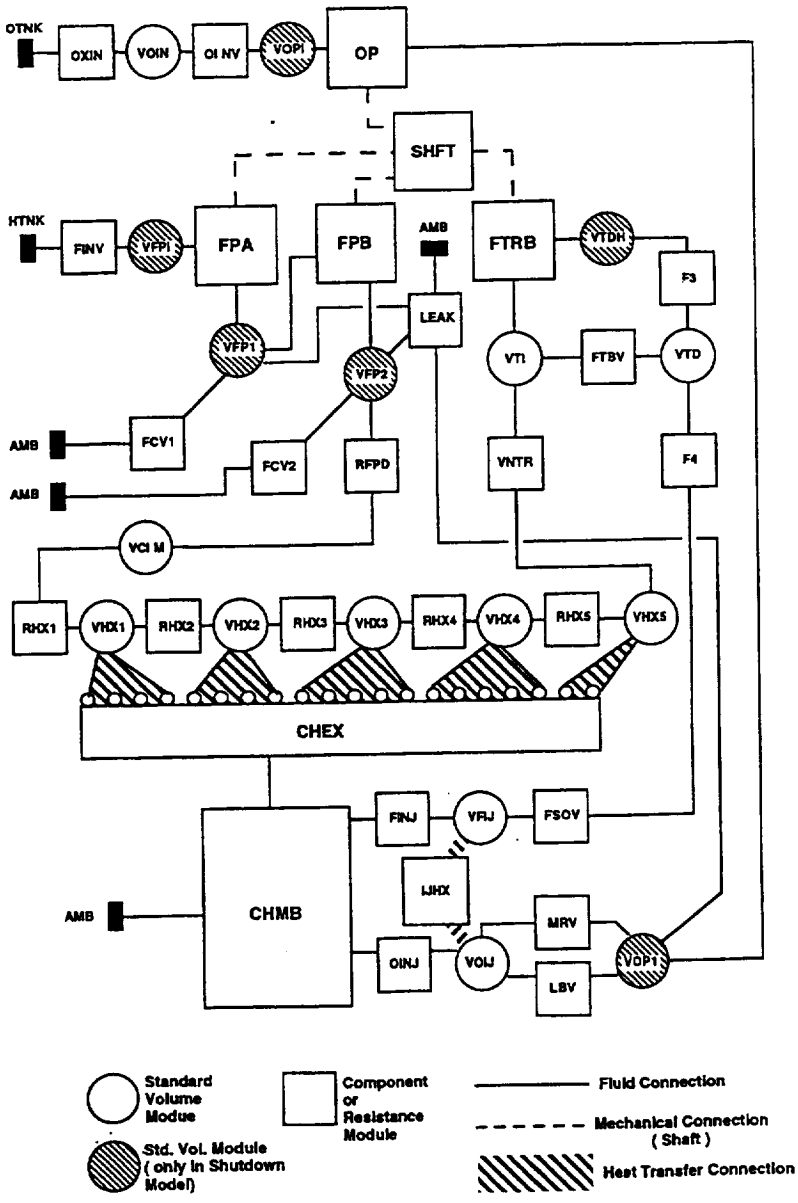

Figure 4.4.1—RL10A-3-3A Engine System Model Schematic

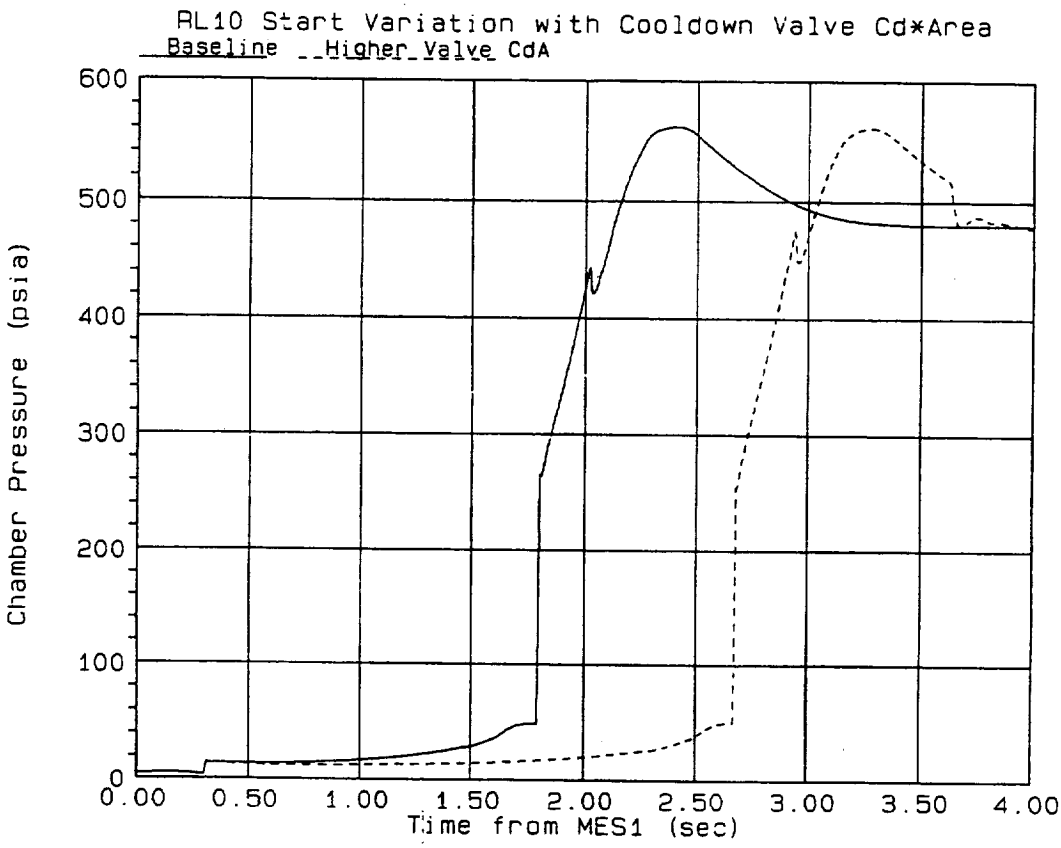

Figure 5.1.1—Variation in Start with Cooldown Valve Effective Area

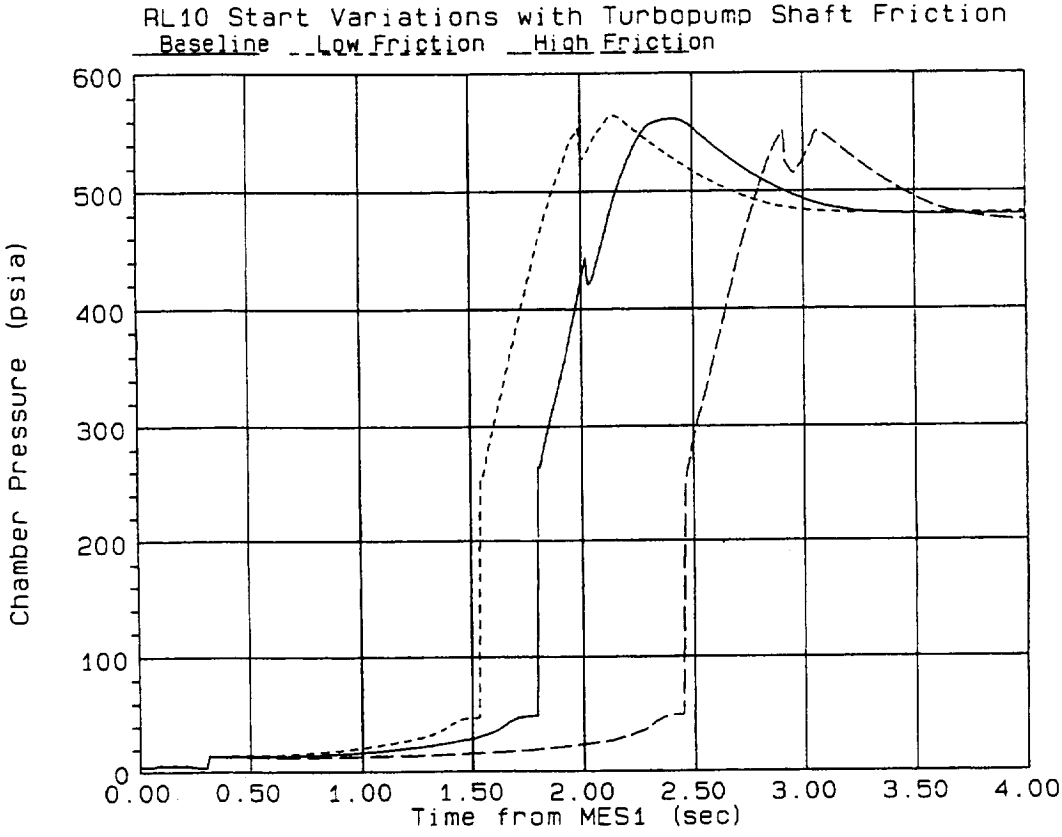

Figure 5.1.2—Variation in Start with Turbopump Drag Torque

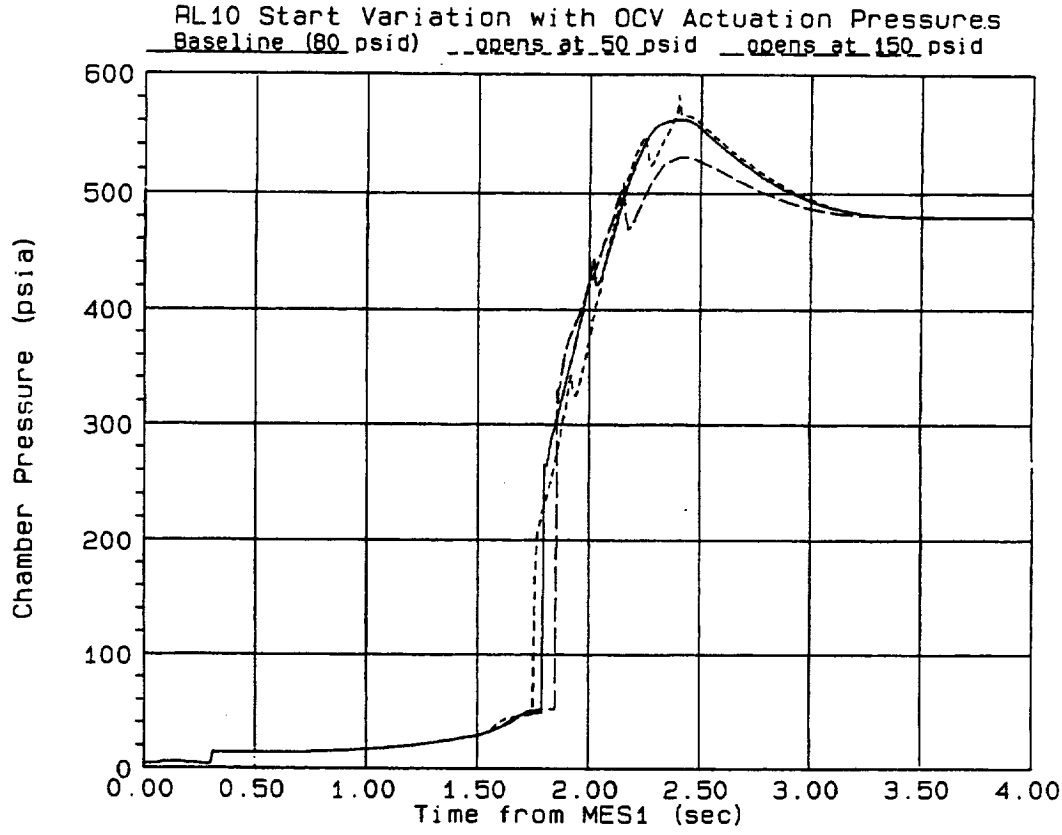

Figure 5.2.1—Variation in Start with OCV Actuation Pressure

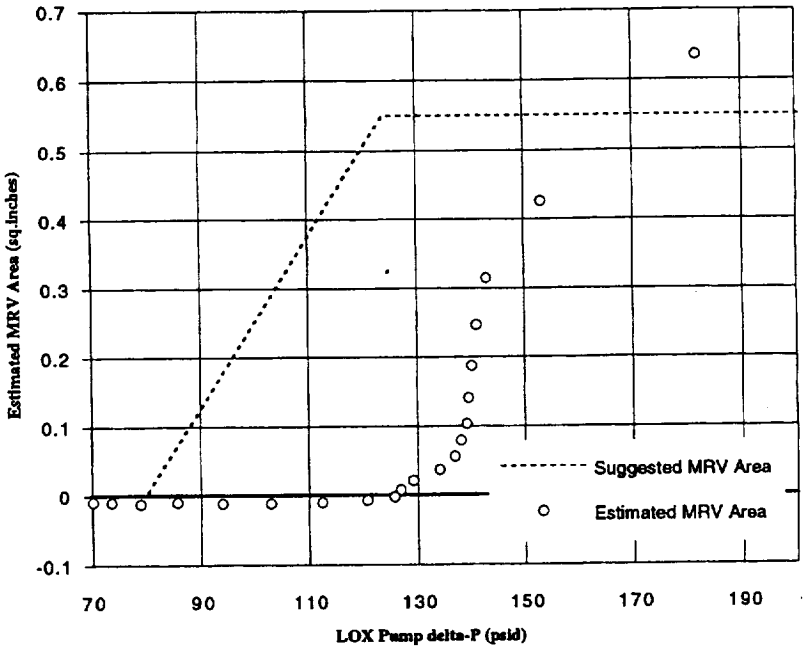

Figure 5.2.2—OCV Position during Start as Estimated from Test Data

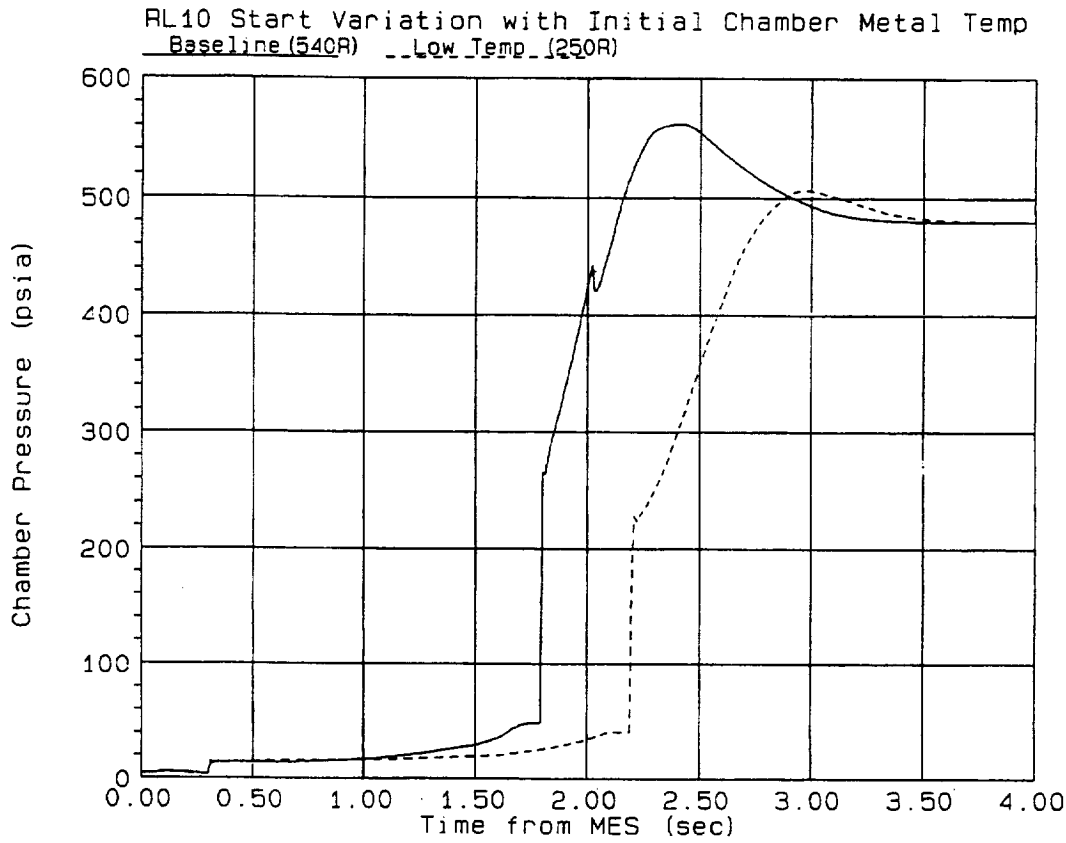

Figure 5.3.1—Variation in Start with Initial Jacket Metal Temperature

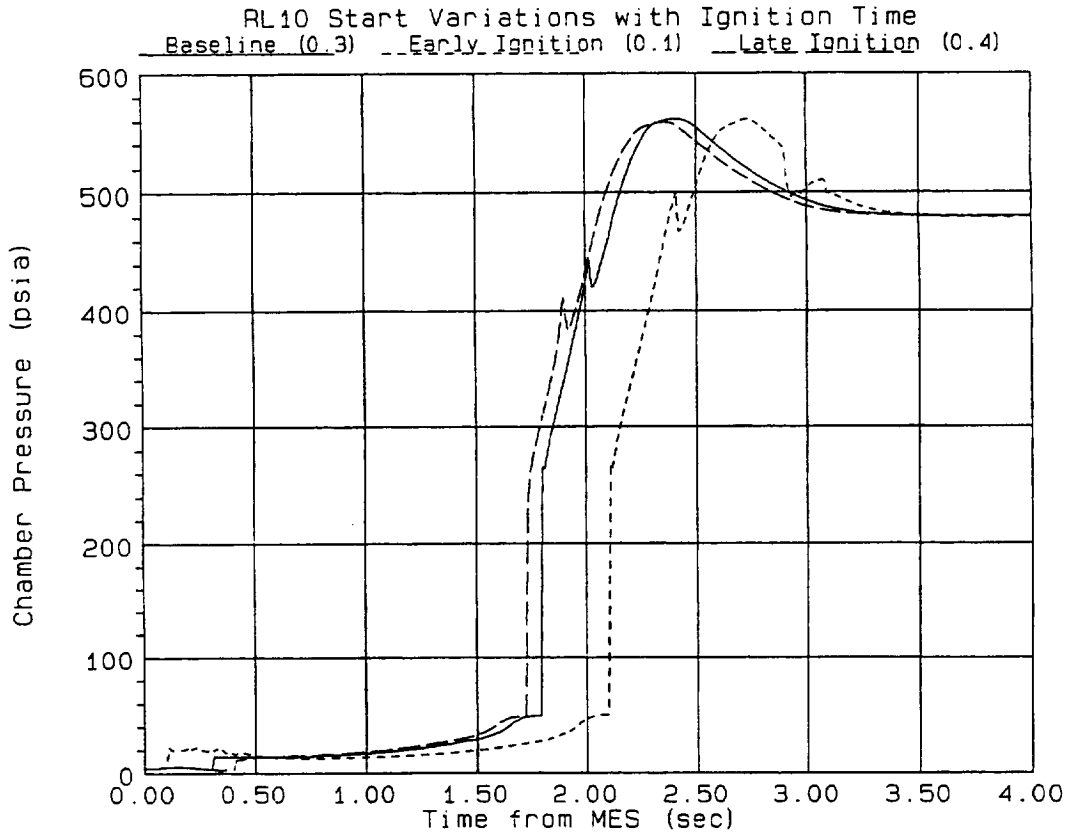

Figure 5.4.1—Variation in Start with Assumed Ignition Time-delay

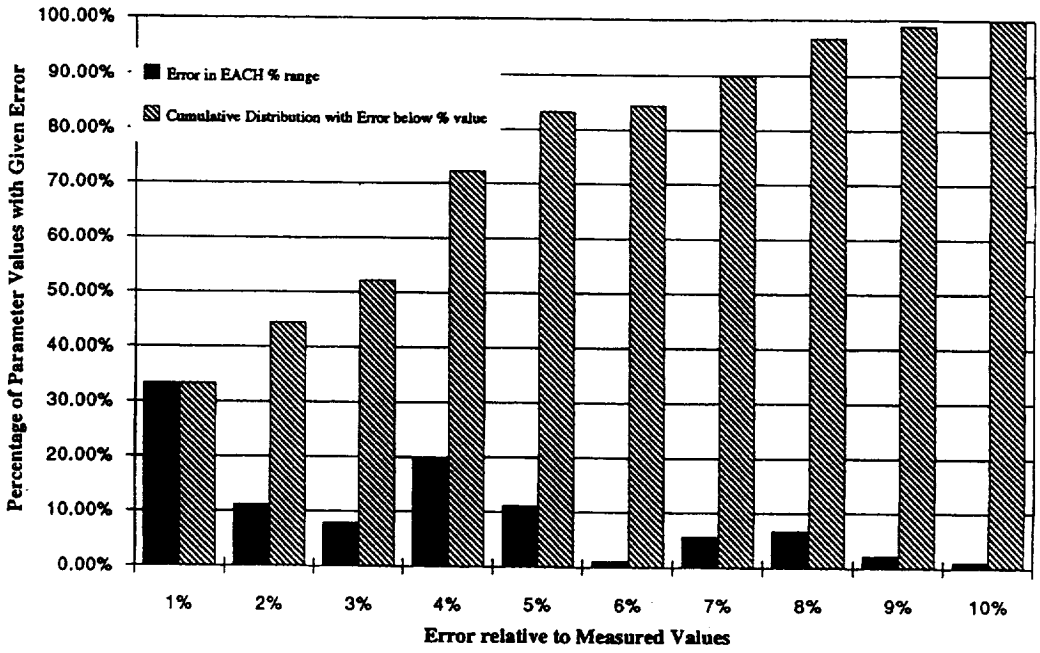

Figure 6.1.1—Steady-State Predictions vs. Measured Values (error distribution)

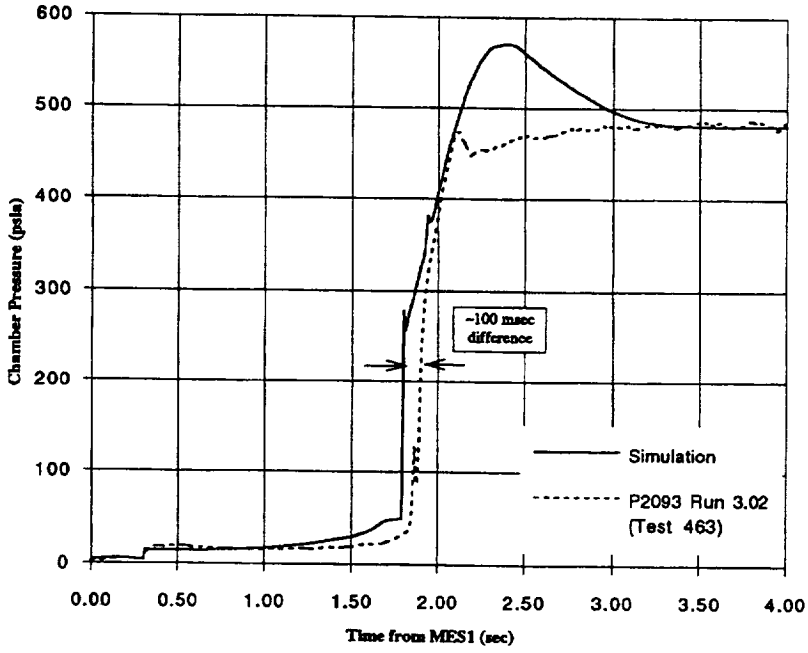

Figure 6.2.1—MES1 Chamber Pressure - Simulation vs. Ground-Test Data

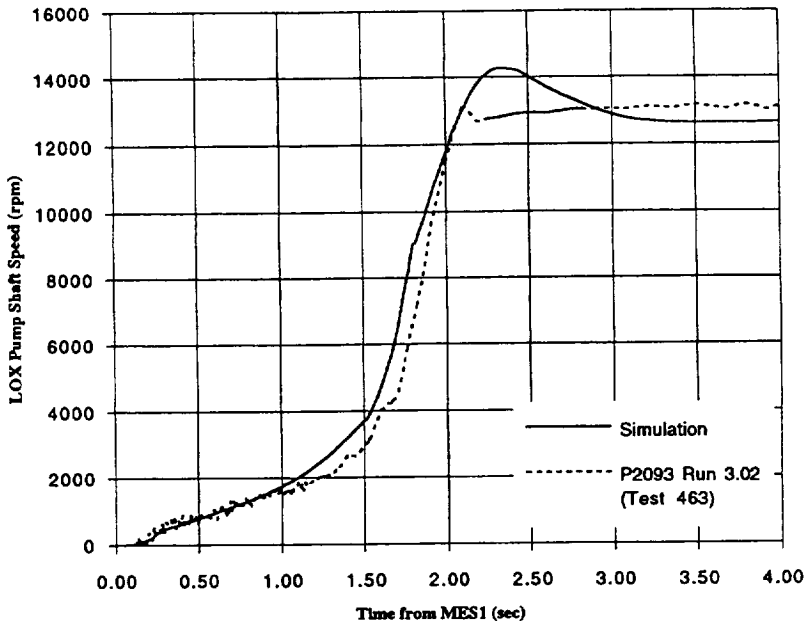

Figure 6.2.2—MES1 LOX Pump Shaft Speed - Simulation vs. Ground-Test Data

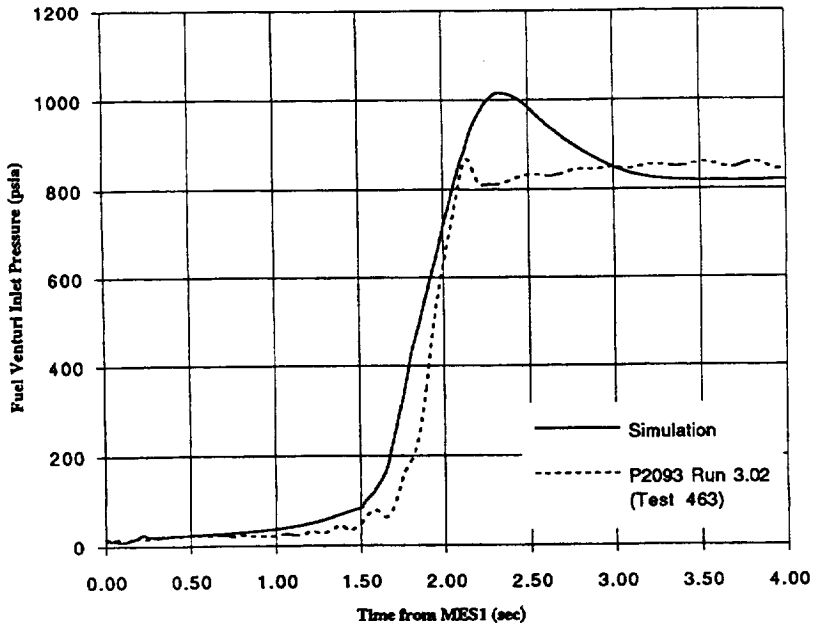

Figure 6.2.3—MES1 Fuel Venturi Inlet Pressure - Simulation vs. Ground-Test Data

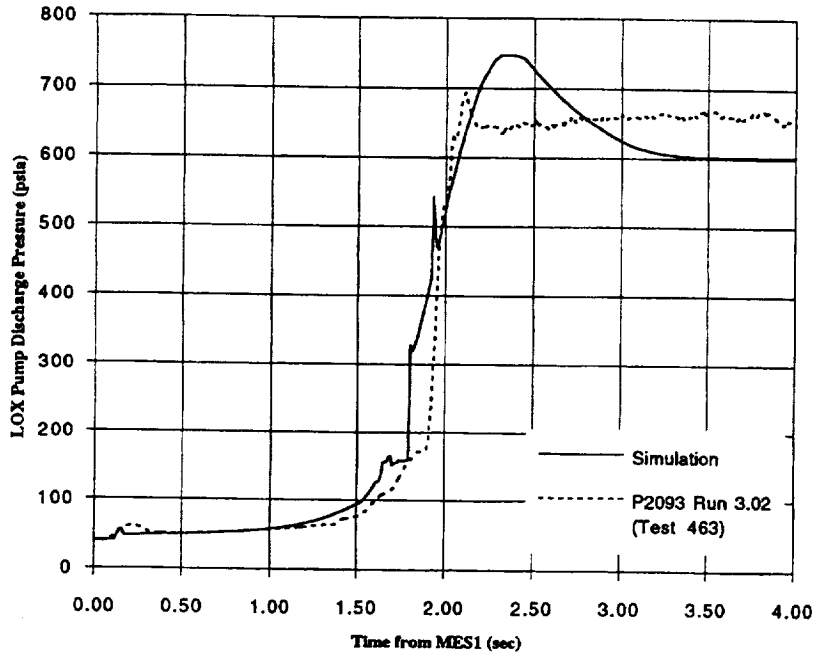

Figure 6.2.4—MES1 LOX Pump Discharge Pressure - Simulation vs. Ground-Test Data

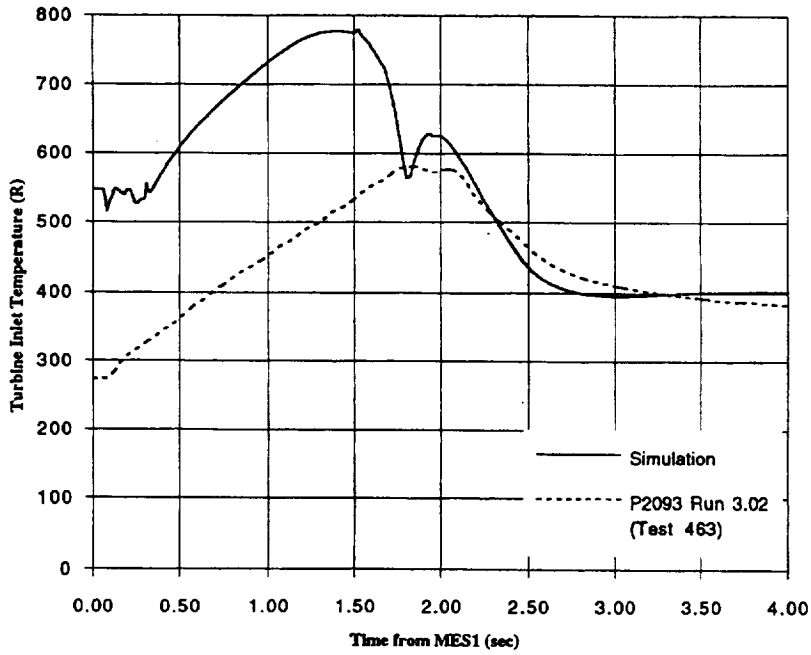

Figure 6.2.5—MES1 Turbine Inlet Temperature - Simulation vs. Ground-Test Data

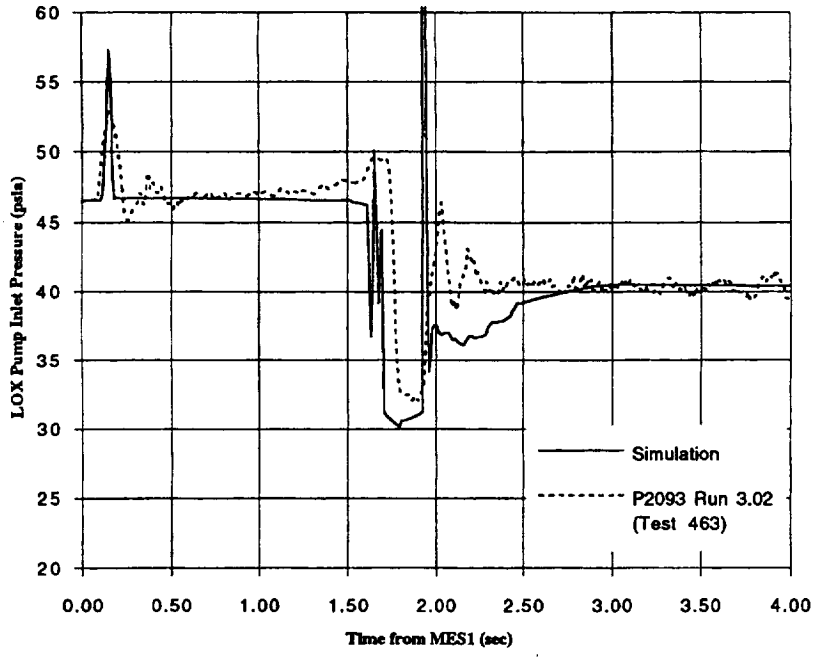

Figure 6.2.6—MES1 LOX Pump Inlet Pressure - Simulation vs. Ground-Test Data

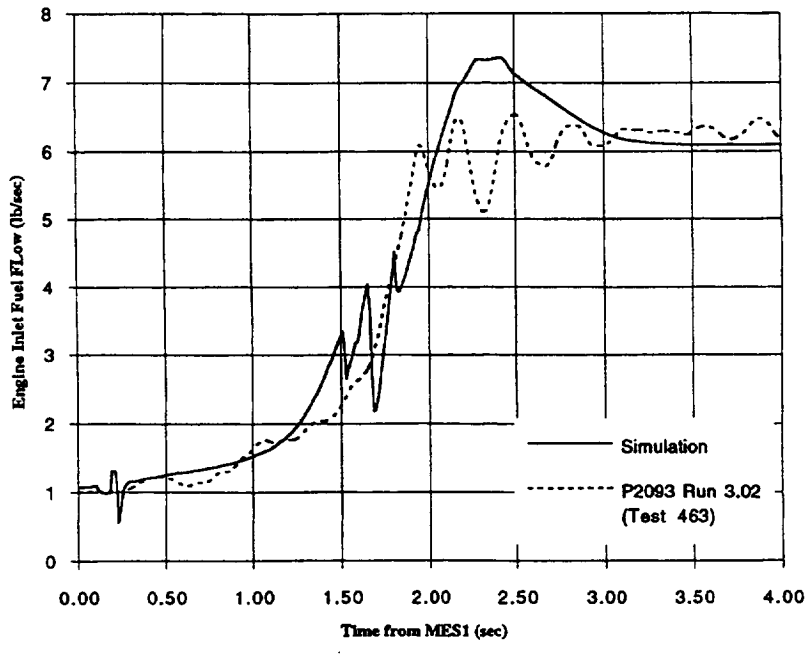

Figure 6.2.7—MES1 Engine Fuel Inlet Flow - Simulation vs. Ground-Test Data

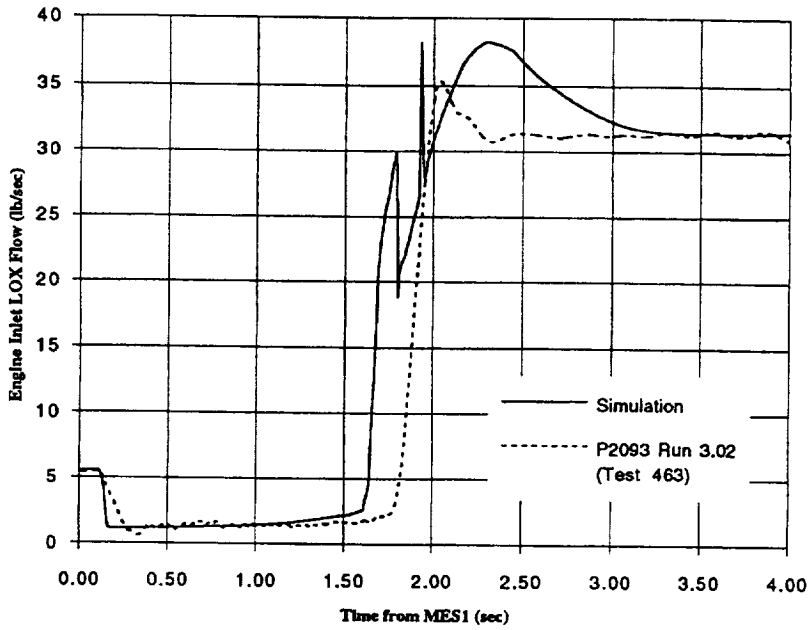

Figure 6.2.8—MES1 Engine LOX Inlet Flow - Simulation vs. Ground-Test Data

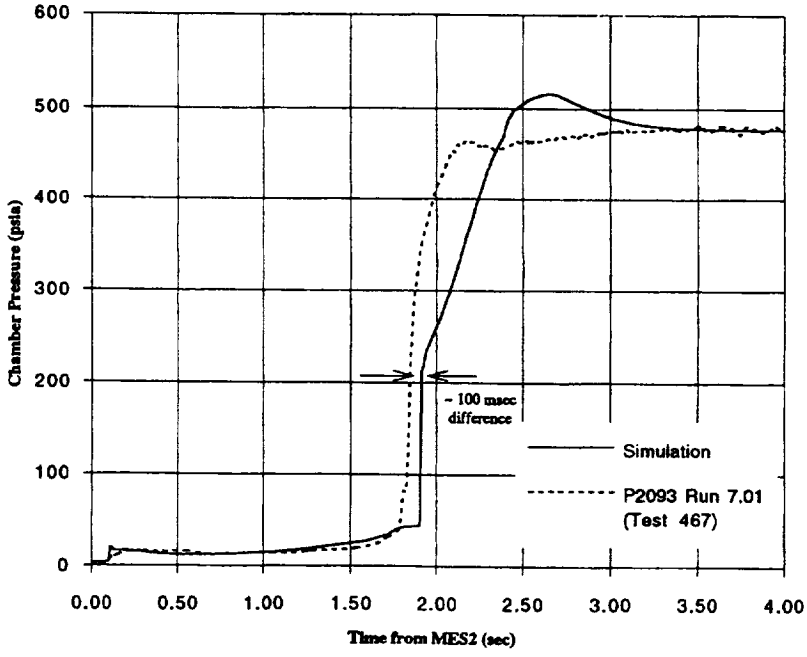

Figure 6.2.9—MES2 Chamber Pressure during Start - Simulation vs. Ground-Test Data

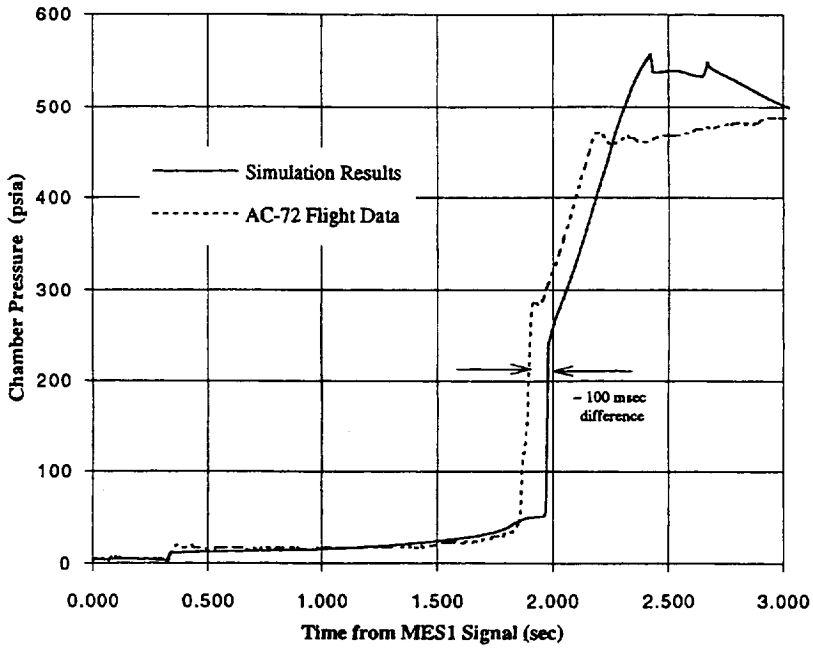

Figure 6.2.10—MES1 Chamber Pressure - Simulation vs. Centaur Flight Data

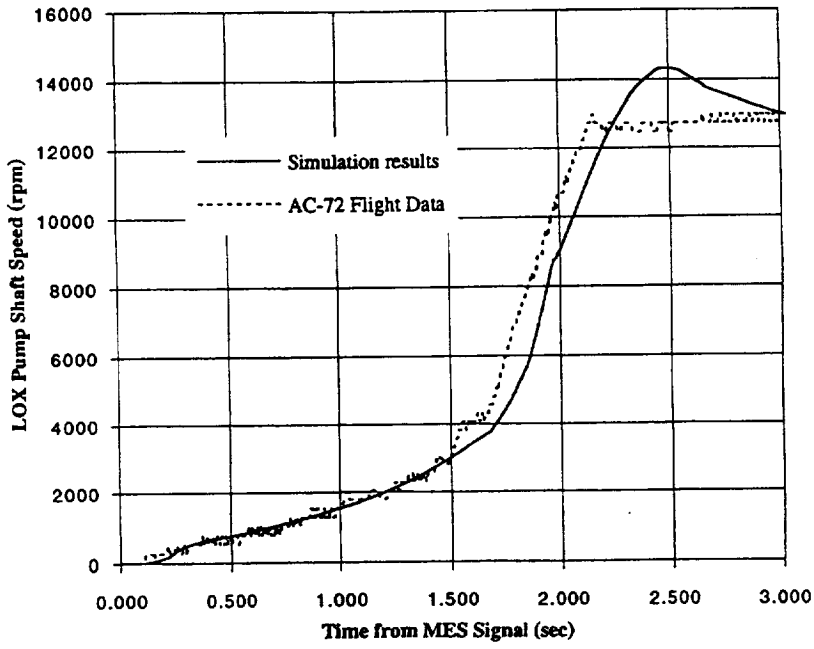

Figure 6.2.11—MES1 LOX Pump Shaft Speed - Simulation vs. Centaur Flight Data

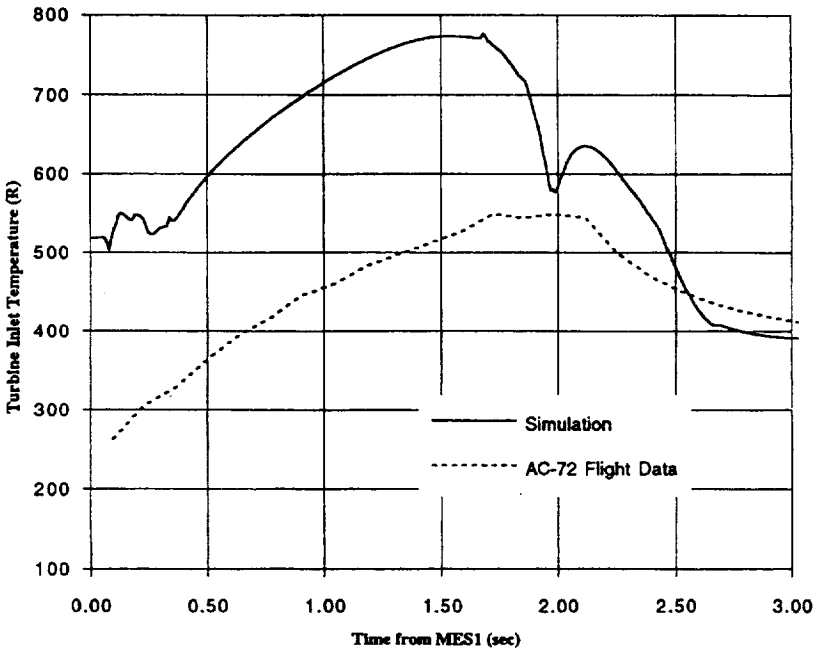

Figure 6.2.12—MES1 Turbine Inlet Temperature - Simulation vs. Centaur Flight Data

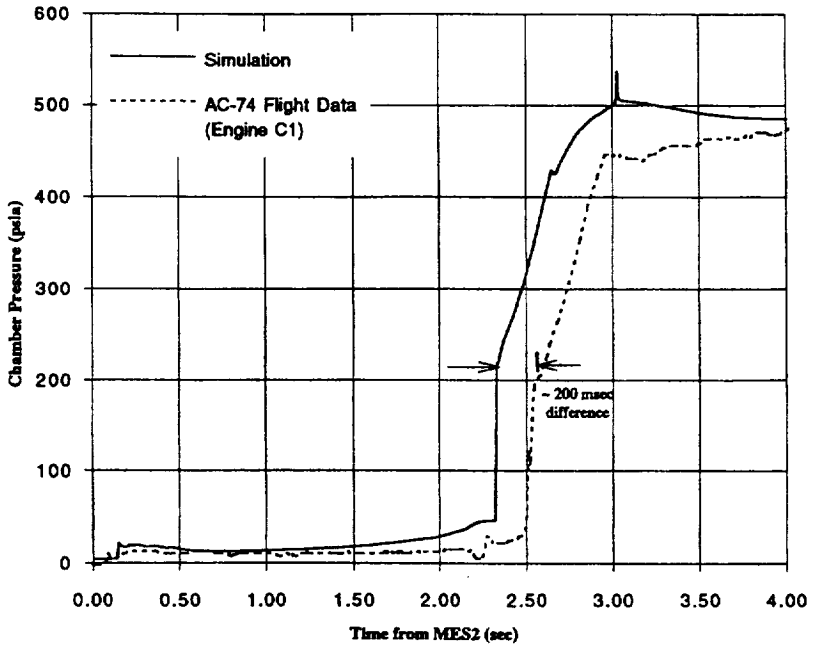

Figure 6.2.13—MES2 Chamber Pressure - Simulation vs. Centaur Flight Data

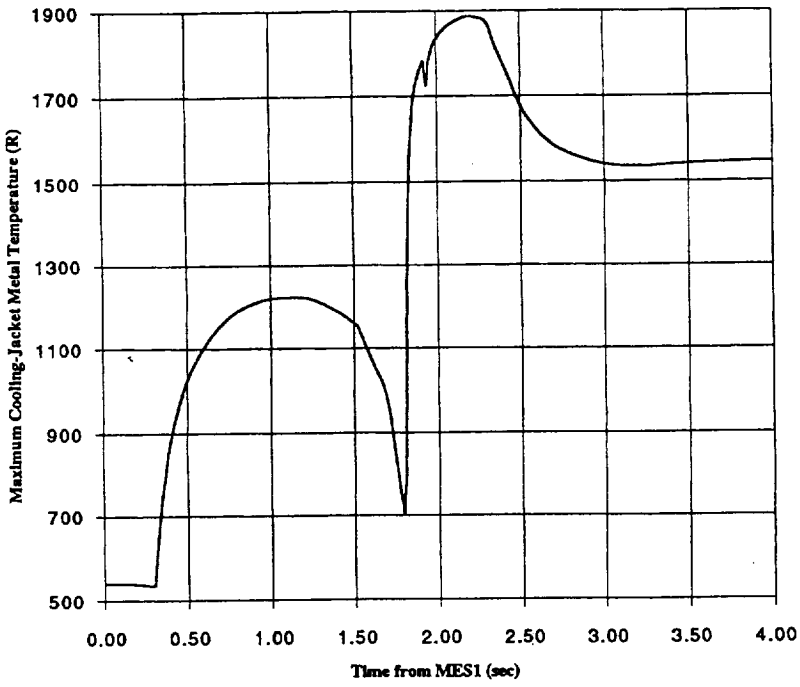

Figure 6.2.14—Predicted Maximum Metal Temperature during Start Transient

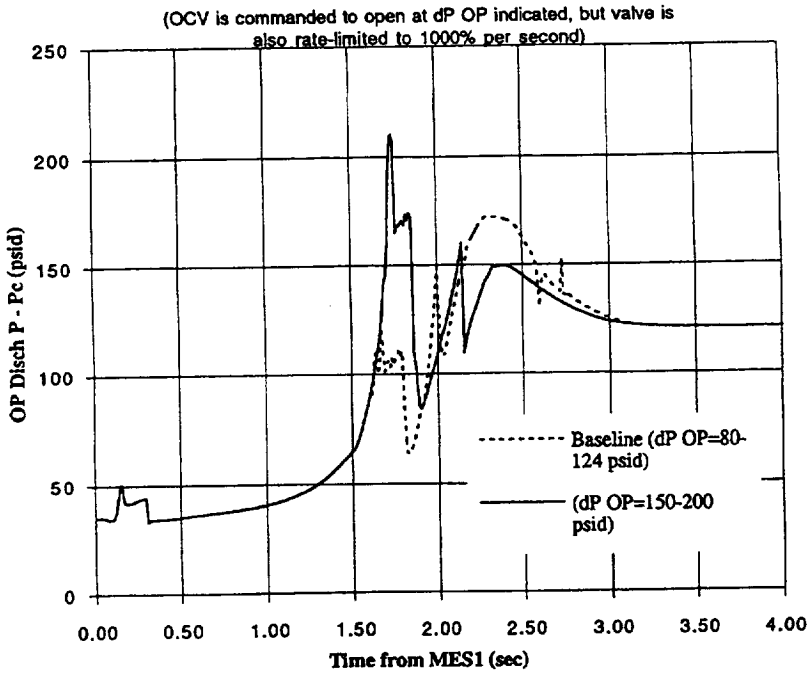

Figure 6.2.15—Predicted Ignitor GOX Supply delta-P during Start (variation with OCV opening pressure)

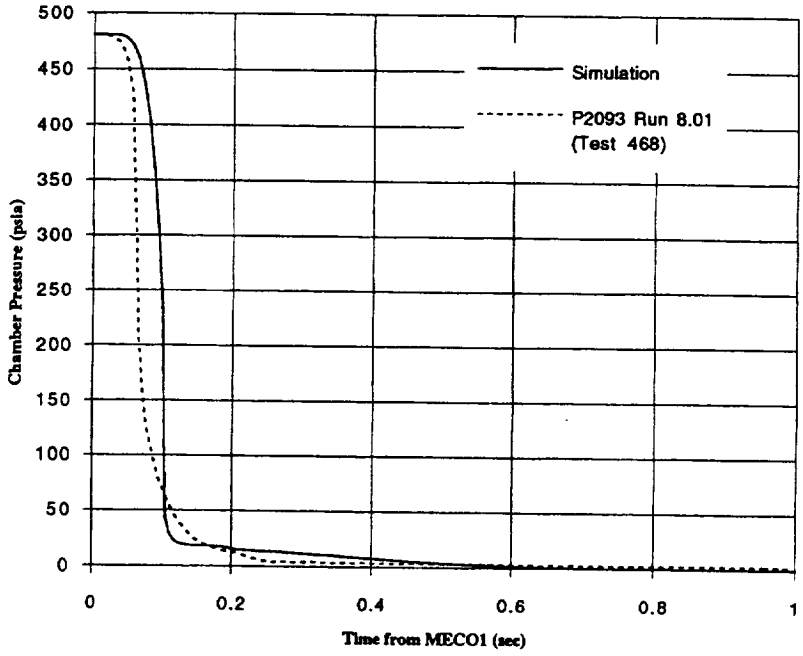

Figure 6.3.1—MECO1 Chamber Pressure - Simulation vs. Ground-Test Data

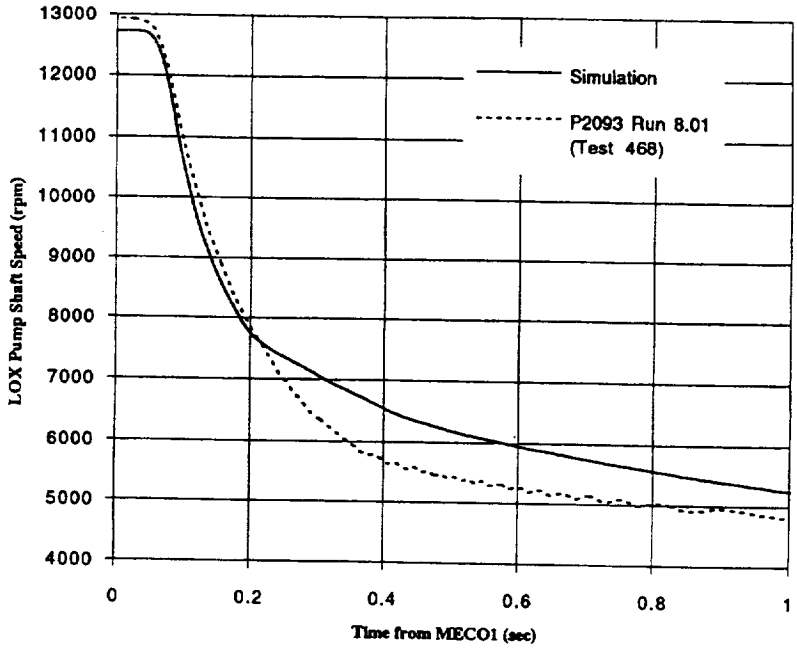

Figure 6.3.2—MECO1 LOX Pump Shaft Speed - Simulation vs. Ground-Test Data

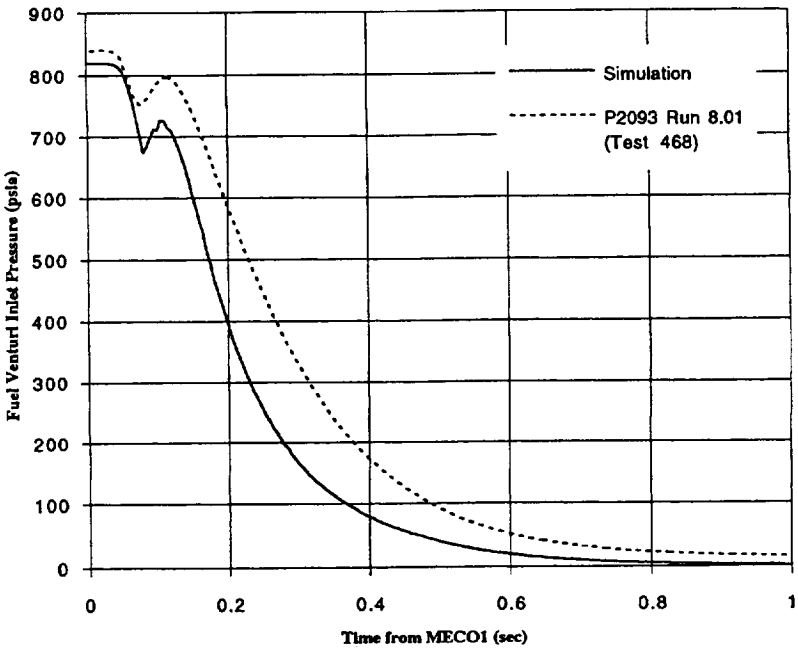

Figure 6.3.3—MECO1 Fuel Venturi Inlet Pressure - Simulation vs. Ground-Test Data

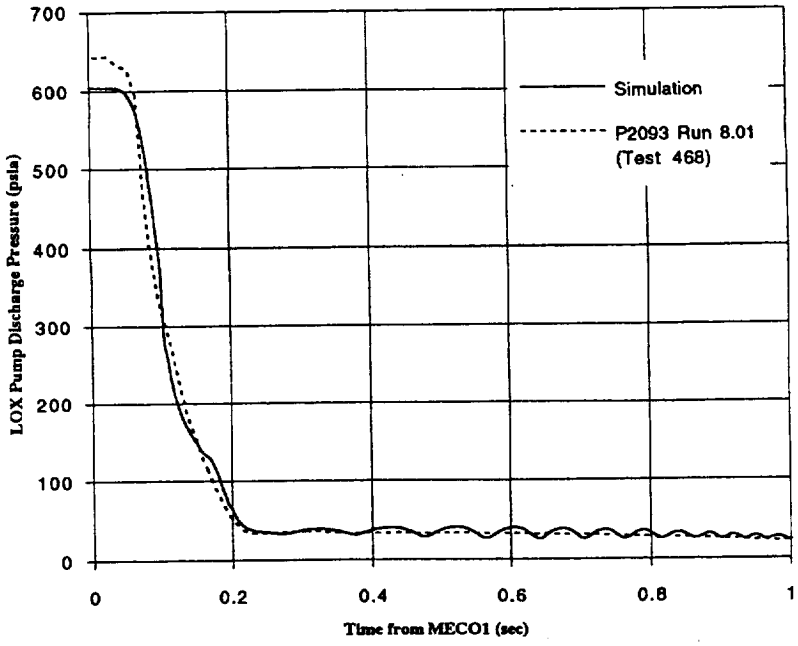

Figure 6.3.4—MECO1 LOX Pump Discharge Pressure - Simulation vs. Ground-Test Data

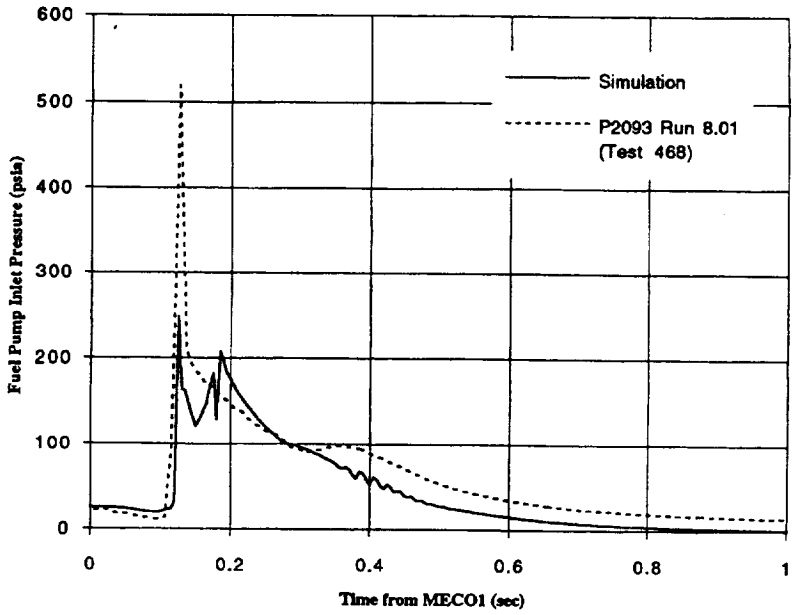

Figure 6.3.5—MECO1 Fuel Pump Inlet Pressure - Simulation vs. Ground-Test Data

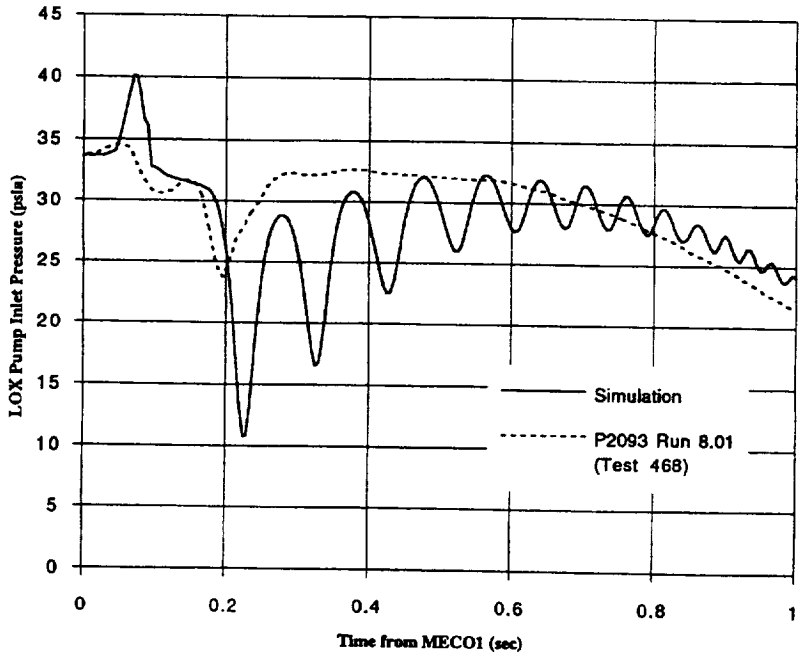

Figure 6.3.6—MECO1 LOX Pump Inlet Pressure - Simulation vs. Ground-Test Data

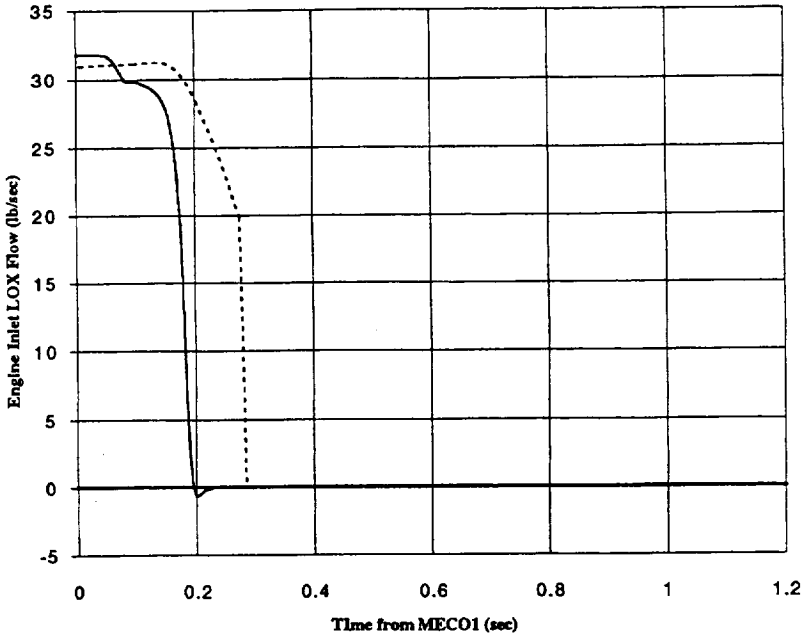

Figure 6.3.7—MECO1 Engine Inlet LOX Flow - Simulation vs. Ground-Test Data

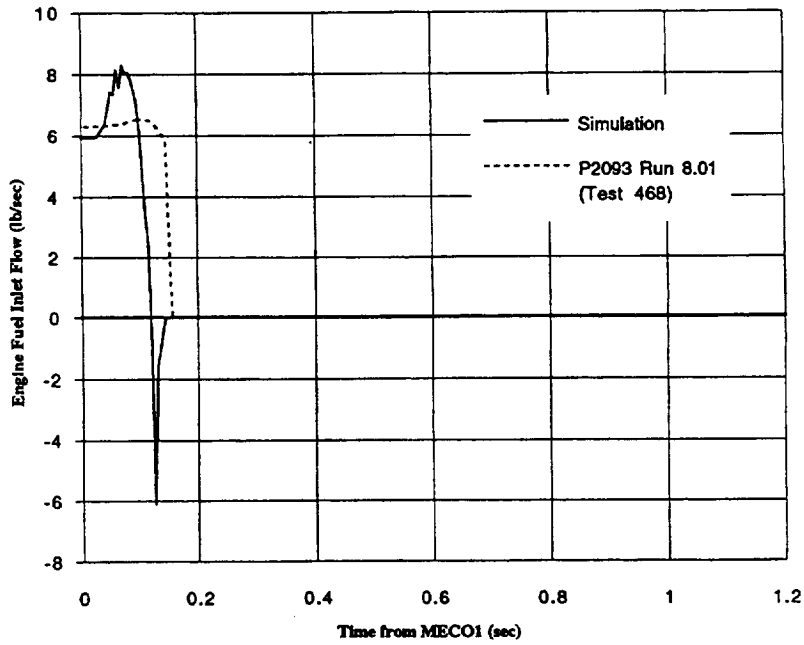

Figure 6.3.8—MECO1 Engine Inlet Fuel Flow - Simulation vs. Ground-Test Data

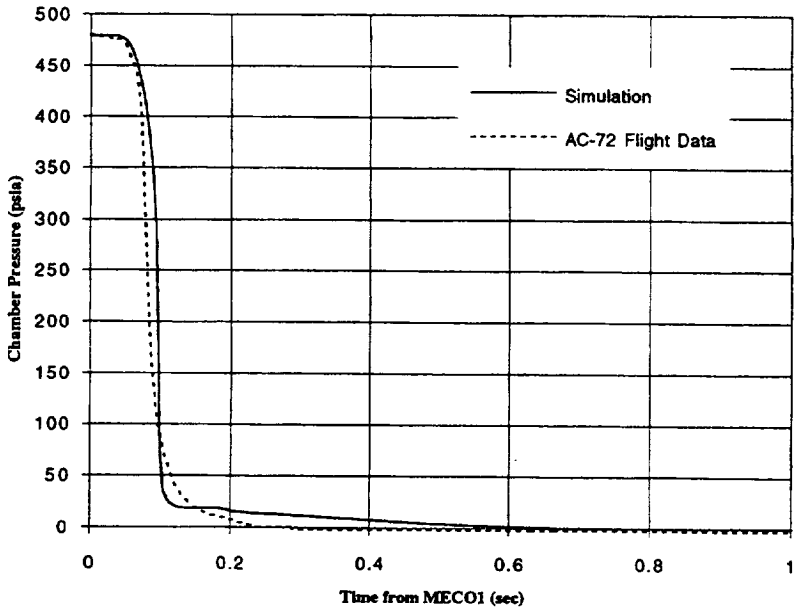

Figure 6.3.9—MECO1 Chamber Pressure - Simulation vs. Centaur Flight Data

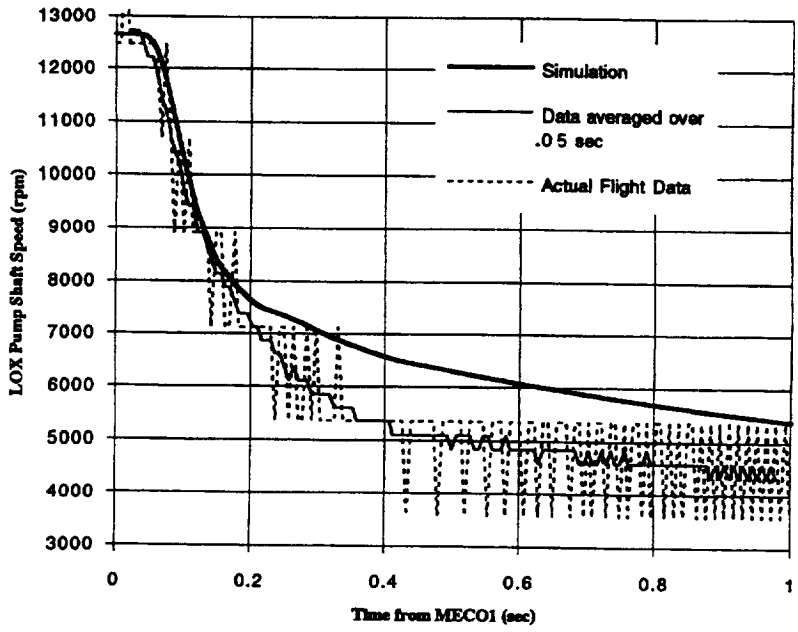

Figure 6.3.10—MECO1 LOX Pump Shaft Speed - Simulation vs. Centaur Flight Data

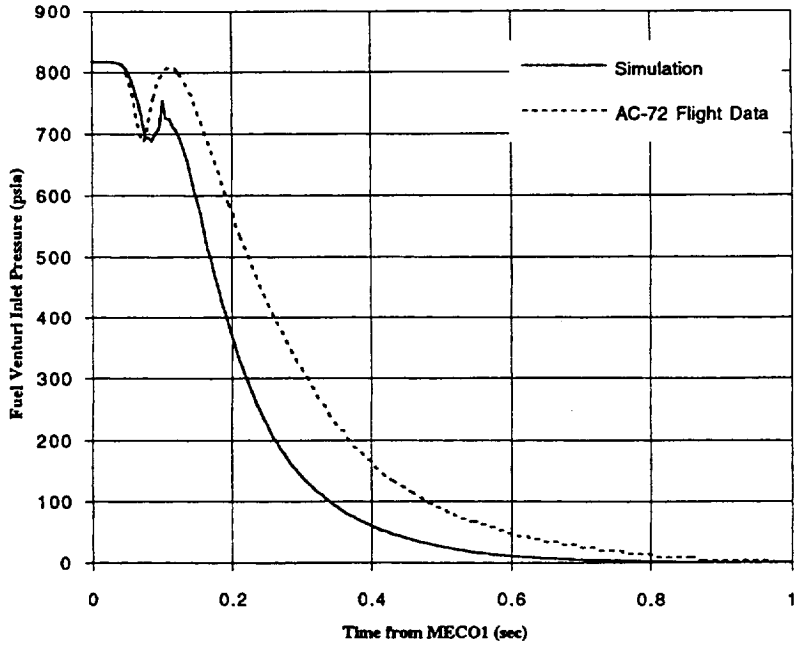

Figure 6.3.11—MECO1 Fuel Venturi Inlet Pressure - Simulation vs. Centaur Flight Data

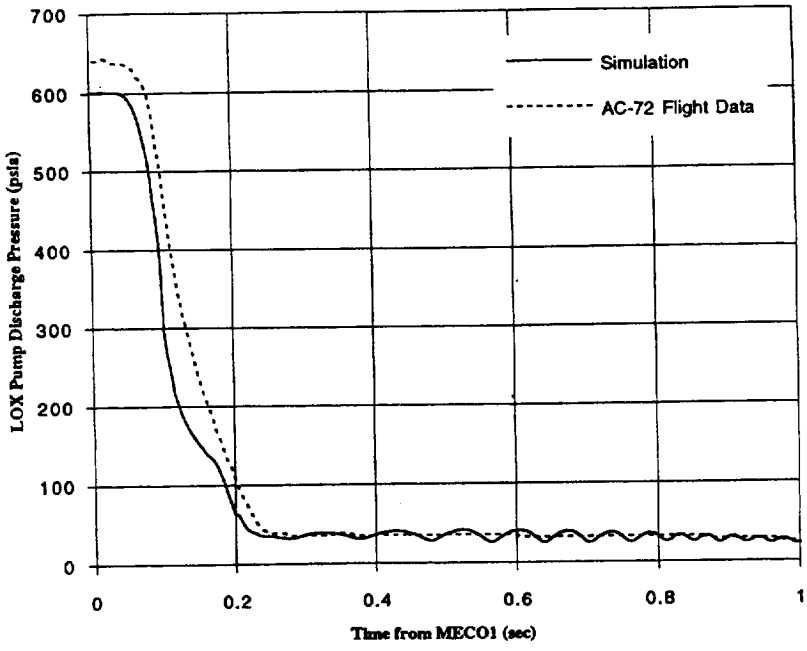

Figure 6.3.12—MECO1 LOX Pump Discharge Pressure - Simulation vs. Centaur Flight Data

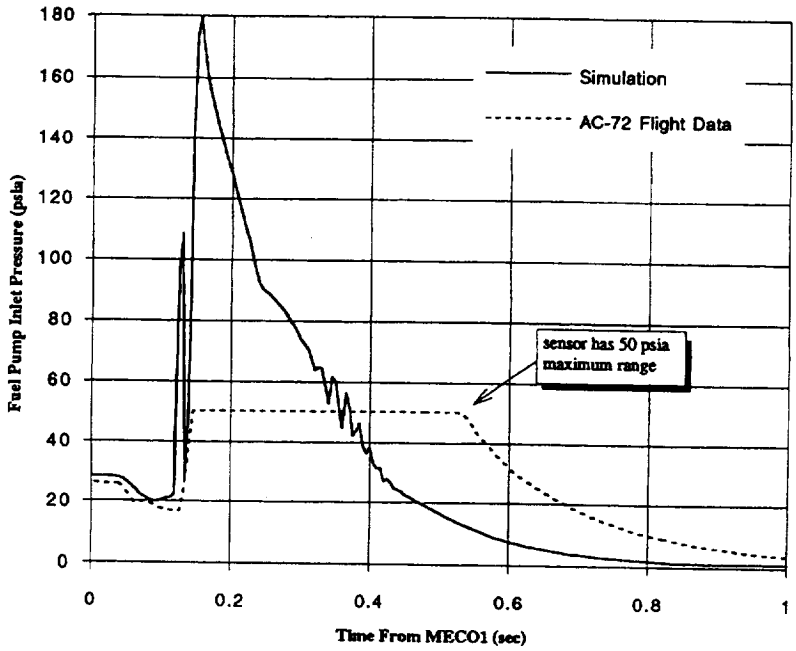

Figure 6.3.13—MECO1 Fuel Pump Inlet Pressure - Simulation vs. Centaur Flight Data

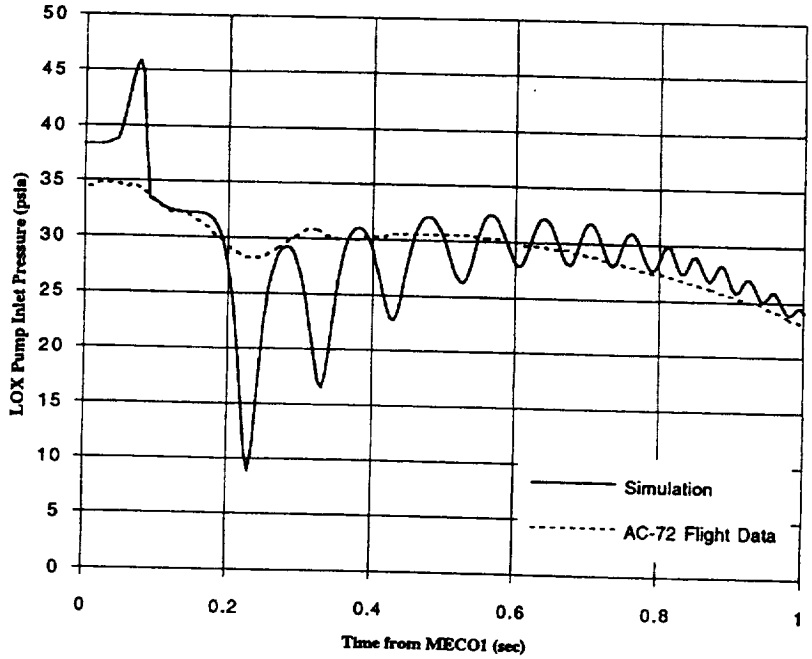

Figure 6.3.14—MECO1 LOX Pump Inlet Pressure - Simulation vs. Centaur Flight Data

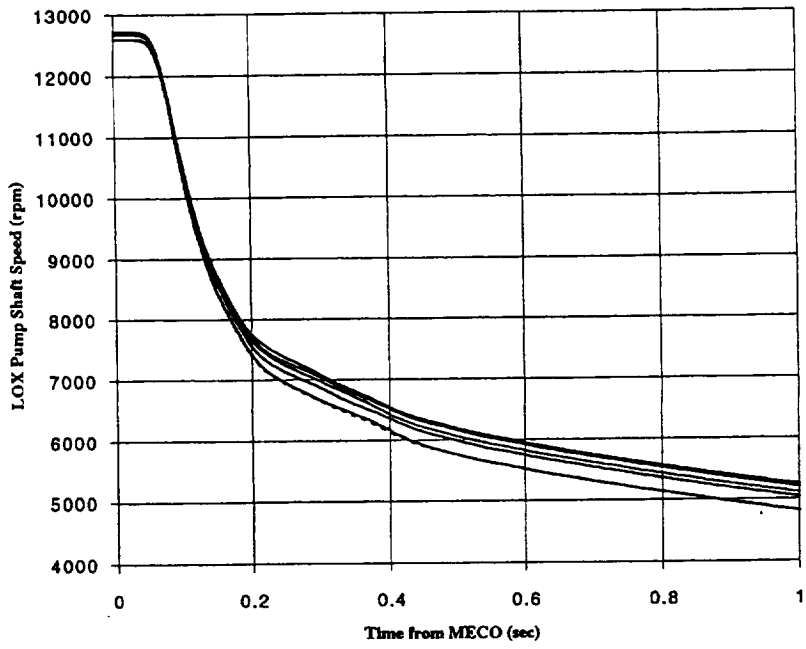

Figure 6.3.15—Range of Predicted Shutdown Profiles (Ground Test Conditions)

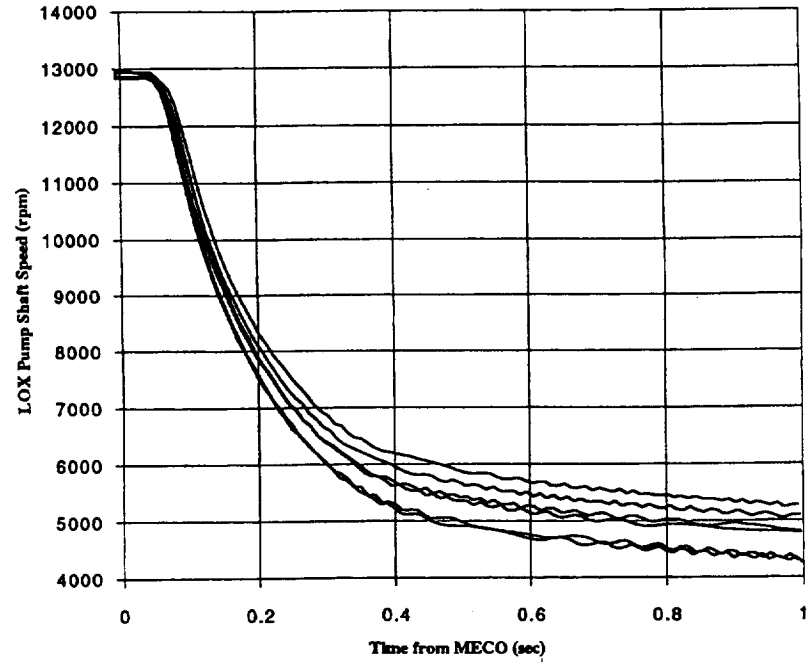

Figure 6.3.16—Range of Measured Shutdown Profiles (Ground Test Data)

APPENDIX A
RL10A-3-3A Engine System Model for ROCETS

The RL10A-3-3A rocket engine was simulated using the Rocket Engine Transient Simulator (ROCETS) program (Reference A1). The model of the RL10 is comprised of four elements: 1) the system configuration file(s), 2) the run input file and guess file, 3) the component model subroutines, and 4) the utility and solver subroutines. This utility and solver routines are the same for any ROCETS model and are not discussed further in this report.

The system configuration file contains information about what components are included, what subroutine is used to model them, and how they are connected. Two models of the RL10 exist; one for the start transient and steady-state performance, the other for the shutdown transient. Both models are represented schematically in Figure A.1. The ROCETS preprocessor software (which must be run before compiling and linking the simulation) uses the configuration input files to write FORTRAN code for the system simulation. Equations in the input file are written as expressions in the FORTRAN code. Component 'Modules' and 'Property Package' blocks are converted into calls to the appropriate subroutines. The preprocessor uses information stored in the headers of each component subroutine to write its call list in the FORTRAN program. The configuration input files also contain information about state substitutions and additional algebraic balances.

The run input files contain execution instructions for each simulation run. These files contain descriptions of model boundary conditions (such as tank pressures and temperatures), initial conditions (such as jacket metal temperature), and schedules for ignition and valve movement. The run input files also contain a great deal of instructions governing the convergence of the model solver; this information must be especially detailed for the transient simulations, which often encounter conditions where numerical convergence may be difficult (zero flow, zero rotation, sudden valve movements or ignition, etc.). The run input files also define the type of run to be performed (steady-state or transient). During execution, a guess subroutine is called which sets the initial values of state variables in the model. The guess file can contain simple value assignments or procedural code (to set initial enthalpy based on user input temperatures, for example). A single guess file is used for all RL10 simulations (start, steady-state, shutdown).

Each component in the engine system is modeled by a FORTRAN subroutine. Several components, the pumps for example, may use the same basic routine, but with different design information (values or maps).

To obtain a copy of the RL10A-3-3A model input files and component subroutines, the interested reader should contact Mr. Joseph Hemminger at the NASA Lewis Research Center. To obtain a copy of the ROCETS program (utility and solver software), please contact Mr. David Seymour at the NASA Marshall Space Center.

References

A1. Pratt & Whitney Government Engines, *Design Report for RL10A-3-3A Rocket Engine*, (NASA Contract NAS3-22339, Pratt & Whitney Report No. FR-15876), January 1982.

Figure A1

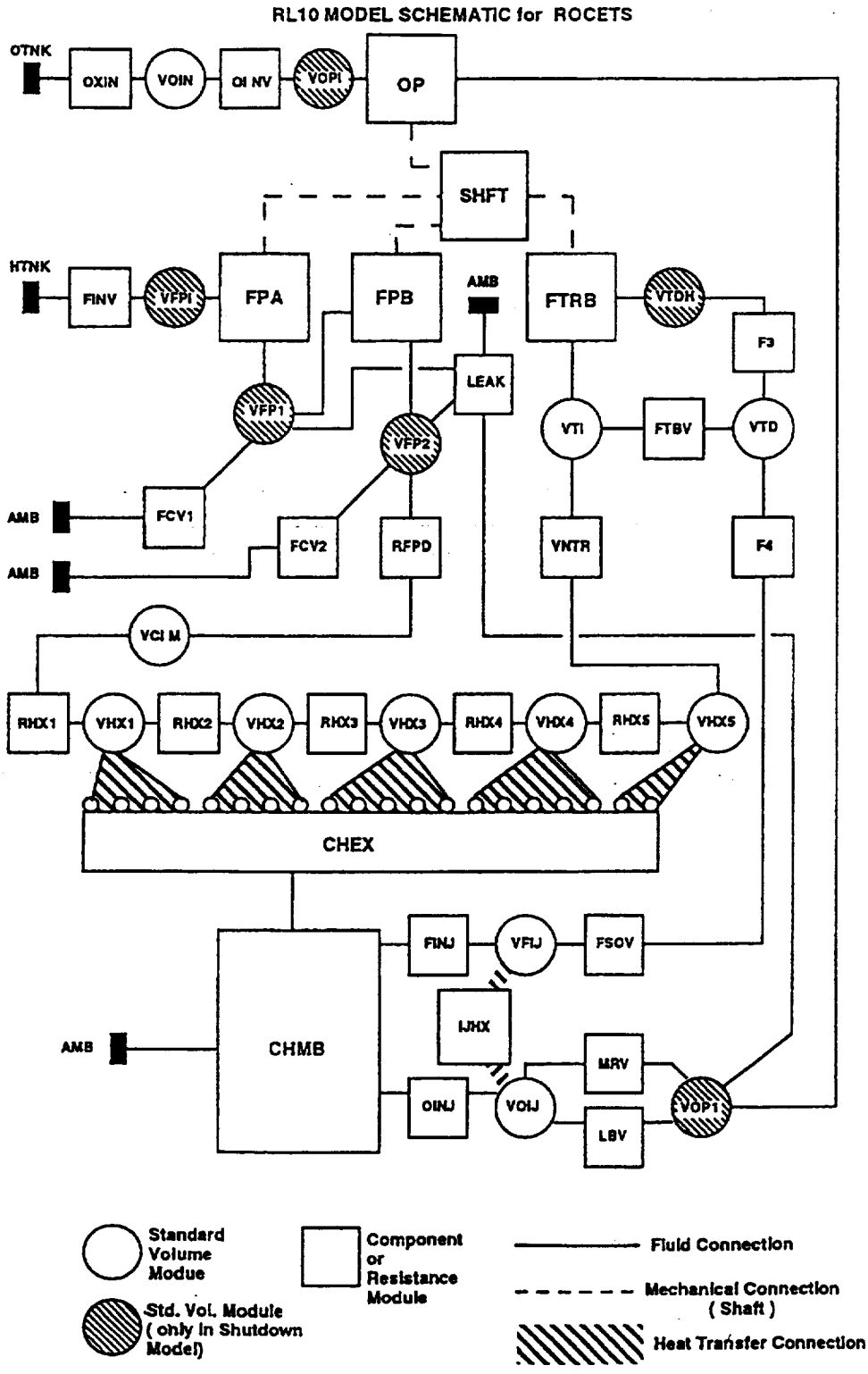
RL10 MODEL SCHEMATIC for ROCETS
OTNK
OXIN
VOIN
OI NV
VOPI
OP
SHFT
HTNK
FINV
VFPI
FPA
FPB
AMB
FTRB
VTDH
F3
LEAK
VFP1
VFP2
VTI
FTBV
VTD
AMB
FCV1
FCV2
RFPD
VNTR
F4
AMB
VCI M
RHX1
VHX1
RHX2
VHX2
RHX3
VHX3
RHX4
VHX4
RHX5
VHX5
CHEX
FINJ
VFIJ
FSOV
IJHX
AMB
CHMB
MRV
OINJ
VOIJ
VOP1
LBV
Standard Volume Module
Component or Resistance Module
Fluid Connection
Std. Vol. Module (only in Shutdown Model)
Mechanical Connection (Shaft)
Heat Transfer Connection

APPENDIX B
Component Modeling of RL10 Fuel and Oxidizer Pumps

This appendix to the RL10A-3-3A Modeling Project Final Report describes efforts to predict the performance of the RL10 fuel and oxidizer pump using component analysis programs available to the NASA Lewis Research Center Space Propulsion Technology Division (SPTD). Cross-sectional views of the pumps are shown in Figures B1 and B2.

B1. Analytic Tools used

The SPTD has been working to develop turbomachinery design and off-design programs for several years. Since the RL10 design geometry was already set, only the off-design performance codes were used in this project. The programs utilized were PUMPA (Reference B1) and LSISO (Reference B2). These codes are one-dimensional mean-line codes, which means that two and three dimensional effects are either averaged across the flow-area, or corrected for using empirical factors. A third program was written to predict low-speed pump performance from a given design point using a method described in Reference B3.

The PUMPA analysis code uses a combination of theoretical calculations and empirical correction factors. Velocity triangles are used to determine the theoretical head rise though the impeller. The corresponding discharge pressure is then corrected using empirical relations for design efficiency, variations in efficiency with speed, and two-dimensional effects at the impeller exit (expressed as an empirical function of geometry, flow and speed). Likewise, diffuser and volute losses are determined based on flow velocities. The empirical corrections are distilled from test data on a number of different types of turbopumps (not including the RL10 turbopump). The corrections can therefor be considered *generic* empiricisms which may be applied to any problem, and are not tailored for the RL10 alone.

LSISO (Loss Isolation program) appears to involve fewer explicit empirical correlations than PUMPA, but data contained in the program has almost certainly been tailored to better match test cases in the past as well. The effects modeled in LSISO are similar to those described in PUMPA but do not include calculations for the exit diffuser.

The third program, which has no official name, was written for this project and is also a one-dimensional meanline analysis. It uses velocity triangles and assumed friction effects to predict the very low speed performance of a pump. This program requires the pump design point performance as input.

B2. Predictions from PUMPA code

Figures B3 through B8 show PUMPA predictions of the head-rise and efficiency for the fuel pump first stage (including inducer), fuel pump second stage and LOX pump (single stage). In general, the predictions of head rise in the fuel pumps are quite good. The PUMPA predicted values of head rise are approximately the same as those indicated by the test data maps, although the predicted maps do show more curvature at high flow conditions. Preliminary simulations using the predicted maps indicate that these small differences in shape at high speeds do not cause a significant difference in overall engine performance.

Unfortunately, the efficiency maps predicted using PUMPA (Figures B4, B6, and B8) were not in agreement with the test-data maps. There is a significant difference (5 to 10 %) in the maximum efficiency values. We have already seen that even relatively minor differences in efficiency can cause significant timing differences in engine start. In view of these discrepancies, it was decided not to include the predicted maps directly in the new RL10 system model. Instead, low speed performance predictions made with this model were used qualitatively to guide extrapolation from test data.

The head performance curves predicted with PUMPA for the low speed region are shown in Figures B9 through B11 for the fuel pump first stage, fuel pump second stage and LOX pump respectively. The head curves for the second stage fuel pump and the LOX pump intercept the zero-speed axis with shallow slopes, similar to the curve for a typical centrifugal pump as shown in Figure B12 (from Reference B4). The predicted head curve for the first stage fuel pump, however, turns down as it approaches the zero-speed axis (more indicative of a mixed flow pump). This difference has been hypothesized as being due to the non-radial vanes of the first stage impeller. It might also be an effect of the inducer. These predicted pump characteristics were used to guide extrapolation of the pump test data, as discussed in section B6 below.

In a typical application, the PUMPA model would be corrected to match the best efficiency point and the model would then be used to predict off-design (for which test data may not be available). In the RL10 modeling project, one goal was to benchmark the component analysis codes, including PUMPA, to see how close we could predict performance without making empirical corrections. The correction of the pump models to better match the best efficiency point was therefor not done for the RL10 pumps.

The PUMPA software is indicative of the state-of-the-art in pump analysis codes. It serves well for performing conceptual and parametric design analyses, but usually requires at least some test data to anchor it to a specific pump design if greater accuracy is required. When this study was performed, PUMPA was still in the process of development and technical review at NASA Lewis Research Center. A subsequent version of the PUMPA code has been released which appears to more accurately predict the RL10A-3-3A pump efficiencies at design conditions. The new version PUMPA was completed too late for a comprehensive analysis to be made of the RL10 components.

B3. Predictions from LSISO code

The LSISO code was originally developed to analyze secondary flows in centrifugal pumps. In order to perform such analyses, however, it is necessary to also predict the impeller performance, and this feature has been used to consider the RL10 components.

The head and efficiency predicted by LSISO for the fuel pump second stage are shown relative to the test-data maps in Figures B13 and B14. The predicted head coefficient is reasonably close to the suggested values for lower flow coefficients, but the two maps diverge at higher flow coefficients. The predicted efficiency map displays more significant discrepancies when compared with the test data maps.

The precise causes of the mismatch are not known, but several potentially related concerns with LSISO have been noted. The backflow recirculation losses at the impeller exit are probably too low. A better model of this effect is available, but adding the new model to LSISO is beyond the scope of this project. LSISO also assumes the fluid is incompressible, which is not necessarily accurate for liquid hydrogen at Centaur tank pressure and temperature. Finally, the predicted rate of leakage from the impeller exit to inlet appears too high. This area of the model would require some effort to resolve.

In summary, the LSISO predictions were not suitable for inclusion in the RL10 engine model. LSISO is also not designed to predict pump performance at start conditions, and could not be used to generate any valuable information for that regime.

B.4 Low-speed Performance Prediction Program

As mentioned above, another code was written for the RL10 Modeling Project in order to predict the low-speed operation of the pumps. This program was created by Dean Scheer based on a method described by Rostefinski in Reference B3. We shall therefore refer to it here as the

Rostefinski/Scheer (or R/S) model. The program models losses in the impeller only (no diffuser or inducer effects); a separate model of the diffuser section has been created for that purpose.

Figures B15 through B17 show the predicted head-rise (or *drop* as is the case here) through the impellers of the three pump stages. These maps all have the basic shape suggested in Reference B4. The R/S model predictions are similar to those of the PUMPA code at low speed, except for the first stage fuel pump. The predicted first stage fuel pump head does turn down at very low speeds, as was indicated by the PUMPA code. The R/S predictions also indicate an overall loss which is smaller than that suggested by the RL10 engine data. This may be due to the absence of inducer and exit diffuser effects in the model.

A model of the LOX pump exit diffuser throat was created to see how much we might expect diffuser losses to contribute. The behavior of the exit diffuser was modeled as isentropic flow of a two-phase fluid through a venturi, including the possibility of choking. The configuration of the diffuser model is described in Figure B18.

If we combine this diffuser model with the R/S predictions for the LOX pump impeller, we obtain the curve shown in Figure B19. This is for nominal pump inlet conditions of 46.5 psia and 176.5 R. The predictions including the diffuser losses match the RL10 engine start conditions much better at zero speed (theta=0). These losses also change the shape of the curve significantly. The abrupt jump from the lower curve to the upper one occurs when the diffuser throat becomes unchoked. When the diffuser is unchoked, the model indicates virtually no loss (the slight mismatch between the predictions with and without the diffuser model is attributable to model convergence error). If similar diffuser models were added to the R/S predictions of fuel pump performance as well, we might reasonably expect all pump stage head maps to exhibit this characteristic shape.

The predictions including the diffuser model also showed a marked sensitivity to the pump inlet conditions. The low speed portion of the LOX pump heap map will change considerably if different tank pressures or temperatures are assumed (the values used here are considered nominal and the good agreement with test data at zero speed may be a coincidence). Variations in the PUMPA predictions with different assumed inlet conditions was not studied. It is reasonable to believe that such variations may occur, but further research on this subject is beyond the scope of this project.

Due to the variable effects of pump inlet conditions on the diffuser model, it proved impractical to create a combined impeller/diffuser map that could be used in the RL10 engine model during start. It was also found that including the diffuser calculations in the model (rather than mapping them) caused the start simulation to run too slowly for practical use. Numerical instabilities in the model also presented a problem, especially when integrated with the other components in the system simulation. We therefor elected not to include these results in the new engine system model.

B5. Cavitation and Surge Predictions

The detailed component analyses discussed in the previous sections were intended primarily to examine conditions during RL10 engine start. During RL10 engine shutdown, the pumps experience cavitation and even reverse flow conditions. Only limited PUMPA analysis was done to predict the onset of cavitation in the RL10 pumps; no analysis was done to predict reverse flow behavior. The generic pump maps shown in Figure B12 do cover the reverse flow condition (theta values from π to 2π radians). Because these maps are probably based on testing with water, the condition of reverse flow of a gas is not likely to be included here either.

Because the conditions in the RL10 pumps during engine shutdown or so uncommon in other

applications, very little supporting information could be found. A data reduction model of the RL10 was also used in an attempt to characterize the pump performance during engine shutdown, but the transient nature of data during shutdown made the results unreliable. The solution ultimately chosen was to create curves fit to test data, with shapes indicated by the generic maps in Figure B12. The minima and maxima in the generic curve shapes (a theta values of XX and XX respectively) were modified to approximate the transient behavior of the pumps inferred from engine test data. Additional factors (not shown in the maps) were added to account for reverse flow of a gas through the pumps, again using engine test data to provide clues regarding this behavior.

B6. Pump Performance Maps Generated for RL10 Engine Model.

The full-range pump maps created for the RL10A-3-3A engine simulation are a combination of component and engine test data, generic pump characteristics found in the literature, and predictions from the PUMPA models. For the low-speed extremes, curves were fit to match the existing test data maps at high speed, to exhibit the appropriate shape as indicated by the PUMPA analyses at low speeds, and to cross the zero-speed axis at points indicated by engine data. For the reverse flow extremes (high theta values), curves were chosen to match test data in the normal operating region, to exhibit shapes as indicated by the generic curves from Reference B4, and to match the overall transient behavior indicated by engine test data.

The complete pump maps used in the RL10 system simulation are shown in Figures B20 through B25. Torque predictions from the maps shown in Figures B21, B23, and B25 are additionally corrected for non-ideal speed effects using data provided by Pratt & Whitney (Figures B26 and B27) before being used in the system simulation.

For further information about the pump component models, the interested reader is referred to the system model and component subroutine listings given in Appendix A.

Reference List

(may contain duplicate references with Part 1 and other References)

B1. Veres, J., *Centrifugal and Axial Pump Design and Off-Design Performance Prediction*, NASA TM-106745, October 1994.

B2. Gulbrandsen, N. *Centrifugal Pump Loss Isolation Program (LSISO)*, COSMIC Program # MFS-13029, April 1967. *(note that the version of LSISO used in this study is not publicly available, this reference gives a general description of the program in its original, publicly disseminated form).

B3. Rostafinski, W., *An Analytical Method for Predicting the Performance of Centrifugal Pumps During Pressurized Startup*, NASA TN D-4967, January 1969.

B4. Chaudhry,H., *Applied Hydraulic Transients - 2nd Edition*, Van Nostrand Reinhold, New York 1987.

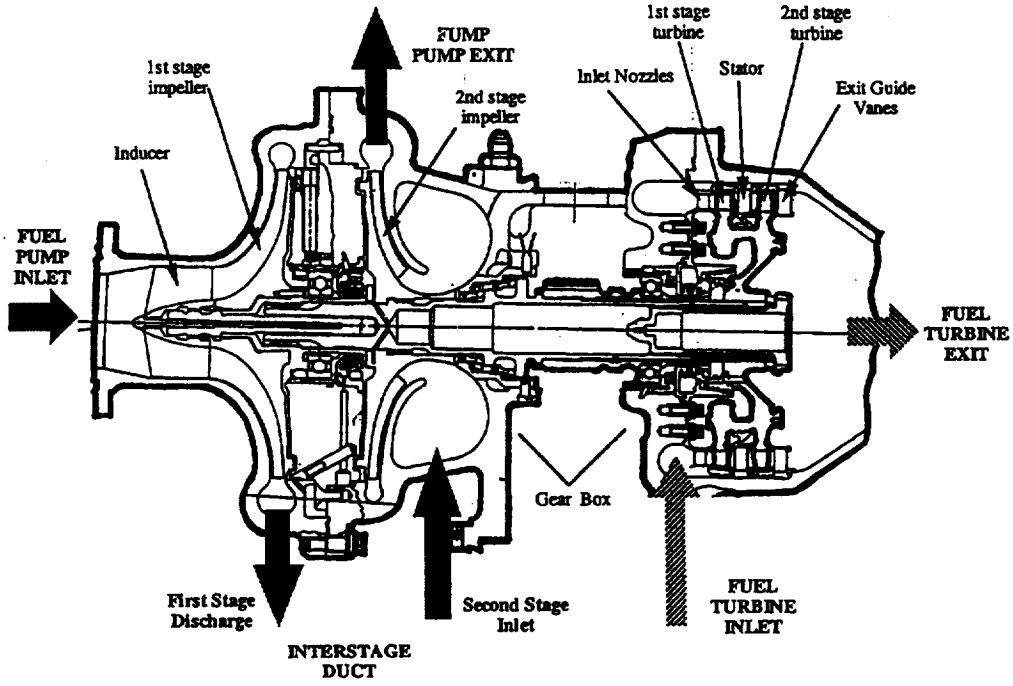

Figure B1

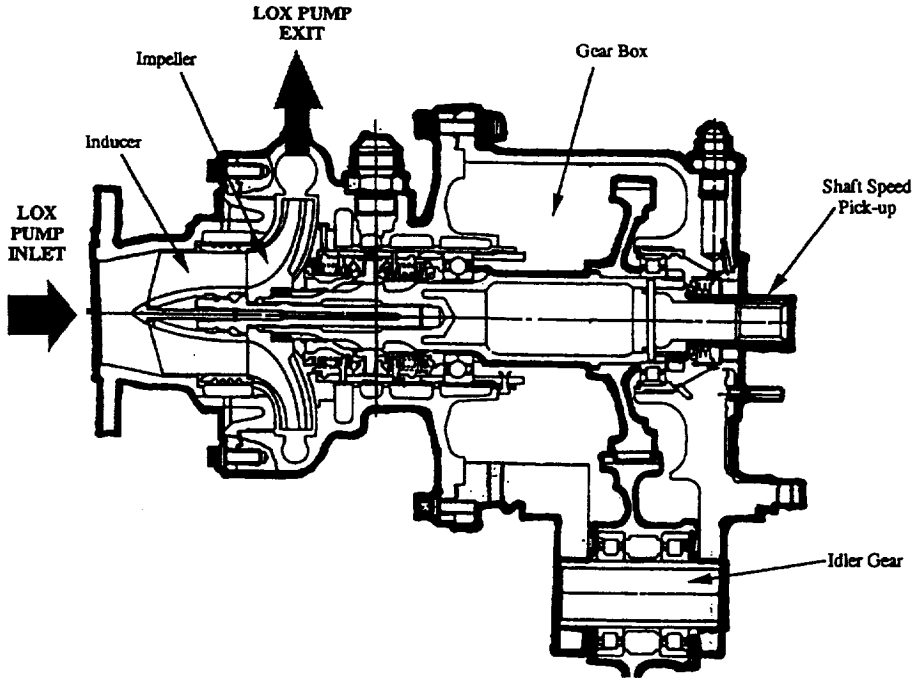

Figure B2

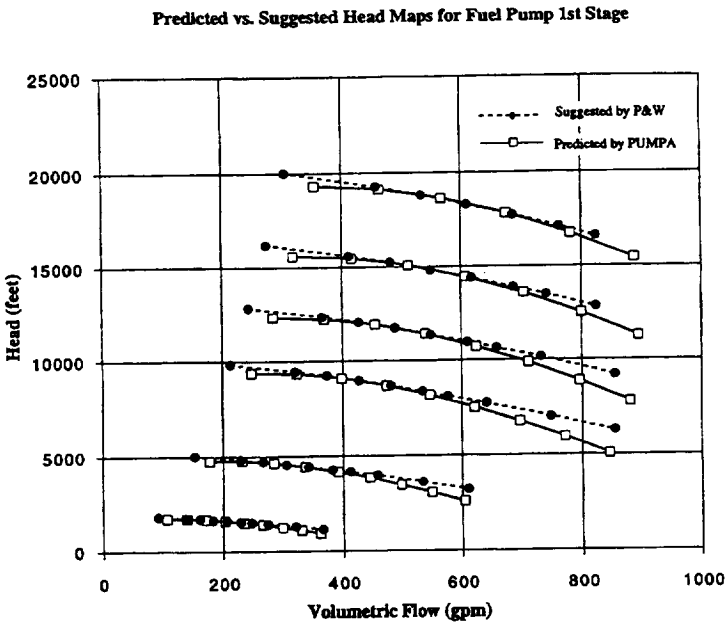

Figure B3

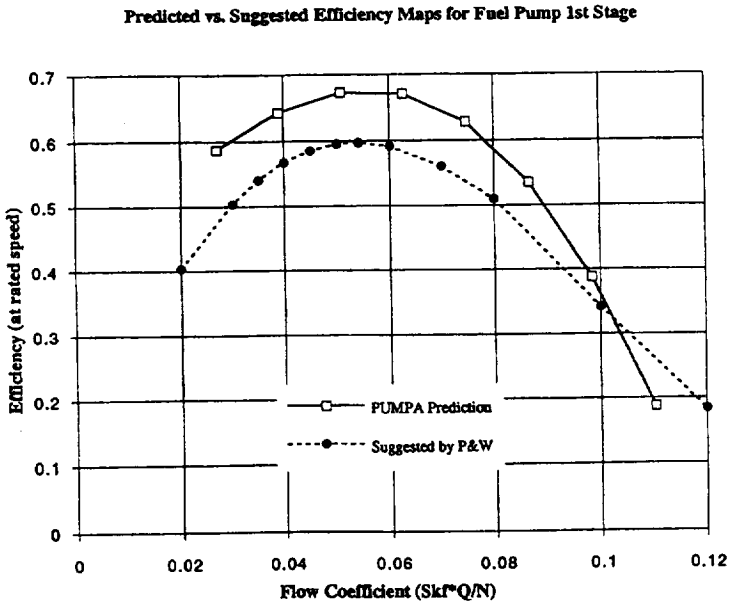

Figure B4

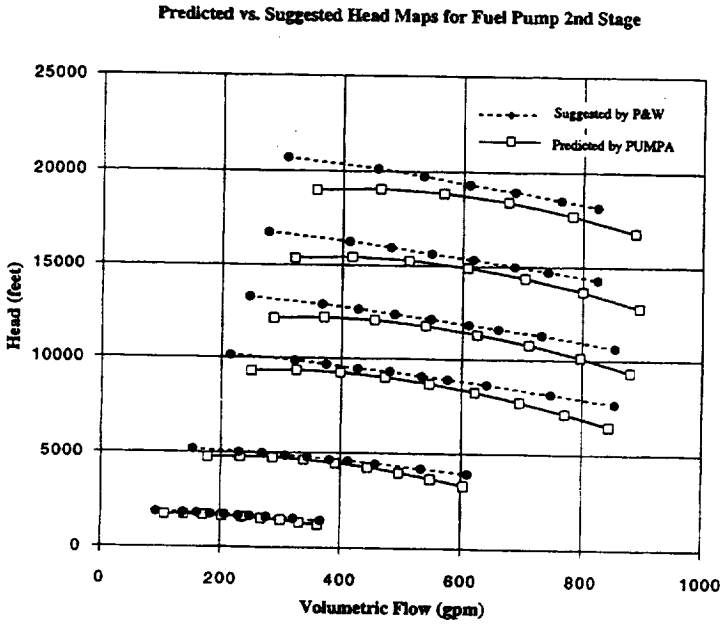

Figure B5

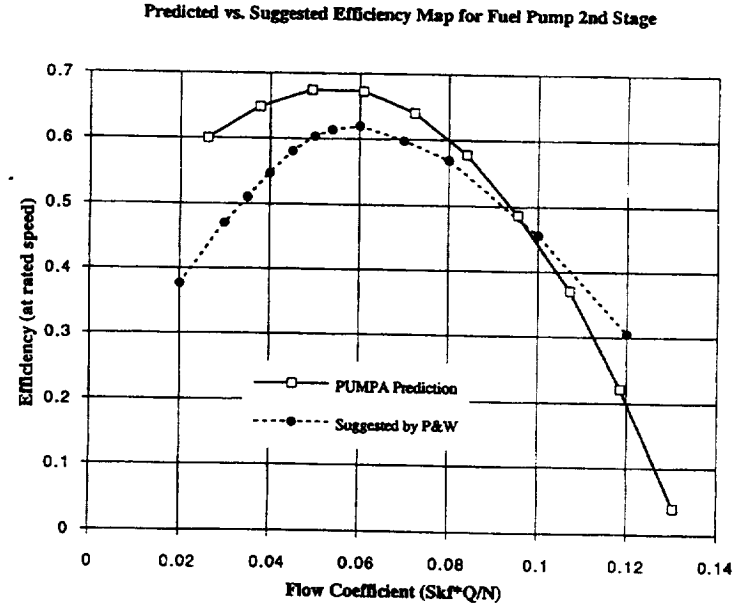

Figure B6

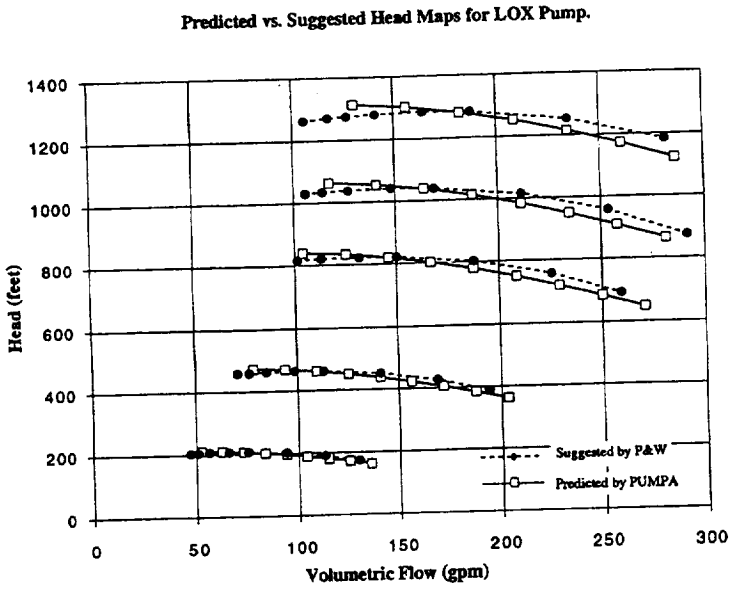

Figure B7

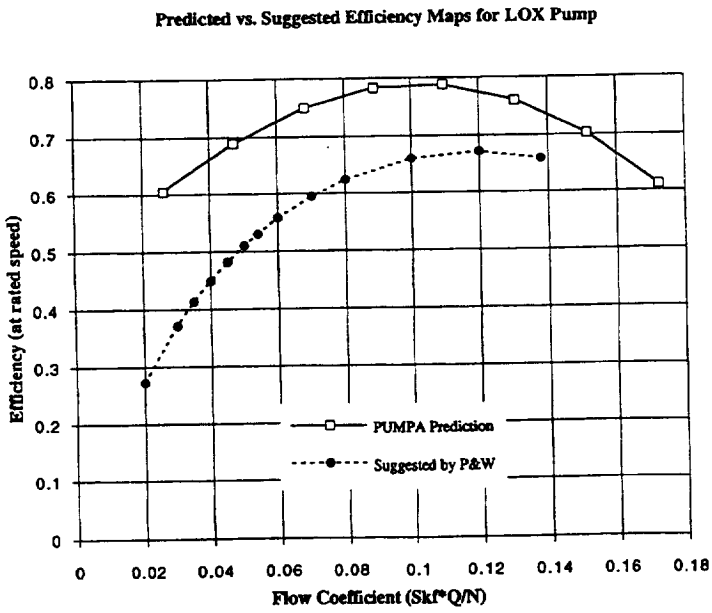

Figure B8

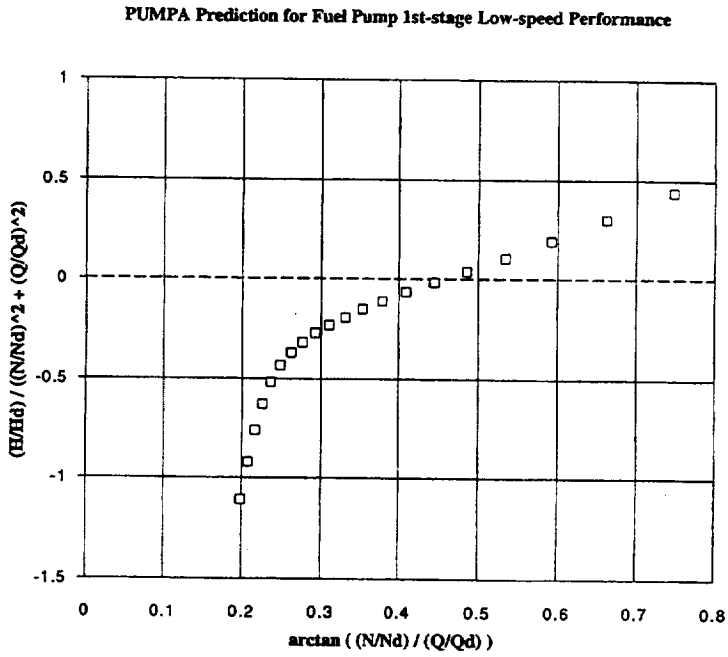

Figure B9

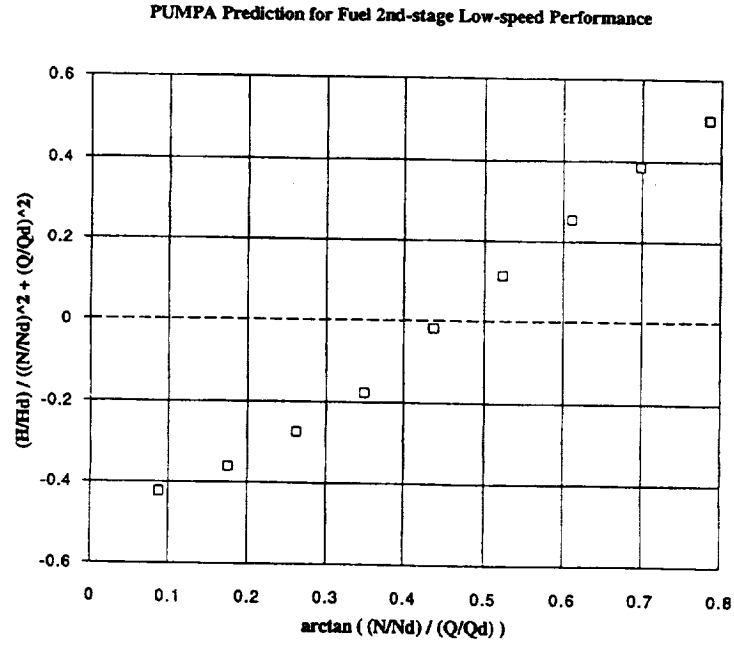

Figure B10

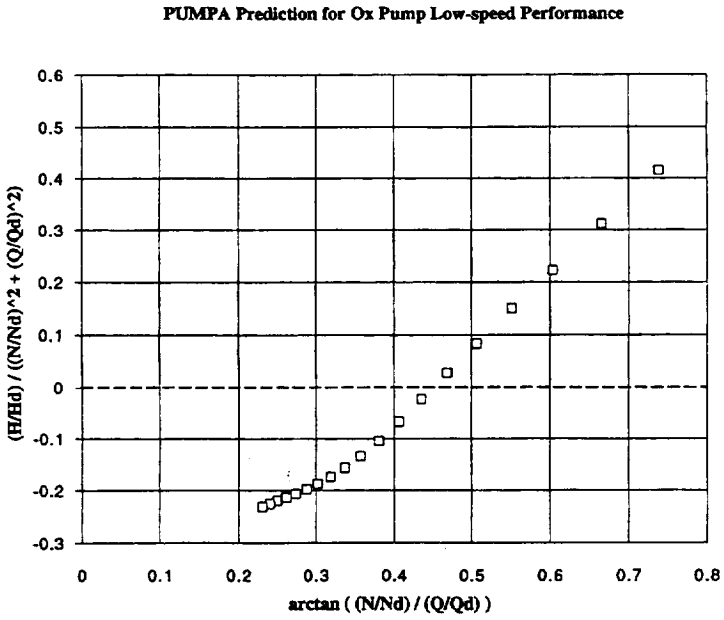

Figure B11

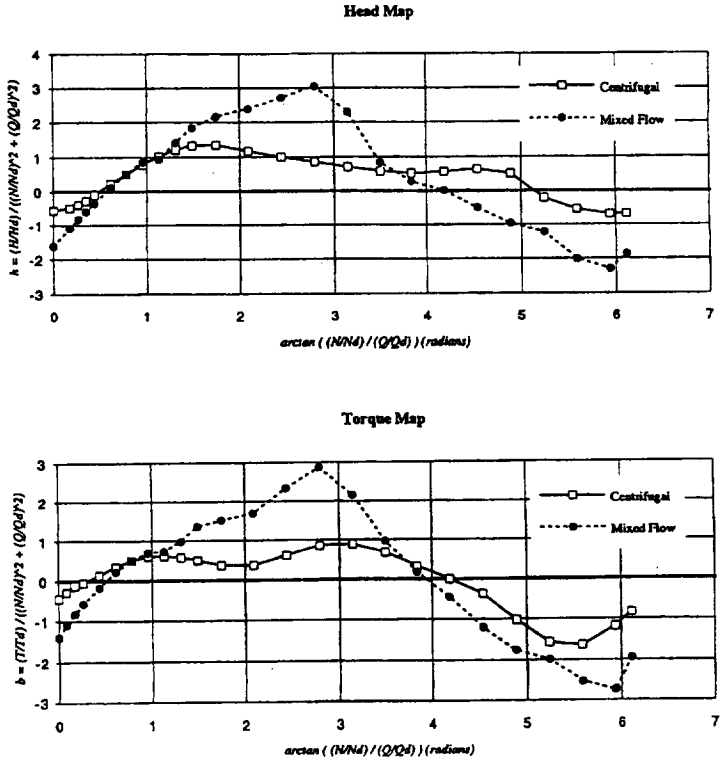

Figure B12

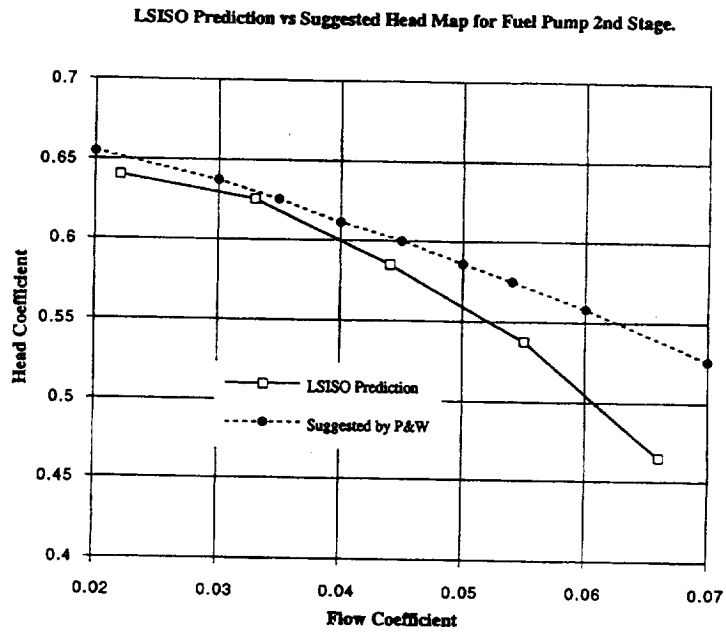

Figure B13

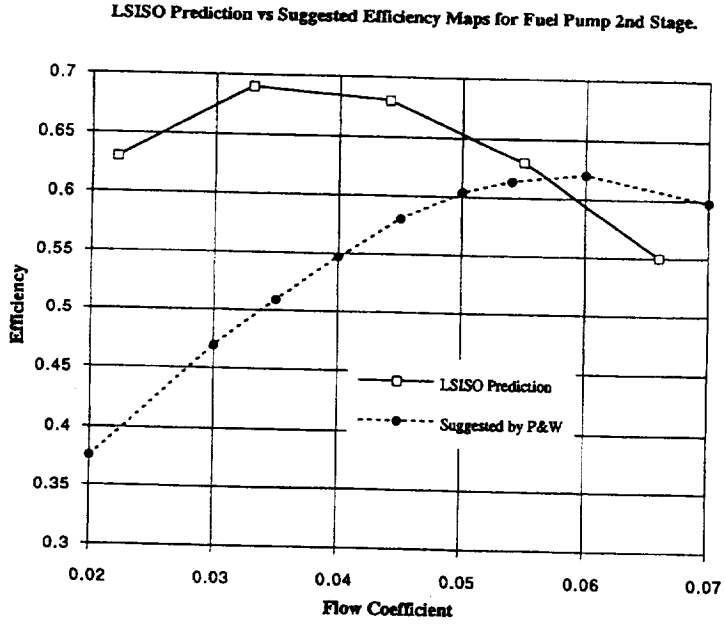

Figure B14

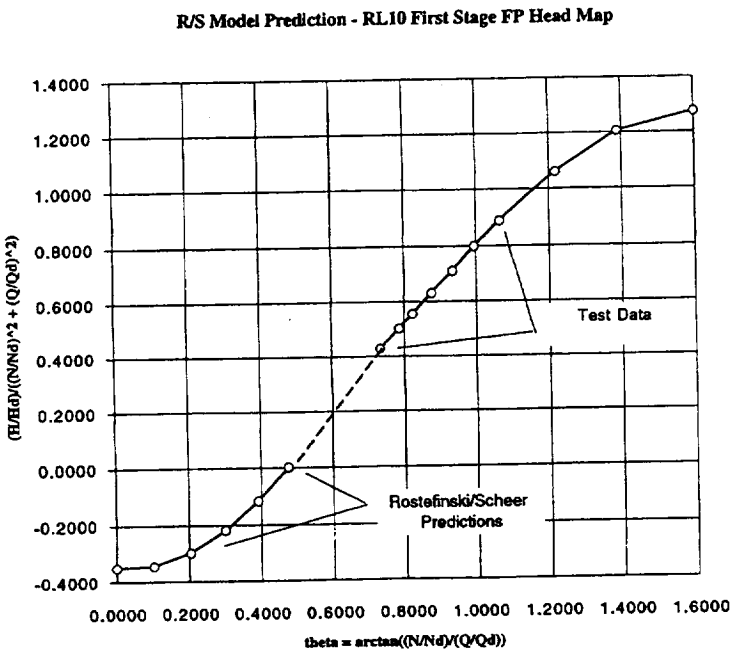

Figure B15

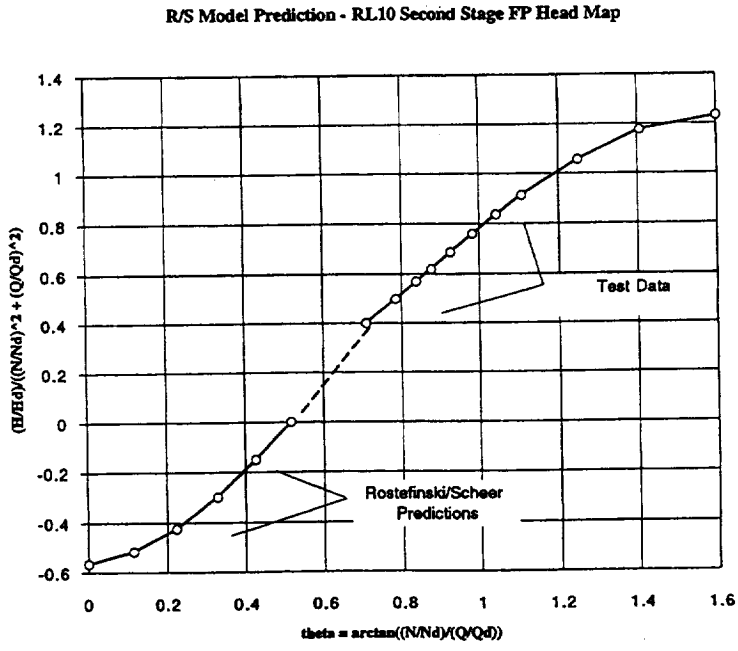

Figure B16

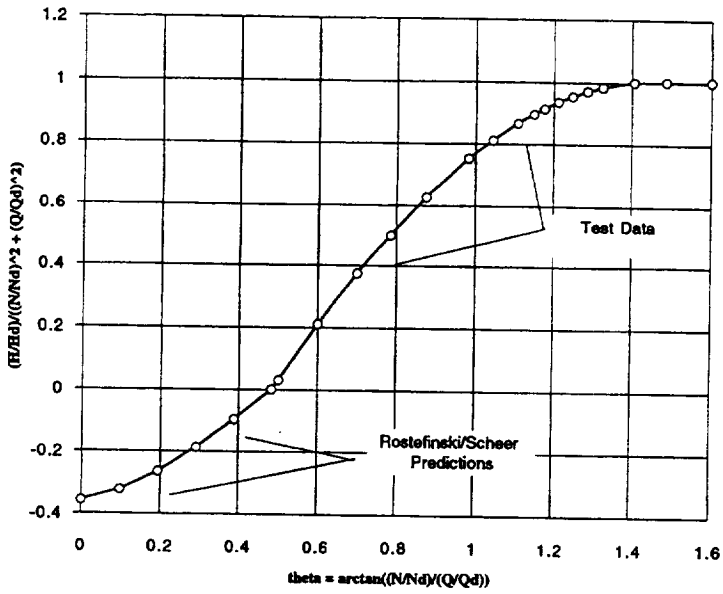

Figure B17

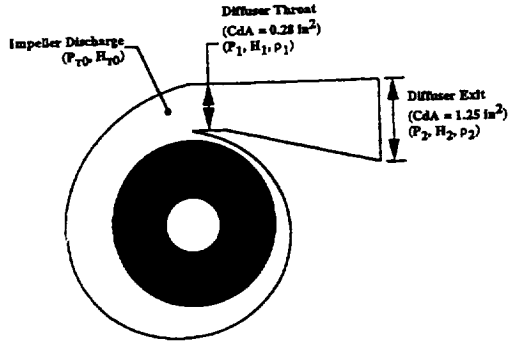

Solution Process:
The impeller performance maps are designed to give discharge pressure and enthalpy (stagnation conditions) for a given volumetric flow and shaft speed.

Step 1: Determine mass flow for use in reading impeller maps

Start with a guessed stagnation pressure and enthalpy at the impeller discharge. Mass flow through the diffuser is calculated using the following basic expression:

$$\dot{m}_x^2 = 2g\,(C_d A)_x^2\,\rho_x^2 \int_{P_{T0}}^{P_x} \left(\frac{1}{\rho}\right) dp$$

The integrand (1/ρ) above is evaluated using the pressure and assuming a constant total entropy throughout. Oxygen property tables are used to look up density for a given P and S.

Using this expression, two mass flows are computed: the critical mass flow at the diffuser throat, and the unchoked flow at the diffuser exit. For the critical flow, the throat pressure (which is not known a priori) is iterated until a local maximum in the mass flux is found. The unchoked mass flux at the diffuser exit is found by simply using the known static pressure there. In each case, the appropriate CdA is used.

The actual mass flow through the diffuser is assumed to be the smaller of the two flows calculated above.

Step 2: Use the calculate diffuser mass flow to read the impeller head map, calculate a new total pressure and enthalpy at the impeller discharge.

Step 3: Using an iterative solver for the pressure and back-substitution for enthalpy, the guessed total pressure and enthalpy at the impeller discharge are updated and the process loops back to step 1. A solution is considered complete when the guessed pressure equals the pressure found using the pump maps.

Figure B18

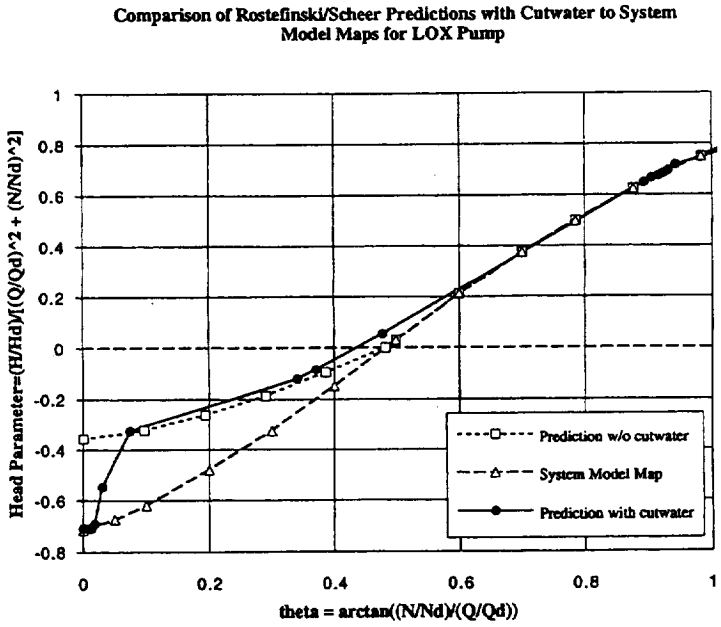

Figure B19

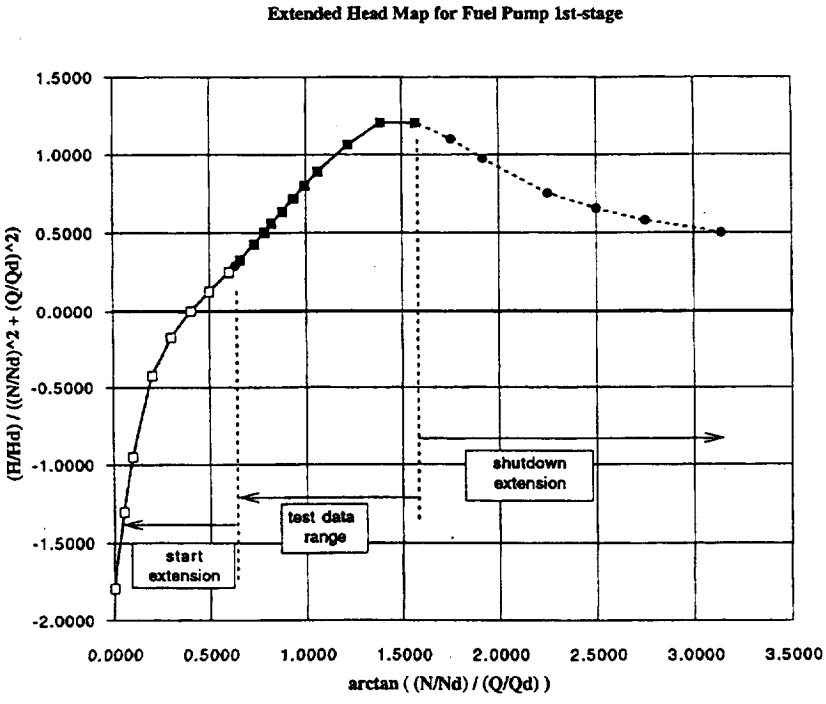

Figure B20

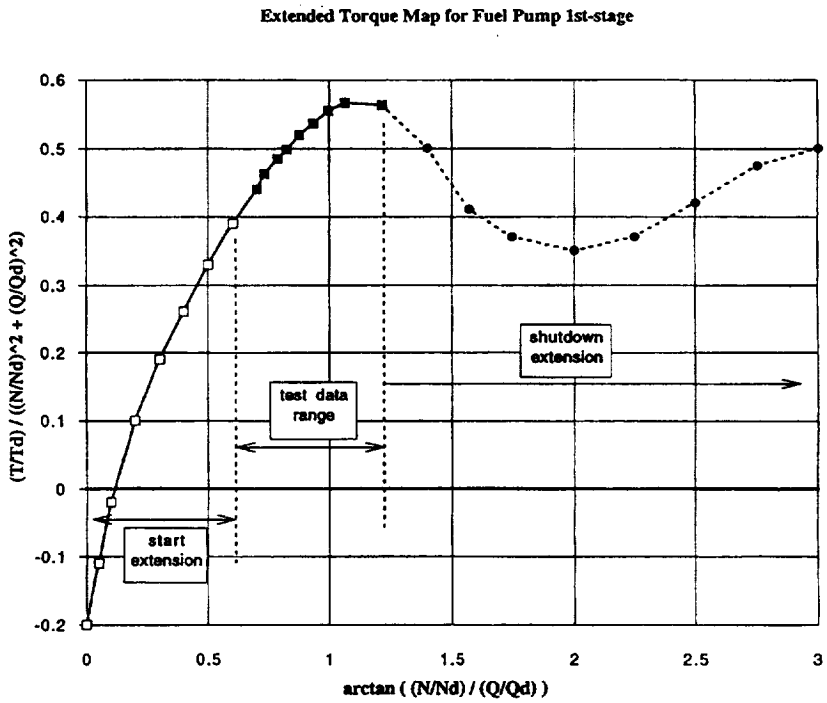

Figure B21

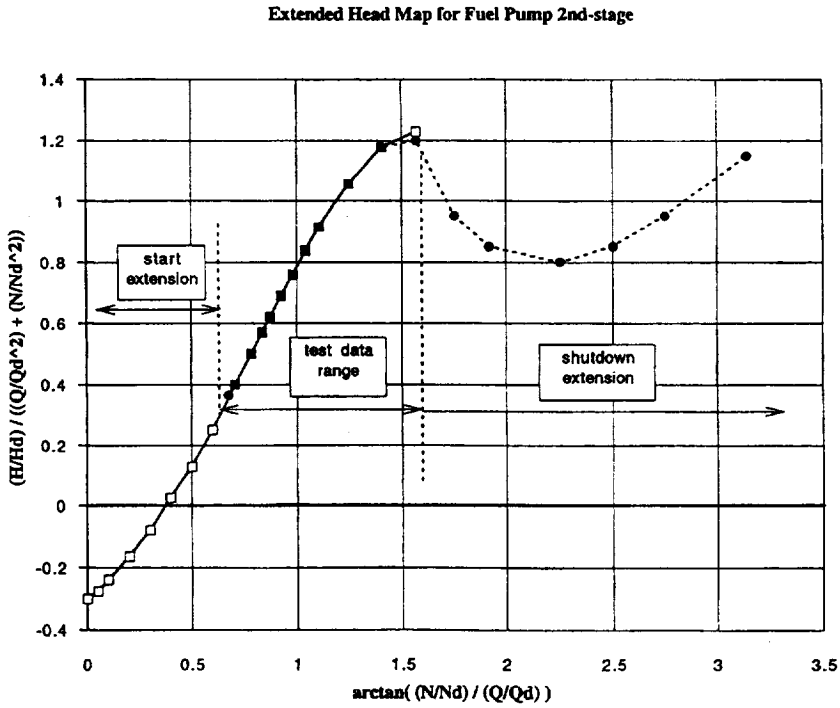

Figure B22

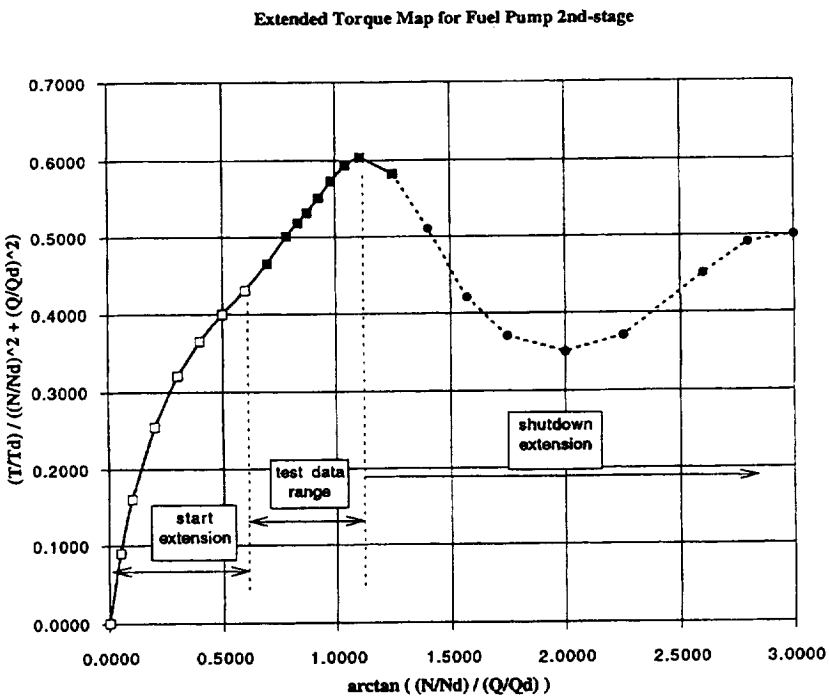

Figure B23

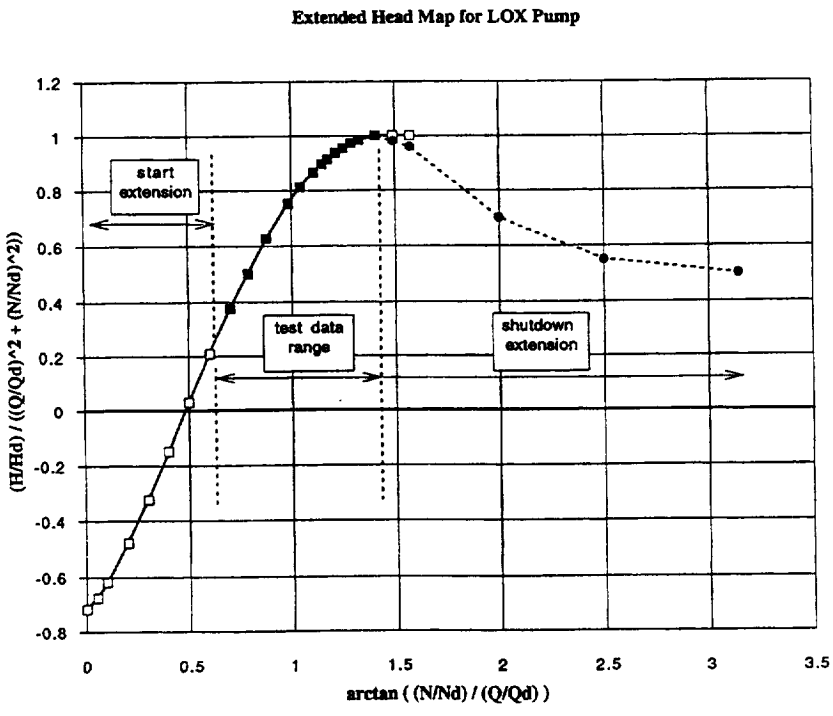

Figure B24

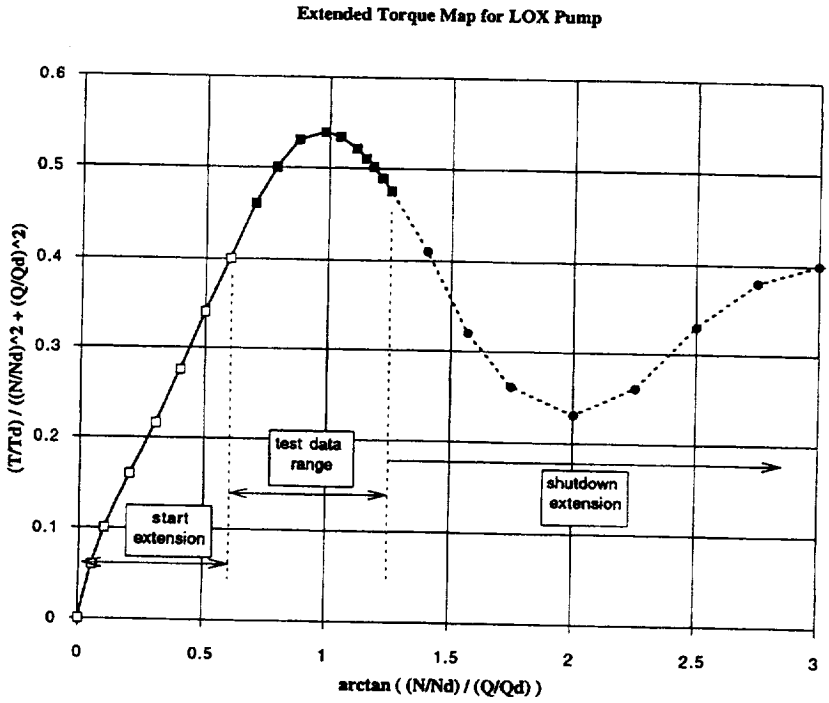

Figure B25

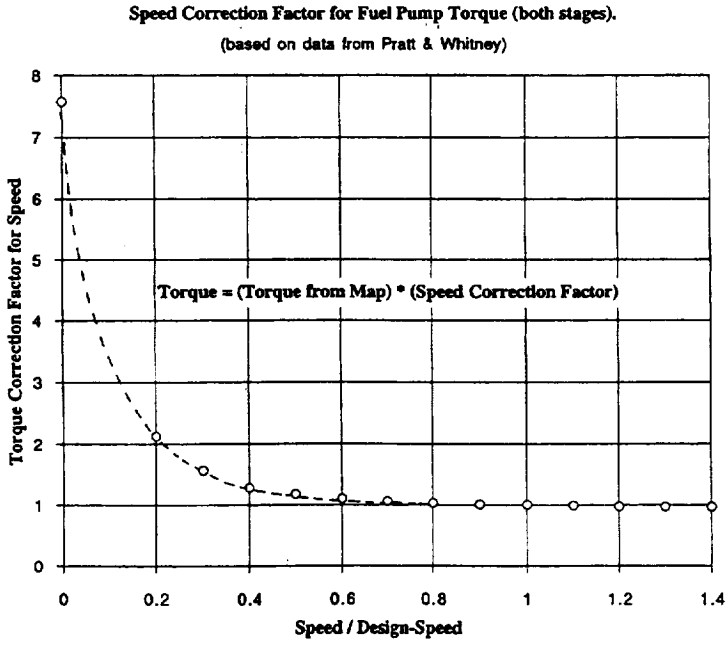

Figure B26

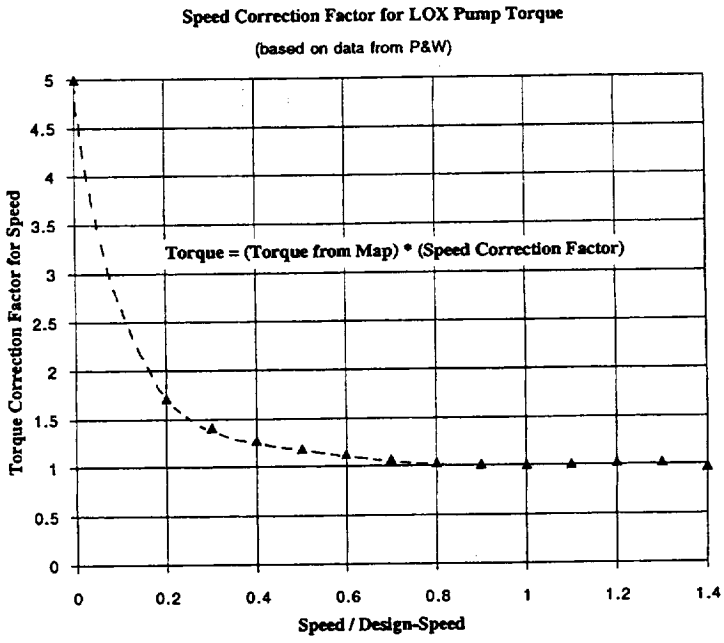
Speed Correction Factor for LOX Pump Torque
(based on data from P&W)
Torque = (Torque from Map) * (Speed Correction Factor)
Torque Correction Factor for Speed
Speed / Design-Speed
5
4.5
4
3.5
3
2.5
2
1.5
1
0.5
0
0
0.2
0.4
0.6
0.8
1
1.2
1.4

Figure B27

APPENDIX C
Component Modeling of RL10 Fuel Turbine

This appendix to the RL10A-3-3A Modeling Project Final Report describes efforts to predict the performance of the RL10 fuel turbine using component analysis programs available to the NASA Lewis Research Center Space Propulsion Technology Division (SPTD). A cross sectional representation of the RL10 fuel turbine is shown in Figure C1.

C.1 Analysis Tools Used

The SPTD has been working to develop turbomachinery design and off-design programs for several years. Since the RL10 design was already set, only the off-design performance codes were used in this project. The program used to analyze the RL10 fuel turbine is call TURBA (reference C1). This is a one-dimensional mean-line analysis tool. Given the geometry for the nozzles, rotors and stators, TURBA uses a combination of theoretical and empirical methods to predict the turbine performance. Basic flow and momentum equations are used to define the interaction between the fluid and each row of rotor blades and stators. The geometry of the flow passages is calculated to include metal and boundary-layer blockage effects. Design point efficiency is estimated using an empirical correlation derived from testing of various other turbine designs. An empirical correlation is also used to characterize the off-design-point efficiencies. It is possible to adjust the assumed fluid losses through the turbine to better match test data if desired.

C.2 Predictions from TURBA code

TURBA was used to analyze the performance of the RL10 fuel turbine, which has two stages. Figures C2 through C5 show the predicted flow parameters (related to the fluid resistance) and efficiencies of the turbine stages. The turbine performance maps provided by Pratt & Whitney (and presumed to be based on test data) are for both stages combined, rather than for each stage individually. These maps are shown in Figures C6 and C7. The flow resistance is represented by an effective orifice Cd*Area as a function of overall speed-ratio and pressure-ratio. The combined-two-stage efficiency of the turbine is also given as a function of overall speed-ratio. The way in which the turbine stage performance maps have been combined by Pratt &Whitney makes it difficult to perform one-to-one comparisons with the TURBA predictions.

In order to compare the combined maps provided by Pratt & Whitney with the single-stage maps predicted by TURBA, each set was used in a simulation which defines similar shaft speed, inlet and exit conditions. From these simulations, the mass flowrates and overall turbine efficiencies from the two models can be compared. These results are shown in Figures C8 and C9 as functions of shaft speed at several pressure-ratios. These figures indicate that the TURBA predictions for efficiency and flow resistance differ significantly (at least 5%) from the P&W values, especially at very low speeds.

Due to schedule limitations, it was not possible to investigate the differences between the TURBA predictions and P&W-specified maps in detail. Although the maps from Pratt & Whitney appear to be based on test-data, there are some issues regarding these maps which warrant further investigation in the future (resources permitting). In particular, it has been noted that the turbine performance maps suggested for the start-transient model are different from those suggested for the steady-state system model. The TURBA simulations were not as exhaustive as those for pump performance and should also be evaluated in the future, resources permitting.

C.3 Sensitivity of System Model to Turbine Performance Variations

As discussed in section 4.1.2.4 of the report, it has been found that the timing of the RL10 engine start is extremely sensitive to small variations in the turbine efficiency and flow resistance. Consider the two efficiency maps shown in Figure C10. The curves shown here are two polynomials intended to fit the same test data, but with different assumptions for order and residual error. Although they are quite similar overall, the slopes of the two curves differ by approximately

10% at low values of speed-ratio. The engine system dwells at these low speed-ratios for the majority of the start sequence. As can be seen from Figure C11, even such relatively small differences in turbine efficiency maps can create a significant difference in the engine time-to-accelerate. In light of these results, it seems highly unlikely that the predicted maps from TURBA will accurately predict the RL10 start transient (as the Pratt & Whitney maps appear to). Indeed, the sensitivity of the system to turbine performance variations is so great that no degree of modeling error can be accepted. It is unlikely that any turbine model not anchored by test data will attain the accuracy required to accurately reproduce the engine start transient. The significance of these findings extends beyond the RL10 Modeling Project, and casts serious doubt on future efforts to accurately model the start transient of any expander cycle engine based on theoretical models of the turbine. Other cycles with larger power margins during start may be less sensitive to small errors in the predicted turbine performance.

The turbine performance maps provided by Pratt & Whitney have been retained in the new RL10 engine transient model.

Glossary

Speed Ratio : Turbine blade tip velocity divided by nozzle spouting velocity.

$$u = \frac{N * D * \pi}{60}$$

$$c_0 = \sqrt{2g * J * \Delta H_{nozzle}}$$

$$\text{Speed Ratio} = u / c_0$$

Reduced Speed : Rotation Rate (in rpm) divided by the square root of the inlet temperature (R).

$$\text{Reduced Speed} = \frac{N}{\sqrt{T_{inlet}}}$$

Flow Parameter : multiplying the flow parameter by the inlet pressure divided by the square-root of the inlet temperature gives the mass flow rate.

$$\text{Flow Parameter} = \frac{\left(\frac{dm}{dt}\right) * \sqrt{T_{inlet}}}{P_{inlet}}$$

References

C1. Veres, J., *Axial Turbine Design and Off-Design Performance Prediction (TURBA)*, NASA TM (number pending), 1995.

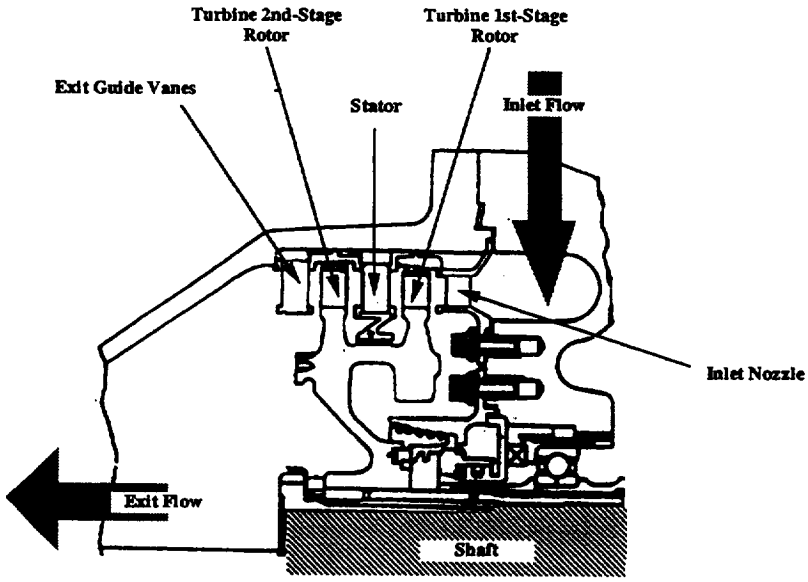

Figure C1

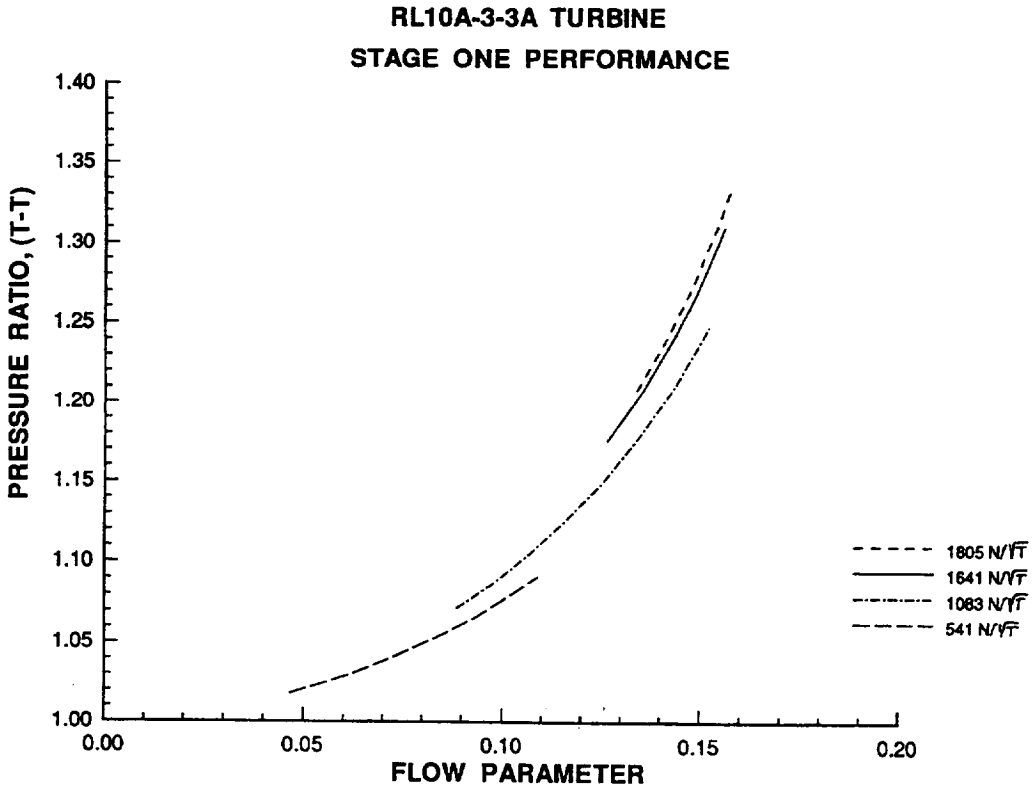

Figure C2

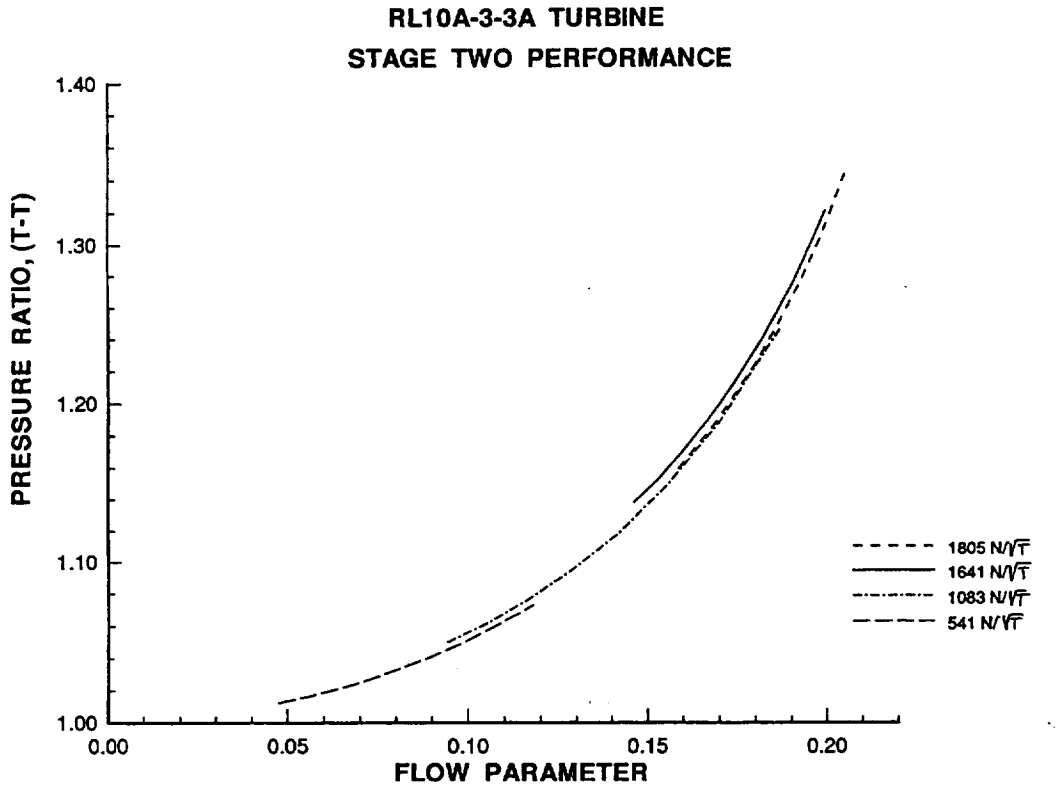

Figure C3

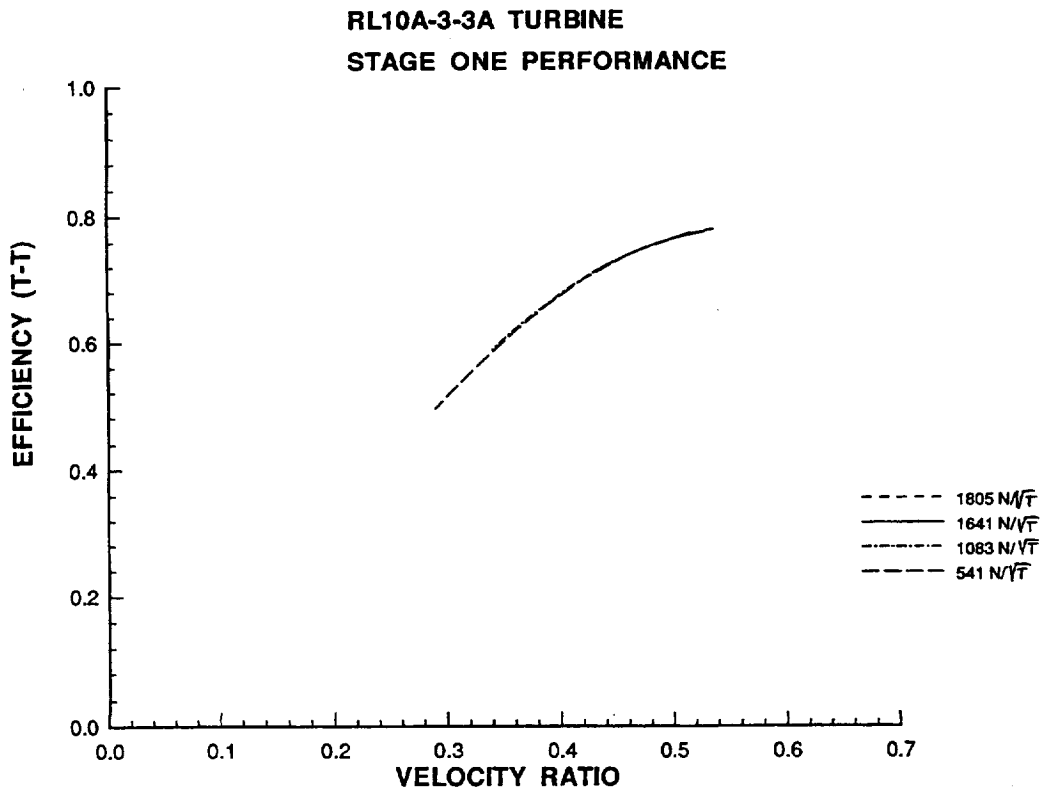

Figure C4

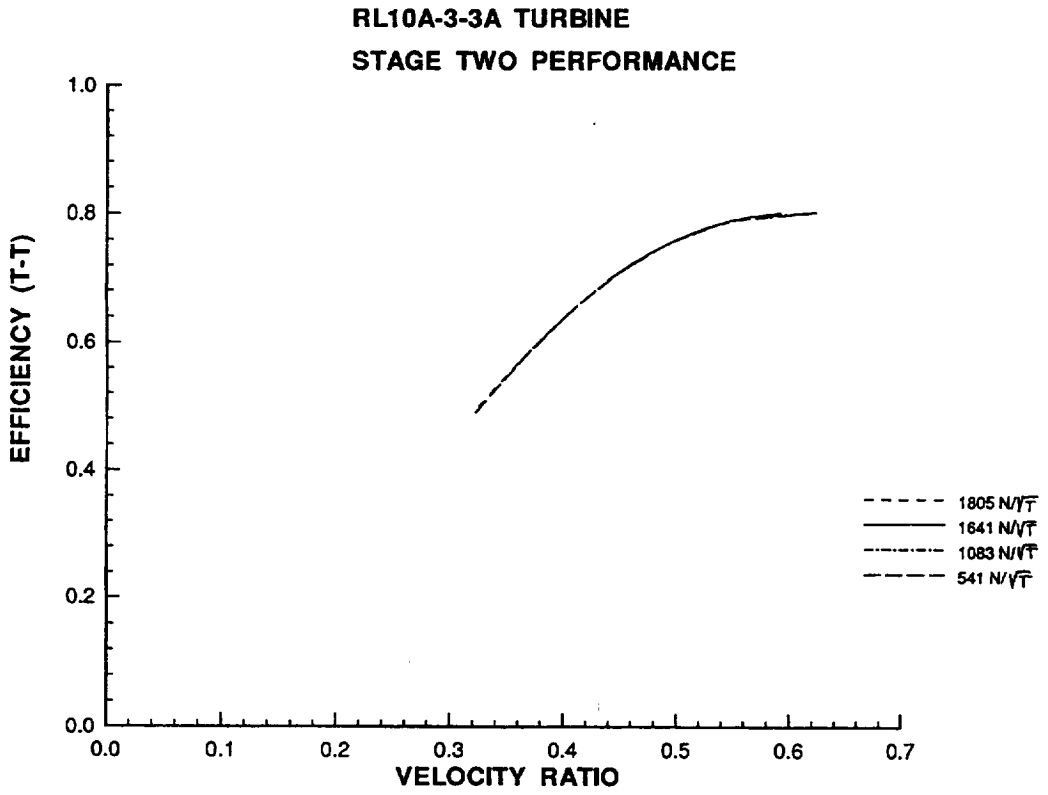

Figure C5

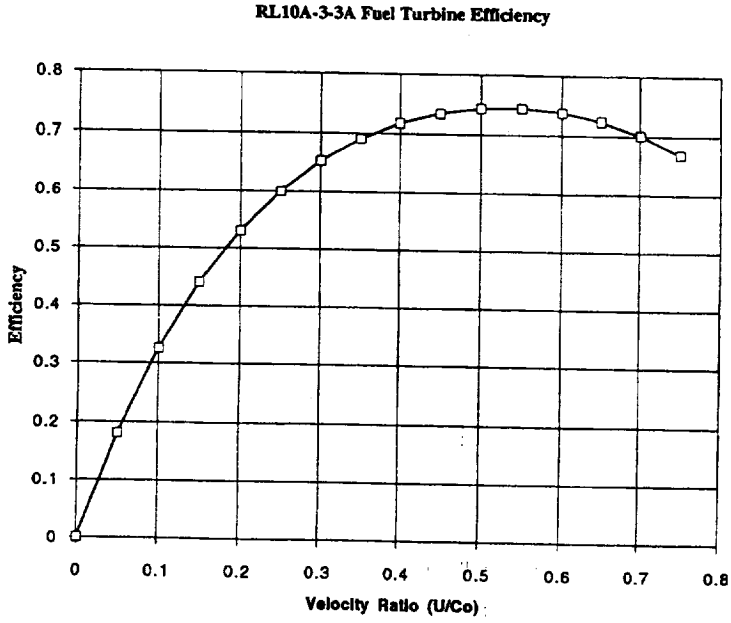

Figure C6

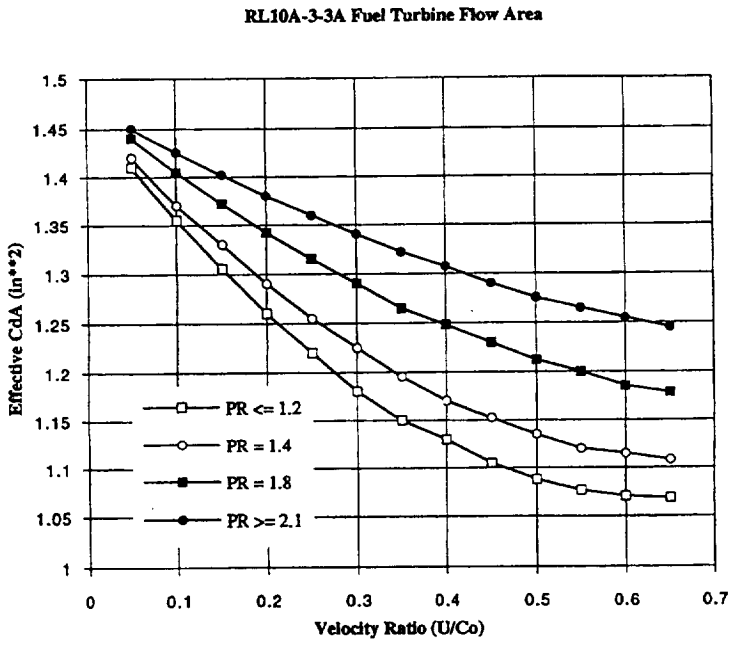

Figure C7

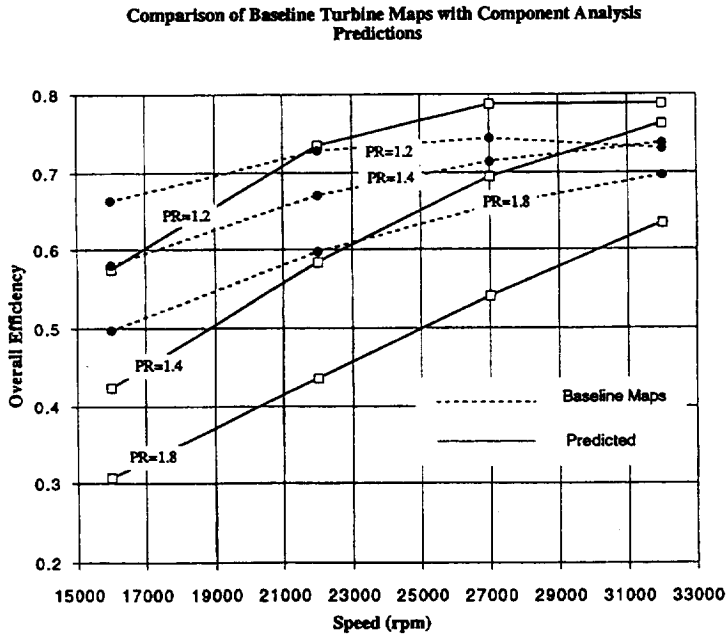

Figure C8

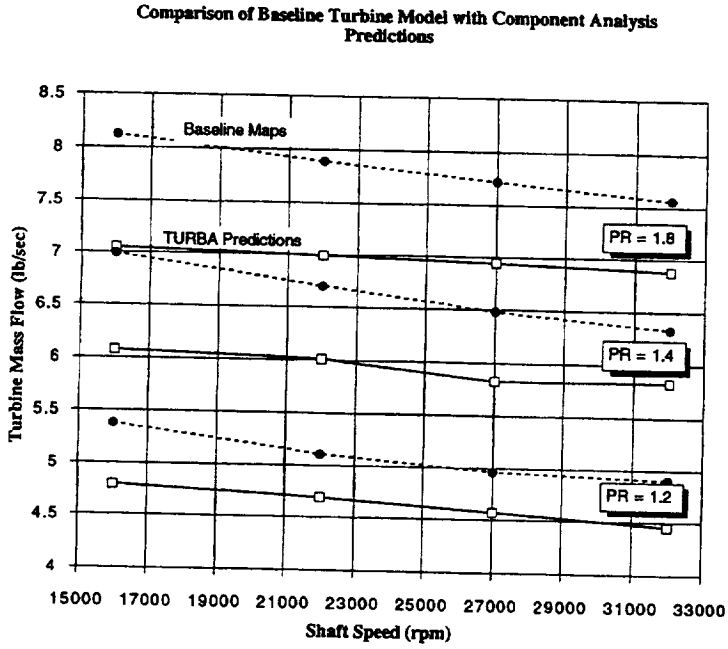

Figure C9

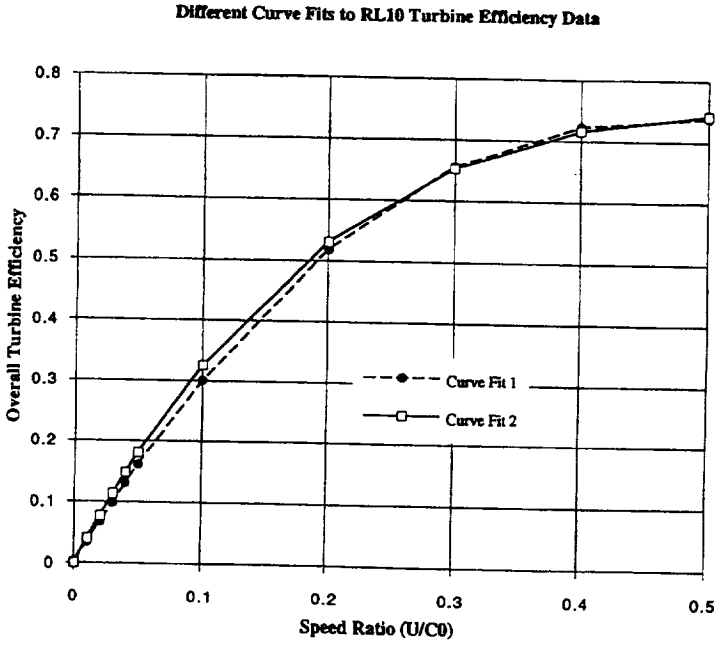

Figure C10

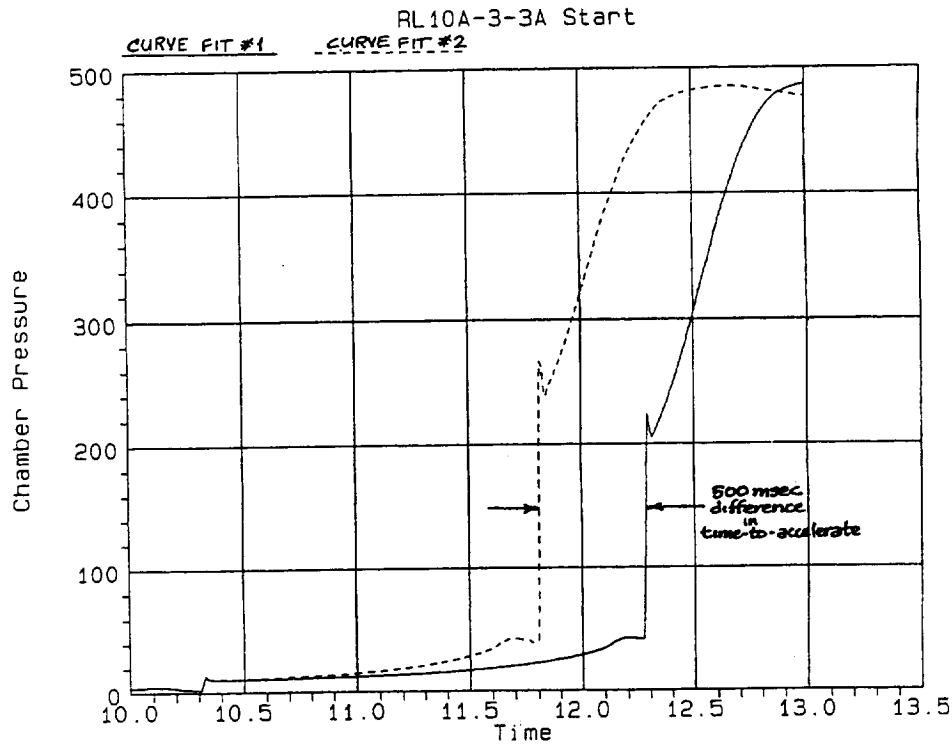
RL10A-3-3A Start
CURVE FIT #1
CURVE FIT #2
Chamber Pressure
500
400
300
200
100
0
10.0
10.5
11.0
11.5
12.0
12.5
13.0
13.5
Time
500 msec difference in time-to-accelerate

Figure C11

APPENDIX D
Component Modeling of the RL10A-3-3A Cooling Jacket

D.1 Introduction

Appendix D of the RL10A-3-3A Modeling Project Final Report describes work focused at improving the steady-state and transient heat transfer model predictions of the RL10 ROCETS engine system model. The approach taken was to predict the performance of the RL10 cooling jacket using the RTE (Rocket Thermal Evaluation) code, a three-dimensional (3-D) thermal analysis program available to the NASA Lewis Research Center (LeRC) Space Propulsion Technology Division (SPTD). The results of the thermal analysis were compared to engine and component test data and simulation output. The following sections provide a discussion of the RL10 heat transfer models.

D.2 Cooling Jacket Description

The RL10A-3-3A thrust chamber is a regeneratively-cooled one-and-one-half pass chamber with two main functions: to provide a convergent-divergent nozzle for the expansion of propellant; to serve as a heat exchanger which supplies fluid power to drive the fuel and oxidizer turbopumps. The cooling jacket assembly is constructed of 360 stainless steel tubes of type 347SS. The tubes are furnace-brazed together and reinforced by metal bands and a "Mae-West" structural reinforcing jacket. There are 180 short, single-tapered tubes which flow hydrogen coolant from the inlet manifold, located downstream of the chamber throat, aft towards the turn-around manifold at the nozzle exit plane. There are also 180 long, double-tapered tubes which carry hydrogen coolant forward from the turn-around manifold at the nozzle exit to the coolant discharge manifold located near the combustion chamber injector plane. The short and long tubes are arranged side-by-side in the nozzle section to form a seal for the hot combustion gas; only the long double-tapered tubes provide cooling of both the combustion chamber and nozzle sections. A cast silver throat insert is installed in the throat region. This insert reduces the effective throat diameter formed by the coolant tubes and increases the expansion area ratio from 57:1 to 61:1. Profiles of the long and short tube contour are shown in Figure D-1.

D.3 RL10 Cooling Jacket Heat Transfer Model

The RL10 cooling jacket model is based on the enthalpy driven potential method for calculating the hot-gas side heat flux. The hot and cold-side heat transfer coefficients are computed using the Bartz and Colburn equations, respectively. The numerical procedure for computing the hot-gas side and cold-side heat flux for the RL10 model is described below.

D.3.1 Hot-Gas Side Heat Transfer Model

The Bartz correlation (Ref. D1) for the hot-gas side heat transfer coefficient is determined given P_g, H_g, H_{g0} and T_{hw}. The hot-gas side wall enthalpy is estimated from static pressure and wall temperature.

$$H_{hw} = f(P_g , T_{hw})$$

The Eckert reference enthalpy (Ref. D2) is a function of gas static and total enthalpy.

$$H_{gr} = 0.5 (H_{hw} + H_g) + 0.18 (H_g0 - H_g)$$

Combustion gas reference properties generated using the CET93 code (Ref. D3) are looked up from data tables.

$$T_{gr} = f(P_g , H_{gr})$$

$$Pr_{gr} = f(P_g , H_{gr})$$

$$c_{p_{gr}} = f(P_g , H_{gr})$$

$$\mu_{gr} = f(P_g , H_{gr})$$

$$k_{gr} = f(P_g , H_{gr})$$

The hot-gas side adiabatic wall enthalpy is also dependant on gas enthalpy terms.

$$H_{aw} = H_g + Pr_{gr}^{1/3} (H_g 0 - H_g)$$

The Bartz expression for the hot-gas side heat transfer coefficient is determined from combustion gas properties and RL10 geometric parameters.

$$h_{gr} = 0.026 \frac{k_{gr}}{D_{hyd}} \left(\frac{c_{p_{gr}}}{k_{gr} \mu_{gr}} \right)^{0.4} \left(\frac{\dot{m}_g D_{hyd}}{A_{chmb}} \right)^{0.8} \left(\frac{T_g}{T_{gr}} \right)^{0.8} \phi_B$$

Note: the ϕ_B term shown in the Bartz equation is a correction factor added to the original equation to better match RL10 test data. The value of ϕ_B was analytically determined to be 1.08.

The heat transfer coefficient and enthalpy-driven heat transfer rate is used to predict the RL10 coolant jacket heat pick-up.

$$h_g = \frac{h_{gr}}{c_{p_{gr}}}$$

$$\dot{q}_{hw} = h_g A_{sm_w} (H_{aw} - H_{hw})$$

Numerically, the hot-gas side heat transfer rate is calculated at each of the twenty (20) node locations along the RL10 chamber and nozzle. The calculation iterates until convergence is reached on the hot-gas side wall temperature T_{hw} and coolant-side wall temperature.

D.3.2 Coolant-Side Heat Transfer Model

The coolant-side heat transfer coefficient is determined by the Colburn equation given coolant P_c, T_c and T_{cw}.

$$h_c = 0.023 \frac{k_{c_f}}{D_c} \left(\frac{c_{p_{c_f}}}{k_{c_f} \mu_{c_f}} \right)^{0.4} \left(\frac{\dot{m}_c D_c}{A_c} \right)^{0.8} \phi_{Curv}$$

Coolant properties are evaluated at the static pressure and film temperature.

$$T_{c_f} = \frac{T_c + T_{cw}}{2}$$

A correction factor for the tube radius of curvature (Ref. D4) accounts for heat transfer enhancement in the throat and nozzle inlet regions.

$$\phi_{Curv} = \left[Re_c \left(\frac{0.5\, D_c}{R_{curv}} \right)^2 \right]^{\pm 0.05}$$

In the above expression, D_c is the hydraulic diameter of the coolant passage, R_{curv} is the radius of curvature, the positive (+) sign denotes concave curvature and the negative sign (-) indicates convex curvature.

The heat transfer rate to the coolant through the cold-side boundary layer is determined by a forced-convection temperature difference equation.

$$\dot{q}_{cw} = h_c\, A_{sm_{cw}}\, (T_{cw} - T_c)$$

D.3.3 Conduction Heat Transfer Model
The heat transfer rate across the tube metal wall is calculated by the conduction equation.

$$\dot{q}_m = k_m\, A_{sm}\, \delta_x\, (T_{hw} - T_{cw})$$

Thermal conductivity is determined at the average metal wall temperature.

$$T_m = \frac{T_{cw} + T_{hw}}{2}$$

D.4 RTE Analytical Model

This section describes the RTE analytical program (Ref. D5) used in the evaluation of the RL10 cooling jacket model. Heat flux, wall temperature and coolant temperature and pressure profiles were predicted for the RL10 using this code. Minor modifications were required to RTE for analyzing the RL10's tubular coolant passage geometry.

The RTE code, developed under grant for the NASA LeRC SPTD, is a 3-D model for analyzing the thermal performance of regeneratively-cooled thrust chambers. The main inputs to the RTE code are coolant inlet temperature and pressure, coolant passage dimensions, nozzle coordinates and chamber conditions; chamber pressure, mixture ratio (O/F) and chamber mass flowrate. The analysis accounts for coolant passage radius of curvature effects, surface roughness and coolant entrance effects. Heat transfer on both the hot-gas side and coolant-side of the tube wall are predicted, as well as the momentum and frictional losses of the coolant flowing through the tubes. Frictional losses are computed using the Darcy correlation (Ref. D6), modified to account for the coolant density change between stations. RTE uses either a temperature-driven or optional enthalpy-driven potential method for estimating heat flux. The Colburn correlation is used to predict heat transfer coefficients on the hot-gas side. The coolant side heat transfer is also computed using the Colburn correlation with corrections to account for the tube curvature effect.

This effect causes the coolant-side heat transfer rate to alternately increase and decrease due to boundary layer thinning as the fluid's momentum forces coolant against the hot-side (concave) and cold-side (convex) of the tube wall (Ref. D7). Heat transfer enhancement (Figure D-2) occurs as the coolant progresses through the throat and then through the chamber convergent section regions, respectively. RTE uses a one-dimensional equilibrium code (CET89) to obtain hot-gas side thermal and transport properties. Hydrogen coolant properties are obtained by RTE from the GASP code (Ref. D8).

D.5 RL10 Predictions using RTE

D.5.1 Baseline RTE analytical results

To determine the effects of spatial resolution, the RL10 cooling jacket was modeled with the RTE code at varying numbers of computational nodes. Figure D-3 shows the RTE predictions converging at a spatial resolution of approximately twenty axial nodes. This indicated that increasing the number of nodes above twenty had little or no effect on predicted heat flux. Based on this "optimized" result, a twenty-node RL10 coolant jacket model was constructed for the RL10 system model.

A comparison was then made of a twenty-node RTE model of the RL10 with limited test data and P&W results that were available. RTE predictions of heat flux, hot-gas side wall temperature, coolant pressure and coolant temperature are compared to "typical" P&W analytical results in Figures D-4 through D-7. Comparing the RTE predictions with Pratt & Whitney's own analysis showed that they are basically similar. Figure D-4 shows that the original RL10 heat transfer model is in poor agreement with both the RTE and P&W analyses. Figures D-6 and D-7 compare the RTE model predictions with the RL10 test data for coolant pressure drop (ΔP) and temperature rise (ΔT). Heat flux, wall temperature, cooling jacket pressures and temperatures are not measured at intermediate points along the cooling jacket so detailed data was not available to validate the RTE predictions.

RTE is limited to the analysis of single-pass, counter-flow cooled thrust chambers. In order to analyze the RL10 with this code, the half-pass, 180 short tubes of the RL10 chamber was treated as strictly counter-flow in the RTE model. The predicted RTE coolant temperature profile shown in Figure D-7 illustrates this effect. The RTE analysis was constructed such that liquid hydrogen coolant entered the jacket at the nozzle exit plane. The coolant inlet temperature used in the analysis was 58°R.

D.6 RL10 Cooling Jacket System Model Construction

D.6.1 Twenty-node RL10 system model subroutine

Based on the RTE analysis for variable nodes, the initial cooling jacket heat transfer subroutine created for the RL10 system model included all twenty (20) thermal and coolant fluid axial-nodes used in RTE. A new combustion gas property routine for the RL10 model was generated from CET93 (Ref. D3). Tables of thermal and transport property data for each hot-gas side axial node were produced. Hydrogen coolant properties for the RL10 system model are obtained from an extensive set of built-in data tables. A comparison of GASP output used by RTE with the existing RL10 hydrogen property data tables indicated no significant differences.

D.6.2 Required corrections to better match RL10 engine test data

During the initial phase of the RL10 analysis, large discrepancies were noted between predicted and measured values of overall cooling jacket pressure drop and temperature rise. It appeared that

the RTE model seriously under-estimated experimental coolant ΔT and ΔP. It was later ascertained that the predictions did match fairly well within P&W's predictions and other engine test cases. There apparently is a large variation in heat transfer and frictional loss between different engines operating at nearly identical conditions. These engine-to-engine variations appear to be about 10 percent in total heat pick-up and coolant ΔP, but there is insufficient test data to confirm this with any confidence.

Another assumption which effects the RL10 coolant jacket heat transfer model is the percentage of tube surface area which is exposed to hot-gas side heat transfer. Low heat transfer predictions could result by assuming too low of an exposed tube surface area. A value of 112 degrees was specified by Pratt & Whitney. It is possible that their value is specifically tuned to P&W's own calculation technique. It is also possible that the actual effective tube surface area is different from engine-to-engine due to manufacturing variations. As long as the heat pick-up is sufficient to start the engine, the engine will not be rejected in manufacturing.

Several experts concede that the state-of-the-art in heat transfer prediction is on the order of 10% to 20% accuracy (Ref. D9). The discrepancies noted above, while undesirable for system analysis, are within the generally accepted range of accuracy for thrust chamber heat transfer models. Ultimately, given the uncertainties in test-to-test variations, a factor of 0.028 in the Bartz equation was employed in the RL10 system model instead of the more generally accepted value of 0.026. It was also determined that a friction factor approximately 94 percent of that recommended by P&W would improve the coolant ΔP predictions.

D.6.3 Enthalpy vs Temperature potential driving heat transfer

The analyses further indicated that when the Bartz or Colburn heat transfer coefficient was used in a temperature-driven heat-transfer equation, the model did not correctly predict the variation in RL10 heat transfer with chamber mixture ratio.

$$\dot{q}_{hw} = h_g A_{sm_w} (T_{aw} - T_{hw})$$

The enthalpy-driven correlation provided a much more accurate model of the heat transfer rate variation with mixture ratio as shown by the RTE results in Figure D-8. The total heat pick-up increased by 6.4% over the test data O/F range of 4.7 to 5.7.

$$h_g = \frac{h_{gr}}{c_{p_g}}$$

$$\dot{q}_{hw} = h_g A_{sm_w} (H_{aw} - H_{hw})$$

D.6.4 Twenty vs Five Coolant property nodes

The final issue to be addressed was the integration of the full twenty-node cooling jacket model with the rest of the RL10 engine transient model. Including separate dynamic fluid volumes for each node was possible but the size of the Jacobian matrix significantly increased. It had already been shown that a five-node model gave serious discrepancies in the wall heat transfer distribution. It was found, however, that if twenty hot-gas nodes and twenty metal nodes were properly connected to five coolant nodes, the heat transfer distribution could be satisfactorily modeled while keeping the Jacobian matrix size to a minimum. A comparison of the full twenty-node model and the proposed hybrid model yielded comparable results for cooling jacket wall temperature, heat flux and coolant temperature. Only the coolant static pressure result of the hybrid model showed some underestimation when compared to the twenty-node model.

The final RL10 cooling jacket model installed in the engine system model consisted of volume

dynamics and fluid inertia modeled in five segments. Each segment has a characteristic length, volume and resistance determined by lumping the fluid node predictions from RTE. Multiple metal nodes are attached to each of the five coolant segments. At each of the twenty metal property nodes, temperatures are tracked in three zones. During start and shutdown transient simulations, these temperatures are integrated explicitly. Temperatures from the previous time step are used to determine the heat transfer rate for the current time step and the heat flux imbalance is added or subtracted to the metal to update the temperature. During steady-state runs, the temperatures are varied to achieve a heat transfer balance.

D.7 Boiling Heat Transfer

After completion of the RTE analysis, a boiling heat transfer routine was added to the RL10 cooling jacket model. Heat transfer instabilities due to boiling have been used to explain the pressure oscillations visible in recorded flight data during the engine start transient (Figure D-9). These oscillations occur at a frequency too low to be attributable to pump stall. The frequency of the oscillations are consistent from test-to-test, but vary between the first and second burns. This is attributed to the difference in the initial cooling jacket temperature prior to engine start. It was of particular interest to some members of our team that an attempt be made to reproduce these oscillations in the engine start model.

Boiling heat transfer effects were modeled based on a free-convection heat transfer correlation modified for two-phase flow as described in reference D10. These equations are semi-empirical and based on fluid quality, the vapor mass fraction in a two-phase flow mixture.

$$x = \frac{\rho_{sv}}{\rho_c} \frac{\rho_{sl} - \rho_c}{\rho_{sl} - \rho_{sv}}$$

The index relating viscous wall resistance in two-phase flow is given by the Lockhart and Martinelli parameter.

$$\chi_{tt} = \left(\frac{1 - x}{x}\right)^{0.9} \left(\frac{\mu_{sl}}{\mu_f}\right)^{0.1} \left(\frac{\rho_f}{\rho_{sl}}\right)^{0.5}$$

If the coolant inlet quality is less than 95%, the two-phase heat transfer coefficient is used to obtain the coolant-side heat flux during simulation of engine start.

$$h_c = 0.023 \frac{k_{c_f}}{D_c} \left(\frac{Pr_{c_f}^{0.4} Re_{c_f}^{0.8}}{0.611 + 1.93 \chi_{tt}}\right) \phi_{Curv}$$

The two-phase heat transfer effects described here were incorporated into the full twenty-node cooling jacket model. Preliminary simulations indicated, however, that the temperature differential between metal and coolant and the amount of heat available at start were so great that the model transitions immediately to the forced convection conditions, and does not dwell in the film boiling region. It might be possible to observe film boiling effects if the number of nodes near the jacket inlet were greatly increased, but that study was beyond the scope of this project. Another possiblity that has not been studied is that the heat transfer instability could be due to effects that cannot be adequately modeled using a one-dimensional analysis. It may be necessary to create time-transient two-dimensional models which describe the dynamics of the film layer and fluid flow. In

summary, the 1-D film boiling model was included in the RL10 engine system model. This model is also based on only five coolant-fluid property nodes. No effects of film boiling have been observed in any of the RL10 simulations performed thus far.

Nomenclature

A_c = cross-sectional flow area of coolant tube (in^2)

A_{chmb} = cross-sectional area of hot-gas-side chamber (in^2)

A_{sm} = metal surface area (in^2)

D_c = hydraulic diameter of coolant tube (in)

D_h = hydraulic diameter for chamber hot-gas flow (in)

c_p = heat capacity at constant pressure (Btu/lb_m-^oR)

h = heat transfer coefficient ($Btu/sec\text{-}in^2\text{-}^oR$)

H = enthalpy (Btu/lb_m)

k = thermal conductivity ($Btu/sec\text{-}in\text{-}^oR$)

m = mass flow rate (lb_m/sec)

P = static pressure (lb_f/in^2)

P_c = chamber pressure (lb_f/in^2)

Pr = Prandtl number ($\mu\ c_p / k$)

$\dot{q}$ = heat transfer rate (Btu/sec)

R_{curv} = coolant tube radius of curvature (in)

Re = coolant Reynolds number ($m_c\ D_c / \mu_c\ A_c$)

T = temperature (^oR)

V = volume (in^3)

x = quality, vapor mass fraction

Greek Symbols

χ_{tt} = Lockhart and Martinelli parameter

δ_x = wall metal thickness (in)

μ = absolute viscosity ($lb_m/in\text{-}sec$)

p = density (lb_m/ft^3)

ϕ_B = empirical correction to the Bartz equation for the RL10 (1.08)

ϕ_{Curv} = correction factor for radius of curvature effect

Subscripts

aw = adiabatic wall

c = bulk coolant

cw = cold-side wall metal

f = film

g = free-stream combustion gas condition

hw = hot-side wall metal

m = metal

r = hot-gas reference condition

sl = saturated liquid

sm = surface of metal

sv = saturated vapor

0 = total or stagnation

References

D1 Bartz, D. R., "Survey of Relationships between Theory and Experiment for Convection Heat Transfer in Rocket Combustion Gases", Advances in Rocket Propulsion, AGARD, Technivision Services, Manchester, England, 1968.

D2 Eckert, E. R. G., and Drake, R. M., "Analysis of Heat and Mass Transfer", McGraw-Hill, 1972.

D3 McBride, B. J., Reno, M. A., and Grodon, S., "CET93 and CETPC: An Interim Updated Version of the NASA Lewis Computer Program for Calculating Complex Chemical Equilibria With Applications", NASA TM-4557, March, 1994.

D4 Owhadi, A., Bell, K. J., and Crain, B., "Forced Convection Boiling Inside Helically-Coiled Tubes", Int'l Journal of Heat and Mass Transfer, Vol. 11, pp. 1779-1793, 1968.

D5 Naraghi, M. H. N., "RTE - A Computer Code for Three-Dimensional Rocket Thermal Evaluation", Prepared for the NASA Lewis Research Center, Grant NAG 3-8892, July 1991.

D6 Moody, L. F., "Friction Factors for Pipe Flow", Transactions of ASME, pp. 671-684, 1944.

D7 Hendricks, R. C., Simoneau, R. J., and Smith, R. V., "Survey of Heat Transfer to Near Critical Fluids", Advances in Cryogenic Engineering, Vol. 15, pp 197-237, Plenum Press, 1970.

D8 Hendricks, R. C., Baron, A., Peller, I., and Pew, K. J., "GASP - A Computer Code for Calculating the Thermodynamic and Transport Properties for Eight Fluids - Helium, Methane, Neon, Nitrogen, Carbon Monoxide, Oxygen, Argon, and Carbon Dioxide", Presented at the XIII Int'l Congress of Refrigeration, NAS/NRC, Washington D.C., 1971.

D9 Quentmeyer, R. J., NYMA Inc., Cleveland, OH, personal communication, August 1994.

D10 Hendricks, R. C., Graham, R. W., and Friedman, R., "Experimental Heat Transfer and Pressure Drop of Liquid Hydrogen Flowing Through a Heated Tube", NASA TN D-765, 1961.

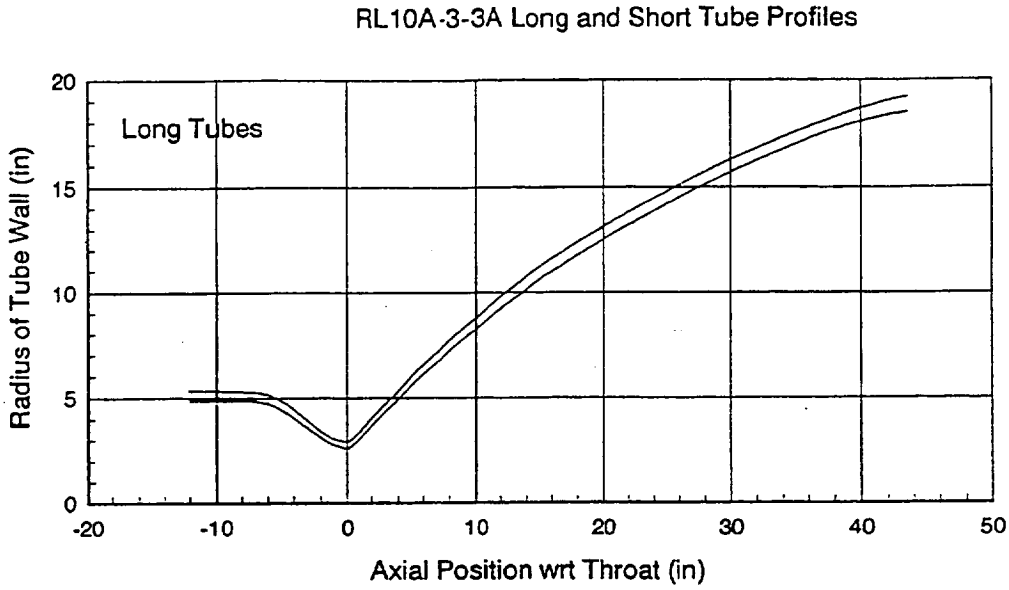
RL10A-3-3A Long and Short Tube Profiles
Long Tubes
Radius of Tube Wall (in)
Axial Position wrt Throat (in)
20
15
10
5
0
-20
-10
0
10
20
30
40
50

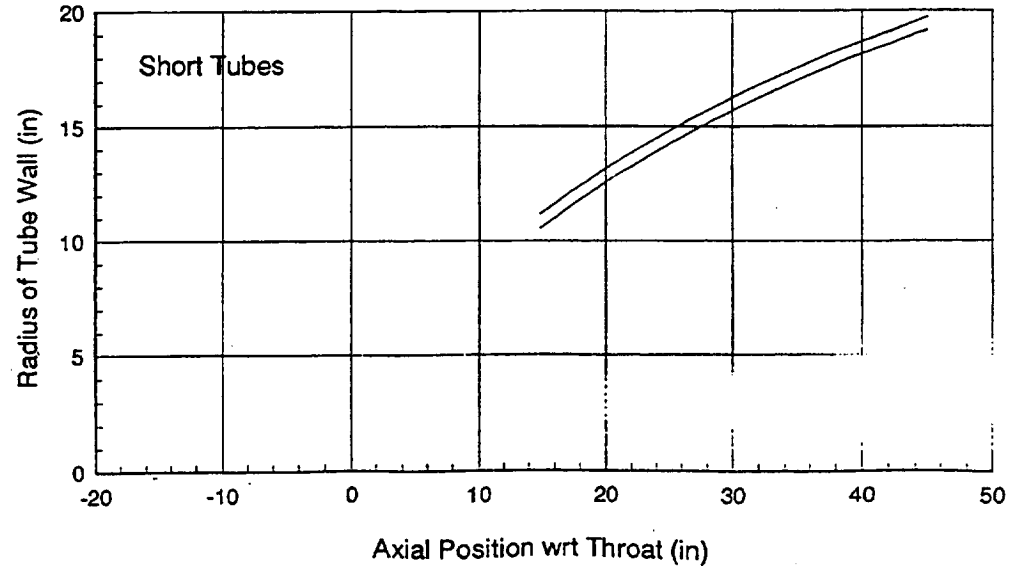
Short Tubes
Radius of Tube Wall (in)
Axial Position wrt Throat (in)
20
15
10
5
0
-20
-10
0
10
20
30
40
50

Figure D1

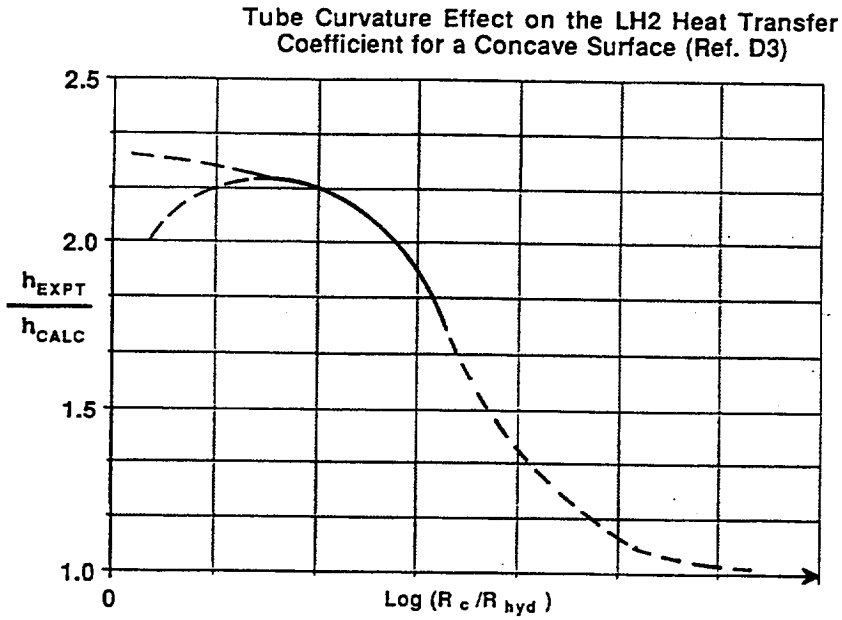

Figure D2

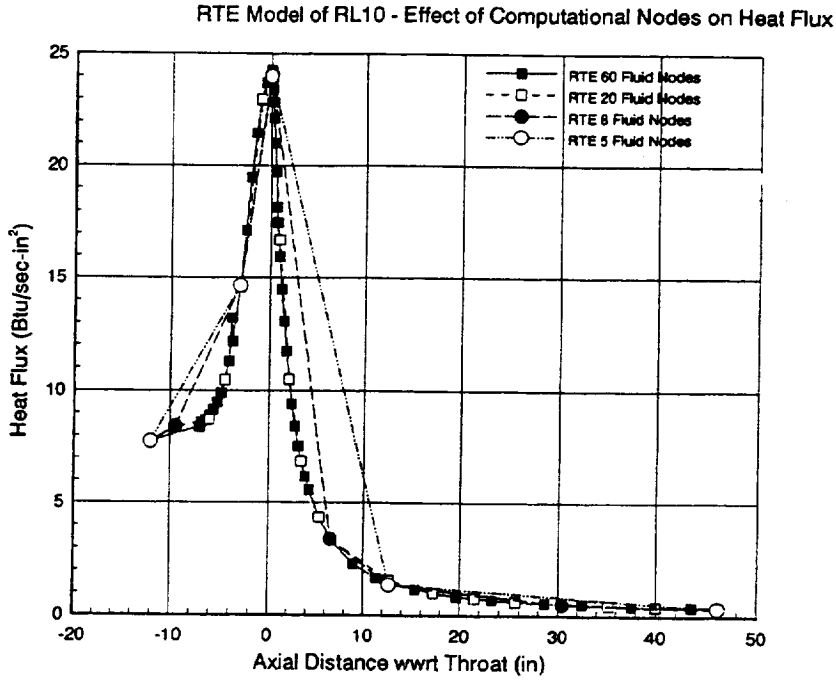

Figure D3

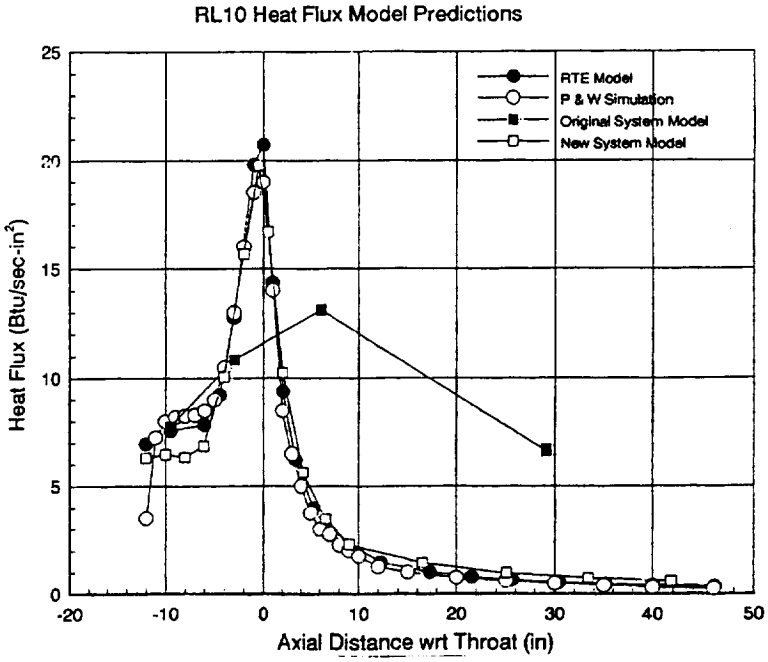

Figure D4

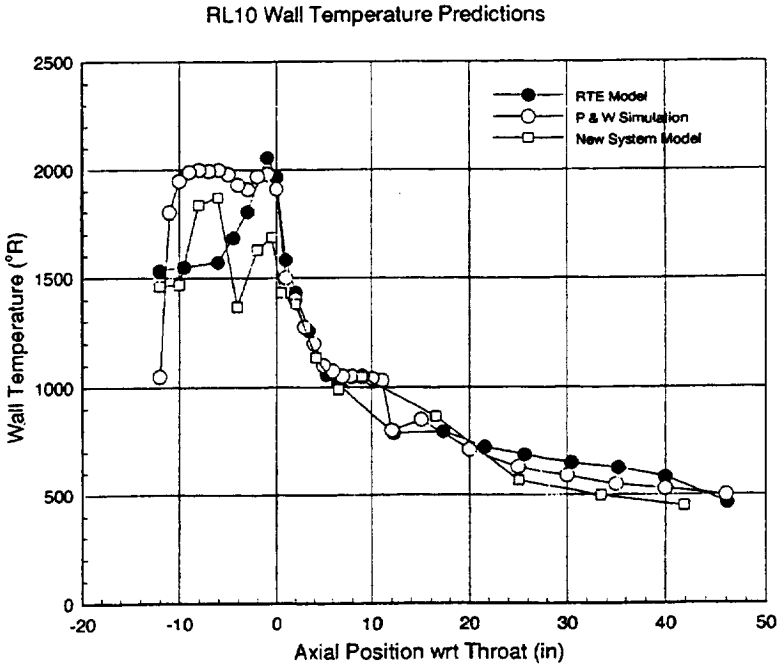

Figure D5

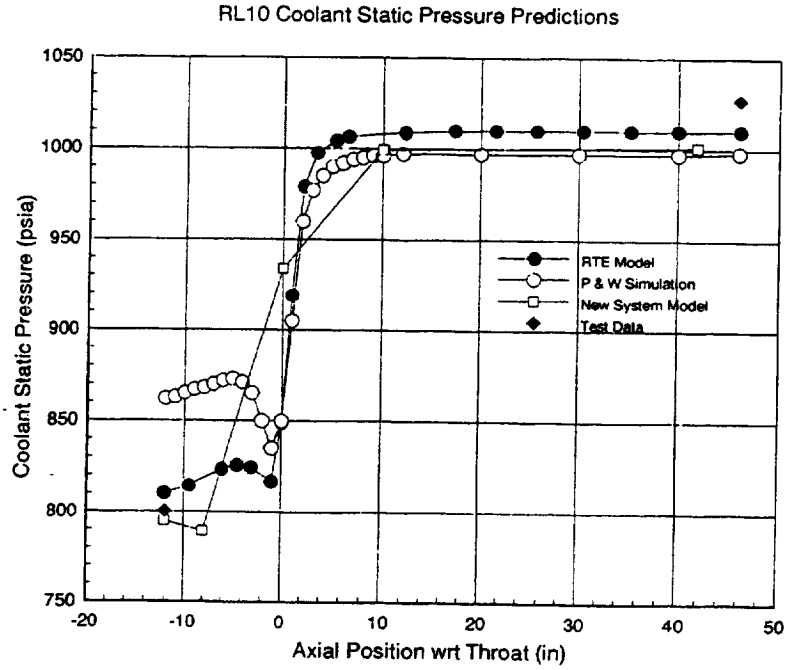

Figure D6

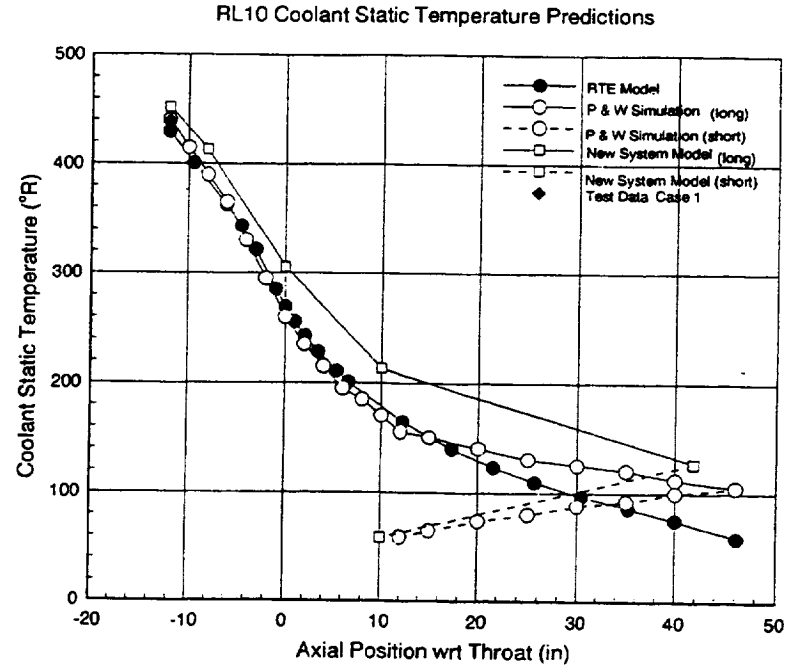

Figure D7

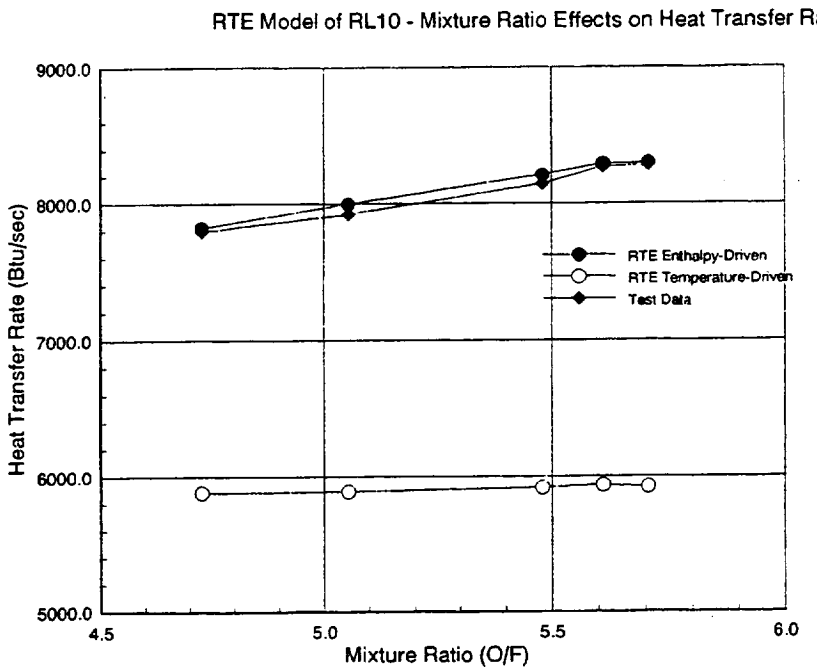

Figure D8

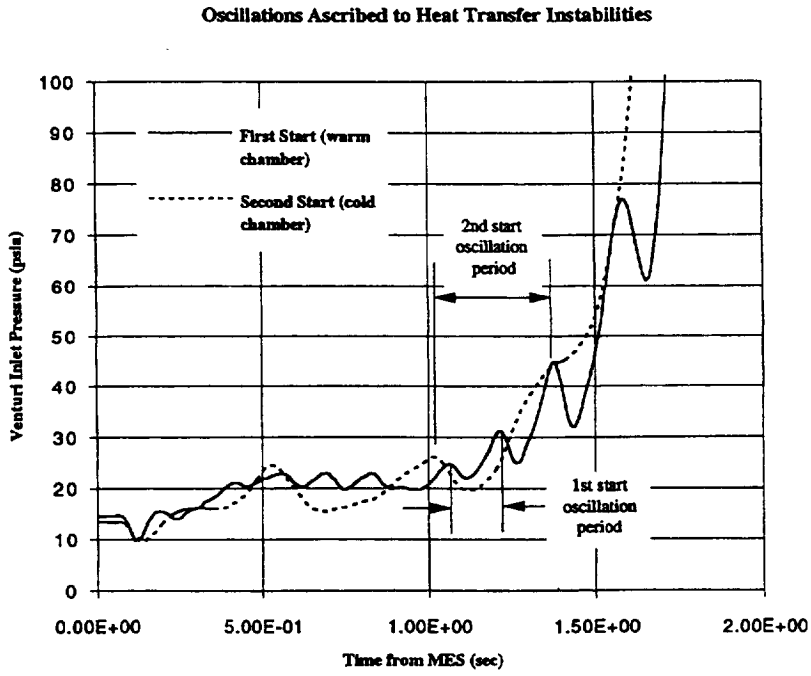

Figure D9

APPENDIX E
Component Modeling of RL10 Injector, Combustion Chamber, and Nozzle

This appendix to the RL10A-3-3A Modeling Project Final Report describes efforts to predict the performance of the RL10 propellant injectors, combustion chamber and nozzle using component analysis programs available to the NASA Lewis Research Center Space Propulsion Technology Division (SPTD). A view of the combustion chamber and nozzle axial profile is shown in Figure E1. Cross-sectional views of the propellant injectors are shown in Figure E2.

E.1 Combustion Gas Property Tables

The CET93 program (Reference E1) was used to calculate properties at each of fourteen axial locations along the chamber and nozzle. These locations correspond to the heat transfer calculation nodes for the regenerative cooling jacket. CET93 is a one-dimensional equilibrium (ODE) program, and includes effects not considered in a chemically 'frozen' expansion. Figure E1 shows the location of the property nodes for the RL10 model; these axial locations and the corresponding expansion ratios are listed in Table E1.

CET93 was used to create tables of static pressure, temperature and Mach Number at each axial node for a wide range of assumed injector-face pressures, mixture ratios (O/F) and propellant inlet mixture enthalpies. Tables for other required properties such as density, enthalpy, Mach Number, thermal conductivity, viscosity were compiled as functions of static pressure, temperature and O/F at any given location. Where necessary, extrapolation and limit-logic has been imposed on the tables to maintain physically realistic results, primarily in cases of extreme condensation within the engine exhaust gases (low temperature, large expansion ratio, etc.).

These property tables have been encoded for use with the ROCETS simulation software and are archived in the THERM3 library.

E.2 Nozzle Performance Analysis.

Nozzle performance is represented in the system model by maps of characteristic velocity, specific impulse, and discharge coefficient. Various analytic codes were used to predict these parameters for the RL10 design. Consider the tables of ideal characteristic velocity (c_{ideal}^*) as predicted by CET93. The ideal and actual characteristic velocities are related by the c*-efficiency (η_{c^*}).

$$c^* = c_{ideal}^* \bullet \eta_{c^*}$$

Figure E3 shows a comparison of the ODE predictions with values specified by Pratt & Whitney for liquid-liquid injection. The points on the CET93 tables fall right on top of the suggested curves from Pratt & Whitney. For gaseous fuel injected with liquid oxidizer, the points from CET93 match the P&W curves for O/F values greater than 3, as shown in Figure E4; below that, there is a small deviation. The RL10 start and shutdown transients are typically LOX-rich and only operate below an O/F of 4 for a short interval. The Pratt & Whitney curves are more computationally efficient than the CET93 output tables because they use a correction for fuel enthalpy rather than making enthalpy a third input variable in the c_{ideal}^* property table. The Pratt & Whitney curves also provide greater resolution with respect to variations in mixture ratio, having many more O/F data points than the tables generated using CET93. Since the c* data provided by Pratt & Whitney were verified using the ODE analysis, it was decided to continue using the provided c_{ideal}^* curves in the new system model. Efforts to predict the c*-efficiency are discussed in the section E.3 below.

CET93 was also used to predict the ideal specific impulse $(I_{sp})_{ideal}$ for the RL10 engine. Specific impulse is used to predict engine thrust and overall efficiency. Rocket engine nozzle flows

typically involve significant losses due to two-dimensional, boundary layer, finite-rate chemistry effects which are not included in ODE calculations as described above. These effects can be estimated with tools which have been used extensively by engineers over the past thirty years. The TDK (two-dimensional kinematics) program (Reference E2) used on the RL10 project is a standard and well-accepted tool for making such predictions. The actual specific impulse is related to the ideal specific impulse by the expression

$$(Isp)_{TDK} = (I_{sp})_{ideal} * \eta_{Cf} * \eta_{c*}$$

A table of thrust-coefficient efficiency (η_{Cf}) was generated for the RL10A-3-3A based on TDK output, and is shown in Table E3 and Figure E7.

Figure E8 shows a comparison of the predicted actual Isp (as calculated using the expression above) with the values specified by Pratt & Whitney. The figure portrays the variation in Isp as functions of O/F at different Pc values. As can be seen in the figure, the predicted and suggested values match well, especially at pressures and mixture ratios near the RL10 engine's normal operating condition (O/F = 5., Pc=475.). The predicted and suggested curves diverge from each other at high and low mixture ratios, and there is a general disagreement between the two data sets at very low pressures. The Isp data set provided by Pratt & Whitney combines a table of ideal vacuum Isp with simple empirical corrections for non-ideal effects. Although the range of pressure and mixture-ratio provided suggests that the tables can be used at very low pressures, the applicable range of O/F is not clear. At very low pressures and very high mixture ratios, the suggested empirical corrections may, in fact, predict negative Isp values (which is not reasonable). After considering these issues, it was decided to use the η_{Cf} tables predicted by TDK and the $(I_{sp})_{ideal}$ tables predicted by CET93 in the new system model.

Other analyses were done to estimate the nozzle discharge coefficient (C_d). A Navier-Stokes analysis (Reference E3) was used to predict C_d at the engine's design conditions (Figure E5). From this analysis, the effective discharge coefficient of the nozzle was estimated to be 0.976. Another analysis was performed using a simple one-dimensional nozzle flow model and trimming the assumed C_d to match chamber pressure; this analysis gave 0.975. The TDK program was also used to predict C_d at off-design conditions, scaled to match the Navier-Stokes prediction at the design point. The off-design C_d values are shown in Table E2 and Figure E6. Variations in C_d with Pc and O/F can be attributed to finite-rate kinetics and viscous effects. In this case, however, we were unable to adequately explain some of the dramatic C_d variations predicted by TDK (at mixture ratios of 4 and 20, for example). The RL10A-3-3A has a silver throat insert that creates a sharp edge, not typically used and difficult for TDK to model. Although preliminary engine simulations using the variable nozzle C_d predictions showed virtually no differences with simulations using constant C_d, it was ultimately decided not to include the variable C_d tables in the new engine system model. A constant C_d value of 0.975 is used instead.

E.3 Combustion/Injector Performance Analysis

ODE and TDK can be used to predict the performance of the chamber and nozzle given ideal conditions at the injector. In reality, there are certain inefficiencies associated with the injector that will significantly effect the overall performance of the engine. The ROCCID program (Reference E4) was used to predict these effects, which are represented by η_{c*} (c-star efficiency) for use in the engine simulation. ROCCID also predicts the distribution of propellant mixture ratio across the chamber cross-section and the axial burning efficiency as well.

The RL10A-3-3A injector (see Figure E2) is rather complicated, involving several different injector

element designs. Most of the injector elements are co-axial, the hydrogen in injected through annular orifices around each LOX element. The outer concentric row of elements, however, inject hydrogen only (which will affect wall cooling). It is possible that some of the error encountered in the heat transfer model (Appendix D) is due to not including this film cooling effect in those predictions. Except for the inner row, all of the coaxial elements have LOX flow swirlers. The faceplate of the injector is transpiration cooled by a small flow of hydrogen through a rigimesh material.

Not all of the features in the RL10A-3-3A injector design could be modeled in the ROCCID. ROCCID models LOX swirling elements but assumes that the swirl is produced by injecting the LOX tangentially through orifices. This is a more contemporary design than the ribbon-swirler elements actually used in the RL10A-3-3A. It was necessary, therefor, to consider the geometry of the ribbon swirlers and estimate an equivalent configuration for tangential flow injection. The derivation of this estimate is shown in Figure E9. The estimates for orifice size had to be modified subsequently to better match the overall pressure drop measured across the LOX elements. ROCCID also required some estimates of empirical factors and other equivalent design parameters not known for the RL10. The faceplate transpiration cooling flow was not modeled for the RL10 and the inner row of injector elements was considered identical to the other coaxial elements (i.e. with LOX swirler elements).

Figure E10 shows the ROCCID predictions of overall η_{c*} in the chamber as a function of mixture ratio and chamber pressure; the propellant inlet temperature assumed for the prediction is 300 R. The figure also shows the values of η_{c*} specified by Pratt & Whitney for the RL10A-3-3A, which are presumed to be the results of test data. Comparison of the ROCCID predictions with the Pratt & Whitney data shows significant differences. ROCCID predicts that the variation of η_{c*} with pressure will not be the same for all mixture ratios as is suggested by the Pratt & Whitney's curves. The ROCCID analyses also indicate that there will be an appreciable variation in the c*-efficiency with inlet fuel temperature, as illustrated in Figure E11.

Significant uncertainty exists regarding the reliability of both the Pratt & Whitney data and the ROCCID predictions. It should also be noted that the entire range of variation in η_{c*} is only about 4 to 8%; the differences between the predicted and P&W data may not be significantly larger than the measurement accuracy of the test data or the numerical tolerance for the model. Neither η_{c*} map is considered an adequate representation of the combustion performance for start transient simulations. The suggested performance curves from Pratt & Whitney lack any considerations for variation in fuel temperature, which is known to have a significant performance impact. On the other hand, model geometry alterations and persistent stability problems have adversely affect the credibility of the ROCCID predictions. The decision was made to retain the η_{c*} tables provided by Pratt & Whitney in the new RL10 system model.

E.4 Summary

The analyses performed for the RL10A-3-3A combustion chamber and nozzle have been useful in providing insight into the behavior of these components. These modeling activities have also been useful in examining the application of various tools to existing rocket engine designs such as the RL10. Unfortunately, several of the analyses results did not verify the performance data provided to us by Pratt & Whitney. Given the tight schedule imposed on these modeling attempts, it was not possible to make full use of the comparisons to modify the models or suggest more detailed investigations. Under these circumstances, it was decided that only the more detailed gas property and predicted specific impulse tables should be incorporated into the new system model. The Navier-Stokes analysis of the nozzle throat also provided an excellent verification of the discharge coefficient inferred from RL10A-3-3A test data.

References

E1. McBride,B. and Gordon,S. *CET93 and CETPC: An Interim Updated Version of the NASA Lewis Computer Program for Calculating Complex Chemical Equilibria with Applications* , NASA TM-4557, March 1994.

E2. Nickerson,G., *Two-Dimensional Kinetics (TDK) Nozzle Performance Computer Program - Users Manual,* (NASA Contract NAS8-39048), March 1993.

E3. Kacynski, K., *Calculation of Propulsive Nozzle Flowfield in Multidiffusing, Chemicallyreacting Environments*, NASA TM 106532, 1994.

E4. Muss, J. and Nguyen,T., *User's Manual for Rocket Combustor Interactive Design (ROCCID) and Analysis Computer Program*, NASA CR-1087109, May 1991.

Table E1
Hot-Gas Property Node
Axial Locations and Expansion Ratios for
NASA LeRC Model of RL10A-3-3A

Axial Location (inches wrt throat)	Expansion Ratios (wrt throat)
-0.500	1.11 subsonic
0.485	1.29 supersonic
-2.018	1.62 subsonic
2.035	2.35 supersonic
-4.054	2.72 subsonic
-6.068	3.65 subsonic
-8.032	4.00 subsonic
-10.00	4.14 subsonic
-12.00	4.27 subsonic
4.215	4.29 supersonic
6.588	6.93 supersonic
8.989	9.95 supersonic
16.54	20.7 supersonic
25.05	33.2 supersonic
33.41	45.0 supersonic
41.84	56.1 supersonic

Table E2
TDK Predicted Discharge Coefficients for
RL10A-3-3A Nozzle

	Pc=5 psia	Pc=50 psia	Pc=150 psia	Pc=500
O/F=1	0.973	0.975	0.975	0.976
O/F=4	1.011	0.988	0.971	0.977
O/F=6	1.008	0.983	0.976	0.975
O/F=8	1.005	0.981	0.975	0.974
O/F=10	1.005	0.981	0.975	0.974
O/F=20	1.016	0.987	0.989	0.975
O/F=50	0.979	0.978	0.978	0.977

Table E3
TDK / ODE Predicted Thrust-Coefficient Efficiency
(η_{Cf}) for the RL10A-3-3A Nozzle

	Pc=5 psia	Pc=50 psia	Pc=150 psia	Pc=500 psia
O/F=1	0.9381	0.9534	0.9567	0.9593
O/F=4	0.8860	0.9269	0.9419	0.9517
O/F=6	0.8508	0.9024	0.9282	0.9469
O/F=8	0.8463	0.8950	0.9193	0.9414
O/F=10	0.8507	0.8978	0.9214	0.9419
O/F=20	0.8853	0.9226	0.9374	0.9486
O/F=50	0.9568	0.9537	0.9568	0.9596

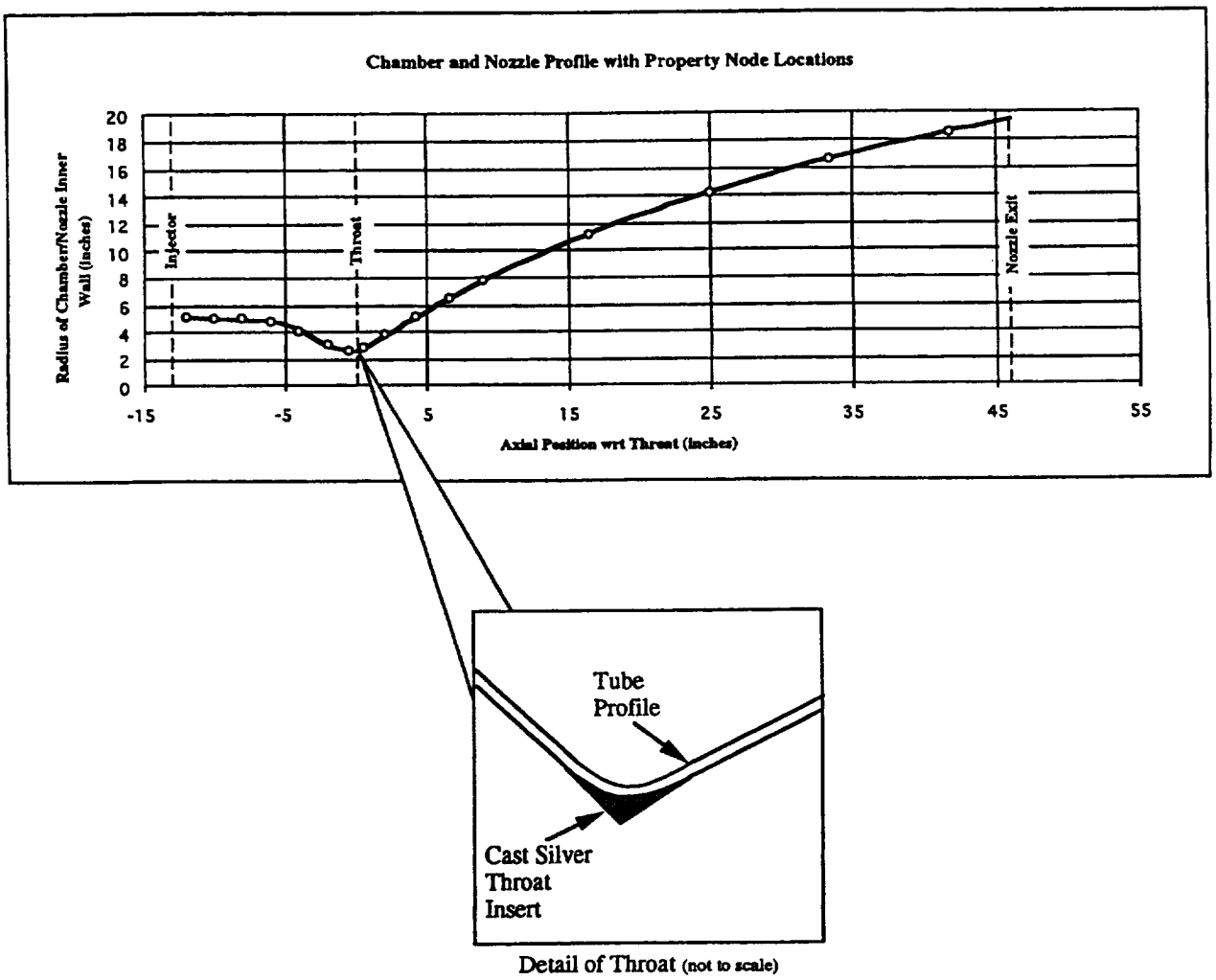
Chamber and Nozzle Profile with Property Node Locations
Radius of Chamber/Nozzle Inner Wall (inches)
20
18
16
14
12
10
8
6
4
2
0
Injector
Throat
Nozzle Exit
-15
-5
5
15
25
35
45
55
Axial Position wrt Throat (inches)
Tube Profile
Cast Silver Throat Insert
Detail of Throat (not to scale)

Figure E1

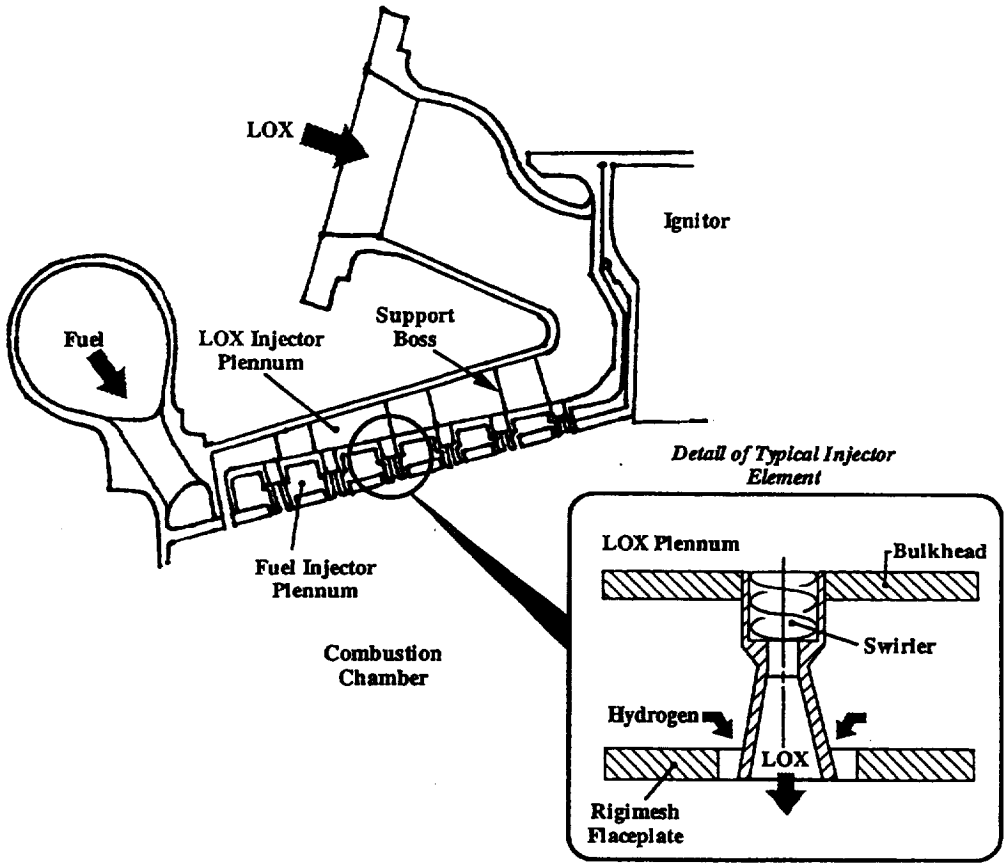
LOX
Ignitor
Fuel
LOX Injector Plennum
Support Boss
Detail of Typical Injector Element
LOX Plennum
Bulkhead
Fuel Injector Plennum
Swirler
Combustion Chamber
Hydrogen
LOX
Rigimesh Flaceplate

Figure E2

Predicted and Suggested c* Maps for Liquid-Liquid Injection

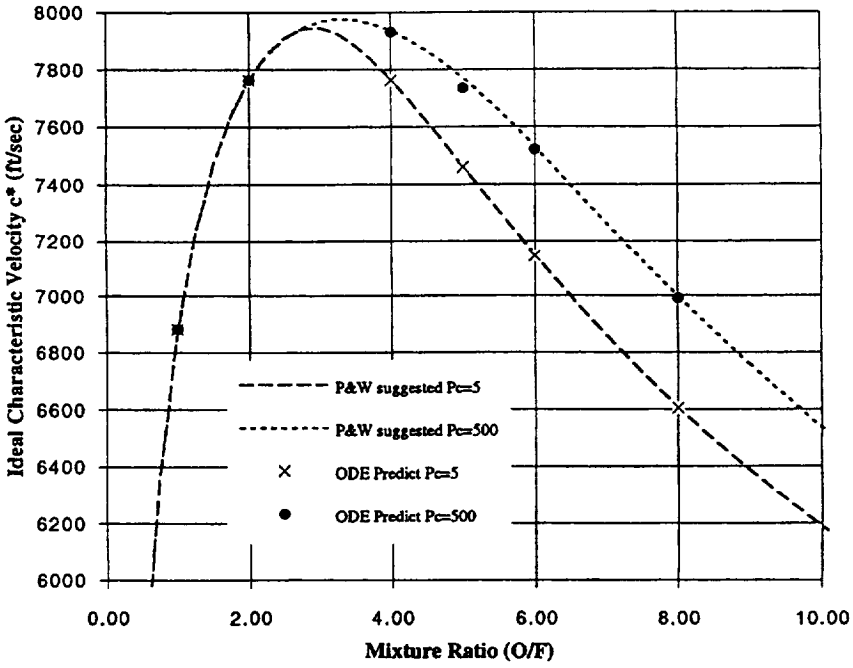

Figure E3

Predicted and Suggested c* Maps for Gas-Liquid Injection

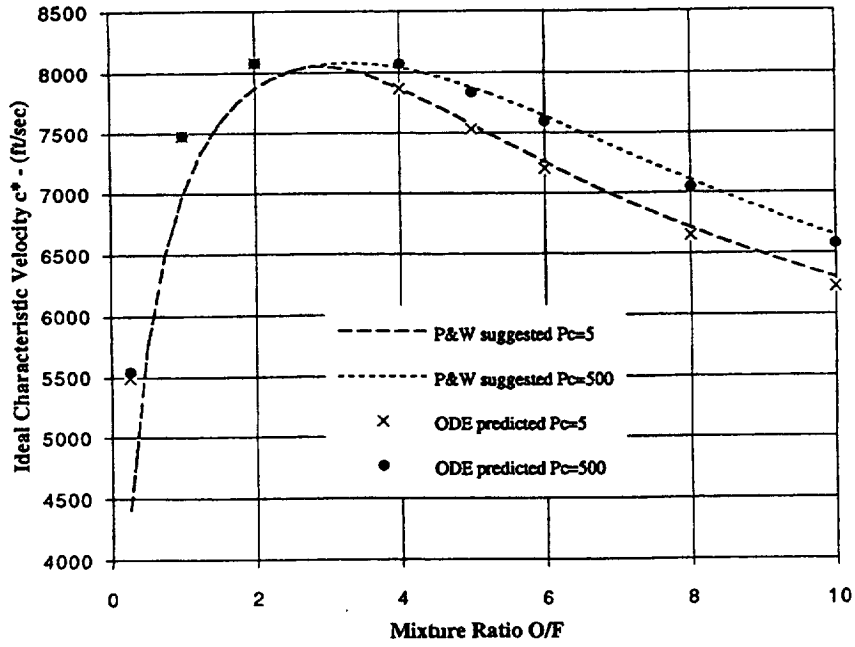

Figure E4

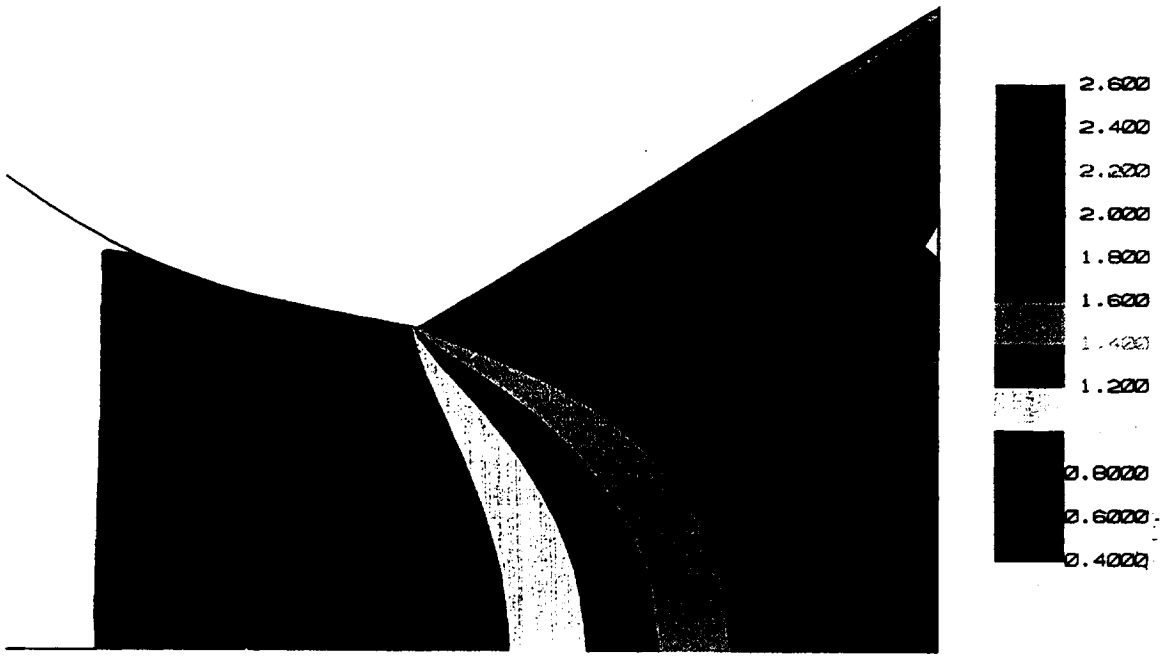

Figure E5

TDK Predicted Discharge Coefficient for RL10A-3-3A Nozzle
as a function of Pc and O/F

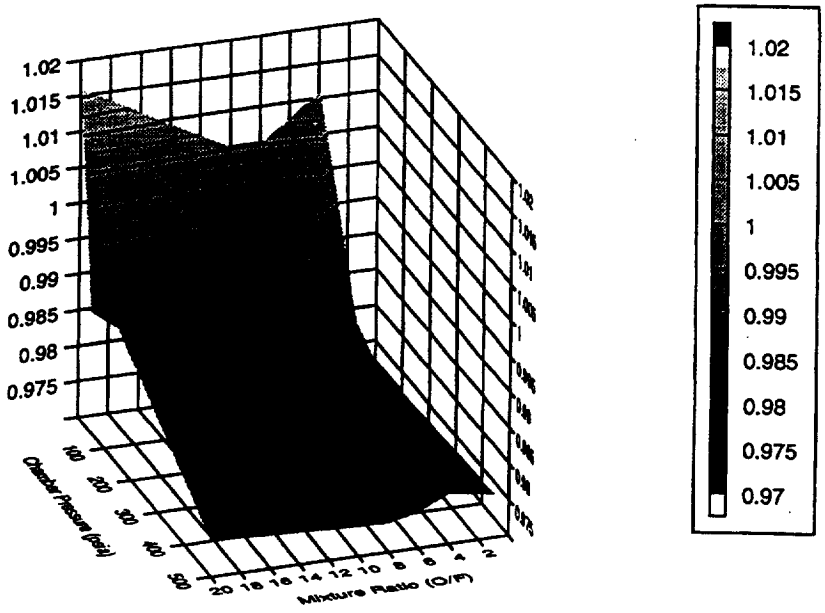

Figure E6

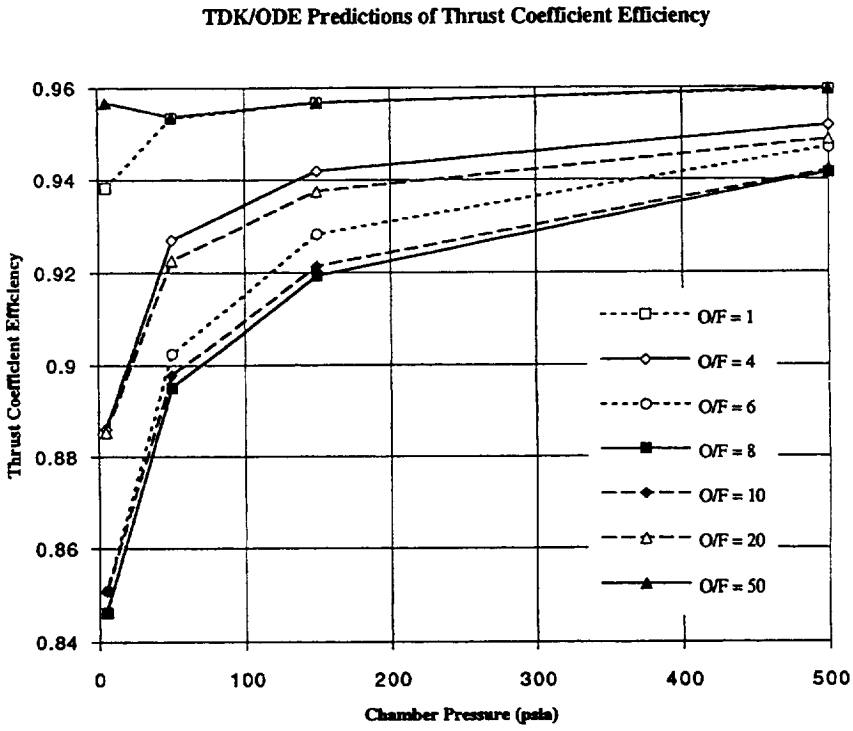

Figure E7

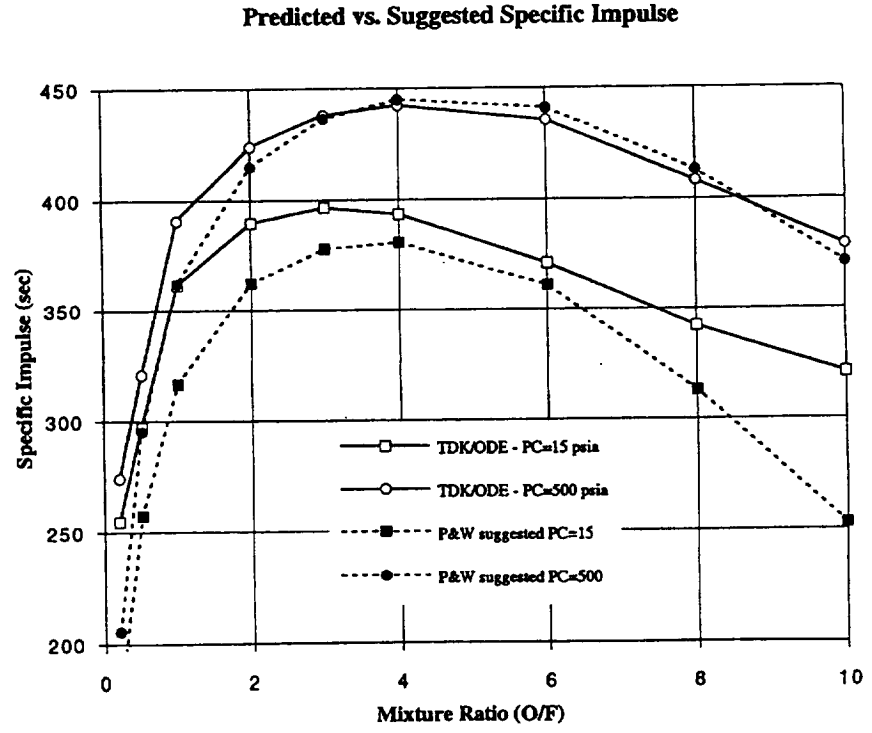

Figure E8

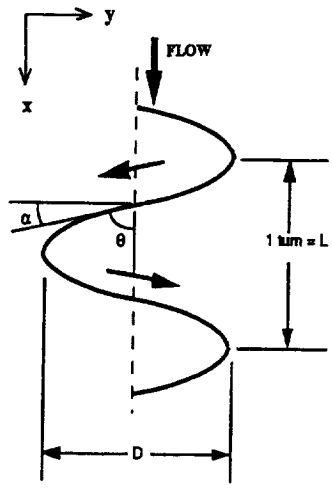

Ribbon Swirler
(side view)

$$y = \frac{D}{2}\cos\left(\frac{2\pi x}{L}\right)$$

$$\frac{dy}{dx} = -\frac{\pi D}{L}\sin\left(\frac{2\pi x}{L}\right)$$

$$\tan\theta = \left(-\frac{dy}{dx}\right)_{\text{pt. A}} = \frac{\pi D}{L} = \frac{\pi(0.103)}{(0.167)} = 1.938$$

$$\theta = \tan^{-1}(1.938) = 62.7°$$

$$\alpha = 90° - \theta = 27.3°$$

Given this geometric information, we can determine the tangential velocity of fluid around the perimeter of the swirler element. Given that velocity, we can determine the total size of orifices that would produce the desired velocity. Consider the three orifice configuration shown below.

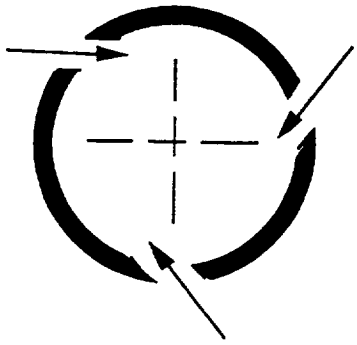

Tangential Inflow Swirler
(view along element axis)

$$V_{\text{tangential}} = \frac{V_{\text{axial}}}{\tan\alpha} = \frac{(dm/dt)}{\rho\left(\frac{\pi D^2}{4}\right)\tan\alpha}$$

$$A_{\text{total}} = \frac{(dm/dt)}{\rho V_{\text{tangential}}} \quad \text{is the total orifice area}$$

$$A_{\text{total}} = \frac{(dm/dt)}{\rho\left[\frac{(dm/dt)}{\rho\left(\frac{\pi D^2}{4}\right)\tan\alpha}\right]} = \left(\frac{\pi D^2}{4}\right)\tan\alpha$$

$$A_{\text{per orifice}} = \frac{A_{\text{total}}}{3} = \frac{1}{3}\left(\frac{\pi(0.103)^2}{4}\right) = 0.001434\ \text{in}^2$$

We have chosen 3 orifices here but other values could be chosen. The number of orifices could be chosen, for example, to better match the overall resistance of the actual ribbon-swirler LOX injectors.

Figure E9

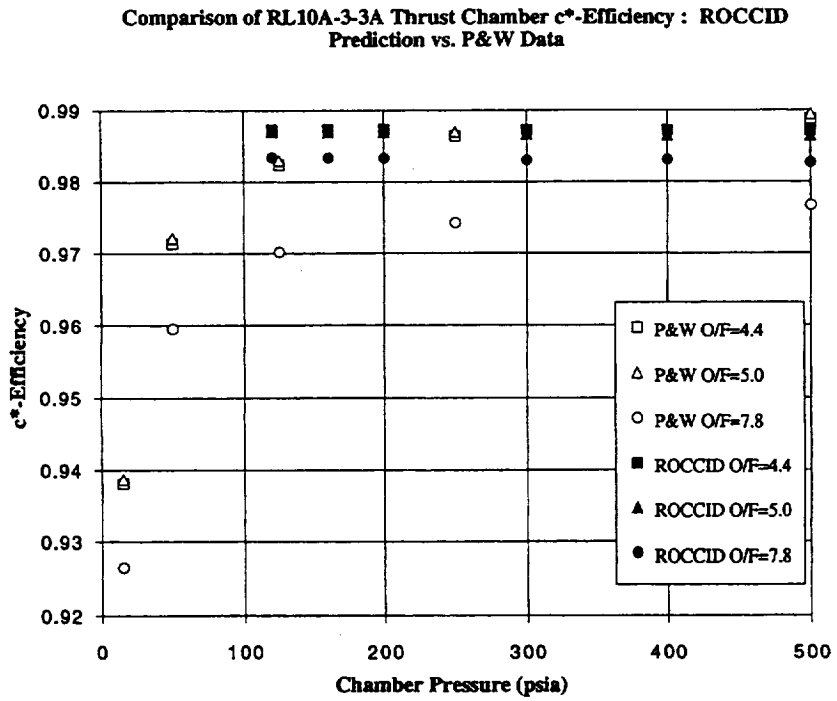

Figure E10

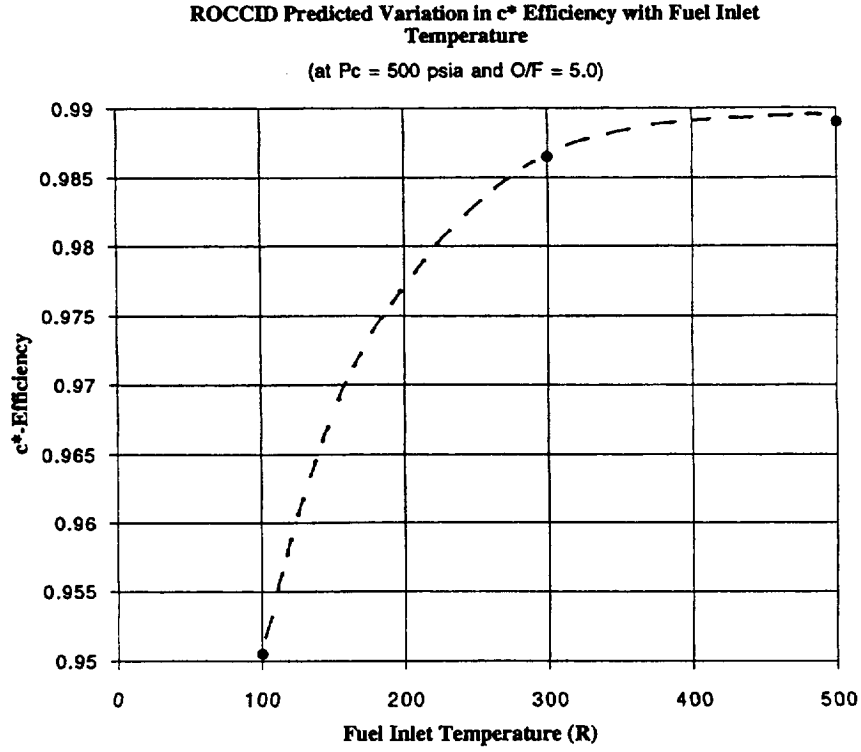

Figure E11

APPENDIX F
Component Modeling of RL10 Injector Heat Transfer

This appendix to the RL10A-3-3A Modeling Project Final Report describes efforts to estimate the heat transfer between the warm hydrogen and cold LOX in the RL10 injector plenum. A cross-sectional view of the injector plenum is shown in Figure F1. The effect being modeled here was noted in Reference F1, but has never been measured specifically. It has been found that the inclusion of this heat transfer appears to be important in predicting the initial conditions of the engine at start. At full-power, the engine operation is not significantly affected by this phenomenon.

F.1 Description of the model.

The model of the RL10 injector heat transfer was created without the use of any detailed analysis programs. The analysis is based on a lumped volume approach where the spatial and temporal variations have been ignored, substituting averaged properties where necessary. The model of the heat transfer itself in also quasi-static, the heat capacity of the metal has been ignored. The enthalpy and density dynamics of the propellants have been included (since these effects are handled by dynamic modules elsewhere in the engine model). The heat transfer correlations used are based on simple semi-empirical relationships for in References F2 and F3.

A schematic of the model is shown in Figure F2. The basic components of heat transfer are 1) the heat flux across the walls of the LOX injector elements and 2) the heat flux across the bulkhead which separates the LOX and hydrogen plenums. Heat transfer from the main chamber into the hydrogen plenum is ignored.

F.2 Heat Transfer across walls of LOX injector elements

The first component of heat transfer, that across the walls of the LOX injector elements, is governed by three relationships. Although not all of the elements are identical, an average geometry was used for these calculations, as shown in Figure F2. The heat transfer from the hydrogen to the walls of the LOX elements is based on correlations derived for heat exchangers where the fluid flows transversely over a group of pipes. Reference F2 defines this relationship as

$$h_{fl} = \frac{0.025}{(4.3\text{x}10^{4})_{*}} \frac{(0.735 + .000576T_{fuel})}{(O.D._{tube}/\ 12_{*})^{0.42}} \left(v_{fuel}\rho_{fuel}(5.184\text{x}10^{5})_{*}\right)^{0.58}$$

where the asterisks denote constants added for units conversions

A second source, Reference F3 gives a different relationship that appears to be more theoretically based:

$$h_{fl} = \frac{0.24\ k_{fuel}}{O.D._{tube}} \left(\frac{O.D._{tube}\rho_{fuel}v_{fuel}}{\mu_{fuel}}\right)^{0.6}$$

It was found that the two expressions given above predict similar heat transfer coefficient values for the fuel side. The second expression is actually used in the new system model.

Heat transfer from the walls of the injector elements to the LOX flowing through them is described by the Colburn correlation as cited in Reference F2 :

$$h_{o1} = 0.023 \frac{k_{lox}}{(I.D._{tube})^{0.2}} (v_{lox}\rho_{lox})^{0.8} \left(\frac{(c_p)_{lox}}{\mu_{lox}} \right)^{0.4}$$

The heat transfer across the metal of the LOX elements is described by the basic conduction equation for a solid:

$$h_{m1} = \frac{k_{post-metal}}{t_{post-wall}}$$

The flow velocity of the hydrogen across the LOX injector elements is based on the average flow area of the fuel plenum and half the inlet flow (since the amount of hydrogen flowing over the elements is steadily decreasing as it is injected into the chamber). The LOX flow area, the surface area of the elements, and the metal thickness of the elements are all based on simple averaging of the actual geometry obtained from blue-prints.

Assuming the heat flux is the same on the hydrogen and oxygen sides (a quasi-static approximation), the overall heat transfer coefficient will be :

$$h_1 = \left[\frac{1}{h_{f1}} + \frac{1}{h_{o1}} + \frac{1}{h_{m1}} \right]^{-1}$$

$$\dot{q}_{element} = h_1 A_1 (T_{fuel} - T_{LOX})$$

$$\dot{q}_1 = 162 * \dot{q}_{element}$$

where 162 is the total number of coaxial elements and A_1 is the surface area of the injector element, taken at the mid-point between inner and outer diameters.

F.3 Heat Transfer across plenum bulkhead

The second component of heat transfer is across the wall separating the hydrogen from oxygen. Reference F2 gives the heat transfer for parallel flows over a flat plate as

$$h = \left(\frac{0.055\, k}{L_{plate}} \right) * \left(\frac{L_{plate} v\, \rho}{\mu} \right)^{0.75}$$

This expression for the heat transfer coefficient is used on both the fuel and oxidizer sides of the bulkhead.

$$h_{f2} = \left(\frac{0.055\, k_{fuel}}{L_{plate}} \right) * \left(\frac{L_{plate} v_{fuel}\, \rho_{fuel}}{\mu_{fuel}} \right)^{0.75}$$

$$h_{o2} = \left(\frac{0.055\, k_{lox}}{L_{plate}} \right) * \left(\frac{L_{plate} v_{lox}\, \rho_{lox}}{\mu_{lox}} \right)^{0.75}$$

In this case, the flowpath length along the plate is taken to be half the radius of the injector bulkhead (L_{plate} = 1.947 inches). Half the radius is used to account for the fact that fuel and LOX

flow are both bled off by the infector orifices as the flows pass over the plate.

The basic expression for metal conduction as shown in the previous section is used again here.

$$h_{m2} = \frac{k_{\text{plate metal}}}{t_{\text{plate}}}$$

The fluid velocities for both propellants are based on the average flow areas in the plenums and half the inlet flows (assuming uniform rate of injection into the chamber). All areas are inferred from blueprints. Once again the heat flux is considered uniform across the wall and so

$$h_2 = \left[\frac{1}{h_{f2}} + \frac{1}{h_{o2}} + \frac{1}{h_{m2}}\right]^{-1}$$

$$\dot{q}_2 = h_2 A_{\text{plate}} (T_{\text{fuel}} - T_{\text{LOX}})$$

The total heat transfer rate from hydrogen to oxygen is therefore

$$\dot{q}_{\text{total}} = \dot{q}_1 + \dot{q}_2$$

F.4 Results of the Model

The equations described above were included in the RLOINJHX subroutine. Based on these correlations, the six parameters that we might expect to affect the injector heat transfer are the fuel and oxidizer flowrates, the fuel and oxidizer temperatures, and the fuel and oxidizer pressures. The relative contributions of the two components of heat transfer (injector elements and bulkhead) will vary as well.

Figure F3 shows the combined heat transfer coefficients (for injector elements and bulkhead separately) as functions of time during start. Figure F4 shows the total plenum heat transfer rate during start. At the beginning of the start transient, it is assumed that the injector metal is in thermal equilibrium with the LOX and the hydrogen shut-off valve is closed (only a small leakage fuel flow). The result is that there is no heat transfer to the LOX at first. Any heat flux due to fuel leakage past the FSOV or to the ambient conditions is considered negligible. As the FSOV opens, the hydrogen flow begins, and the heat transfer rate jumps to about 10 BTU/sec. It had been found previously that without any heat transfer included, the LOX injector pressure is considerably lower than test data during start. The addition of heat to the oxidizer elevates the injector pressure early in the engine start process (see Figure F5). As the engine begins to accelerate, the injector heat transfer reaches a peak of about 85 BTU/sec, presumably due to the transient peak in fuel temperature. The heat transfer ultimately settles to a steady-state value of around 45 BTU/sec. The injector heat transfer can apparently have a significant effect on the engine time-to-accelerate; the added heat actually delays the bootstrap by approximately 100 msec (Figure F6). The additional heat does not appear to soften the priming of the LOX injector plenum, however. After the engine bootstraps, the injector heat transfer no longer makes a significant difference in the engine cycle balance.

Although this model is very simple and involves several assumptions, it appears to provide an adequate approximation for the RL10 start transient simulation. Insufficient test data existsto determine the actual heat transfer rates. This module is included in the new system models for both start and shutdown.

References

F1. Wanhainen, R., *Throttling Characteristics of a Hydrogen-Oxygen, Regeneratively Cooled, Pump-Fed Rocket Engine*, NASA TM X-1043, December 1964.

F2. Brown,A. and Marco,S., *Introduction to Heat Transfer*, McGraw Hill, New York 1951.

F3. Faires,V., *Applied Thermodynamics*, MacMillan Company, New York 1947.

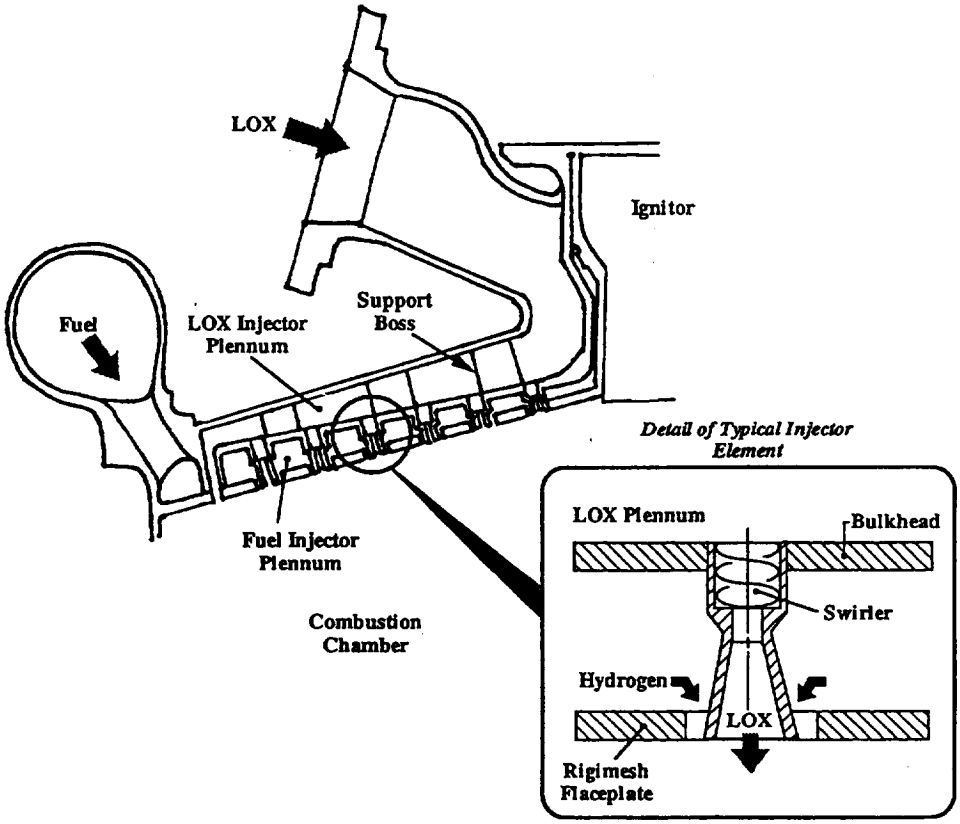

Figure F1

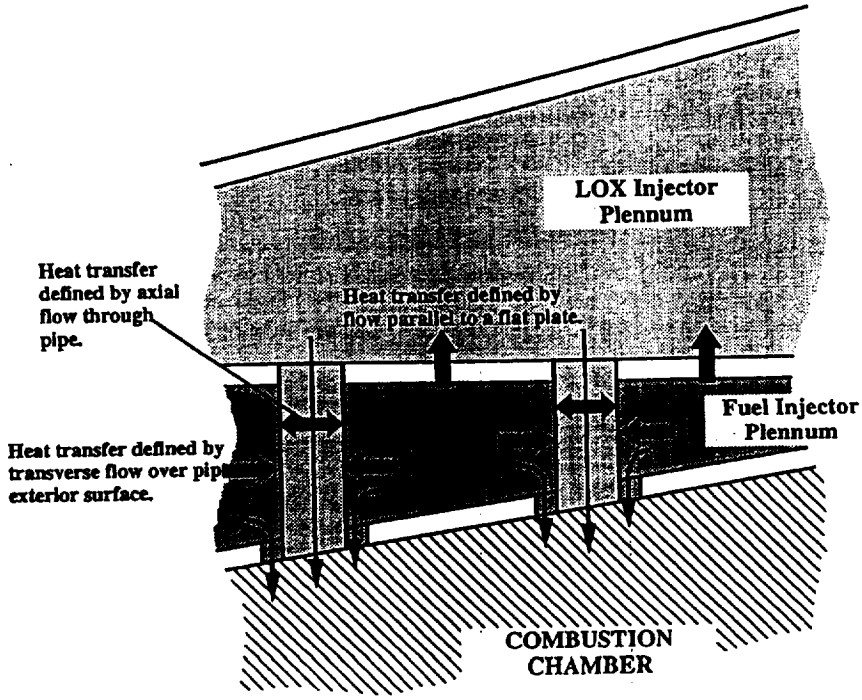

Figure F2

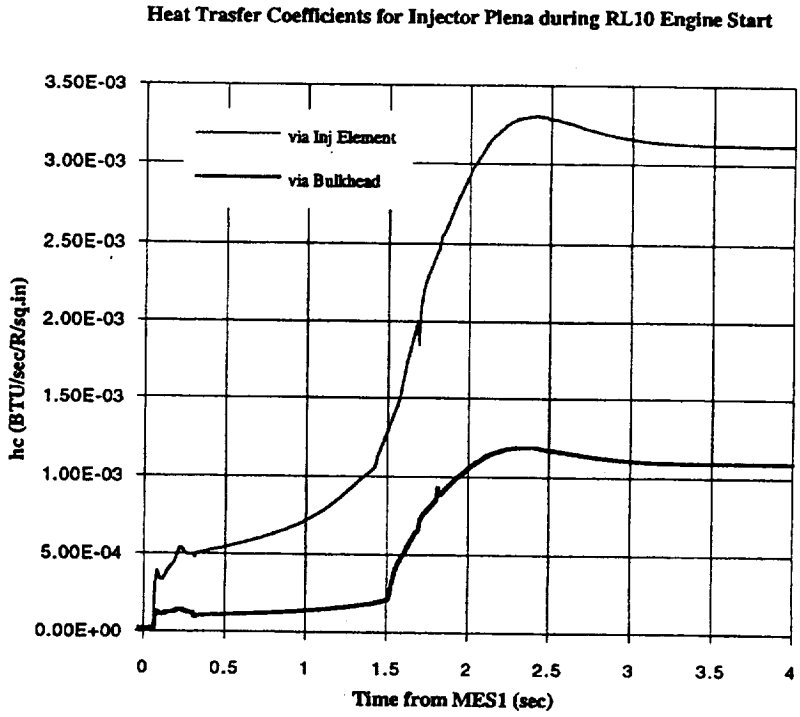

Figure F3

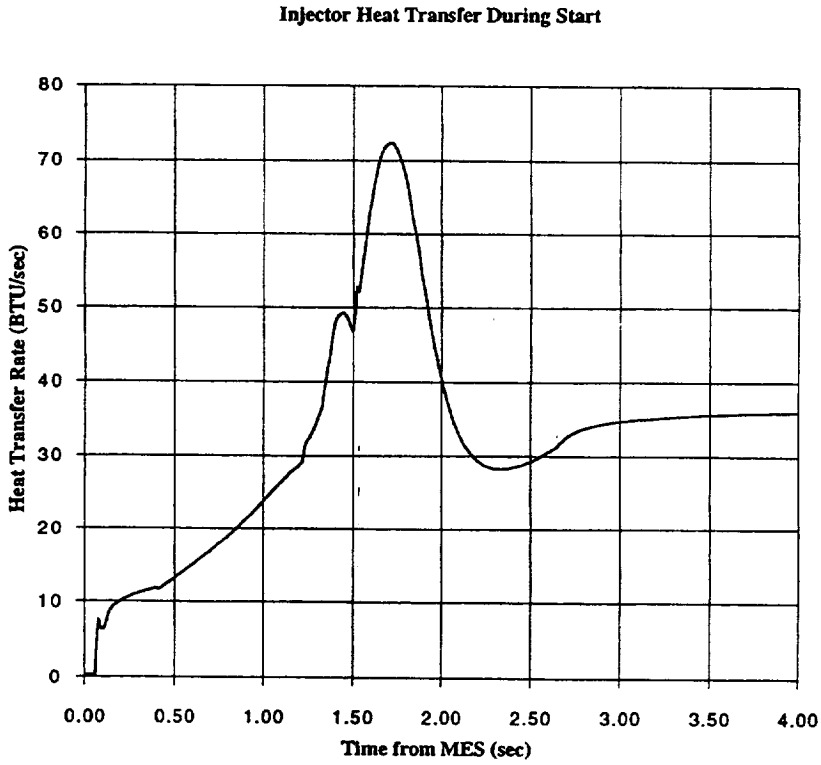

Figure F4

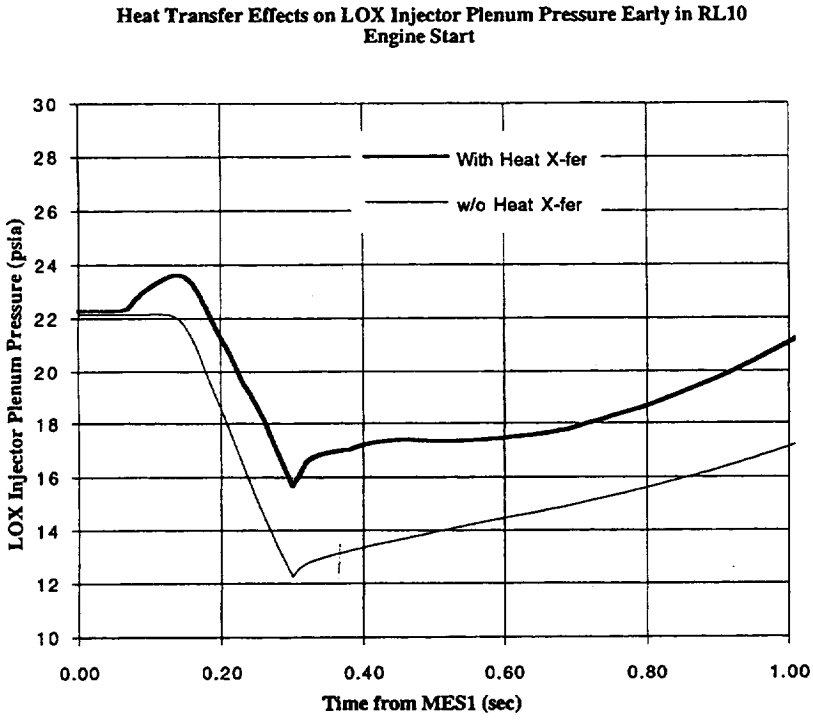

Figure F5

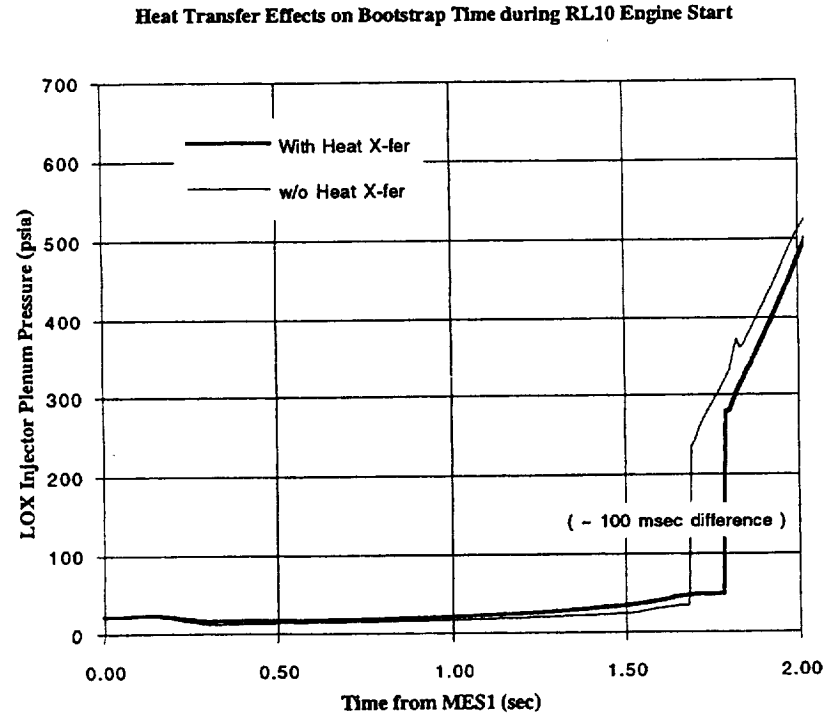

Figure F6

APPENDIX G
Component Modeling of RL10 Duct Flow

Duct or manifold flow-resistence is typically established by test. Pratt & Whitney provided us with flow-resistences based on such tests for the RL10 engine. The resistence values specified were typically 'lumped', with several sections of ductwork combined into a single resistence. Our goal in this project was not to replace the P&W values but to benchmark the accuracy of simple one-dimensional flow models against the P&W resistences. If the models showed promise, they could be used to predict the effects of design changes in the RL10, and to predict the resistences of ducts and manifolds in new engine designs. Toward that end, we selected a single flow-resistence from the P&W data, one which could be clearly identified with a single physical component in the engine.

The duct chosen was that from the turbine housing discharge to the main fuel shut off valve. This duct is shown in Figure G1. The analysis performed was a based on Darcy's formula for compressibile flow. The analysis was done both manually and using the Crane software as described in References G1 and G2. The solution is complicated because of the large number of non-90-degree bends and the fact that the friction factor for the duct material is not known.

It should be noted that friction losses were also calculated by the RTE code using similar methods for the cooling jacket tubes. In that case, there are no discrete bends but the tubes are curved along their entire length. RTE calculates losses due to the curvature using a semi-empirical correlation (see Reference G3). It is not known how accurate the RTE prediction is, although one estimate of error could be set at about 6%. Further discussion of the prediction of cooling tube losses is not given here.

G.1 Estimates of duct segment equivalent lengths

The duct in question was decomposed into a series of curved and straight sections, as shown in Figure G1. Although the segments do not lie in a plane, any three-dimensional effects which might exist are not considered. Based on the angle of the bend, the radius of the bend, and a constant duct diameter assumed to be 2.402 inches, the bends were modeled as an 'equivalent' length in straight pipe. This is done automatically by the Crane software (probably by prorating the bend angle from 90 degrees). Table G1 shows the equivalent lengths estimated by the program for the bends in the duct.

Adding up the equivalent lengths of the bends and the straight section lengths, we obtain an over equivalent length of 123.8 inches, or 51.5 times the diameter of the pipe.

G.2 Determination of Pipe K factor

The friction losses in a pipe are often described by a K-factor, as defined by the equation below

$$\dot{m} = \frac{A * Y}{\sqrt{K}} \sqrt{2g * \Delta P * \rho}$$

In this expression for mass flow, Y is an expansion factor (used only for compressible flows), ΔP is the pressure difference across the pipe, ρ is the density and g is the gravitational constant. K is determined by the expression

$$K = \frac{f L}{D}$$

where f is the friction factor, L is the equivalent length, and D is the pipe inner diameter. f is not

known precisely and is often determined empirically for any given material and surface finish. Generally, the smoothest commercial pipe will have a friction factor (f) of at least 0.018. The ductwork of the RL10 is not, of course, commercial pipe. The friction factor is determined by the surface roughness and the fluid Reynold's Number (which gives an indication of its viscosity and degree of turbulence). A second estimate for the friction coefficient (f) of the duct may be obtained by using an absolute roughness similar to that of the cooling jacket tubes (4.6×10^{-5}inches), for example. The friction factor would then be 0.0095 for completly turbulent flow. Using these two values of f for commercial pipe and jacket tubing as upper and lower bounds, the predicted K for the duct would be between 0.928 and 0.487.

G.3 Comparison of Prediction with suggested value.
Pratt & Whitney has specified that the flow though this duct be modeled by the expression

$$\dot{m} = \sqrt{\frac{\Delta P * P_{inlet}}{K_C * T_{inlet}}}$$

and K_C=0.4335 as suggested by Pratt & Whitney.

This formula was probably empirically determined. This representation can be converted to the Darcy equation if we assume an ideal gas correlation for the hydrogen, modified by the compressibility

$$\rho = \frac{P}{R * T}$$

Then K can be expressed by

$$K = K_C * (2g / R * A^2 * Y^2)$$

If the expansion factor Y is assumed to be 0.931 (as predicted by the Crane software), then we see that the suggested value of K is 0.648.

The predicted range of K values (0.487 to 0.928) encompasses the value specified by Pratt & Whitney. The predicted range of values includes uncertainty in the friction coefficient, f, and in the proper equivalent lengths for all the duct bends.

It might be possible to calibrate the f for the RL10 ducts using the value of Kc provided by P&W and described above. If necessary, this value could be used in conjunction with simple 1D models to predict the effect of changes to the RL10 ductwork. For new engine designs, there will be some uncertainty regarding the duct interior surface roughness. One dimensional models such as were used here can be used to predict the flow-resistence with uncertainty for new designs. Two and three dimensional flow analysis tools might also be used to refine estimates of flow resistence, especially in predicting the losses due to bends, flanges and other features. Tools of this kind are typically complicated and difficult to use, and were considered beyond the scope of this project. The best method is still to use test data when available.

References

G1. Crane Company, *Technical Paper No. 410, Flow of Fluids Through Valves, Fittings, and Pipe*, 1982.

G2. Crane Co. and ABZ Inc., *Crane Companion to Flow of Fluids Through Valves, Fittings, and Pipe*, (software), 1992.

G3. Naraghi, M.H.N., *RTE - A Computer Code for Three-Dimensional Rocket Thermal Evaluation*, (NASA Grant NAG 3-892), July 1991.

Table G1
Estimated Equivalent Lengths of Duct Sections

Description	Manual Estimate (in.)	Software Estimate (in.)
0.185 in. straight section	0.185	0.185
97.5 deg.bend (R=3.75 in.)	35.21	34.8
2.825 in. straight section	2.825	2.825
67.5deg.bend (R=12 in.)	33.36	28.80
1.519 in. straight section	1.519	1.519
104.5 deg.bend (R=6.25 in.)	30.63	32.40
3.572 in. straight section	3.572	3.572
30 deg.bend (R=10 in.)	5.212	13.20
6.452 in. straight section	6.452	6.452
Total	119.0	123.8

*Actual length of the duct is approximately 51.7 inches.

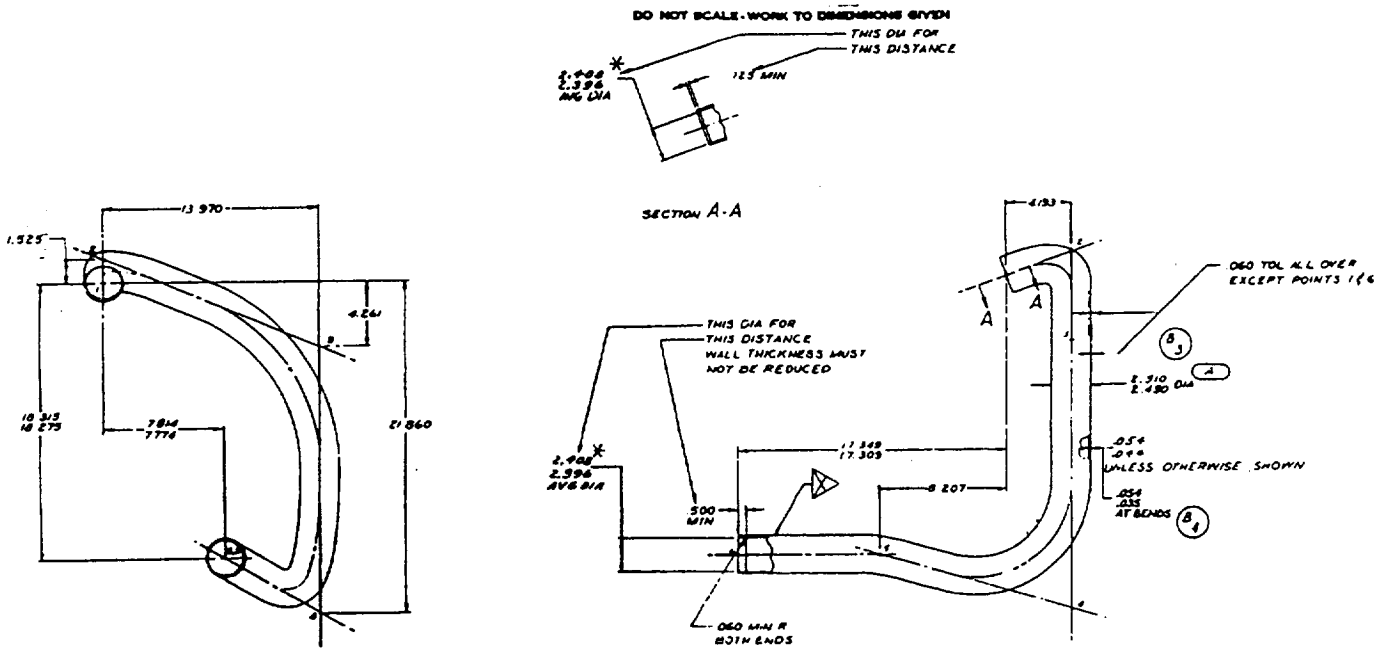

TUBE LENGTH OF STRAIGHT			ANGLE OF TUBE	BEND				MIN WALL THICKNESS AT BEND	MIN WALL THICKNESS OF STRAIGHT
				LOCATION	RADIUS (CL BEND)	∠			
1-2	.185	——	——	2	3.750	97° 51'	4.277	.833	——
2-3	——	2.825	71°26'	3	12.000	67° 30'	8.018	——	——
3-4	——	1.849	45° 67°31'	4	6.250	104° 26'	8.062	——	——
4-5	——	3.572	90° 116°38'	5	10.600	23° 54'	2.670	——	——
5-6	6.432	——	——	——	——	——	——	——	——

Figure G1

APPENDIX H
Modeling of Two-Phase (Liquid/Gas) Flow

The RL10A-3-3A rocket engine experiences two-phase liquid-gas flow at several locations during start and shutdown transients. These locations include the pump volute tongues, fuel-pump cool-down valves, oxidizer control valve, LOX injector elements, and combustion chamber throat. A model of this behavior in required which includes the transition between choked and unchoked flow, and the transition between single and two-phase flows.

H.1 Research performed regarding two-phase flow

There is a great deal of documentation on two-phase flow available (see references list). Unfortunately, much of this information is not applicable to rocket engine modeling. Many of the studies are strictly for water-steam flows (where most of the industrial interest lies) and contain empirical factors that don't necessarily apply to other fluids. Other research has been performed to investigate the physics of two-phase flow but has not produced useable correlations to predict the flow quantitatively. Still other correlations exist which are adequate for describing the flow in one regime (choked or unchoked, liquid, gas, or a two-phase mixture), but these expressions are incapable of estimating the transition between different behaviors. There are also several models which, although general, are so complex and computationally intensive that they proved to be beyond the scope of this project to incorporate. The approach that has been taken to model two-phase flow in the RL10 is based on several research papers (References H4 to H7). In some cases, the correlations suggested by this research have been replaced with simplified expressions and the transitions predicted by averaging the gas and liquid flow predictions.

H.2 Heterogenous fluid approaches

Heterogenous models keep the liquid and gas components of the two-phase mixture separate and distinct. The velocity of the gas bubbles is considered, as well as interactions (phase transitions) between the liquid and gas components caused by pressure and temperature variations along the path of the fluid. This can lead to a rather complex set of equations that must be solved simultaneously.

One such description of two-phase flow in short tubes, nozzles, and orifices is presented in Reference H4. In order to create such a heterogenous model, many estimates and assumptions pertaining to bubble formation and velocity, interphase mass and energy transfer, etc. are required. We were unable to reliably estimate such parameters for the RL10 components. It was therefore decided to focus on homogenous models instead, and return to the study of heterogenous models only if necessary. No further work was done on heterogenous models for the RL10 project.

H.3 Homogenous fluid approaches

Homogenous models treat the two-phase mixture as a single phase fluid with averaged properties. A number of different homogenous models have also been proposed (References H1 to H3), but most are based on empirical data and may not be applicable to cryogenic fluids. One relatively general approach is described in References H5 and H6. This method assumes isentropic flow through an orifice and can be used for both choked and unchoked flow. The expression for mass flux in this model is

$$G^2_{throat} = \frac{2}{V^2_{throat}} \int_{P_o}^{P_{throat}} V dP$$

$$V = \frac{1}{\rho} = \text{specific volume}$$

$$\rho = f(P, S_o) \text{ and } S_o = f(P_o, H_o)$$

from property tables

The choked condition can be determined by finding the throat static pressure which maximizes flow velocity at the throat. Although it is possible, in principle, to find the maximum using the derivative ($dG/dP_{throat} = 0$), this method was found to be numerically unstable. Instead, a 'golden section' search strategy has been used here to locate the maximum and calculate the throat pressure that results in choked flow.

The predicted critical mass flux of hydrogen at a temperature of 38 R and a range of upstream total pressures is shown in Figure H1. Reference H5 states that the predictions of the homogenous model may be low by as much as 50% in the subcooled region near saturation. This discrepancy will be discussed further in the next section of this appendix. It should also be noted that the above method of calculating critical mass flux proved impractical for transient simulations, the execution is simply too slow.

H.4 Simplified correlations and transitions

Most of the empirical expressions for two-phase flow are simple, but contain constants that are probably applicable only for the fluid tested (usually water and steam). Reference H7, however, describes some simple correlations which appear to be generally applicable. These expressions cover the case where the inlet pressure is at least 20% greater than the fluid saturation pressure. For fluids which are incompressible at the orifice inlet conditions, the suggested expression for critical flow is

$$\dot{m}_{crit} = C_d * A_{throat} \sqrt{2g * \rho_{inlet} * (P_{inlet} - P_{sat})}$$

For unchoked incompressible flow, the reference suggests using the actual downstream pressure rather than the vapor pressure in the expression above. This expression for flow matches the homogenous isentropic treatment described in the previous section for inlet pressures 20% greater than the fluid saturation pressure (see Figure H1).

As the upstream pressure approaches the saturation pressure, the expression above will predict a mass flow which approaches zero. If the actual discharge pressure is considerably below saturation, this prediction will obviously be incorrect (the flow won't stop if there is a pressure gradient across the orifice). The critical mass flow for inlet pressures less than approximately 20% above P_{sat} must be predicted by some other expression. As mentioned above, the homogenous isentropic calculation appears to underpredict the mass flow in this region, so that technique may not be valid there either. Pratt & Whitney had suggested that for some applications (like the LOX injector), the critical two-phase flow might be predicted as

$$\dot{m}_{crit} = C_d * A_{throat} \sqrt{2g * \rho_{inlet} * (P_{inlet} - P_{crit})}$$

where the P_{crit} is the critical throat pressure for isentropic expansion of an ideal gas through an

orifice. In fact, Pratt & Whitney has suggested that the specific heat ratio used to calculate this pressure be 1.4 (even for LOX). Consequently, P_{crit} is the inlet total pressure divided by 1.89. This assumption may be associated with the manner in which Pratt & Whitney determined the effective areas of the cooldown valves and LOX injector from the calibration test data.

Why should there be different expressions for critical two-phase flow in different components? After some consideration, we arrived at the following explanation. For sufficiently high inlet pressures and sufficiently low discharge pressures, the fluid will flash to vapor at the throat (but not upstream of it). Under these conditions, the flow characteristics would still be that of an incompressible fluid, but the flashing would create an area near the throat that would be equal to the saturation pressure of the fluid, even if the downstream pressure continued to decline (see Figure H2). As the inlet pressure decreases, there will be a threshold where the static pressure of the fluid at the throat will drop below the saturation pressure. At this point, the fluid will flash upstream of the throat. If we assume that the flashing creates densities low enough and fluid velocities high enough to go sonic at the throat, then the throat pressure will be limited by the corresponding critical pressure. Often cryogens (including hydrogen and oxygen) behave much like an ideal gas for pressures only slightly below the point of vaporization. This tends to support using the critical pressure as defined for flow of an ideal gas through the orifice. The flow still proceeds primarily as an incompressible fluid, but it becomes gaseous near the throat and its choking is governed by gas laws. For sufficiently low inlet pressures, the flow will be entirely vapor. These arguments have lead to the following expressions and rules for the new system model, as were also cited in the main report.

$$\dot{m} = C_d * A * \sqrt{2g * \rho_{inlet} * \delta_p}$$

$\delta_p = (P_{inlet} - P_{exit})$ for $P_{exit} > P_{sat}$

$\delta_p = (P_{inlet} - P_{exit})$ for $P_{crit} < P_{sat}$ and $P_{exit} > P_{crit}$

$\delta_p = (P_{inlet} - P_{sat})$ for $P_{crit} > P_{sat}$ and $P_{exit} < P_{sat}$

$\delta_p = (P_{inlet} - P_{crit})$ for $P_{crit} < P_{sat}$ and $P_{exit} < P_{crit}$

where P_{sat} = function of S_{inlet} looked up from tables

and $$P_{crit} = \left(\frac{2}{\gamma+1}\right)^{\frac{\gamma}{\gamma-1}}$$

The predicted flow rate using this method is shown in Figure H1, compared with the homogenous flux predictions. There was insufficient data in the literature to make a comparison with the heterogenous model described in Reference H4. The simple hybrid correlation described above predicts a flux of approximately twice that of the integral method near saturation. As was noted previously, Reference H5 suggests that this would better match experimental data and predictions of a heterogenous model.

This simple model provides a robust, efficient, and stable solution for two-phase choked and unchoked flows in the RL10 system during start and shutdown. This model also appears to correlate well with the available RL10 engine test data for the fuel cooldown valves and LOX injector.

For the OCV, we found that the hybrid solution gave flow rates that were too high when LOX pump discharge pressures approached saturation. This created greater losses in the LOX pump and lead to instabilities associated with phase transition. For reasons which are not yet understood, it appears that the OCV does not transition to the region of incompressible flow limited by critical pressure at the throat. Instead, that valve flow appears to continue along the curve limited by saturation pressure. At sufficiently low inlet pressures, the lower bound of OCV flow is predicted assuming critical, isentropic flow of an ideal gas (rather than two-phase flow).

$$\dot{m}_{liquid} = C_d * A * \sqrt{2g * \rho_{inlet} * \delta_p}$$

$$\delta_p = (P_{inlet} - P_{exit}) \qquad \text{for } P_{inlet} \text{ and } P_{exit} > P_{sat}$$

$$\delta_p = (P_{inlet} - P_{sat}) \qquad \text{for } P_{inlet} \text{ and } P_{exit} < P_{sat}$$

$$\dot{m}_{gas} = \sqrt{\frac{g_c \gamma}{R}} \left(\frac{2}{\gamma+1} \right)^{\frac{\gamma+1}{2(\gamma-1)}} \frac{A * P_0}{\sqrt{T_0}}$$

then

$$\dot{m} = \dot{m}_{liquid} \qquad \text{for } P_{inlet} > 1.2 * P_{sat}$$

$$\dot{m} = \text{maximum of } \dot{m}_{liquid} \text{ and } \dot{m}_{gas} \qquad \text{for } P_{inlet} < 1.2 * P_{sat}$$

H.5 Summary

Many options have been considered for predicting two-phase flow in the RL10 components. Much of the available information is strictly empirical and cannot always be applied. Although more general models were found in the literature, they were found to be impractical for use in the transient engine simulation. Ultimately, we decided on semi-empirical correlations which provide a reasonable match with RL10 data and which could be justified in some way based on physical arguments. It appears that there is still much opportunity for improvement in the analytic tools and our general understanding of two-phase flow under various conditions.

References

H1. Tong,L., *Boiling Heat Transfer and Two Phase Flow*, J. Wiley and Sons, New York 1965.

H2. Wallis,G.B., *One-Dimensional Two-phase Flow* , McGraw Hill, NewYork 1969.

H3. Smith, R.V., *Choking Two-phase Flow Literature Summary and Idealized Design Solutions for Hydrogen, Nitrogen, Oxygen and Refrigerants 12 and 11*, National Bureau of Standards Technical Note 179, August 1963.

H4. Henry, R. and Fauske, H., *The Two-phase Critical Flow of One-Component Mixtures in Nozzles, Orifices, and Short Tubes*, ASME Journal of Heat Transfer, May 1971.

H5. Simoneau, R. and Hendricks, R., *Generalized Charts for the Computation of Two-phase Choked Flow of Simple Cryogen Fluids*, Cryogenics, February 1977.

H6. Hendricks, R. and Stetz, T., *Flow Rate and Pressure Profiles for One to Four Axially Alined Orifice Inlets*, NASA TP-2460, May 1985.

H7. Applied Physics Laboratory, *JANNAF Rocket Engine Performance Test Data Acquisition and Interpretation Manual*, CPIA Publication 245, April 1975.

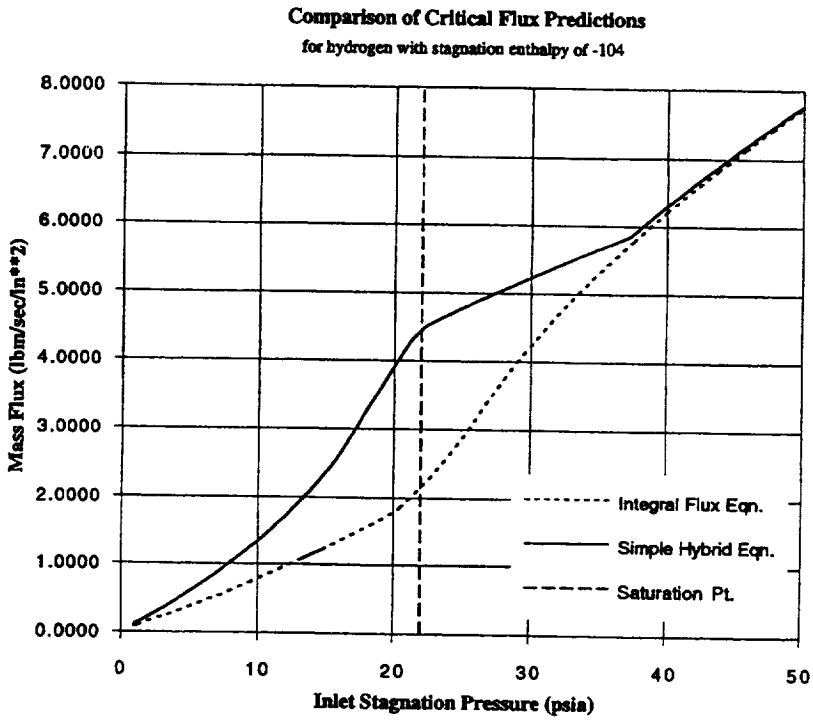
Comparison of Critical Flux Predictions
for hydrogen with stagnation enthalpy of -104
Mass Flux (lbm/sec/in**2)
8.0000
7.0000
6.0000
5.0000
4.0000
3.0000
2.0000
1.0000
0.0000
0
10
20
30
40
50
Inlet Stagnation Pressure (psia)
Integral Flux Eqn.
Simple Hybrid Eqn.
Saturation Pt.

Figure H1

Simple Incompressible Correlations for Critical Two-Phase Flow through an Orifice

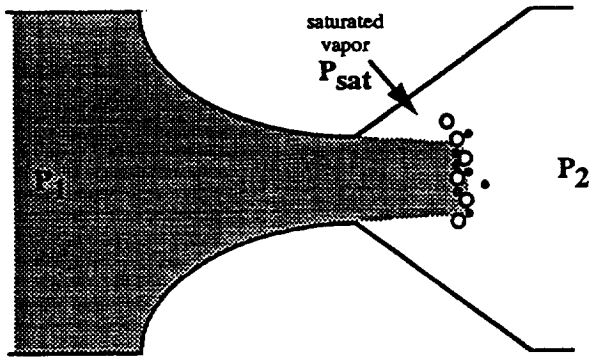

Case 1: fluid flashes at the throat (but not upstream of it).

$$\text{flow} = C_d * A_{throat} * (2g * \rho_1 * (P_1 - P_{sat}))^{1/2}$$

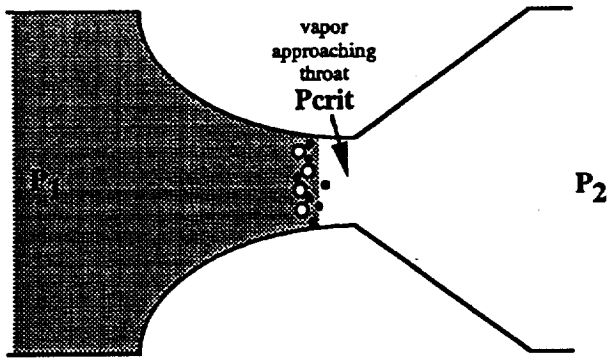

Case 2: fluid flashes upstream of throat.

$$\text{flow} = C_d * A_{throat} * (2g * \rho_1 * (P_1 - P_{crit}))^{1/2}$$

where P_{crit} is based on ideal gas assumptions

Figure H2

APPENDIX I
SYMBOLS

A	Area (in^2)
Cd	Discharge coefficient (dimensionless)
c_p	specific heat capacity at contant pressure (BTU / lb)
c_v	specific heat capacity at contant volume (BTU / lb)
g	gravitational acceleration (386.1 in / sec^2)
h	head parameter for extended pump performance maps.
H	enthalpy (BTU / lb)
htc	heat transfer coefficient (BTU / sec / R)
$\dot{m}$	mass flowrate (lbm/sec)
N	Rotational speed (revolutions / minute (rpm))
P	Pressure (lbf / in^2)
Q	Volumetric Flow (gallons / minute (gpm))
$\dot{q}$	heat transfer rate (BTU/sec)
Re	Reynold's Number =
t	time (sec)
T	Temperature (R)
β	the torque parameter for extended pump maps
γ	specific heat ratio (c_p / c_v)
Δ	change in associated parameter
δ_p	effective pressure difference (choked or unchoked flow)
μ	absolute viscosity
τ	torque (lb-in)
ϕ	pump flow coefficient
ψ	pump head coefficient

Subscripts:

d	design point conditions (usually point of maximum efficiency)
g	hot-gas side conditions
c	coolant-side contions
0	stagnation conditions OR inital conditions (depending on context)

APPENDIX J
GLOSSARY OF MODEL COMPONENT NAMES

AMB	Ambient Conditions
CHEX	Combustion Chamber Heat Exchanger (Cooling Jacket)
CHMB	Combustion Chamber and Nozzle
FCV1	Fuel-pump Interstage Cool-down Valve (also ISCDV)
FCV2	Fuel-pump Discharge Cool-down Valve (also FDCDV)
FINJ	Fuel Injector Resistance
FINV	Fuel Engine Inlet Valve
FPA	Fuel Pump First Stage
FPB	Fuel Pump Second Stage
FSOV	Fuel Shut Off Valve
FTBV	Fuel Turbine Bypass Valve (see also TCV - Thrust Control Valve)
FTRB	Fuel Turbine
F3	Fuel Turbine Discharge Housing Resistance
F4	Resistance of Duct from Turbine Discharge Flange to FSOV
IJHX	Injector inter-propellant heat transfer
LBV	LOX Bypass Valve (part of the Oxidizer Control Valve)
LEAK	Gear-box leakage rate schedules
MRV	Mixture Ratio Valve (part of the Oxidizer Control Valve)
OCV	Oxidizer Control Valve (the MRV and LBV combined unit).
OINJ	Oxidizer Injector Resistance
OINV	Oxidizer Inlet Valve
OXIN	LOX Engine Feed-Duct Inertia
RFPD	Fuel Pump Discharge Duct with Calibrated Orifice
RHX1	Cooling Jacket Resistance (Inlet manifold to turnaround duct)
RHX2	Cooling Jacket Resistance (Turnaround duct to 360-180 tube X-over)
RHX3	Cooling Jacket Resistance (360-180 tube X-over to throat)
RHX4	Cooling Jacket Resistance (Throat to converging section inlet)
RHX5	Cooling Jacket Resistance (Converging section inlet to Injector face)
SHFT	Turbopump rotordynamics (inertia, bearing friction, gear ratios)
TCV	Thrust Control Valve (see also FTBV - Fuel Turbine Bypass Valve)
VCIM	Cooling Jacket Inlet Manifold Volume and metal temp. dynamics
VFIJ	Fuel Injector Plenum Volume dynamics
VFPI	Fuel Pump Inlet Volume dynamics
VFP1	Fuel Pump Interstage Duct Volume dynamics
VFP2	Fuel Pump Discharge Duct Volume dynamics
VHX1	Cooling Jacket Vol. dyn. (Inlet manifold to turnaround duct)
VHX2	Cooling Jacket Vol. dyn. (Turnaround duct to 360-180 tube X-over)
VHX3	Cooling Jacket Vol. dyn. (360-180 tube X-over to throat)
VHX4	Cooling Jacket Vol. dyn. (Throat to converging section inlet)
VHX5	Cooling Jacket Vol. dyn. (Converging section inlet to Injector face)
VNTR	Venturi Resistance
VOIJ	LOX Injector Plenum Volume dynamics
VOIN	LOX Engine Feed-duct Volume dynamics
VOPI	LOX Pump Inlet Volume dynamics
VOP1	LOX Pump Discharge Duct Volume dynamics
VTI	Turbine Inlet Duct Volume dynamics
VTD	Volume dynamics for Duct from Turbine Discharge Flange to FSOV
VTDH	Turbine Discharge Housing Volume dynamics

13. REFERENCES

1. Binder, M. - Sverdrup Technology Inc., *An RL10A-3-3A Rocket Engine Model Using the ROCETS Software*, AIAA Paper 93-2357, June 1993.

2. Pratt & Whitney Government Engines, *Design Report for RL10A-3-3A Rocket Engine*, (NASA Contract NAS3-22339, Pratt & Whitney Report No. FR-15876), January 1982.

3. Chaudhry, H., *Applied Hydraulic Transients - 2nd Edition*, Van Nostrand Reinhold, New York 1987.

4. Veres, J., *A Pump Meanline Analysis Code (PUMPA)*, NASA TM-106745, October 1994.

5. Gulbrandsen, N. *Centrifugal Pump Loss Isolation Program (LSISO)*, COSMIC Program # MFS-13029, April 1967. *(note that the version of LSISO used in this study is not publicly available, this reference gives a general description of the program in its original, publicly disseminated form).

6. Steppanoff, A.J., *Centrifugal and Axial Flow Pumps, 2nd Edition*, J. Wiley and Sons, New York, 1957

7. Rostafinski, W., *An Analytical Method for Predicting the Performance of Centrifugal Pumps During Pressurized Startup*, NASA TN D-4967, January 1969.

8. Veres, J., *A Turbine Meanline Analysis Code (TURBA)*, NASA TM (number pending), 1995.

9. Pratt & Whitney Government Engines, *System Design Specification for the ROCETS System - Final Report*, NASA CR-184099, July 1990.

10. McBride, B. and Gordon, S. *CET93 and CETPC: An Interim Updated Version of the NASA Lewis Computer Program for Calculating Complex Chemical Equilibria with Applications* , NASA TM-4557, March 1994.

11. Private discussions with Tom Tomsik (NASA LeRC 5320) and Dick Quentmeyer (NYMA Inc. NASA LeRC SETAR)

12. Naraghi, M.H.N., *RTE - A Computer Code for Three-Dimensional Rocket Thermal Evaluation*, (NASA Grant NAG 3-892), July 1991.

13. Sutton, G., *Rocket Propulsion Elements - Sixth Edition*, J.Wiley and Sons, New York 1992.

14. Muss, J. and Nguyen, T., *User's Manual for Rocket Combustor Interactive Design (ROCCID) and Analysis Computer Program*, NASA CR-1087109, May 1991.

15. Wanhainen, R., *Throttling Characteristics of a Hydrogen-Oxygen, Regeneratively Cooled, Pump-Fed Rocket Engine*, NASA TM X-1043, December 1964.

16. Nickerson, G., *Two-Dimensional Kinetics (TDK) Nozzle Performance Computer Program - Users Manual*, (NASA Contract NAS8-39048), March 1993.

17. Crane Company, *Technical Paper No. 410, Flow of Fluids Through Valves, Fittings, and Pipe*, 1982.

18. Crane Co. and ABZ Inc., *Crane Companion to Flow of Fluids Through Valves, Fittings, and Pipe*, (software), 1992.

19. Henry, R. and Fauske, H., *The Two-phase Critical Flow of One-Component Mixtures in Nozzles, Orifices, and Short Tubes*, ASME Journal of Heat Transfer, May 1971.

20. Tong, L., *Boiling Heat Transfer and Two Phase Flow*, J. Wiley and Sons, New York 1965.

21. Wallis, G.B., *One-Dimensional Two-phase Flow* , McGraw Hill, NewYork 1969.

22. Simoneau, R. and Hendricks, R., *Generalized Charts for the Computation of Two-phase Choked Flow of Simple Cryogen Fluids*, Cryogenics, February 1977.

23. Applied Physics Laboratory, *JANNAF Rocket Engine Performance Test Data Acquisition and Interpretation Manual*, CPIA Publication 245, April 1975.

24. Smith, R.V., *Choking Two-phase Flow Literature Summary and Idealized Design Solutions for Hydrogen, Nitrogen, Oxygen and Refrigerants 12 and 11*, National Bureau of Standards Technical Note 179, August 1963.

25. Streeter, V. and Wylie, E., *Fluid Mechanics - Seventh Edition*, McGraw Hill, New York 1979.

26. Perry, R. and Chilton, C., *Chemical Engineer's Handbook - Fifth Edition*, McGraw Hill, New York 1973.

27. Private discussions with Todd Denman, Pratt & Whitney Government Engines, West Palm Beach, Florida

28. RL-10 Start Capability Working Group (government/industry cooperative), *AC-71 Failure Investigation - Final Report*, (no contract or report number given), December 1993.

REPORT DOCUMENTATION PAGE

Form Approved
OMB No. 0704-0188

1. AGENCY USE ONLY (*Leave blank*)	2. REPORT DATE	3. REPORT TYPE AND DATES COVERED
	January 1997	Technical Memorandum

4. TITLE AND SUBTITLE

RL10A-3-3A Rocket Engine Modeling Project

5. FUNDING NUMBERS

WU-564-09-10

6. AUTHOR(S)

Michael Binder, Thomas Tomsik, and Joseph P. Veres

7. PERFORMING ORGANIZATION NAME(S) AND ADDRESS(ES)

National Aeronautics and Space Administration
Lewis Research Center
Cleveland, Ohio 44135-3191

8. PERFORMING ORGANIZATION REPORT NUMBER

E-10414

9. SPONSORING/MONITORING AGENCY NAME(S) AND ADDRESS(ES)

National Aeronautics and Space Administration
Washington, D.C. 20546-0001

10. SPONSORING/MONITORING AGENCY REPORT NUMBER

NASA TM-107318

11. SUPPLEMENTARY NOTES

Michael Binder, NYMA, Inc., 2001 Aerospace Parkway, Brook Park, Ohio 44142 (work funded under NASA Contract NAS3-27186); Thomas Tomsik and Joseph P. Veres, NASA Lewis Research Center. Responsible person, Thomas Tomsik, organization code 5340, (216) 977-7519.

12a. DISTRIBUTION/AVAILABILITY STATEMENT

Unclassified - Unlimited
Subject Category 20

This publication is available from the NASA Center for AeroSpace Information, (301) 621-0390.

12b. DISTRIBUTION CODE

13. ABSTRACT ***(Maximum 200 words)***

Two RL10A-3-3A rocket engines comprise the main propulsion system for the Centaur upper stage vehicle. Centaur is used with both Titan and Atlas launch vehicles, carrying military and civilian payloads from high altitudes into orbit and beyond. The RL10 has delivered highly reliable service for the past 30 years. Recently, however, there have been two in-flight failures which have refocused attention on the RL10. This heightened interest has sparked a desire for an independent RL10 modeling capability within NASA and the Air Force. Pratt & Whitney, which presently has the most detailed model of the RL10, also sees merit in having an independent model which could be used as a cross-check with their own simulations. The Space Propulsion Technology Division (SPTD) at the NASA Lewis Research Center has developed a computer model of the RL10A-3-3A. A project team was formed, consisting of experts in the areas of turbomachinery, combustion, and heat transfer. The overall goal of the project was to provide a model of the entire RL10 rocket engine for government use. In the course of the project, the major engine components have been modeled using a combination of simple correlations and detailed component analysis tools (computer codes). The results of these component analyses were verified with data provided by Pratt & Whitney. Select modeling results and test data curves were then integrated to form the RL10 engine system model. The purpose of this report is to introduce the reader to the RL10 rocket engine and to describe the engine system model. The RL10 engine and its application to U.S. launch vehicles are described first, followed by a summary of the SPTD project organization, goals, and accomplishments. Simulated output from the system model are shown in comparison with test and flight data for start transient, steady state, and shut-down transient operations. Detailed descriptions of all component analyses, including those not selected for integration with the system model, are included as appendices.

14. SUBJECT TERMS	15. NUMBER OF PAGES
RL10; RL10A-3-3A; Rocket engine; Simulation; Models	182
	16. PRICE CODE: A09

17. SECURITY CLASSIFICATION OF REPORT	18. SECURITY CLASSIFICATION OF THIS PAGE	19. SECURITY CLASSIFICATION OF ABSTRACT	20. LIMITATION OF ABSTRACT
Unclassified	Unclassified	Unclassified	